# THERE
# AND
# BACK
# AGAIN

The journey of sinking marine microplankton and
its implication for past, present and future climate
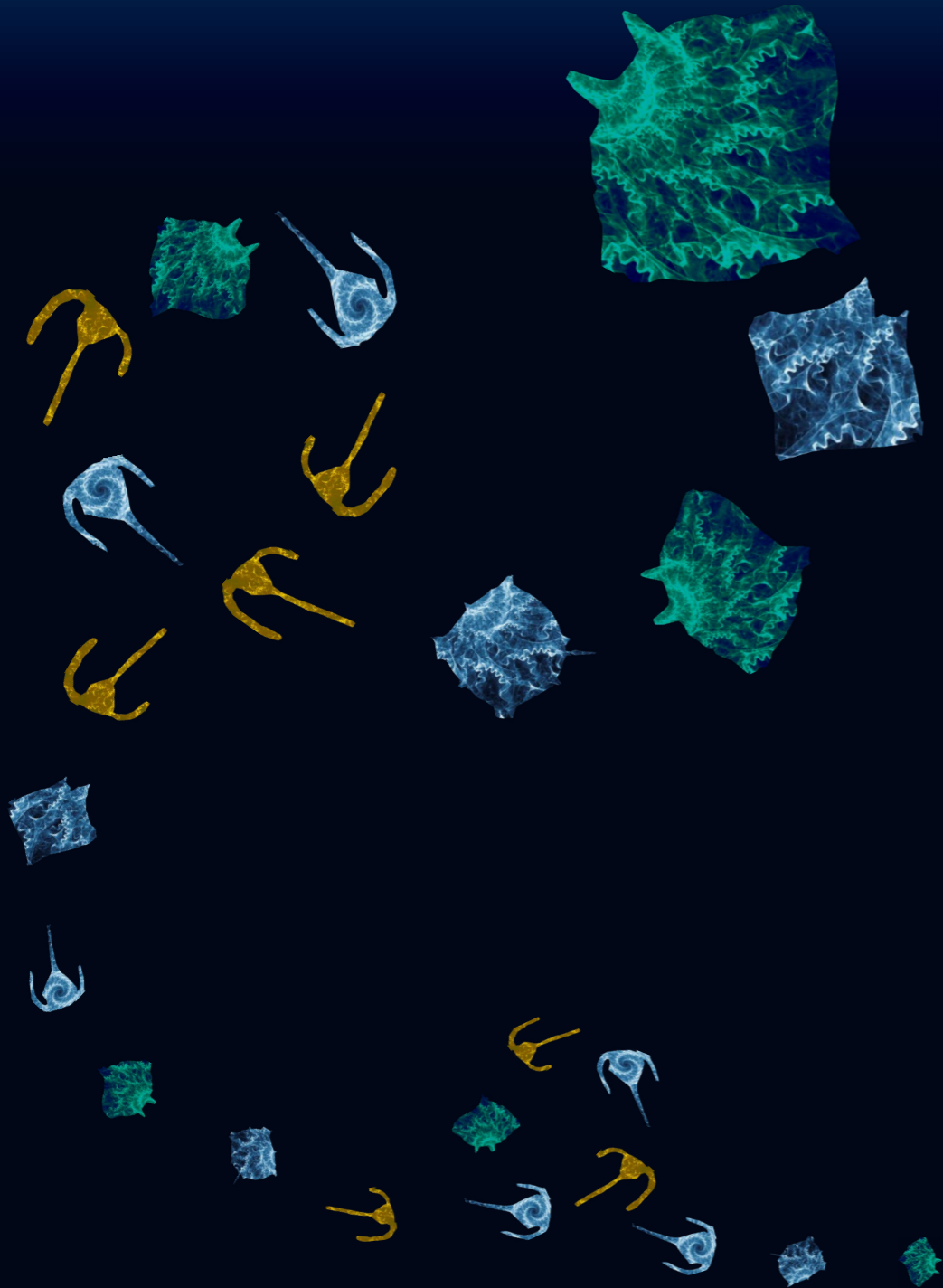
## Peter Nooteboom

# There and back again

The journey of sinking marine microplankton and its implication for past, present and future climate

Peter Nooteboom

2022

# There and back again

The journey of sinking marine microplankton and
its implication for past, present and future climate


## Daarheen en weer terug

De reis van zinkend marien microplankton en de implicaties voor
het klimaat van de toekomst, de huidige tijd en in het verleden

(met een samenvatting in het Nederlands)


## Proefschrift


ter verkrijging van de graad van doctor aan de Universiteit Utrecht op
gezag van de rector magnificus, prof. dr. H.R.B.M. Kummeling, inge-
volge het besluit van het college voor promoties in het openbaar te
verdedigen op 21 februari 2022 des middags te 4.15 uur


door


## Peter Dirk Nooteboom

geboren op 29 juli 1993
te Amersfoort

Promotor:     Prof. dr. ir. H.A. Dijkstra
Copromotor:   Dr. A.S. von der Heydt

# Contents

## List of Appendices

## Back Matter

# List of Frequently used Acronyms

| | |
|---|---|
| **AB** | Advection Bias |
| **ACC** | Antarctic Circumpolar Current |
| **APDF** | Advection PDF |
| **CESM** | Community Earth System Model |
| **dinocyst** | dinoflagellate cyst |
| **DP** | Drake Passage |
| **EAC** | East Australian Current |
| **EOT** | Eocene-Oligocene Transition |
| **GCM** | General Circulation Model |
| **GM** | Gent-McWilliams (i.e. the parameterisation of eddy-induced tracer mixing) |
| **LPDF** | Local PDF |
| **Ma** | Mega annum |
| **MHT** | Meridional Heat Transport |
| **MOC** | Meridional Overturning Circulation |
| **MSF** | Meridional Stream Function |
| **NEMO** | Nucleus for European Modelling of the Ocean |
| **OGCM** | Ocean General Circulation Model |
| **OFES** | OGCM for the Earth Simulator |
| **PI** | Pre-Industrial |
| **PIC** | Pre-Industrial Carbon (i.e. 280ppm $CO_2$ – 671ppb $CH_4$) |
| **POP** | Parallel Ocean Program |
| **PSU** | Practical Salinity Unit (i.e. ppt or g/kg) |
| **PDF** | Probability Density Function |
| **PW** | Petawatt (i.e. $10^{15}$W) |
| **SSH** | Sea Surface Height |
| **SSS** | Sea Surface Salinity |
| **SST** | Sea Surface Temperature |
| **Sv** | Sverdrup (i.e. $10^6$m$^3$/s) |
| **TG** | Tasmanian Gateway |

# Samenvatting in het Nederlands

Klimaatverandering is een van de grootste uitdagingen van de mensheid vandaag de dag. Hoe zal de aarde reageren op een stijging van de atmosferische broeikasgassen die nooit eerder met dezelfde snelheid heeft plaatsgevonden? Klimaatmodellen projecteren dat de gemiddelde temperatuur en de zeespiegel op aarde zal stijgen, de komende decennia en eeuwen.

Deze klimaatmodellen worden vaak gevalideerd met observaties uit de huidige tijd, maar kunnen die modellen dan ook worden gebruikt om een 'extreem' klimaat te representeren dat in de toekomst mogelijk is? Om een dergelijk 'extreem' klimaat beter te begrijpen, kunnen uitkomsten van klimaatmodellen vergeleken worden gedurende een periode uit het geologisch verleden, die het klimaat vertegenwoordigen in een periode waarin het warmer was dan vandaag.

Helaas zijn er geen satelliet observaties beschikbaar voor de afgelopen 100 miljoen jaar. De metingen van het klimaat in het verleden zijn meestal indirect (een proxy). Een groot deel van de klimaatproxy's komen uit microplankton. Microplankton zijn kleine ($\sim \mu$m) organismen die vaak dicht bij het oppervlak van de oceaan leven in een omgeving die zij fijn vinden. Deze microplankton zinkt (bijvoorbeeld na afsterven) naar de oceaanbodem, waar het in sedimenten eindigt en mogelijk gepreserveerd blijft. Zodoende eindigt het microplankton op de bodem van de oceaan, dat als 'archief' kan worden gebruikt voor het bepalen van het klimaat aan het bovenliggende oceaanoppervlak. Echter, het microplankton wordt getransporteerd door oceaanstromingen tijdens zijn reis naar de oceaanbodem. Als resultaat van deze zijdelingse verplaatsing, kan het zijn dat microplankton niet de bovenliggende oceaan representeert, maar het oceaanoppervlak op een andere locatie.

In dit proefschrift onderzoeken wij hoe ver zinkend microplankton zijdelings kan verplaatsen door de oceaan stromen tijdens de reis naar de oceaanbodem. Wij proberen hiermee te achterhalen waardoor de distributies van microplankton soorten in oceaan sedimenten bepaald wordt, en wat voor gevolgen dat heeft voor klimaat reconstructies die gebruik maken van deze microplankton.

Deze techniek wordt toegepast in het late Eoceen (38 miljoen jaar geleden), dat $\sim 8°$C warmer was dan vandaag en de vorming van permanent ijs op Antarctica vooraf ging ($\sim$34 miljoen jaar geleden). Als er bijvoorbeeld subtropische microplankton soorten gevonden worden bij Antarctica in een dergelijke tijdsperiode, dan zijn er twee hypotheses die getest kunnen worden met deze methode: (a) Antarctica had een subtropisch klimaat in dit tijdsinterval of (b) Antarctica had geen subtropisch klimaat en deze microplankton soort is vanaf een subtropisch gebied

naar Antarctica toe getransporteerd door oceaanstromen.

Dit proefschrift gaat over microplankton deeltjes die op de bodem van de oceaan liggen, die *daarheen* zijn getransporteerd door oceaanstromingen terwijl ze aan het zinken waren. Wij bepalen (*weer terug*) waar deze microplankton deeltjes vandaan zijn gekomen. Het doel is om hiermee te verklaren waarom er een discrepantie kan bestaan tussen klimaatmodellen en klimaatproxy's van het verleden. We bestuderen zodoende het klimaat van het verleden (*weer terug*), om een idee te krijgen in wat voor klimaat de mensheid in de toekomst (*daarheen*) terecht zou kunnen komen.
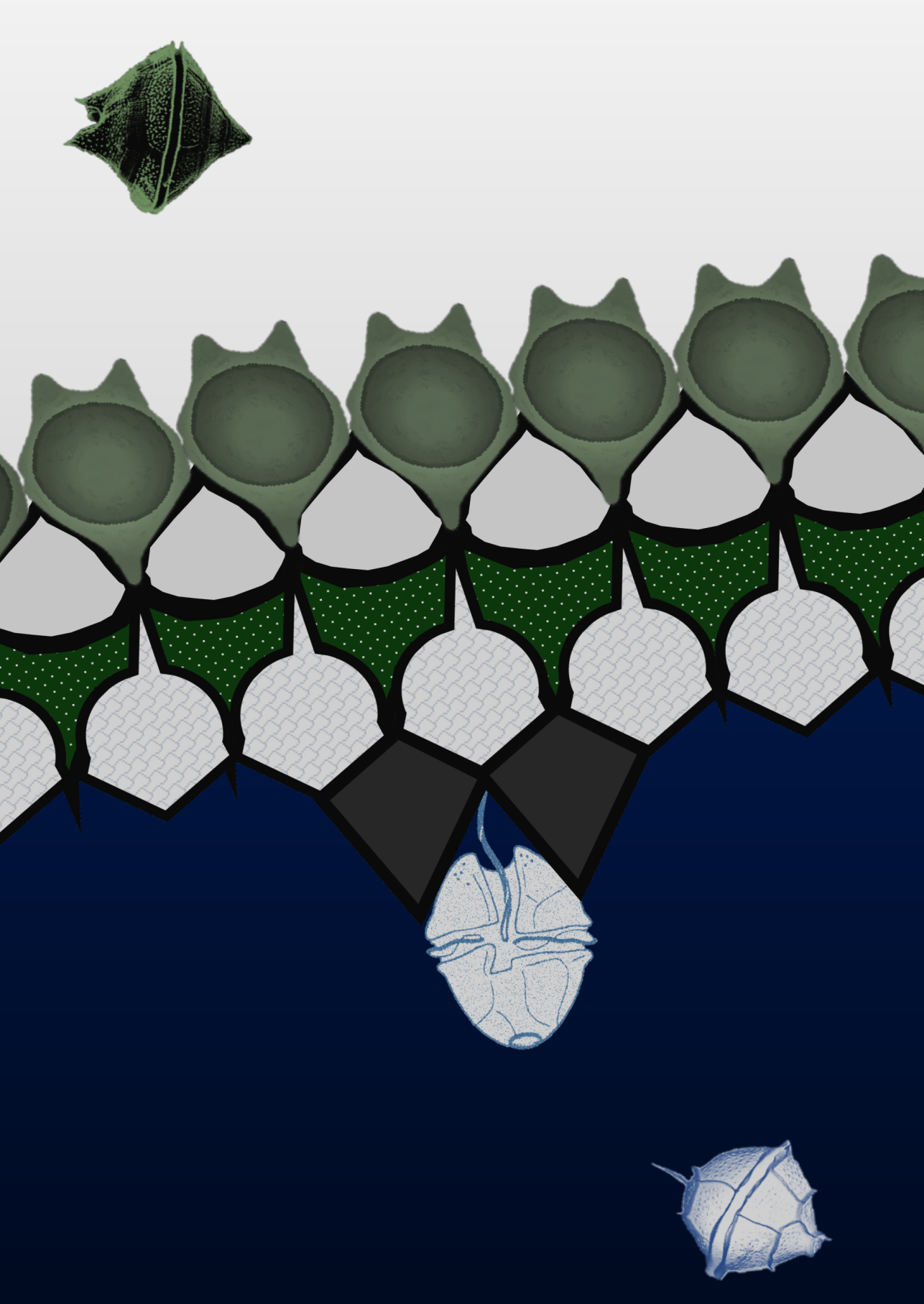
# CHAPTER 1

---

Introduction

1

Anthropogenic climate change is one of the greatest challenges for humanity today. How does the Earth system react to the atmospheric greenhouse gas increase that has never happened before with such speed in Earth's history? So far, climate models project an increase of the global average temperature, sea level (Church et al., 2013) and the number of 'extremely' warm days in the coming decades (Kirtman et al., 2013) and centuries (Collins et al., 2013). Although it is clear that the Earth is warming, uncertainty remains in the progression of those developments.

These climate models are inherently wrong (Box, 1976), but are they useful? Climate models give a proper representation of present-day climate, which we know from validations with observations. These models, which contain fundamental physical processes and have been developed over the past decades, cannot be validated in the increased greenhouse-climate of the future. We can however, compare the models with observations of warmer climates in the past, which are similar to the future climate, to get an understanding of these type of 'extreme' climates.

Although (unfortunately) no direct observations are available for the past hundred millions of years, we do find indirect evidence about the past climate (for example fossils or ice cores). These so-called proxies provide an archive of past climate and can be used to compare with climate model simulations (Haywood et al., 2019). As a result, the combination of models and proxies of past climate can be used to get a better understanding of how a future climate, which is warmer than today, may look like (Masson-Delmote et al., 2013; Tierney et al., 2020b).

A primary part of the Earth's archive to reconstruct past climates is provided by marine sediments, consisting of (fossil remains from) microplankton. The microplankton species in the bottom sediments originated from a location close to the ocean surface before they started sinking to the bottom. Hence, microplankton at the ocean bottom is representative of the ocean surface environment. It is often assumed that these planktonic species sunk vertically downwards. However, the microplankton is transported laterally by ocean currents during its sinking journey.

In this thesis, we investigate how sedimentary distributions of microplankton can be explained. We determine how sinking microplankton is advected by ocean currents, which may have great implications for the interpretation of sedimentary microplankton data. For example, subtropical and (sub)polar microplankton species alternate in sediment cores near Antarctica from 34 million years ago until the present-day (Bijl et al., 2018). If subtropical microplankton species are found near Antarctica in a specific time period, two hypotheses can be tested: (a) Antarctica had a subtropical climate, or (b) Antarctica was not subtropical, but the microplankton were transported laterally by ocean currents and originated from another region with a subtropical climate.

We study microplankton particles at the ocean bottom, which got *there* after a sinking journey, and determine their origin at the ocean surface *back again*. The ultimate goal is to bridge a gap between the models, which represent the global climate, and

the measurements, representing the climate at specific geographic locations. As such, we study past climates *back again*, to get an idea how we get *there* in the future.

Two scientific disciplines meet in this thesis: one is about climate proxies (biology) and the other is about climate models (physics). Therefore, we will give a brief background on the biology and physics context. Then we formulate the research questions and describe the full thesis outline.

## 1.1 Marine microplankton through the Cenozoic

If one is interested in how Earth's climate develops the coming century, which past time period is the best to study? Unfortunately, a time period which provides the perfect analogue to the future climate does not exist (or is not known of). First, such a perfect analogue must have had a similar state of the Earth system compared to the pre-industrial period. This implies that atmospheric $CO_2$ concentrations were 260-280ppmv and the Earth system (and its temperature) must have been in equilibrium to these $CO_2$ concentrations. Second, a perfect analogue requires a similar increase in $CO_2$ to what we are experiencing today since the pre-industrial period (which did not occur with a similar speed in Earth's past) (Lunt et al., 2013), in order to investigate how the Earth system may respond to such a large atmospheric $CO_2$ increase (i.e. the so-called transient response). Nevertheless, even if such a 'perfect' analogue would exist in the geologic record, the geography, bathymetry and land surface were different in the past compared to the present-day, which complicates a useful comparison between past and present climate.

Even though the perfect analogue of future climate does not exist in the past, the Cenozoic (66Ma until the present-day; figure 1.1) is the most recent time period in which the atmosphere contained similar $CO_2$ concentrations to what the Earth may experience the coming centuries. Hence, the Cenozoic contains time periods with global mean temperatures which are similar to those in the future, if the climate system fully responds to the increased $CO_2$ concentration (i.e. the climate is near equilibrium).

Some examples of Cenozoic climate analogues of the future are (Burke et al., 2018; Lear et al., 2020):

- After the Cenozoic onset at 66Ma (also known as the dinosaur mass extinction; K-Pg boundary), temperature increases until the **early Eocene** climate optimum (almost 16 °C warmer than today), after which it started cooling until the present-day. The early Eocene provides an analogue for the year 2250 (in a future scenario with relatively low/no mitigation of carbon emmissions; Fig. 1.1).
- The Eocene transits into the Oligocene (Eocene-Oligocene Transition; **EOT**) when permanent ice emerges on Antarctica (34Ma; from here the $\delta^{18}O$ signal in Fig 1.1 is also determined by ice volume) (Baatsen, 2018). Late Eocene atmospheric $CO_2$ is approximated to be 500-1200ppm (Anagnostou et al., 2016; Beerling & Royer, 2011).

- The Earth was $\sim 2°C$ warmer than today during the **Miocene** (Steinthorsdottir et al., 2021). The Miocene is an interesting future analogue, in particular because transitions may occur in climate subsystems from $2°C$ future warming, which may accellerate global warming (Steffen et al., 2018).
- Atmospheric $CO_2$ levels were similar to today in the **Pliocene**: An analogue for the climate of the coming decades (Dowsett et al., 2012).

Numerous palaeoclimate proxy types have been used to reconstruct past climates. Some of these proxies are found on land (Nooteboom, 2011) and others in ice (Cook, 2010 has an extensive overview of palaeoclimate proxies). A large part of these climate proxies do not go far back in time (e.g. up to at most 1.5 million years ago for ice cores; Parrenin et al., 2017). However, atmospheric $CO_2$ concentrations in 2025 could be similar to $CO_2$ values of around 3.3 million years ago (Ma) (Vega et al., 2020). If one pursues to study the equilibrium climate with atmospheric $CO_2$ concentrations representative of the year 2025 or later, we need climate proxies which go back more than 1.5Ma.

Microplankton in ocean bottom sediments provide proxies with one of the most extended reconstructions throughout the Cenozoic (Westerhold et al., 2020). These reconstructions sometimes use relative microplankton species abundances (i.e. percentages of microplankton species at a sedimentary location), assuming that the sediment sample content is determined by abiotic drivers such as temperature. Other reconstruction types make use of isotope geochemistry, using for instance the relative presence of $^{18}O$ compared to $^{16}O$ isotopes in the fossil microplankton to reconstruct temperature ($\delta^{18}O$; Epstein et al., 1953).

Although figure 1.1 uses benthic (i.e. deep-sea living) foraminifera, this thesis is mostly about near-surface living microplankton: specifically planktic foraminifera and dinoflagellate cysts. While these microplankton live in surface waters, their remains sink. When found in sediment samples at the ocean bottom, they can be used to reconstruct the surface ocean conditions where they originated from, such as Sea Surface Temperature (SST) (Brassell et al., 1986; Dowsett et al., 2012; Houben et al., 2012; Pearson et al., 2001; Schouten et al., 2002). It is the proxy signal from these near-surface living microplankton types that are influenced by ocean advection during their sinking journey from the ocean surface to the bottom.

## 1.2 Palaeoclimate modelling

Proxies provide indirect measurements of past climate. For a long time, one has tried to make sense of these proxy data: first by comparing the data with relatively simple statistical-dynamical models, and later by comparing them with general circulation models (GCMs) (Kutzbach, 1985; Phillips, 1956). GCMs make use of an ocean and/or atmoshere which is defined as a three-dimensional grid of boxes that communicate with each other and set up a circulation. As such, a GCM solves a set of conservation equations on a discretized grid. Especially the GCMs became popu-
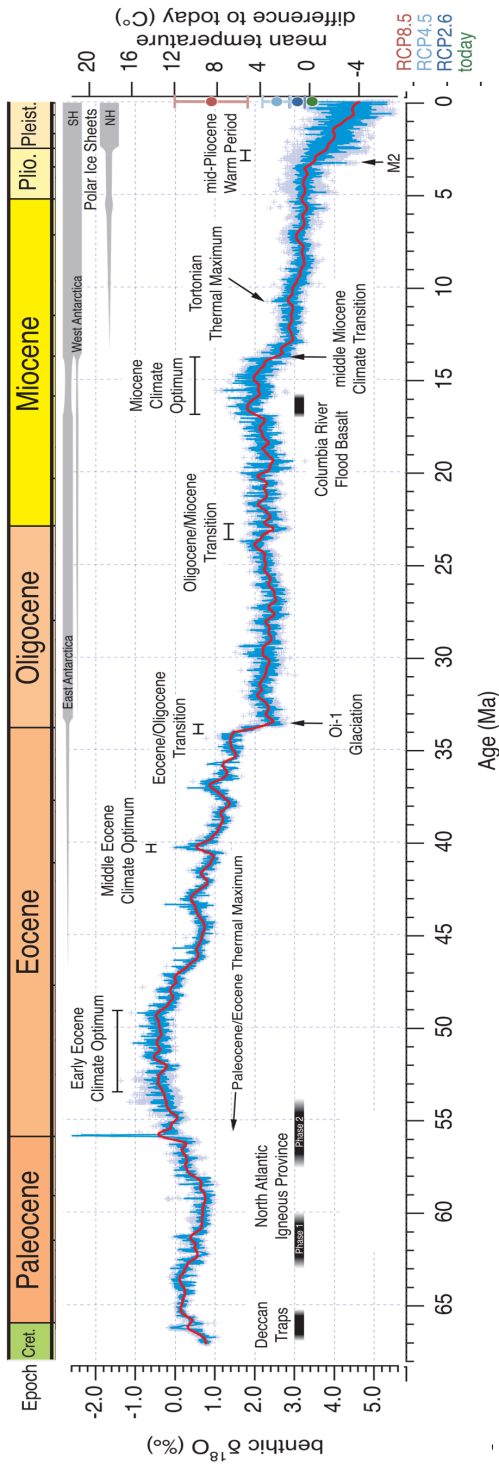
**Figure 1.1:** Cenozoic Global Reference benthic (i.e. living in the deep-sea) foraminifer oxygen Isotope ($\delta^{18}$O) Dataset (CENOGRID) from ocean drilling core sites spanning the past 66 million years. $\delta^{18}$O represents the ratio between $^{18}$O and $^{16}$O within the foraminifera and is a proxy of temperature and global ice mass (from 34Ma when permanent ice emerged). Oxygen isotope data have been converted to average temperature differences with respect to today. Future projections for global temperature (Palmer et al., 2018) in the year 2300 are shown by plotting three representative concentration pathways (RCP) scenarios (light blue, dark blue, and red dots). Gray horizontal bars mark rough estimates of ice volume in each hemisphere. Absolute ages for epochs and stages of the Cenozoic (GTS2012) are provided for reference. The oxygen isotope data axis is reversed to reflect warmer temperatures at times of lower $\delta^{18}$O values. This figure is adapted from Westerhold et al., 2020.

1

lar as computational power increased, which allowed to include more components (i.e. increasing the number of processes) and to increase the GCM complexity (i.e. solving smaller scales). GCMs use parameterisations for the small scales that are not resolved by the model (i.e. the sub-grid processes).

Roughly four factors determine the outcome of a GCM simulation. First, it is the boundary conditions. These are fixed during a particular simulation, such as incoming solar radiation, and the heat flux at the ocean surface. Second, the initial condition, which is the climate state from which the model starts simulating. The initial state of the model simulation is in particular important if there are multiple stable climate states, toward which the system can be attracted over time (Baatsen et al., 2018a; Gent, 2018; Hawkins et al., 2011; Weijer et al., 2019). Third, the model resolution (vertical and horizontal) determines to which level of detail the model resolves processes. Fourth, the type of model determines how the model is set-up, how many components of the climate system are included in the model and how the unresolved processes (e.g. the formation of clouds) are parameterised.

State-of-the-art global palaeoclimate GCMs currently contain an ocean, atmosphere, land surface and sea ice component which communicate with each other. The horizontal resolution is not below $1°$ ($\sim$100km) in the ocean and $2°$ ($\sim$200km) in the atmosphere (Hutchinson et al., 2018), which is limited by computational costs. Especially in palaeoclimate, GCM simulations are computationally expensive, because equilibria have to be computed. These simulations are initialised by a crude initial guess (i.e. initial condition), and run for thousands of model years until they are in (quasi-)equilibrium (after spin-up). It is the equilibrium output which is compared with the climate proxies (Lunt et al., 2013).

## 1.3 The middle-late Eocene

In this thesis we apply sinking Lagrangian particles to determine the lateral transport of microplankton in the middle-late Eocene (38Ma). This time period preceedes the Antarctic ice formation and rapid cooling during the EOT ($\sim$34Ma). Originally, the proposed mechanisms of the ice formation and rapid cooling during the EOT are (a) the thermal isolation of Antarctica by tectonic opening of the Drake Passage (DP; between South-America and Antarctica) and the Tasman Gateway (TG; between Australia and Antarctica), which resulted in a proto Antarctic Circumpolar Current (ACC; Kennett, 1977; Raymo & Ruddiman, 1992), and (b) a cooling of the atmosphere by declining $CO_2$ concentration. Both mechanisms are thought to compete with each other (Goldner et al., 2014), although both could have contributed to the Antarctic glaciation.

Many palaeoclimate modelling studies exist of the middle-late Eocene (Hutchinson et al., 2018; Tardif et al., 2020). The goal of many studies is to explain the Antarctic ice formation and rapid cooling during the EOT ($\sim$34Ma; Elsworth et al., 2017; Gasson et al., 2014; Hill et al., 2013; Kennedy et al., 2015; Kennedy-Asser et al., 2019; Kennedy-Asser et al., 2020; Ladant et al., 2018; Lunt et al., 2016), e.g. by

investigating the effect of gateway changes to ocean heat transport and hence the thermal isolation of Antarctica (Baatsen, 2018; Tumoulin et al., 2020). Although these changes in the palaeobathymetry were found to have a major impact on ocean heat transport (Viebahn et al., 2016) and climate in general (Lunt et al., 2017; Starz et al., 2017), increasing evidence exists that the drop in $CO_2$ is the leading mechanism of the two (Anagnostou et al., 2016; DeConto & Pollard, 2003; Houben et al., 2019; Huber & Nof, 2006; Huber et al., 2004; Kennedy-Asser et al., 2020; Pearson et al., 2009). Moreover, some issues remain with the thermal isolation mechanism being an important contributor to Antarctic glaciation: the timing of gateway openings is uncertain, and the effect of a changing bathymetry on ocean heat transport is mainly regional (Viebahn et al., 2016) and may not be large enough to trigger ice growth on a full continent (Huber et al., 2004). However, no GCM has been able to simulate the full transition to permanent Antarctic ice.

The conclusions from these studies about the Antarctic glaciation at the EOT rely on model-data comparisons. However, for a correct interpretation of the proxy data, the lateral transport of sinking microplankton by ocean currents has to be taken into account. One goal of this thesis is to build a framework where we can create a comparison between model simulations of the middle-late Eocene and marine proxy data, while taking into account the lateral advection of sinking microplankton. Ideally, this framework could also be applied to other time periods, to explain other outstanding questions than ice formation at the EOT, such as the occurrence of subtropical microplankton species near Antarctica in the Miocene (Bijl et al., 2018).

## 1.4 Research questions and thesis outline

In this thesis, we aim to answer the following questions:
1. How much can the lateral transport of microplankton influence their sedimentary species composition, and does this impact their relation with environmental variables at the ocean surface?
2. What is the impact of resolving eddies in an ocean model on sinking Lagrangian particles, and hence the modelled transport of sinking microplankton?
3. Do model-data comparisons of past climates improve if an eddying ocean model is used instead of a non-eddying model?

Here we provide the thesis outline that we use to answer these research questions.

In **chapter 2** we explain the methods that are used throughout the thesis. These include a description of the microplankton types that are studied, the method that is used to determine the sinking particle trajectories in ocean models and the background on processes that determine the sinking speed of particles.

Present-day, state-of-the-art climate model simulations are the most realistic ones (compared to those of the geologic past), since they are well tested with detailed observations (often made with satellites). Hence, the present-day provides a test case to compare sinking Lagrangian particles in these models with sedimentary mi-

1

croplankton. In **chapter 3**, we determine how far microplankton can travel laterally through transport by ocean currents in these models. We assess how much the sedimentary microplankton signal (in terms of e.g. temperature) is biased, by comparing the environment at their modelled origin location to the overlying surface. We also provide a case study of a specific microplankton species (*S.antarctica*). We show that *S.antarctica* represents a consistently colder environment than previously thought, because it was transported towards sites that are relatively warm.

One result of chapter 3, is that microplankton transport by ocean currents is spatially varying, which means that in some areas (e.g. near the Gulf Stream), sinking particles are transported far from their sedimentary location and can come from all kinds of directions, while in other areas (e.g. near the centre of a gyre) there is barely any lateral transport. In **chapter 4**, we investigate whether the spatially varying character of this lateral transport systematically influences the sedimentary microplankton composition. We use clustering techniques to determine oceanographically isolated areas (i.e. where particles are less 'mixed up' during their sinking journey compared to outside of these areas) and oceanographically disconnected areas. We show that the sediment samples in isolated clusters often contain a less biodiverse sedimentary microplankton composition and have a better statistical relation with surface environmental variables compared to sediment samples outside of these isolated areas.

Next, we would like to apply these virtual Lagrangian particles in climate model simulations which are representative of the past. However, state-of-the-art climate models of the past typically use a lower resolution ocean grid (not below $1°$ horizontally) compared to the resolution of present-day models ($\sim 0.1°$ horizontally). It is well known that this model resolution difference has major implications on the modelled ocean velocity field, especially that a high-resolution model provides an eddying flow field and a low-resolution model is non-eddying. In **chapter 5**, we test the implications of using a low-resolution model on the trajectories of sinking Lagrangian particles. We also test if a parameterisation can mimic the effect of eddies on sinking Lagrangian particles in the non-eddying low-resolution models.

The results from chapter 5 show that one should apply sinking Lagrangian particles in eddying ocean models, and we cannot use the non-eddying models of past climates that have so far been available. Hence, in **chapter 6** we perform the first eddying simulations of the middle-late Eocene ocean (38 Ma). We investigate how the increase of detail in the ocean model influences the sinking Lagrangian particles and its implications for comparison of the model with microplankton data. We compare the sinking Lagrangian particles with Antarctic-endemic dinocyst species occurrence, which provide a proxy for the regional flow. We also compare the model simulations with sea surface temperature reconstructions. We show that the mismatch between proxy data and non-eddying ocean models can be explained by the lack of eddies in the ocean models.

We end the thesis with a summary of the answers to the research questions formulated above and an outlook of future research that these answers imply in **Chapter 7**.
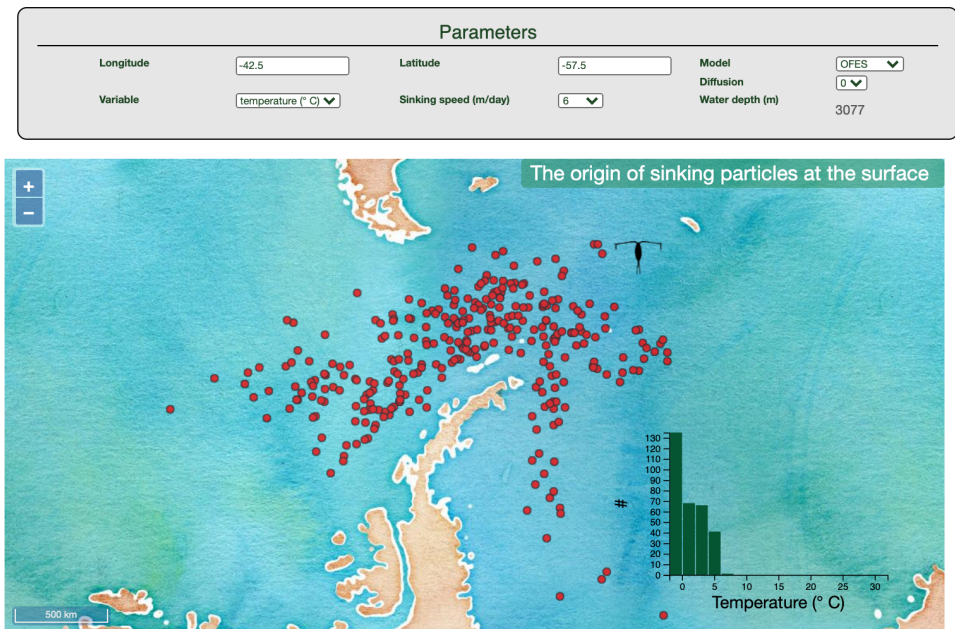
**Figure 1.2:** Illustration of the planktondrift.science.uu.nl website in the South Atlantic (near the Drake Passage). The black copepod points to the sedimentary release location. The red dots represent the particle distribution of surface origin locations for this release location. The histogram shows the distribution of sea surface temperature at the origin locations and the moment that sinking particles start their sinking journey. The 'parameters' box contains the particle release location of the copepod (°E and °N), the OGCM used, the variable that is shown in the histogram, the used sinking speed (m day$^{-1}$) and the water depth at the release location.

## 1.5 Website and code availability

Some of the results in this thesis consider sinking particles in ocean GCMs of the present-day. In order to disseminate these results, we created an interactive website (Fig. 1.2) where they can be accessed: planktondrift.science.uu.nl. Users of the online tool can choose a location at the bottom of the ocean in a map, to obtain a particle distribution of ocean surface origin locations of the particles that got there after their sinking journey. Users can choose several parameters (e.g. the sinking speed), and download the results. The website allows anyone who works with e.g. sedimentary microplankton assemblages or plastic to see how the sinking particles could be displaced laterally, and what the environment (e.g. sea surface temperature and salinity) is at the displaced location. Hence, the advection bias (chapter 3) of the sedimentary assemblages can be determined in the present-day ocean.

We created github repositories with the code that can be used to reproduce the results in this thesis. The URL to the github repository is added at the end of every

1
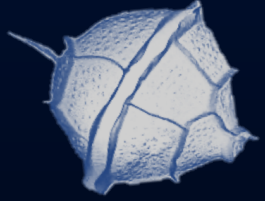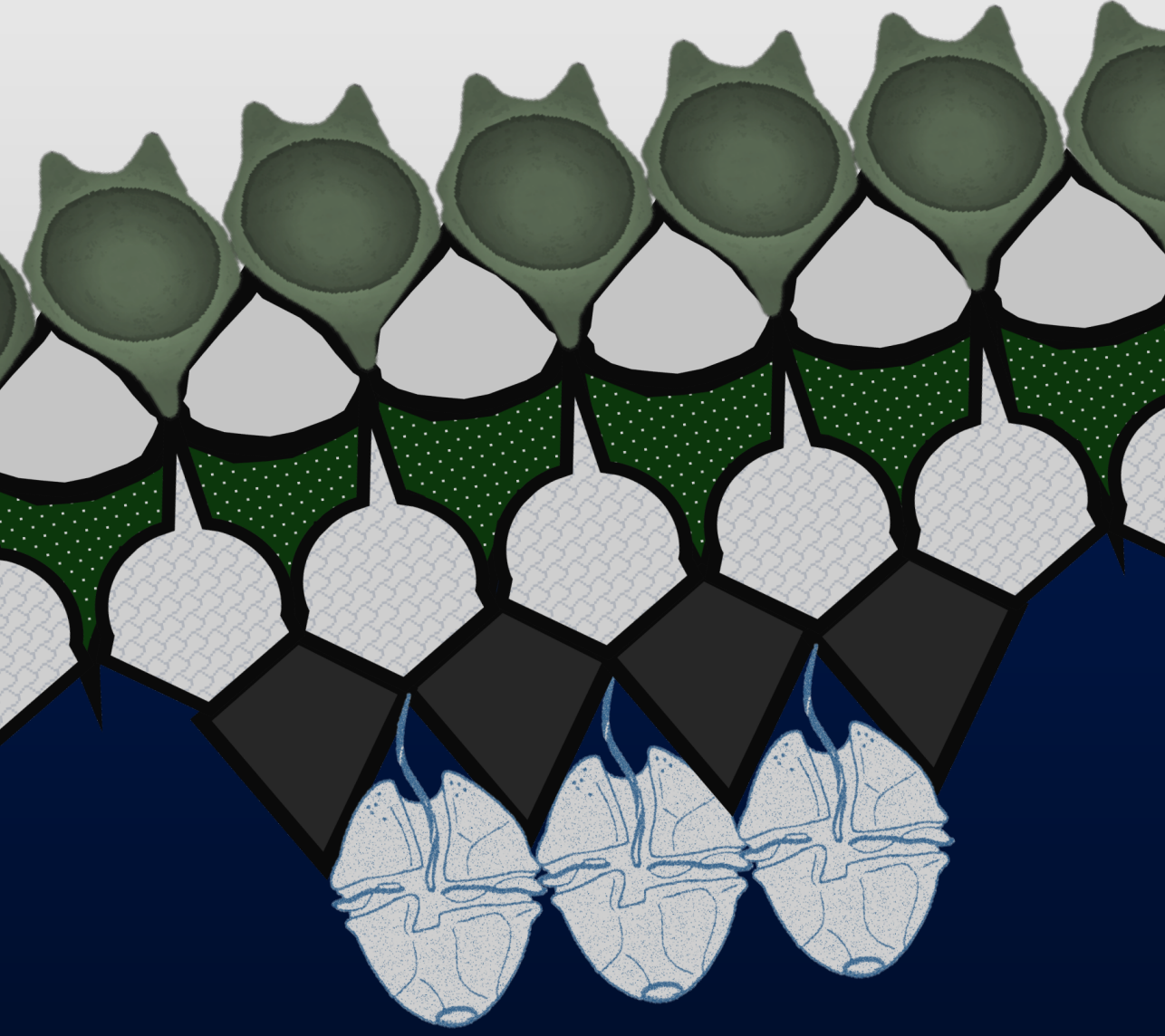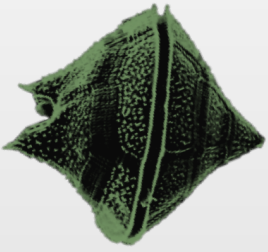
chapter.

# CHAPTER 2

---

## Sinking marine microplankton
### background and methods

## 2.1 The dinoflagellate cyst

In this thesis, we mostly focus on a specific type of sinking particle that is used for climate reconstructions: The dinoflagellate cysts (dinocyst). Dinocysts are formed by dinoflagellates, which are a common part of the ocean surface microplankton community. Dinoflagellates are unicellular and have two flagella, which ables them to swim (Fenchel, 2001) with a velocity in the order of 0.5 mm s$^{-1}$ (Hwan et al., 2011). This swimming velocity can be strong enough to swim against the ocean currents and stay in their typical habitat environment (Shulman et al., 2012; Smayda, 2002).

About 20% of the dinoflagellate species forms a cyst as part of their life cycle (Bravo & Figueroa, 2014; Evitt, 1985). The cyst is a protective biopolymer wall around the dormant dinoflagellate, in which it can sometimes survive up to a century if necessary (Ribeiro et al., 2011). If the dinoflagellate survives in the environment, it can also leave the cyst otherwise (Evitt, 1985). A cyst-producing dinoflagellate loses its mobility at cyst formation. From that time onward, the cyst is sinking while passively subject to ocean current transport until it reaches the ocean floor. As such, hatching of the dinoflagelate leaves the cyst as a microfossil trace in the sedimentary record if it is preserved.

It was shown that the composition of sedimentary dinocyst species relate to environmental conditions at the ocean surface, which makes them useful for climate reconstruction (Zonneveld et al., 2013b). For many cyst species, it is unknown which dinoflagellate produces a specific cyst. As a result, ecologic affinity of a dinocyst species in most cases cannot be derived from its biological producer, the dinoflagellate. Hence, the relationships between the nonmotile cysts and surface conditions are made independent of the taxonomy and biology of the motile dinoflagellates. Both quantitative (Frieling & Sluijs, 2018; Marret et al., 2001) and qualitative (Bijl et al., 2011, 2018; Cramwinckel et al., 2018; Crouch et al., 2014; Houben et al., 2013; Sluijs et al., 2005, 2006) paleoceanographic reconstructions based on dinocysts exist. These recontructions mostly use the species assemblages themselves as being representative for surface environmental variables (e.g. sea surface temperature or salinity), but also e.g. carbon isotopes that may be used to reconstruct carbon dioxide concentrations (Sluijs et al., 2018). Next to environmental variables, other mechanisms also determine dinocyst distributions at the ocean surface and in sediments such as ocean connectivity (Appendix D; chapters 3 and 4) and microplankton species interactions (Lima-Mendez et al., 2015).

## 2.2 The planktic foraminifera

In addition to dinocysts, we also use another type of microplankton in some chapters: Planktic foraminifera. During their life span, those zooplankton species can control their buoyancy (Furbish & Arnold, 1997), to remain at their ideal depth habitat while passively advected by ocean currents. Foraminifera grow a calcium

2
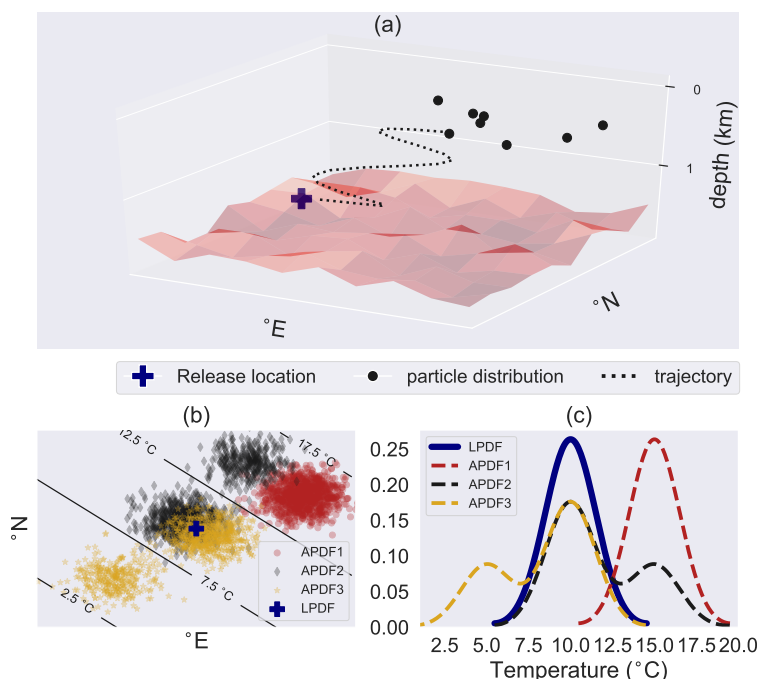


**Figure 2.1:** Schematic of (a) the backtracking analysis, (b) of possible back-tracked particle distributions and (c) of their temperature Probability Density Function (PDF), locally (LPDF) and after backtracking (APDF). (a) Three-dimensional plot. The particles are released at the sediment sample site at the blue cross and tracked back in time until the ocean surface is reached. (b) Map view. The blue plus represents the location of the sediment sample site. Red, black, and yellow are the backtracked locations in respectively the first, second, and third oceanographic setting. The contours show the annual average sea surface temperature. (c) The LPDF and the APDFs of sea surface temperature for the three backtracking scenarios in (b). In the first oceanographic setting (red; APDF1), all backtracked particles come from a warmer region, leading to a warm shift of the APDF with respect to the LPDF. The second (black; APDF2) and the third (yellow; APDF3) oceanographic setting result in, respectively, warm and cold tail with respect to the LPDF.

carbonate shell until they die and start sinking, and may end up in the sediments if they are preserved. Similarly to the dinocysts, relative foraminifera species abundances can be used for palaeoclimate reconstructions (Kucera et al., 2005). However, it is mostly the biogeochemical properties of the shell that are used for climate reconstructions (Katz et al., 2010), for example the $\delta^{18}O$ being a proxy for both sea surface temperature and global ice volume.

The sedimentary signal from planktic foraminifera biogeochemistry that is used to make palaeoceanographic reconstructions, is an accumulation of the shell isotopic composition. This shell is build along the trajectory that foraminifera travel during their life span. Hence, also the sedimentary foraminifera, and their biogeochemical properties, might be representative of an environment different than the overlying

surface of the sediment site (Boltovskoy et al., 2000; Sebille et al., 2015b; Weyl, 1978). Foraminifera have a high sinking velocity compared to dinocysts (~100m day$^{-1}$ versus ~10m day$^{-1}$). Hence, their sedimentary composition is likely more influenced by (near) surface currents, by which the foraminifera are advected during the life span, compared to their advection during the sinking journey. Hence, their biogechemical composition is mostly influenced by the average environment that the foraminifera experience during this life span.

## 2.3 Virtual sinking Lagrangian particles

The Lagrangian tracking method is specifically applied to the characteristics of the dinocysts in this thesis. Particles are released at the bottom of the ocean and tracked back in time until they reach the surface. As a result, a virtual particle is representative of a dinocyst which is found at the bottom, and can be related to the environment at the surface origin location of the particle after backtracking. Hence, it is assumed that the dinoflagellate was in its habitat when it formed the cyst. It is likely that this assumption is valid, since dinoflagellates are swimmers which tend to stay in an environment they like, and the dinoflagellate dies and is not preserved if it does not stay in this environment (it is the cyst that is preserved, not the dinoflagellate).

The use of a single particle which is advected by ocean flow cannot be representative of a dinocyst, because it could end up in a lot of different locations due to the turbulent nature of ocean flow and the chaotic character of the particle trajectories (Regier & Stommel, 1979). Hence, particles are released e.g. every day for several years at the ocean bottom, and tracked back in time along the three-dimensional velocity field $\vec{v}$ (which is changing in time), until they almost reach the surface (10m depth specifically; see Fig 2.1). The backtracking analysis results in distributions of particles at the ocean surface and of the environmental variables (e.g. temperature, salinity) at these locations (Fig. 2.1a, b). The resulting particle distributions allow us to investigate the statistics of particle ensembles, rather than single trajectories, which is often done in Lagrangian analyses (Sebille et al., 2018).

The particle distributions contain information of all possible dinocyst origin locations due to the flow transport. However, some of these pathways may not be representative of a sedimentary dinocyst. An origin location in the model could be in an environment where the cyst producing dinoflagellate does not occur in reality. Because the productivity of dinocyst species is generally not known at the ocean surface, we have to deal with a distribution which contains a larger habitat area than the dinocyst may have in reality.

The velocity field is provided by a general circulation model on a grid with a specific time resolution (~daily in this thesis). The velocity field at the particle location is determined with Parcels (Delandmeter & Sebille, 2019a; Lange & Sebille, 2017a), by interpolation. The particle is advected in time steps $\Delta t$ ($\Delta t$ ~10 minutes in this
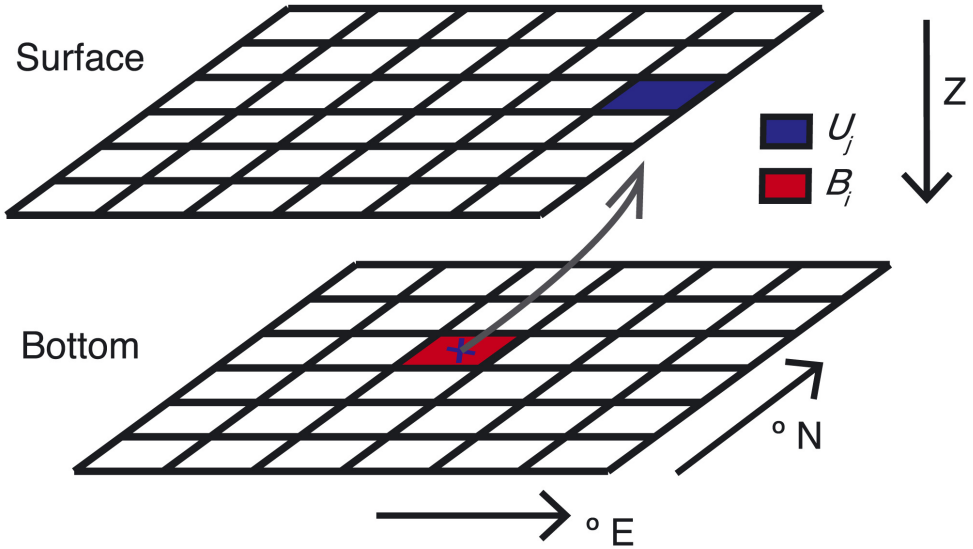
**Figure 2.2:** Illustration of the surface-bottom transportation matrix. The transportation matrix contains the probabilities that a particle which is found in bottom box $B_i$ came from box $U_j$ at the surface, for all $(i, j)$.

thesis) by:

$$\underbrace{\vec{x}(t-\Delta t)}_{\text{old position}} = \underbrace{\vec{x}(t)}_{\text{present position}} + \underbrace{\int_t^{t-\Delta t} \vec{v}(\vec{x}, \tau)d\tau}_{\text{flow transport}} + \underbrace{\vec{c}\Delta t}_{\text{sinking}} + \underbrace{\vec{q}\sqrt{2\nu(\vec{x})\Delta t}}_{\text{horizontal diffusion}} , \qquad (2.1)$$

with $\vec{x}(t)$ the three-dimensional position of the particle at time $t$, $\vec{v}(\vec{x}, t)$ the velocity field at location $\vec{x}$ and time $t$, $\Delta t$ is the time step, and $\vec{c} = \begin{pmatrix} 0 & 0 & -w_f \end{pmatrix}^T$ the sinking velocity. This implementation neglects the minor effects of particle inertia and Coriolis (Monroy et al., 2017). The flow transport is computed with a 4th order Runge-Kutta scheme.

The last term of Eq. 2.1 is the stochastic horizontal diffusivity term (only used in chapter 5). This term can be used to describe the particle advection due to processes that occur on a scale which is too small for the model to resolve. $\vec{q} = \begin{pmatrix} R_1 & R_2 & 0 \end{pmatrix}^T$ represents white noise in the zonal and meridional direction ($R_1$ and $R_2$ are independent of each other), with mean $\mu_{R_1} = \mu_{R_2} = 0$ and variance $\sigma_{R_1}^2 = \sigma_{R_2}^2 = 1$. The strength of the diffusivity term is given by the eddy diffusivity $\nu(\vec{x})$. It is often described by: $\nu(\vec{x}) = c_s A D_m$, where $A$ is the surface area of a grid cell in the ocean model and $c_s$ is a model-dependent constant. $D_m$ can be given by all sorts of parameterisations (Nicoud & Ducros, 1999; Nicoud et al., 2011; Smagorinsky, 1963; Vreman, 2004), and depends on the flow at the particle location.

One method to analyse the trajectories of the sinking particles (from Fig. 2.2) is the 'transportation' matrix ($T$). This matrix contains the probabilities that particles

move from some location at the surface to some other location at the bottom. The ocean bottom $Y$ is divided into the boxes $\{B_i\}_{i=1}^N$ and the surface of the ocean (or any other horizontal layer within the ocean) $Z$ is divided into the boxes $\{U_j\}_{j=1}^N$ (see figure 2.2). Particles are released every five days at the bottom of the ocean at uniformly distributed locations. The probability that a particle which is initialised at the bottom in any box $B_i$, reaches the surface in box $U_j$ within the total time period considered is calculated according to:

$$P_{ij} = \frac{\#\{y : y \in B_i \text{ and } T(y) \in U_j\}}{\#\{y : y \in B_i\}}. \tag{2.2}$$

Here $T(y) : Y \rightarrow Z$ maps a particle $y$ which is released at the bottom to the surface box where the cyst once formed at the surface. Hence $P_{ij}$ estimates the probability that a particle which is measured in box $B_i$ at the bottom comes from box $U_j$ at the surface where it once formed. This matrix allows us to investigate the validity of the assumption that particles sink vertically to the bottom up to a degree of uncertainty which is determined by the size of the boxes. Moreover, we can quantify the ocean surface area that is spanned by a sediment sample site in any bottom box by summing over the surface area of the connected surface boxes, which also depends on the choice of the box size. This box size is typically larger than the grid box sizes of the ocean model that provides the velocity field, in order to reduce computational costs.

## 2.4 The sinking speed of marine particles

One needs to choose a sinking velocity $w_f$ in Eq. 2.1 to represent a virtual sinking particle. For specific individual dinocyst species, the sinking speed is $6 - 11\text{m day}^{-1}$ according to lab experiments (Anderson et al., 1985) and it is $\gtrsim 100\text{m day}^{-1}$ for planktic foraminifera (Sebille et al., 2015b). Single dinocysts behave similar to fine silt particles (Dale, 1976). However, several processes can increase or decrease the sinking speed of these particles in the real world (Boyd et al., 2019; Stemmann et al., 2004).

The sinking speed $w_f$ greatly influences the travel time of sinking particles from ocean surface to bottom, and therefore their lateral transport in the backtrack analysis. It is worthwhile to explain the processes that influence $w_f$ and briefly review the literature on estimations of the particle sinking speed in the ocean. We mostly focus on mechanisms that determine the sinking speed of dinocysts here, because the sinking speed of individual foraminifera is typically much higher than dinocysts. Hence, foraminifera displacement is generally smaller during their sinking journey compared to their life span (when it is advected by near-surface currents).

The particle sinking speed is determined by water properties (the water density $\rho_f$, the water (dynamic) viscosity $\mu$) and particle properties (the particle shape, density $\rho_p$ and radius $R$). Stokes sinking is an often used approximation for the sinking speed, which assumes a perfect sphere in a laminar flow (i.e. the Reynolds number
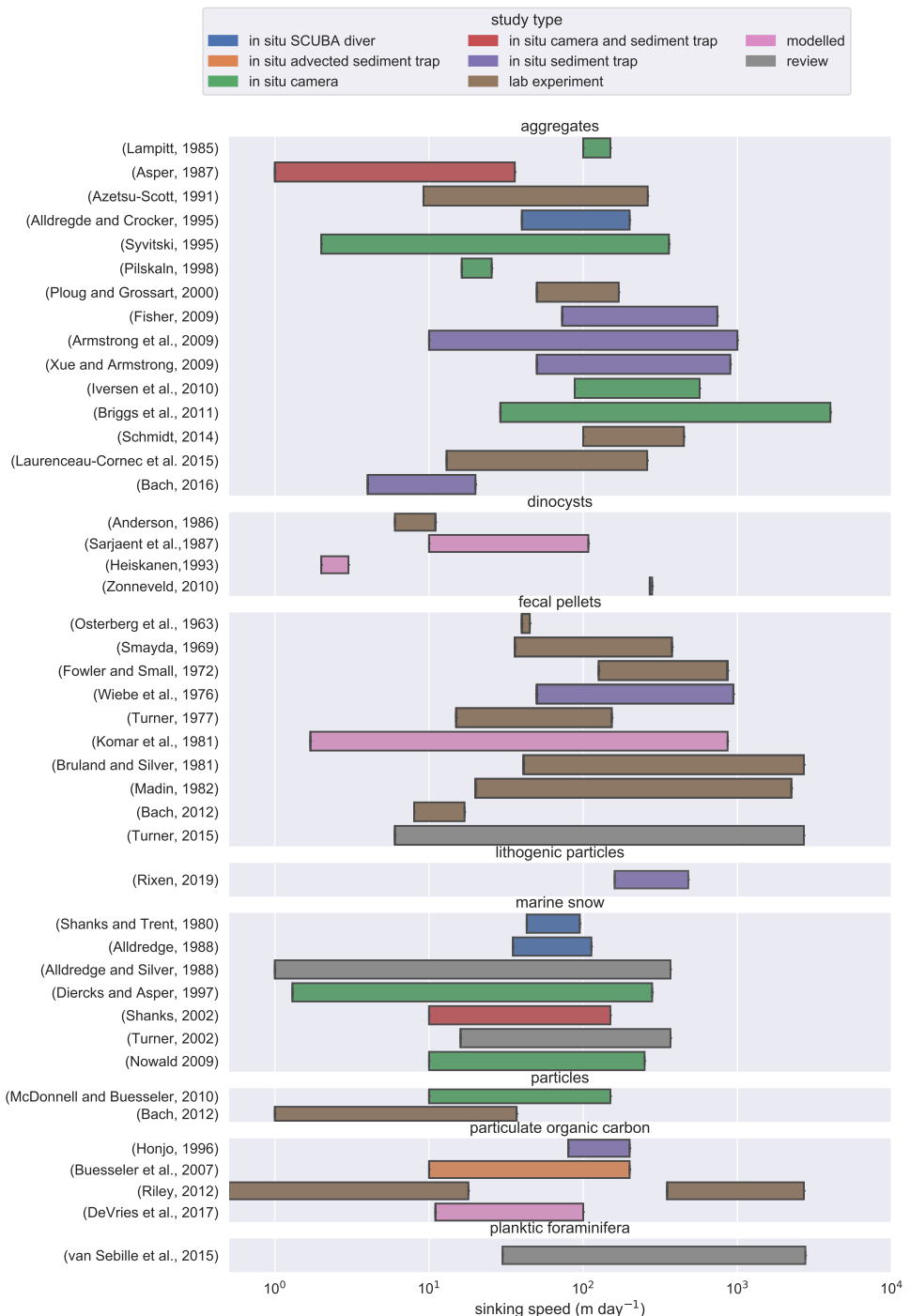
**Figure 2.3:** Overview of literature where a range of sinking speeds is determined for sinking particles in the ocean. The horizontal axis is logarithmic. The sinking speed of particles other than dinocysts is also shown, because the sinking speed of dinocysts could be influenced by interactions with the other particles by e.g. aggregation.

$Re = \frac{UR}{\nu} < 1$, with $U$ the velocity scale of the particle relative to the fluid and $\nu = \frac{\mu}{\rho_f}$ the kinematic viscoscity):

$$w_f = \frac{2}{9}\frac{\rho_p - \rho_f}{\mu}gR^2, \tag{2.3}$$

with $g$ the acceleration of gravity. More complex approximations of the sinking speed exist if these assumptions do not hold, which include parameterisations for the effect of turbulence (Jokulsdottir & Archer, 2016; Laurenceau-cornec et al., 2019), different particle shapes (Elfasakhany & Bai, 2019; Lau et al., 2013; Laurenceau-cornec et al., 2015), particle permeability (Johnson et al., 1996; Kajihara, 1971; Li & Yuan, 2002) and particle compression (Omand et al., 2020) on the sinking speed.

The water properties $\mu$ and $\rho_f$ depend on the fluid temperature and salinity (Commission, 2010; Sharqawy et al., 2010), which can generally be obtained by the ocean general circulation model. Hence, the uncertainty of $\mu$ and $\rho_f$ in Eq 2.3 is determined by how well the GCM computed temperature and salinity compare with reality. Both $\mu$ and $\rho_f$ were measured to have a relevant influence on the sinking speed (Bach et al., 2012; Ploug & Grossart, 2000). Particles were even found to accumulate between density layers (Alldredge & Crocker, 1995; Macintyre et al., 1995). However, this could only happen if the particle denstity is of a similar density to the water ($\rho_f$ typically ranges between $1.000 - 1.040$ kg m$^{-3}$ (Sharqawy et al., 2010)). The water properties $\mu$ and $\rho_f$ generally slow down sinking particles at great depth, since the deep ocean is colder and the pressure is higher compared to the ocean surface and has a higher viscosity and density as a result (Wiebe et al., 1976).

The greatest uncertainty of the dinocyst sinking speed however, is not induced by fluid properties, but by characteristics of the sinking particle; especially due to the interaction of a sinking dinocyst with other marine particles. Hence, the sinking speed greatly depends on the community structure of plankton (Bach et al., 2016) or even of the whole ecosystem (Henson, 2019), which determines the types and amount of available particles. The formation of aggregates (Burd & Jackson, 2009) could change the particle size, density and shape. These aggregates can form by binding of the dinocysts with other particles, often with help of sticky substances such as transparent exopolymer particles (Azetsu-Scott & Passow, 2004; Bach et al., 2016). These sticky particles typically have a lower density than sea water, hence require aggregation with heavy particles in order to sink (Azetsu-Scott & Passow, 2004; Mari et al., 2017). An aggregate could also form after digestion of the dinocyst by other organisms (i.e. fecal pelleting). Moreover, if particle concentrations are high enough, hindered settling could affect the sinking velocity (Middleton, 2003). Hindered settling reduces the sinking speed of particles by an upward flow that is induced by the downward particle flux.

As a result of these interactions between marine particles, the sinking speed will likely change during the sinking journey of dinocysts towards the ocean bottom. The aggregates could continue binding as the particles sink, but they can also fall

2

apart (Jokulsdottir & Archer, 2016). Most measurements of sinking particles, but not all of them (Nowald et al., 2009), show that the particle sinking speed increases with depth (Berelson, 2002; Fischer & Karakas, 2009; Pilskaln et al., 1998; Villa-Alfageme et al., 2016).

Due to the complexity of the interaction between sinking particles, studies find particle sinking speeds with orders of magnitude difference (see Fig. 2.3). A reason for the disagreement between measurements of sinking particles could be that these measurements were done in different areas, since the particulate organic carbon export flux and flux efficiency (i.e. flux relative to surface water primary production; this efficiency is likely higher when primary productivity is relatively low (Henson, 2019)) is varying spatially (Buesseler et al., 2007; Cram et al., 2018; Tang et al., 2019; Villa-Alfageme et al., 2016) due to varying ballasting effect of lithogenic particles (Rixen et al., 2019), or variations in particle composition (Schmidt et al., 2014b).

There might be a bias of larger, fast-sinking particles contributing to the total mass of particulate organic carbon that reaches the seafloor (Boyd et al., 2019; Riley et al., 2012), although there might also not be (Alonso-González et al., 2010; Durkin et al., 2015; Kiko et al., 2017; Villa-Alfageme et al., 2016). The contribution of slowly sinking particles to the downward carbon flux could be relevant, which is also why some biogeochemical models distinguish between slow and fast sinking particles (Aumont & Bopp, 2006; Kriest & Oschlies, 2008; Yool et al., 2011).

Dinocysts have specific interactions with other particles in the water column. Hence, the sinking speed of dinocysts could be different from typical marine aggregates. For instance, it was shown at several locations, both marine snow (Alldredge et al., 1998) and aggregates (Mudie, 1996) are devoid of dinocysts. Marine aggregates could be devoid of dinocysts for two reasons. First, it was suggested that zooplankton select against dinocysts for their lack of nutritional value (Montresor et al., 2003). Second, formation of large particles is the consequence of surface water primary production peaks (Schmidt et al., 2014b). It is unlikely that dinoflagellates encyst during these primary production peaks, since they reproduce asexually when plenty of nutrients are available and return to dormancy when conditions worsen. As a result, encystment will occur at times when surface water primary production is low, and particles avoid the fast-track to the sea bottom in large particles. This was clearly demonstrated for sediment trap studies in the Arabian Sea, where dinocyst flux was highest in low primary production seasons (Pospelova et al., 2018). However, whether dinocysts sink as being part of marine snow could be species specific, as was shown in areas with exceptionally high cyst fluxes (∼50,000 cysts per square meter per day; (Bringué et al., 2018, 2019)).

Overall, the processes that govern the sinking speed of marine particles is complex, especially if the specific role of dinocysts has to be taken into account. Therefore, we generally study the sensitivity of results to different sinking speed scenarios in this thesis. These scenarios will be greatly simplified. Mostly, we will choose a constant

sinking speed in every scenario. Only in chapter 3 two scenarios are used where the sinking speed increases with depth, in accordance with the measurements of sinking particle velocities from (Berelson, 2002).

We mostly compare the lateral transport of virtual particles to data of sedimentary dinocysts. However, the sinking speed of other types of microplankton could also bias paleoceanographic reconstructions, such as planktic foraminifera (Sebille et al., 2015b) and coccoliths (Zhang et al., 2018).
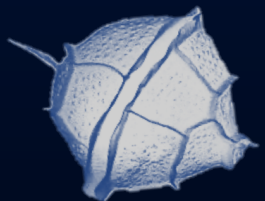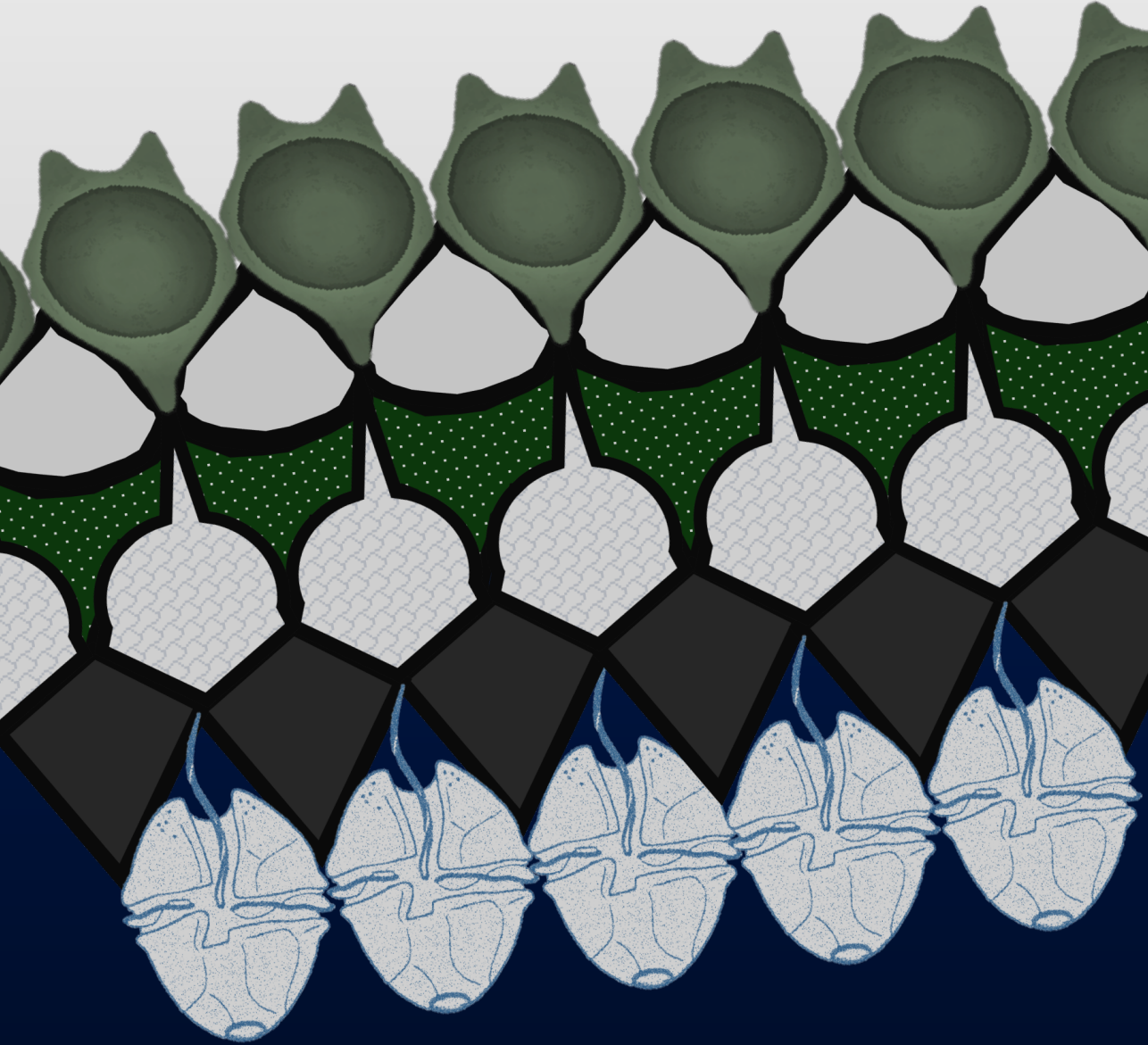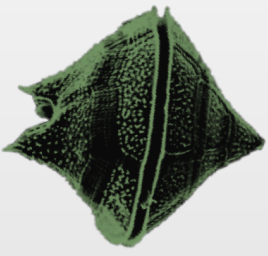
# CHAPTER 3

Transport bias by ocean currents in sedimentary microplankton assemblages of the present-day

3

**Microfossils from plankton are used for paleoceanographic reconstructions. An often-made assumption in quantitative microplankton-based paleoceanographic reconstructions is that sedimentary assemblages represent conditions of the directly overlying surface water. However, any immobile particle sinking down the water column is subjected to transport by three-dimensional currents, which results in a lateral relocation along transport. We model dinoflagellate cyst (dinocyst) transport in a high-resolution (0.1° horizontally) global model of the present-day ocean, and compare ocean conditions in the simulated origin of sedimentary particles to that in the directly overlying water. We find that the assumption that sedimentary particles represent the overlying surface waters is in most regions not valid. The bias induced by dinocyst transport depends on ocean current strength and direction, aggregation of particles which could increase the sinking speed, and the sediment sample depth. By using realistic sinking speeds of dinocysts and aggregates, extreme biases up to approximately ±16°C warmer or ±4PSU saltier are found, while other regions show lower bias from particle transport. Our model results provide a way to mechanistically and statistically explain the unexpected occurrences of some dinocyst species outside of their 'normal' occurrence region, such as the northerly occurrence of the allegedly sea-ice-affiliated dinocyst *Selenopemphix antarctica*. Exclusion of such outlier occurrences will yield better constrained ecological affinites for dinocyst species, which has implications for microfossil-based quantitative and qualitative proxies for paleoceanographic conditions. We recommend paleoceanographers to a priori evaluate the (paleo-)water depth, oceanographic setting, current strength and particle aggregation probability for their sedimentary microplankton assemblages.**

## 3.1 Introduction

Dinoflagellate cysts show distinct bioprovincialism in the present-day globally (Zonneveld et al., 2013b), regionally (Matthiessen, 1997; Prebble et al., 2013), and for long-extinct species during time intervals in the geologic past (Bijl et al., 2013; Bijl et al., 2011). It was shown that the composition of sedimentary dinoflagellate cyst (dinocyst) species relate to environmental conditions at the surface ocean, which is used to reconstruct past oceanographic conditions. For many cyst species, it is unknown which dinoflagellate produces a specific cyst. As a result, ecologic affinity of a dinocyst species in most cases cannot be derived from its biological producer, the dinoflagellate. Hence the relationships between the non-motile cysts and surface conditions are made independent of the taxonomy and biology of the motile dinoflagellates. Both quantitative (Frieling & Sluijs, 2018; Marret et al., 2001; Vernal et al., 1992) and qualitative (Bijl et al., 2011, 2018; Cramwinckel et al., 2019; Crouch et al., 2014; Houben et al., 2013; Sluijs et al., 2005, 2006) paleoceanographic reconstructions based on dinocysts exist.

Quantitative reconstructions using transfer functions of modern analogues have been instrumental to reconstruct past-ocean conditions (Datema et al., 2017; Matthiessen, 1997; Vernal et al., 1992). Transfer functions are based on the assumption that

a sedimentary microfossil assemblage composition explains part of the variability of environmental conditions. Transfer functions are used to calculate these relationships using a present-day core top dataset which includes surface sediment microfossil data and compares these to the environmental conditions inferred from the directly overlying water. This technique has also enabled to assess paleoceanographic affinities of extinct dinocyst species, by comparing their relative abundance to proxy reconstructions of past sea surface temperature (SST) in the same samples (De Schepper et al., 2011).

However, applications of these quantitative techniques have large uncertainties or scatter in some regions (Prebble et al., 2013), or show unrealistic values in past time intervals, e.g. near New Zealand (Marret et al., 2001). This induced large error bars of uncertainty and also reduced confidence in using these techniques to reconstruct past oceanographic conditions. Some challenged the quantitative methods on ecological grounds (Dale et al., 2002) and others on statistical grounds (Telford & Birks, 2009). However, sediment trap measurements indicate that sinking particles could be transported laterally (Chen et al., 2012; Fahl & Nöthing, 2007; Honjo et al., 1982). The lateral particle transport in these sediment trap studies could occur during their trajectory from the surface to the bottom of the ocean. Another view for dinocysts however, is that they are mainly transported after resuspension, and the cysts in the deep ocean reflect a specific biogeographic zone in shallow coastal waters (where most cysts appear) (Dale, 1996). Nevertheless, the lateral transport of the sinking cysts by ocean currents could induce a major uncertainty on their use as a proxy of local environmental conditions.

Sea surface temperature is suggested as the variable that explains most of the dinocyst distributions by multivariate statistics on a global dataset of sedimentary distributions (Zonneveld et al., 2013b) (which comprises dinocyst assemblage data from 2405 surface sediment sites), and the average surface oceanographic properties of the overlying water. Nevertheless, this relationship shows profound scatter, also for specific dinocyst species. Of course, some dinocyst species will have a more stringent temperature range than other (more generalistic) species. However, the scatter is a commonly seen feature, and particularly the broad tailing of species' temperature affinity (towards the cold and/or warm end). Although it could be that dinocysts have relatively broad temperature tolerances, perhaps other factors also play a role in the dinocyst-environmental relationships.

To illustrate the potential of these transportation effects, one can perform a quick calculation. If a sedimentary cyst sunk to 4 km depth, at $11$ m day$^{-1}$ (which is a typical sinking speed for dinocysts according to Anderson et al., 1985) through the water collumn with an average horizontal ocean flow speed of $\sim 5$ cm s$^{-1}$, it took almost 1 year before the dinocyst reached the ocean floor and could be displaced by up to 1570 km from its location at the surface. The bias could have major effects on the ability to use sedimentary dinocyst assemblages as proxy for surface ocean conditions. By understanding the surface origin of the cysts in the sediment and quantifying the biases and regional variations of the effects of lateral transport

during sinking, improved relations between cyst species occurrence and sea surface conditions can be obtained.

Ocean models have over the recent years become increasingly sophisticated: OGCMs resolve eddies (Marzocchi et al., 2015) and coupled biogeochemical models provide more properties of the ocean (Aumont et al., 2015; Yool et al., 2013). Together with Lagrangian particle tracking techniques (Sebille et al., 2018) the high-resolution ocean models enable quantitative assessment of the biasing effects of lateral transport of sedimentary microfossil assemblages. These developments have now offered the opportunity to assess the bias potential of lateral transport in sedimentary plankton assemblages.

Here, we investigate the potential bias of the relationship between dinocysts (as example of any microplankton fossil group) and surface conditions that can be induced by the lateral cyst transport by ocean currents in the present-day. We will refer to this bias as the 'advection bias' (AB). We will present and discuss the regional difference in the AB. Moreover, we examine the sensitivity of the AB to the sinking velocity assumptions. The local magnitude of the effect of ocean currents on sedimentary cyst distributions will be quantified.

Section 3.2 describes the data and methods which are used to model and analyse the transport of the cysts. The first part of sectio focuses on the global scale. We determine the geographic regions where particle transport is important and perform a sensitivity analysis of these results to the sinking velocity of the cysts. In the second part of section 3.3, an analysis of the AB is done for a specific location near Antarctica and a specific species (*S. antarctica*). Finally, section 3.4 provides a summary and a discussion on the implications for microplankton-based paleoceanography.

## 3.2 Data and Methods

### 3.2.1 Ocean flow field data

We make use of ocean model simulations to propagate virtual particles. OGCM for the Earth Simulator (OFES) (Chi et al., 2018; Masumoto, 2010; Masumoto et al., 2004; Sasaki et al., 2008) provides a three-dimensional flow field for the years 2000-2005 from the edge of the Antarctic continent at $75°S$ to $75°N$ with 3-daily output. Since the model has no output north of $75°N$, we only show results up to $70°N$ in this chapter. The flow field from OFES is used to calculate the trajectories of sinking particles (similar to Sebille et al., 2015b). Moreover, OFES includes a three-dimensional temperature and salinity field, which are environmental variables that influence the habitat of a dinoflagellate. The model has a $0.1°$ horizontal resolution with $54$ vertical levels and is forced by the National Centers for Environmental Prediction (NCEP) wind and heat/freshwater flux fields.

To study the model dependence of the results, we performed the same analysis with another model: Nucleus for European Modelling of the Ocean (NEMO) (Madec,

2016; Storkey et al., 2014; Uotila et al., 2017) for the same years (2000-2005) (http://opendap4gws.jasmin.ac.uk/thredds/nemo/root/nemo_catalog.html). The NEMO model has a higher horizontal resolution compared to OFES ($1/12°$ horizontally) and 75 vertical layers. The output of this model is 5-daily. Furthermore, it includes the Arctic, as the model uses a tripolar grid which solves the singularity at the north pole. However, we only consider results south of $70°$N as is done for OFES, to be able to compare the NEMO and OFES simulations. The tripolar grid makes interpolation and calculation of the particle trajectories more difficult, but this is recently made possible (Delandmeter & Sebille, 2019a). The results of the analysis from NEMO can be found in the supporting material.

The spatial resolution of the OFES and NEMO models is high enough to resolve meso-scale eddies. The eddies are important to realistically resolve the dynamics of the ocean currents. For example, the $0.1°$ is seen as a threshold to realistically simulate the seperation location and other features of the Gulf Stream (Hecht & Smith, 2013). Moreover, eddies are important for the transport of dinocysts, as is the case for the transport of heat (Volkov et al., 2008), salt (McWilliams et al., 2014) and floating particles at the surface (such as microplastics) (Fraser et al., 2018). Furthermore, the temporal resolution of the OFES and NEMO model outputs is high enough to calculate the particle trajectories within the flow field. To apply a three-dimensional Lagrangian tracking method, the output of the model results must be of high enough temporal resolution (at least 9-daily for $\sim 0.1°$ horizontal resolution (Qin et al., 2014)).

### 3.2.2 Particle tracking and analysis

Although it is unlikely that dinocyst sink via large aggregates, it remains challenging to realistically and adequately incorporate the observations on sinking speeds into our simulations (see chapter 2). In order to evaluate the effect of sinking speed assumptions on the advection bias (AB), we perform a sensitivity test by which we simulate particle transport under a suite of realistic constant sinking speeds of both individually sinking dinocysts (6-11 m day$^{-1}$; Anderson et al., 1985) and aggregates (Berelson, 2002). Moreover, aggregates seem to increase sinking speed with water depth (Berelson, 2002), probably due to increasing size and mass of the aggregates, and decrease of buoyancy. In order to investigate this scenario, we also perform two simulations (SC1 and SC2) where we make the sinking speed $\vec{C}(z)$ of a particle dependent on the depth of the particle ($z$), as follows: In SC1, the sinking speed is 6 m day$^{-1}$ between $10 - 100$m depth, and increases linearly between $100 - 2000$m up to $45$ m day$^{-1}$. SC2 is similar to SC1, but the sinking speed increases further between $2000 - 3500$m depth up to $65$ m day$^{-1}$. So the sinking speed in SC1 and SC2 are respectively defined as:

$$\vec{C}_1(z) = \begin{cases} 6 & 10\text{m} < z \leq 100\text{m} \\ 6 + \frac{(45-6)(z-100)}{2000-100} & 100\text{m} < z \leq 2000\text{m} \\ 45 & z > 2000\text{m} \end{cases},$$

$$\vec{C_2}(z) = \begin{cases} 6 & 10\text{m} < z \le 100\text{m} \\ 6 + \frac{(45-6)(z-100)}{2000-100} & 100\text{m} < z \le 2000\text{m} \\ 45 + \frac{(65-45)(z-2000)}{3500-2000} & 2000\text{m} < z \le 3500\text{m} \\ 65 & z > 3500\text{m} \end{cases}.$$

The sensitivity study provides ways to portray the bias effect for various sinking speeds, making our simulations applicable to any particle. We apply SC2 as the most plausible sinking speed scenario for dinocysts. A constant sinking velocity of $6 \text{ m day}^{-1}$ (see Figures S1, S3, S5, S6, S7, S8, S9 of the supporting material) is considered as an upper bound of the magnitude of the lateral particle transport, because the lateral particle transport is expected to decrease if the sinking speed increases and $6 \text{ m day}^{-1}$ is the lower bound of individually sinking cysts (Anderson et al., 1985). The sinking scenarios ignore any seasonal dependence of the sinking speed and the dinocyst productivity.

Once the virtual dinocysts are tracked with a certain sinking scenario and encystment depth, the AB has to be determined. The ocean surface water conditions where the cysts come from (i.e. where the model simulates the encystment location) are compared to the environment in the surface waters above the release location at the bottom (where cysts are found in a sediment sample). We express environmental conditions at the surface as probability density functions (PDF). The first PDF is inferred from the values of the environmental variable at the surface where the virtual particles first reach the encystment location (10m water depth) in the model. This type of PDF is refered to as the 'advection PDF' (APDF). The second PDF can be determined from the environmental variable that evolves in time at the fixed surface location overlying a sample site. This PDF is refered to as the 'local PDF at a fixed location' (LPDF) (blue in the figures throughout the chapter).

In this chapter, we use two measures for the AB (AB1 and AB2) between the APDF and the LPDF. AB1 and AB2 are defined as the difference between tail of the APDF with respectively the LPDF's mean (often used in quantitative and qualitative methods) or the LPDF's tail (part of the difference between APDF tail to LPDF mean which is caused by lateral particle transport). We define the tail by the $5^{\text{th}}$ or $95^{\text{th}}$ percentile. Hence we use the following measures for temperature AB:

$$AB1^{\text{warm}} = \text{percentile}(APDF, 95) - \mu_{LPDF},$$
$$AB1^{\text{cold}} = \text{percentile}(APDF, 5) - \mu_{LPDF},$$
$$AB2^{\text{warm}} = \text{percentile}(APDF, 95) - \text{percentile}(LPDF, 95),$$
$$AB2^{\text{cold}} = \text{percentile}(APDF, 5) - \text{percentile}(LPDF, 5),$$

where $\mu_{PDF}$ is the mean and percentile$(PDF, k)$ is the $k^{\text{th}}$-percentile of the PDF. The tail of the APDF informs about the environmental conditions of far-travelled particles. The tails of the APDF are used here as a measure of the AB for two reasons. First because we only model the area where the cysts in a sediment core could have come from as a result of the transport by ocean flow. In reality, the

productivity of dinocysts at the surface is not uniform in space and time, and the dinocysts do not necessarily originate from the model predicted locus (e.g. because the ecological preference of the dinocyst does not agree with the model predicted locus). Therefore, we use the tail to obtain a confidence interval with a lower and an upper bound of species properties in a sediment sample. Second, transfer functions of modern analogues, which quantitatively relate sedimentary dinocyst assemblage data to environmental conditions, are very sensitive to extreme occurrences (i.e. occurrences of species outside of their typical habitat with low abundance), and therefore greatly affect the reliability of the proxy (Ohlwein & Wahl, 2012).

## 3.3 Results

We first distinguish regions where lateral particle transport is important from those where it is not. Furthermore, we perform a sensitivity analysis on sinking speed to account for uncertainties in our assumptions on sinking behaviours of dinocysts. Then we show one case study of a specific sediment sample site with a relatively large AB. Finally, we indicate what kind of implications the particle transport could have for the interpretation of dinocyst species and their ecological affinities.

### 3.3.1 Global analysis

We first investigate the lateral transport of the particles using the transportation matrix, without considering the AB of environmental variables. In general we find a relatively small effect of the particle transport by currents at shallow water depths (Figure 3.1). At those areas, most released particles come from the overlying surface gridbox (Figure 3.1a), a sediment sample relates to a relatively smaller surface area (Figure 3.1b) and the average traveled horizontal distance of particles released in the bottom boxes is lower (Figure 3.1c). Hence the assumption that particles sink vertically to the bottom is more plausible in shallow, continental shelf areas.

The lateral particle transport is relatively large in deep ocean basins, and further enhanced near strong currents, such as the western boundary currents and near the Antarctic Circumpolar Current (ACC). The large surface area (Figure 3.1b) is horizontally distant from the release location at the bottom at the ACC, because the ACC strongly transports the particles eastward and the travel distance is large (Figure 3.1c). On the other hand near western boundary currents, the surface area is closer to the release location, because the vertically-integrated currents are weaker compared to the ACC. Locations with relatively large lateral (latitudinal) travel distances that are mapped to a small surface area are rare, because the large travel distances require strong currents, and strong currents are often accompanied by eddies. These eddies increase the variability of the direction and strength of transport pathways, and therewith the surface area which is mapped to a bottom box.

Changing the sinking speed assumption for the particles does not affect the geographical structure of where the lateral transport is important. However, the sinking speed assumption does influence the magnitude of the lateral particle transport
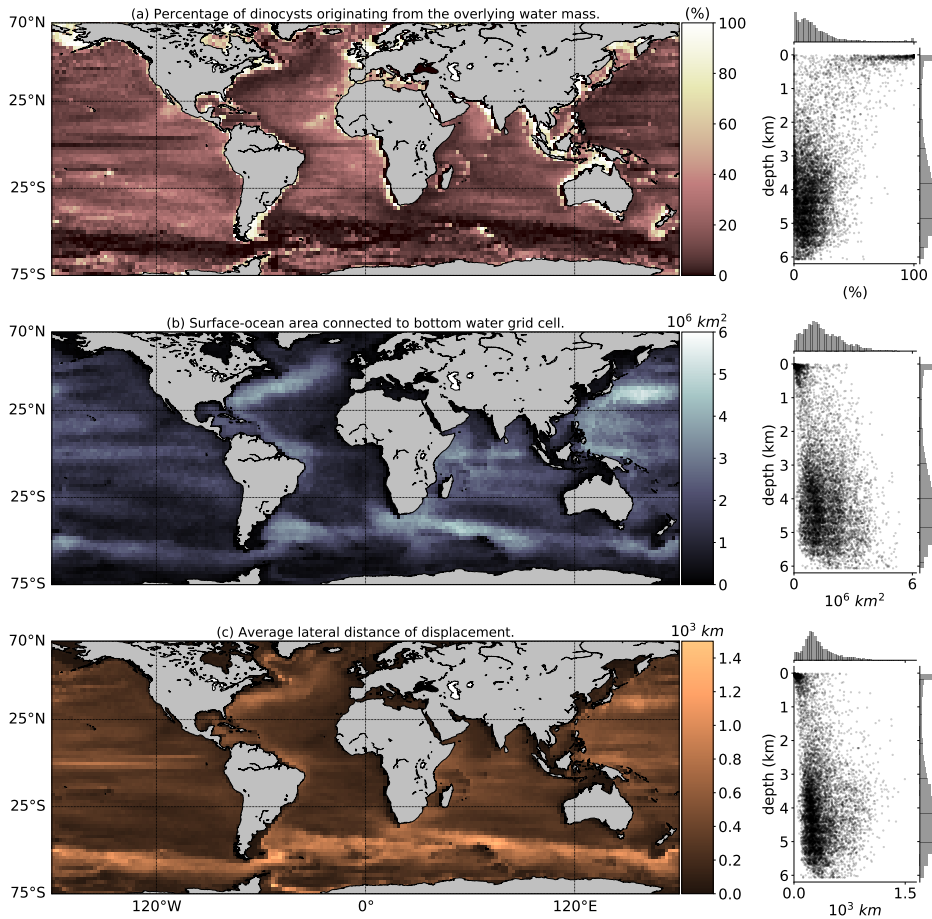
**Figure 3.1:** Transportation matrix results with $2° \times 2°$ surface and bottom boxes with sinking scenario SC2: Geographic plot (left) and scatterplot against depth of the bottom boxes (right). (a) The probability that a particle ends up in the same box at the surface as it is released at the bottom (the diagonal of the transportation matrix). (b) The surface area of all grid boxes at the ocean surface that a bottom box is connected to. (c) The average horizontal distance between the release location and the backtracked encystment location (averaged for a bottom box). See Figures S5 and S6 of the supporting material for the same figure with 6m day$^{-1}$ sinking velocity instead of SC2.
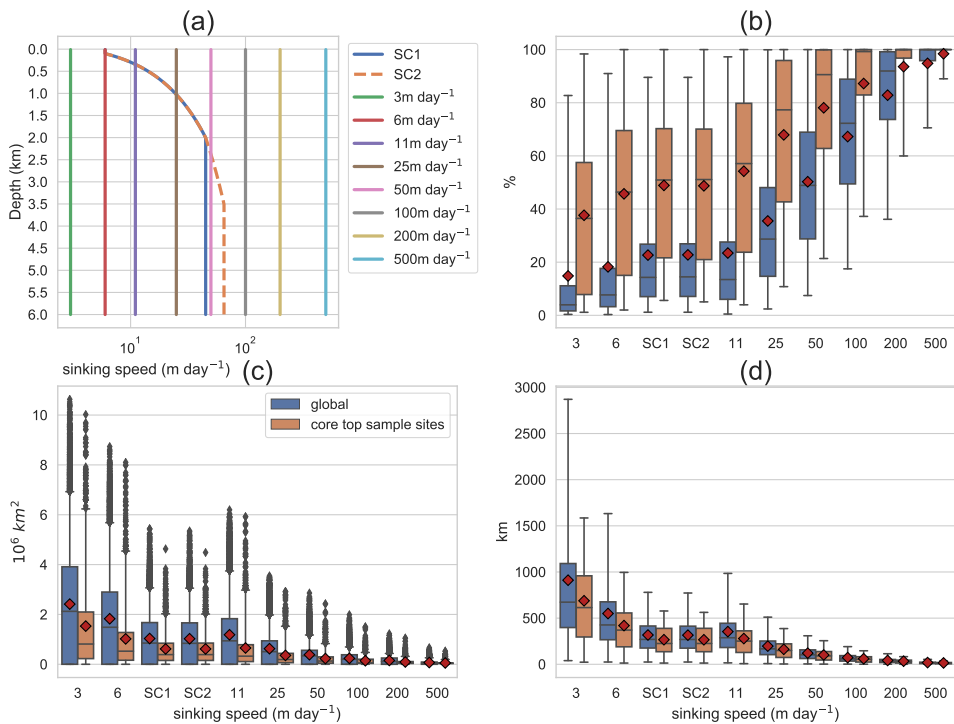
**Figure 3.2:** Sensitivity analysis of the results in Figure 3.1 versus sinking speed. (a) Illustration of the sinking speed scenario's (with constant sinking speeds and SC1, SC2 with sinking speed dependent on depth) which are used in the sensitivity analysis on sinking speed (note that the horizontal axis is logarithmic). Boxplots show the $5^{th}$, $25^{th}$, $75^{th}$ and $95^{th}$ percentile around the median of (b) the probability that a particle ends up in the same box at the surface as it is released at the bottom (diagonal of the transportation matrix), (c) the surface area of all grid boxes at the ocean surface a bottom box is connected to (including outliers), (d) the average travel distance from a bottom box. For all defined bottom grid boxes as in Figure 3.1 in the ocean (blue) and for the locations of present-day surface sediment samples (orange). The red diamonds are the mean of the distribution.
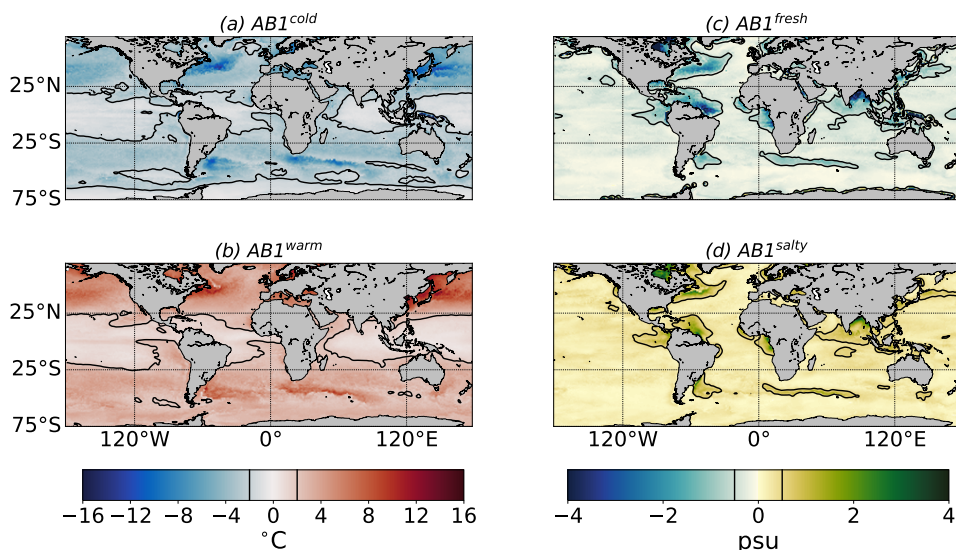
**Figure 3.3:** The tails of the APDFs which include advection with SC2 compared to the local average (mean LPDF). The local average is subtracted from the (a) 5th and (b) 95th percentile for SST of the APDF. (c), (d) the same as (a), (b) but for salinity. The black contours are the $\pm 2°C$ or $\pm 0.5$ PSU levels.

distance, and therefore the magnitude of the potential bias. The lateral particle transport distance reduces if the sinking speed increases (Figure 3.2). However, locally the particle transport distance can still be substantial at higher sinking speeds. The lateral particle transport distance becomes zero if the sinking speed approaches infinity. Most sites in the core top dataset (Zonneveld et al., 2013a) are relatively close to the coast and therefore in relatively shallow regions. Hence the particle transport is on average lower at the sample site locations compared to the global average ocean. The results for the linearly increasing sinking scenarios (SC1 and SC2) yield similar results, so the increase in sinking speed of SC2 below 3500m depth compared to SC1 does not influence the particle transport on average. More importantly, the horizontal particle transports for SC1 and SC2 are not clearly higher compared to the constant $11\text{m day}^{-1}$ simulation, which indicates that a large part of the transport takes place in deeper than $\sim 344\text{m}$ in the $11\text{m day}^{-1}$ simulation (in SC1 and SC2 the sinking speed exceeds $11\text{m day}^{-1}$ at depths $z \gtrsim 344\text{m}$). It also means that even under the aggregate sinking speed velocities available from the literature, transport of dinocysts still plays an important role.

### 3.3.2 Temperature and salinity advection bias

While the amount of lateral transport of sinking particles can be relevant for a substantial part of the ocean, the environment is not necessarily different at the location where the cysts are transported from, compared to the local surface conditions.

That is why we will now compare the tails of the temperature/salinity APDFs with the mean of the temperature/salinity LPDFs: The advection bias (AB1).

The temperature AB1 is relatively large (up to $\pm 16°$C) in specific regions, such as the western boundary currents and north of the Southern Ocean (Figure 3.3), it is smaller (than $\pm 2°$C) in other regions, such as near the equator. For salinity, the AB1 is large (up to $\pm 4$ PSU) in regions with ice melt and near river outflow regions such as near India and the Amazon, while the AB1 is low (smaller than $0.5$ PSU) in the open ocean and away from the strong western boundary currents. Interestingly, not all regions with large transport effects have a large temperature AB: A strong current does not always lead to a large AB, such as in parts of the ACC. The relatively low AB is induced in these regions by a lower temperature or salinity gradient along the transport pathways of the particles, e.g. the transport in parts of the ACC is zonal and the zonal temperature gradient is low.

The Southeast of Brazil (at the Uruguayan margin) is an example with large temperature and salinity AB. In this dynamic region, the nortward branch of the ACC (the Malvinas current) and the southward flowing Brazil Current meet, and locally large temperature and salinity gradients exist (Matano et al., 2010). The APDF, but also the LPDF, therefore have a non-Gaussian shape in this area. As a result, our model simulations predict that a surface sediment sample in this area could contain species which represent SSTs of either $16\ °$C colder (Figure 3.3a) or warmer (Figure 3.3b) compared to the local average (mean of LPDF). Although cyst assemblages in higher latitudes naturally include warmer species that exist in summer together with colder ones from winter, the example indicates that cyst transport could induce a strong AB here. Another interesting example where the LPDF of temperature has a non-Gaussian shape is the Kuroshio current, because the path of the current is bimodal (Schmeits & Dijkstra, 2001).

The AB in terms of the difference between the APDF and LPDF tails (AB2), also shows considerable dependence on sinking speed assumptions (Figure 3.4). For example, comparing the boxplot with sinking speed $6$ m day$^{-1}$ with SC2 (Figure 3.4a): It is at $6$ m day$^{-1}$ very unlikely (below 1% probability) that the sedimentary dinocysts which are found at an arbitrary location are related to a habitat at the surface $6°$C colder than the cold tail of the local temperature (LPDF) due to the particle transport, while for SC2 this is $2.5°$C. Hence the AB2 reduces quickly if the sinking speed is larger.

The tails of APDFs and LPDFs differ little at about $50\%$ of the locations (up to $\pm 0.5°$C or $\pm 0.1\ PSU$ for SC2). At some locations however, the tails of the APDF could become $\sim 3°$C warmer or colder and $\sim 2.5 PSU$ fresher or $\sim 0.5\ PSU$ saltier at SC2. The AB2 for salinity is asymmetric here, because of the backtracking of particles near outflow regions of rivers: A particle which is released in the ocean could end up in a fresh river outflow region after backtracking, leading to a strong fresh AB2. On the other hand, a particle which is released in the river outflow region will likely end up in the same region due to the direction of the current, which leads to a small
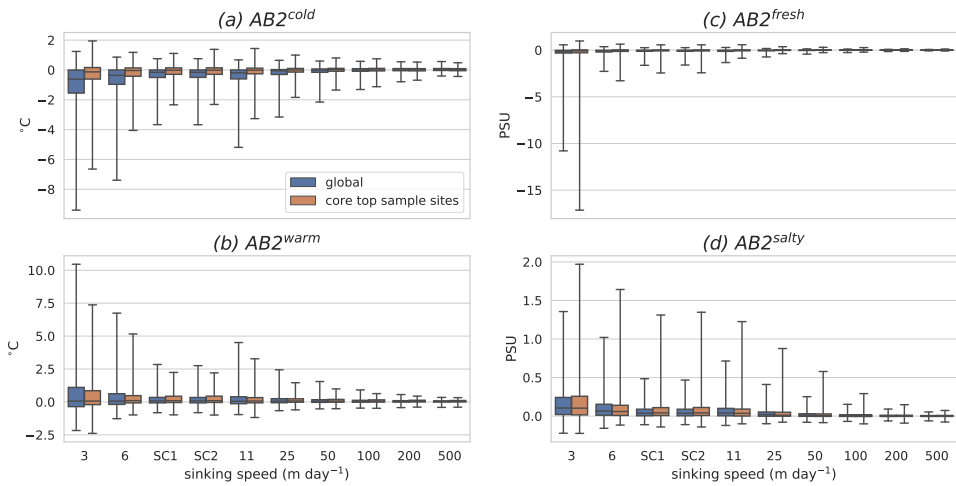
**Figure 3.4:** The sensitivity of the displacement of the PDFs tail due to particle transport on sinking speed (SC1 and SC2 are the two sinking scenario's with increasing sinking speed with depth). Difference of the (a) $5^{th}$ and (b) $95^{th}$ percentile of the temperature APDF from the same percentile of the LPDF. (c), (d) the same as (a), (b) but for salinity. The boxplots show the $1^{th}$, $25^{th}$, $50^{th}$, $75^{th}$ and $99^{th}$ percentile around the median for all locations (blue) and the dinocyst sample locations in (Zonneveld et al., 2013a) (orange).

AB2. The change in the tails decreases quickly for higher sinking speed at the locations where the particle transport matters most. Eventually this change converges towards zero for all variables and all locations if the sinking speed increases upto $500$ m day$^{-1}$. It is interesting to note that the transport of currents does not always cause the tail of the PDF to be fatter, but can also decrease the tail and result in a more confined PDF (with a lower kurtosis). In these cases, the spread of an LPDF is large due to a passing front (such as the Kuroshio current), while the backtracked particles come from a surface location with more constant properties. Most interestingly, however, the lateral particle transport is not important in regions where many large aggregates form, although it can be relevant under realistic aggregate sinking scenarios SC1 and SC2. Hence it is crucial to get a better understanding for mechanisms and factors that control the sinking velocity of particles.

To summarize these global results, the importance of the particle transport at a certain location on the sea floor depends on five factors. First, the water depth at the sample site and second the strength of the current, which both control the distance that cysts travel before they reach the bottom of the ocean. Third, it is the horizontal spread of directions a cyst could travel within the flow field, which determines the surface area at the ocean surface which is measured at a sample site. Fourth, it is the gradient of the environmental variable of interest (such as temperature and salinity) along the trajectories that cysts can travel within the flow field. Fifth, it is the aggregation probability of the microplankton, which influences the sinking speed. We determined in which regions these factors create the largest AB and the sensitivity of the AB to the sinking velocity of the cysts. We further conclude that all these fac-

tors are important to take into account when looking at sedimentary microplankton data, also in sediment cores that aim to reconstruct past oceanograpgic changes. To investigate whether these factors are of importance in the past record, one could apply the back-tracking method to an ocean model which simulates the past ocean circulation.

In order to test for model-dependency of our global results, we also performed the same simulations with the NEMO model (see Figure S1 through S4 of the supporting material). The model-dependency test shows geographic differences between the simulations, because the exact pathways of ocean currents are model dependent. These geographical differences induce larger particle transport and larger AB in the NEMO simulation compared to OFES for the sediment sample site locations. However, the global average of the particle transport by ocean currents is similar (according to the sensitivity study on sinking speed Figure S2). Moreover, the general conclusions regarding the global transport of sinking cysts and the AB are similar.

### 3.3.3 Case study in the Southern Ocean

From the global simulations we were able to identify regions where the particle transport is important in terms of the relation of sedimentary cysts with environmental variables at the surface of the ocean. One of the regions with important particle transport is the Southern Ocean, because a large part of the Southern Ocean has a strong AB due to the combination of strong currents and strong latitudinal sea surface temperature gradients. We will study how the particle transport can be important for the interpretation of a particular sample site as well as the global ecological affinity of two specific species: *Selenopemphix antarctica* and *Spiniferitus delicatus*.

**A subtropical Southern Ocean surface sediment site**

Station 3627 (Zonneveld et al., 2013a) (Figure 3.5) is an example of a Southern Ocean sediment sample site at almost 5 km water depth. The temperature LPDF at this location, which is computed from the evolution of sea surface temperature at the sediment sample location over the six simulated model years, has a unimodal shape. The (blue) LPDF shows that the SST is $9 \pm 1.5°$C (the $90\%$ confidence interval around the average which gives a range of species properties that could be measured in the sediment sample). Hence, if one assumes that the cysts sunk vertically to the ocean floor, the sediment sample relates well to the average of the LPDF. Furthermore, station 3627 is located close to the subtropical front (Orsi et al., 1995) and remote from sea-ice and icebergs (Tournadre et al., 2012).

Moreover, the sediment sample of station 3672 contains a diverse dinocyst assemblage (Figure 3.5d). Some of these species are typically abundant in temperate regions similar to the local conditions (but are sometimes also found in warmer areas), e.g. *Dalella chathamensis, Impagidinium aculeatum, Impagidinium paradoxum, Spiniferitis mirabilis* (Zonneveld et al., 2013b). On the other hand, *Nemaosphaerop-*
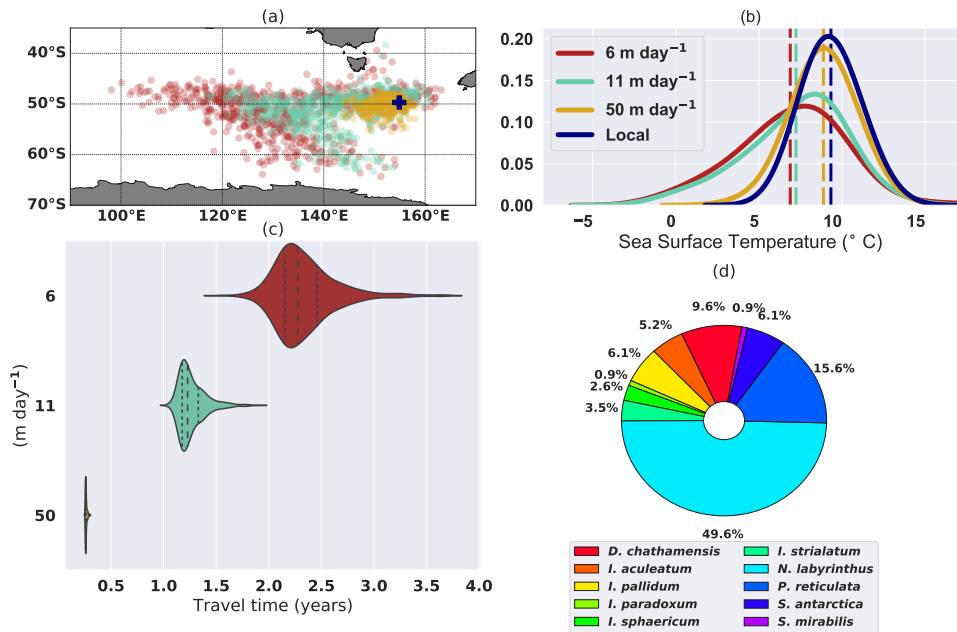
**Figure 3.5:** Example of the particle backtracking for station 3627 ($154.91\ °E$ and $49.71\ °S$) at approximately 4730 m depth. The particles are released at the ocean bottom and tracked back in time with a sinking speed of 6 m day$^{-1}$ (red), 11 m day$^{-1}$ (green) and 50 m day$^{-1}$ (yellow) ($\sim$600 particles for each sinking speed scenario). (a) The release location at the blue cross and in red/green/yellow the locations where the particles reach the encystment location of 10 m. (b) The PDFs which are infered from the evolving temperature at the sea surface location at the station (during the six years of the simulation) (LPDF in blue) and for the SSTs when a particle reaches the encystment location after backtracking in the simulation (APDFs in red/green/yellow). The vertical dashed lines are the PDF means (c) Distribution of the time that particles took to sink (the vertical dashed lines show the median and quartiles). (d) The relative abundances (%) of species found in the surface sediment at station 3627.

*sis labyrinthus* and *Pyxidinopsis reticulata* are particularly abundant at ocean frontal system localities, and particularly the subtropical front. *Impagidinium pallidum* occurs in high abundance in polar regions, although low abundances in other regions have also been reported (Zonneveld et al., 2013a). Finally, *S. antarctica* is only very high in abundance closer to Antarctica south of the polar front and within the sea-ice zone (Prebble et al., 2013; Zonneveld et al., 2013a), has been reported in high abundance in Holocene polynya-derived drift sediments (Hartman et al., 2018), and is used as proxy for sea ice conditions for the geologic past (Bijl et al., 2018; Houben et al., 2013). However, *S. antarctica* also occurs in the sediment sample of station 3627 with 6.1%.

From the local conditions of station 3672, *S. antarctica* and *I. pallidum* are not expected in the sediment samples. However, surface Ekman transport induces northward surface currents, being part of the meridional overturning circulation (Marshall & Radko, 2003), which could transport particles northward, from across the ACC. Hence cold species could be transported from the far South to the site, while warmer species did not travel far, because of limited southward water transport in the region. When looking at our particle back-trajectory calculations, we note under assumptions of sinking speed, that a fraction of the particles come from colder waters close to Antarctica. The cold tail of the APDF represents this additional input of colder water species to the site. The 90% confidence interval around the median of the APDF is $1 - 12°C$ (if the sinking speed is 6m day$^{-1}$).

These simulations also allow for investigation of the travel time of the particles. The travel time of particles ending up at station 3672 exceeds 1 year for all particles in the 6 and 11m day$^{-1}$ simulations. Furthermore, the spread of the travel time between the particles increases if the sinking speed decreases. The spread of the travel time is induced by the varying vertical velocities of the flow field. This means that seasonal variations are averaged out in dinocyst assemblages at this location, on top of the typical mixing of accumulation from multiple years within the surface sediment sample itself.

### Ecological affinities of specific species

The skewness of the APDF in the surface sediment sample of station 3672 is not unique. A mismatch between dinocyst core-top sediment samples and overlying sediment traps is also measured in some other areas of the Southern Ocean, indicating that lateral transport affects the sediment samples (Harland & Pudsey, 1999). The question is whether all samples with cold-water affiliated species have a cold tail in the APDF (which indicates that these species could have been transported to the sites), or whether these species actually occur in relatively warm regions with lower abundances. Therefore, we cluster the sediment samples in the Southern Ocean based on their species constituents, and investigate the tailing of the samples' APDFs in these clusters (Figure 3.6). We compare the tailing of the APDFs in these clusters to the sea-ice affiliated *S. antarctica*.
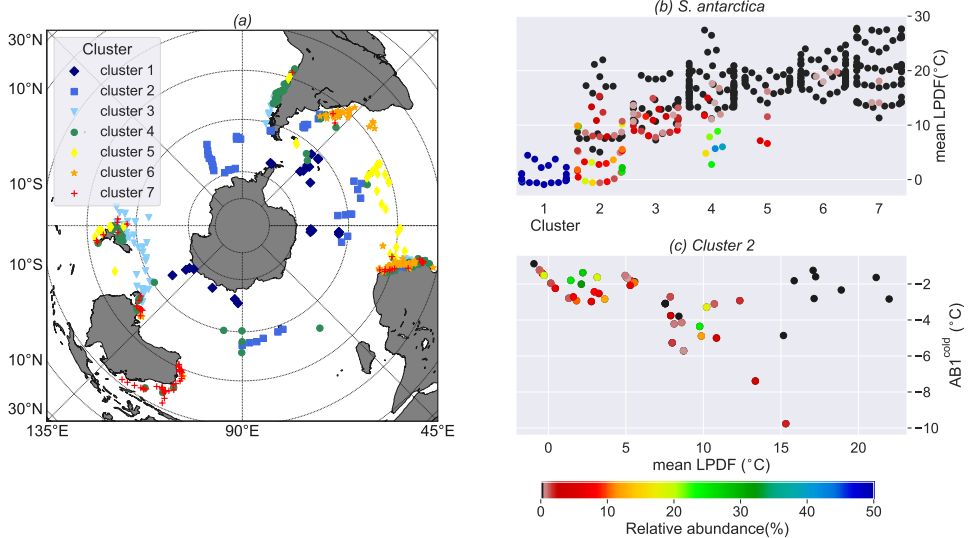
**Figure 3.6:** *S. antarctica* compared to clusters with similar dinocyst assemblages. The clusters are derived with the *k*-means algorithm as in Prebble et al., 2013, for the surface sediment samples south of $12°S$. (a) Map of the sediment sample sites and their cluster. (b) Swarm plot of the local temperatures (mean LPDF) of the surface sediment samples in specific clusters. (c) The local average temperature versus the cold AB1 (with SC2) for the sediment samples of cluster 2. The color is the relative abundance of *S. antarctica* in the surface sediment samples in (b), (c) (black if the relative abundance is zero).

We choose to focus on *S. antarctica* here, because its occurrence in low to moderate abundance north of the polar front and around New Zealand (Crouch et al., 2010; Prebble et al., 2013) led to questioning of the validity of *S. antarctica* as proxy for polar conditions. It was further reported in higher abundance in Pleistocene glacial deposits offshore New Zealand, which caused quantitative reconstructions using dinocyst-based modern analogue technique to suggest much colder glacial SSTs for that region than anticipated by SST reconstructions with foraminifera (Marret et al., 2001). Thus far, these authors have considered *S. antarctica* to be part of the in situ, pelagic sedimentary component, and have interpreted it to be originating from the overlying water mass. However, it could be that *S. antarctica* was actually transported to the site via ocean currents, from the polar front area.

Prebble et al., 2013 statistically clustered Southern Hemisphere dinocyst assemblages from the surface sediment sample dataset into 7 clusters. *S. antarctica* is found in multiple clusters of similar dinocyst assemblages. *S. antarctica* dominates cluster 1, which only contains samples in cold areas close to Antarctica. As expected, the AB is lower in cluster 1 compared to other clusters, because the ACC isolates these sample sites, which prevents southward transport of subtropical species. More interesting are the clusters which do contain *S. antarctica*, but also consist of sample sites in relatively warm areas (e.g. cluster 2 and cluster 4). First of all, we note that in cluster 3, 4 and 5, the stations with S. antarctica come from the stations with relatively cold LPDF (Figure 3.6b). If the occurrence of *S. antarctica* in these sample sites is caused by transport, one expects a relationship between the local temperature and the cold tail of the APDF. This implies that any site with a relatively high local temperature has either an APDF with a relatively large cold tail (colder AB1), or a lower relative abundance (or absence) *S. antarctica*. This is the case in cluster 2 (Figure 3.6c). To conclude, we see that in most regions a sediment sample site contains relatively more *S. antarctica* if a) the local average temperature of is low and/or b) the cold AB1 is large.

These observations support the idea that one could misinterpret the ecological affinity of species with relating sedimentary cyst assemblages to the directly overlying water. We will further substantiate the quantitative effects of this for *S. antarctica*. We apply the backtracking method at all sites where *S. antarctica* is found, but only consider the back-tracked locations which belong to the coldest $n^{\text{th}}$-percentile associated with the site (here $n$ is the relative abundance of *S. antarctica* in the sample) (Figure 3.7a). Under the assumption that the relative abundance scales with the amount of cold backtracked particles, we deduce that the surface locations where *S. antarctica* comes from are almost exclusively constrained within or south of the ACC. It is therefore plausible that *S. antarctica* at temperate to subtropical sites actually originated from colder regions and was transported to the sediment sample location. To further illustrate the consequences of this interpretation, we adjust the SST of each of these sample sites from the mean of the LPDF to the temperature according to their APDF's cold tail (the $\frac{1}{2}n^{\text{th}}$ percentile of the backtracked temperatures). This approach increases the adjustment of the LPDF according to the amount
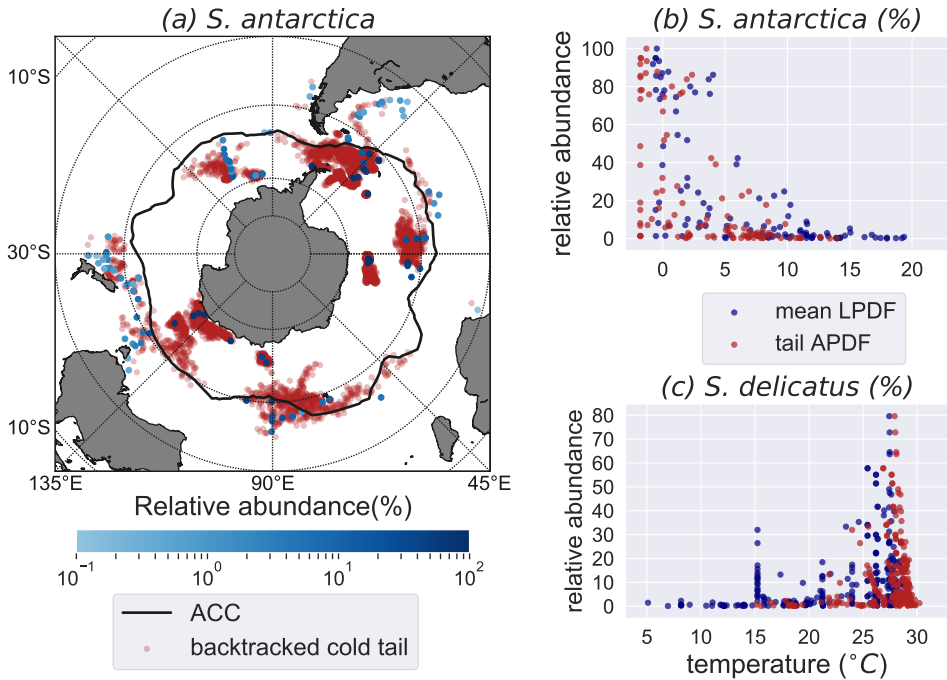
**Figure 3.7:** Biasing effects of ocean currents on dinocyst distributions (with SC2). (a) In blue the sediment sample sites where *S. antarctica* is found, where the color represents the relative abundance ($n$) of *S. antarctica* in the sediment sample. In red a selection of the locations where the virtual particles reached the surface after backtracking from the sediment sample sites. We have only plotted the surface ocean locations where the temperature was lower than the $n$-th percentile of the temperature APDF (see Figure 3.5) associated with the sediment sample site where the particle was released. Hence the higher $n$ at a site, the larger the part of the cold tail of the APDF is considered. The ACC location (black line) is determined by the latitude with strongest average flow at every longitude. (b) In blue the mean of the temperature LPDF of a site against the relative abundance of *S. antarctica* at the site. In red the $\frac{1}{2}n$-th percentile of the temperature APDF of a site against the relative abundance ($n$) of the site. (c) Same as (b), but for *S. delicatus* and the $\left(100 - \frac{1}{2}n\right)$-th percentile in order to represent the warm tail of the PDF.

of cold tailing in the APDF and the relative abundance of *S. antarctica* $n$: the larger the cold tail in the APDF and the lower $n$, the more the temperature of that sample location is adjusted. In this approach, we can constrain the temperature range of *S. antarctica* occurrence to $0 - 13°C$ instead of the original $0 - 20°C$ (Figure 9b); dominant occurrences (>20%) even only occur at SSTs between 0 and 5°C.

Similarly, we show that the warm species *S. delicatus* (which is also shown to have affinity with high nutrient levels (Dale et al., 2002)) could be a warmer species than previously thought. From the means of the LPDFs (blue points in Figure 3.7c) it seems that *S. delicatus* has some local preference at around $16°C$ (Zonneveld et al., 2013b), but does also occur in low abundances at sites with a much colder temperature in the overlying waters. Particularly interesting in this case is the suite of samples with overlying waters around $15°C$, and relative abundances of *S. delicatus* ranging between 0 and 37%. However, we observe in the same figure that all sites where *S. delicatus* is found are related to a temperature APDF which contains a tail towards warm regions. Following this logic, and by applying the same approach as for *S. antarctica* but then for the warm tails, the temperature affinity range of this dinocyst can be constrained to $17 - 30°C$ instead of $4 - 30°C$ (Figure 3.7c), with a strong affiliation of high (>30%) abundance of *S. delicatus* to SSTs above 24°C. Particularly the cluster of sample sites with high abundance of S. delicatus at 15°C has apparently a strong warm tail: the temperature of all these sample sites was adjusted to above 24°C. To conlude, both the APDF tailing of *S. antarctica* and *S.delicatus* serve as examples of how the particle-tracking method can be used to suggest ecological affinities of microplankton species taking particle lateral transport into account. More investigations of specific species of dinocysts and their ecologic affinity can be made available upon request. For other microplankton groups, slight adjustments of the underlying assumptions need to be made in order to make this fully applicable.

## 3.4 Summary and Discussion

We have investigated how lateral dinocyst transport by ocean currents influence sedimentary signals preserved in microfossil assemblages used to reconstruct past climate. Virtual particles are released at the ocean bottom in an OGCM. The particles were tracked back in time, to compute where and at what kind of surface environment they potentially came from for certain sinking scenarios.

First, we identified locations where the particle transport is low (e.g. shallow and equatorial regions) and regions with relatively large particle transport (e.g. western boundary currents, ACC). However, even if we found that the transport of particles is large in space, the environment is not necessarily different from the local surface environment. The temperature AB is typically large in the proximity of ocean fronts (e.g., subtropical front, labrador current), as well as regions where currents flow meridionally (Gulf Stream). A sensitivity analysis on the sinking velocity showed that the transport of particles reduces if the sinking speed increases as expected. In regions with a high degree of aggregate formation, cyst transport will be limited.

However, even under linearly increasing sinking speed assumptions based on sediment trap measurements, transport has a profound influence on the sedimentary dinocyst assemblage composition.

Next we identified a specific station in a region where the particle transport is important. Particles were transported from a colder area to the station. The example of dinocyst species *S. antarctica* at this station showed that a sediment sample is not always related to the average environment of the surface above it. Moreover, the extremes of the environment after the backtracking of particles can be important. In the case of *S. antarctica* this was the cold extreme of the PDF, which includes the advection of the cysts.

Overall we conclude that the cyst transport by currents can have an important effect on the sedimentary dinocyst assemblage composition as a paleoceanographic proxy. If a cyst is found outside of its expected habitat region, information on the particle transport could suggest whether a cyst actually occurs here (but perhaps in lower abundance), or whether the cyst was transported to the sediment sample locations. We recommend five factors to consider when relating micropaleontological data to the overlying surface-water conditions: 1) What was the water depth? 2) Did the microplankton sink through aggregation formation? 3) Was the site under influence of strong ocean currents? 4) What was the orientation of this current? 5) Did strong gradients of environmental variables exist near the site? We further recommend for any microplankton-related dataset to take particle transport into account when relating sedimentary data to oceanography. The particle-tracking method provides an opportunity to quantify the probability that these factors matter at a specific sample location.

In general the inferred PDFs after the backtracking of particles converged sufficiently fast to one shape and comprised multiple seasonal cycles. However, the low abundances of species in surface sediment samples could be related to rare events. Examples of rare events are polynya events (Holland, 2001), marine heatwaves or severe storms (Ummenhofer & Meehl, 2017). Future simulations should run sufficiently long to include strong El Niño and La Niña events which could influence the results. Such variability is averaged out in the surface sediment samples, but are currently not covered in the model runs. However, the rare occurrences have quite profound effects on modern analogue techniques, and therefore it is important that we understand how these arrive at the sample site and what their ecological implications are.

We use the tails of the APDF as a measure of AB in this chapter. However, different measures of AB could be applied in future research. It is intuitive to think about the differences of the PDF's higher order modes such as the mean or standard deviation, altough both are not informative with non-Gaussian PDFs. Furthermore, one could apply a measure which combines differences between the LPDF and the APDF in terms of all their modes (such as the Wasserstein distance (Ramdas et al., 2017)). Then one can investigate whether the APDF is different from the LPDF, but on the other hand it is not clear which mode(s) cause these differences.

No observed data of dinocysts close to the surface exists in the open ocean. Hence we cannot compare our model results of lateral transports with measured data. Dinoflagellate data at the surface do exist (e.g. (Eynaud et al., 1999)) and in broad lines these do seem to confirm the overall sedimentary dinocyst biogeography, but it is not sufficiently known which cyst type the dinoflagellates form. Hence, we are limited to the sedimentary dinocyst assemblages.

Similar backtracking methods could be applied to other sinking proxies, such as planktic foraminifera (Sebille et al., 2015b) and coccoliths. However, it is important to take into account different properties of the proxy. E.g. dinocysts relate directly to the environment at the surface, while another proxy can be influenced by the environment along a trajectory before sinking, or the productivity of other proxies in the water column could be different. Moreover, the sinking velocity of another proxy could be different compared to the sinking velocity of dinocysts. Hence each microplankton group requires a specific type of modeling, and inclusion of specific boundary conditions.

The results in this chapter challenge the conventional transfer-function methods. Future work is required to investigate whether a new type of transfer function, which corrects for lateral transport, could improve the skill of quantitative paleoceanographic reconstructions.

## 3.5 Code availability and Supporting Information

The code that is used to obtain the results in this chapter is distributed under the MIT license and can be found here: `https://github.com/pdnooteboom/PO-dinocysts`. The planktondrift.science.uu.nl website contains the results which are presented in this chapter, for every release location in every configuration. The supporting information can be accessed here: `https://agupubs.onlinelibrary.wiley.com/doi/full/10.1029/2019PA003606`.
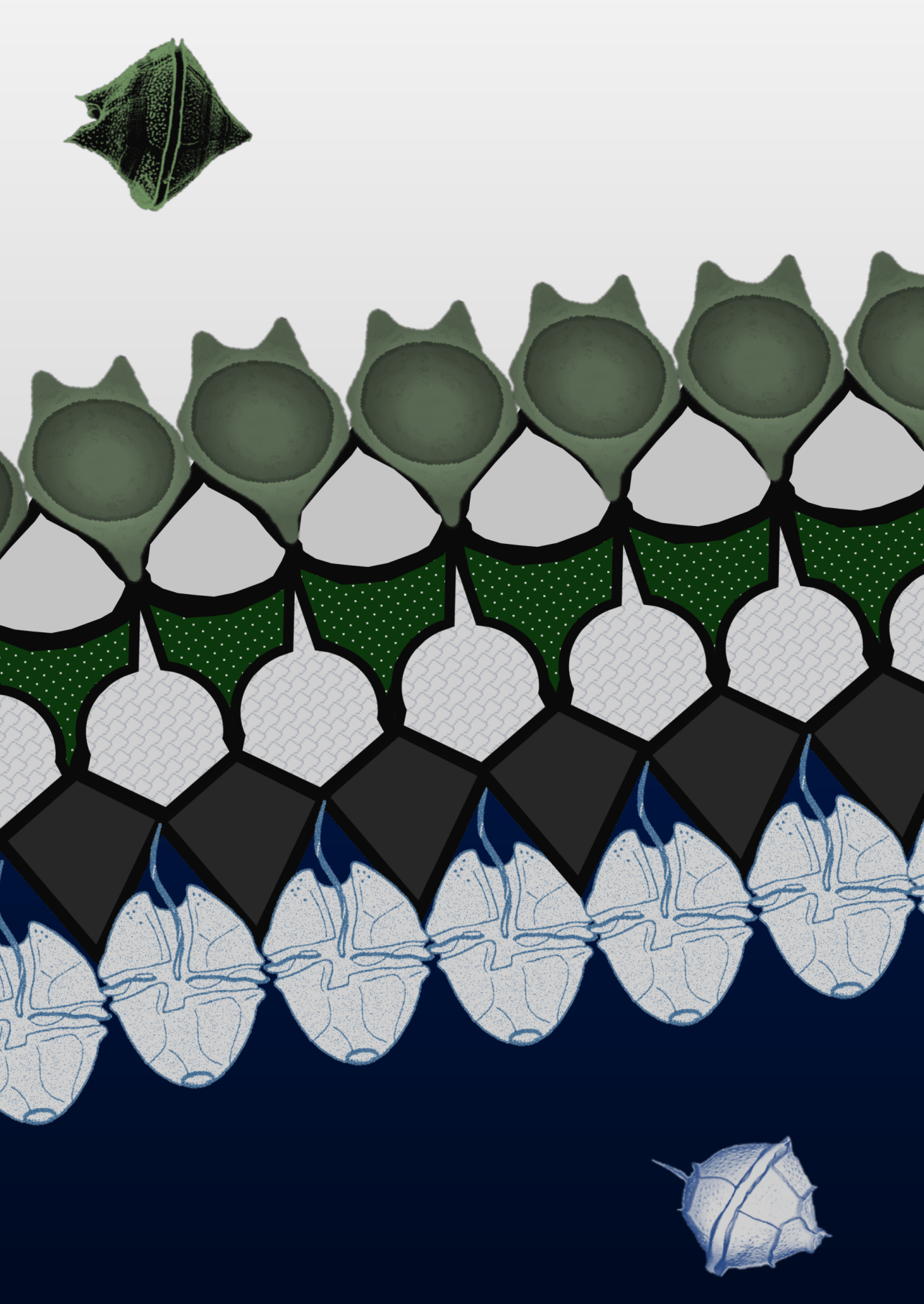
# CHAPTER 4

The sedimentary microplankton distribution is shaped by oceanographically connected areas

Nooteboom, P. D., P. K. Bijl, C. Kehl, E. V. Sebille, M. Ziegler, A. S. von der Heydt, et al. (2021), "Sedimentary microplankton distributions are shaped by oceanographically connected areas", *Earth Syst. Dyn. Discuss.* No. August, pp. 1–23

**Having descended through the water column, microplankton in ocean sediments are representative for the ocean surface environment, where they originated from. Sedimentary microplankton is therefore used as an archive of past and present surface oceanographic conditions. However, these particles are advected by turbulent ocean currents during their sinking journey. So far, it is unknown to what extent this particle advection shapes the microplankton composition in sediments. Here we use global simulations of sinking particles in a strongly eddying global ocean model, and define ocean bottom provinces based on the particle surface origin locations. We find that these provinces can be detected in global datasets of sedimentary microplankton assemblages, demonstrating the effect provincialism has on the composition of sedimentary remains of surface plankton. These provinces explain the microplankton composition, together with e.g. ocean surface environment. Connected provinces have implications on the optimal spatial extent of microplankton sediment sample datasets that are used for palaeoceanographic reconstructions, and on the optimal spatial averaging of sediment samples over global datasets.**

## 4.1 Introduction

Microplankton communities are sensitive to surface oceanographic conditions in which they live. Their remains are preserved in the sedimentary archive of the ocean basins and are therefore used to recontruct present and past surface ocean conditions. However, the sedimentary microplankton community is not driven by abiotic climate variables (e.g. temperature or nutrient availability) alone. Statistical analyses show that these climate variables only explain part of the sedimentary species variability, for both dinoflagellate cysts (Esper & Zonneveld, 2007; Zonneveld et al., 2010) and planktic foraminifera (Morey et al., 2005). Hence, it is crucial to investigate, which other processes determine the species distribution in the sedimentary archive, especially when such distributions are used to reconstruct these sea surface variables in the geologic past.

Global surface-ocean currents, and the way in which these currents connect the ocean, are shown to shape the plankton community structure near the ocean surface (Hellweger, 2014; Jonnson & Watson, 2016; Wilkins et al., 2013). Connectivity of the two-dimensional (2D) surface ocean flow is well-studied in models (Froyland et al., 2007, 2014; McAdam & Sebille, 2018; Onink et al., 2019). Floating particles accumulate towards the so-called garbage patches on decadal time scales (Lebreton et al., 2012), which often match well with relatively high concentrations of surface drifters (Sebille et al., 2012) and microplastics (Sebille et al., 2015a). In addition to the ocean surface connectivity, the three-dimensional (3D) ocean connectivity will also have an influence on the distribution of sedimentary particles.

Studies show that advection of sinking particles in 3D ocean flow has implications for sedimentary microplankton distributions (Nooteboom et al., 2019; Sebille et al., 2015b; Weyl, 1978). An initially uniform distribution of particles at the ocean surface becomes more heterogeneous (i.e. mixed) when these particles are sinking (Drótos et al., 2019; Monroy et al., 2019). At the same time, the influence of ocean currents on sedimentary particle distributions is spatially varying (see chapters 3

and 5). Hence, one might expect that the sedimentary archive is shaped by 3D particle advection by ocean currents while sinking.

The behavior of sinking particles in a 3D flow is quite different compared to that in a 2D flow. For instance, a 2D flow is divergent in an upwelling region which drives the particle convergence in garbage patches, while a 3D flow is non-divergent. However, attracting structures (Bettencourt et al., 2012) and transport barriers (Bettencourt et al., 2015; Chang et al., 2018) of 3D particle paths can also emerge inside the ocean. In this way, particles can cluster in specific areas when they are collected at a 2D surface after their sinking journey (Eaton & Fessler, 1994; Monroy et al., 2017), as is also measured at the ocean subsurface (Logan & Wilkinson, 1990; Mitchell et al., 2008).

In this chapter, we investigate how oceanographically connected areas shape the sedimentary microplankton composition. We cluster sedimentary sites based on similar ocean surface origin locations of particles that ended up at these sediment sites after their sinking journey. We use the clustering methods to distinguish between sediment sites within and outside of clusters. We find that sediment sites within isolated clusters contain a lower biodiversity and a clearer relationship with surface environmental variables compared to the sediment sites outside of the isolated clusters.

## 4.2 Method

### 4.2.1 Sedimentary data

We use two global datasets of sedimentary microplankton, one with dinoflagellate cysts (dinocysts; Marret et al., 2019) and the second with planktic foraminifera (Siccha & Kucera, 2017). We use the surface sediment samples from sites South of $65°$N (2849 and 4017 sites for the dinocysts and foraminifera respectively), because the OFES ocean model (which is used for particle advection) ends at $75°$N, which makes the clustering results at high Norhtern latitudes unreliable. For some statistical analyses, we only consider sites in the Southern Hemisphere (725 and 1858 sites for respectively the dinocysts and foraminifera), in order to limit the total diversity of microplankton species in the datasets. We consider the fraction (i.e. the relative abundance) of microplankton species for every surface sediment sample.

The foraminifera dataset also contains deep dwelling species, which live near the thermocline (typically a few 100 meters depth). Although it is often assumed that these deep dwelling species relate to sea surface variables in statistical analyses, this assumption might not be valid (Telford & Kucera, 2013). We also applied the CCA analysis while only using the species which are known to be near-surface dwelling in the subtropical Atlantic (the red group in figure 7 of (Rebotim et al., 2017); Appendix Fig. A.8). This leads to similar conclusions, although less significant values are obtained because the dataset size is lower if only near-surface dwelling species are included.

## 4.2.2 Clustering methods and particle tracking

The particle tracking results from chapter 3 provide us with distributions of surface origin locations for a global $1° \times 1°$ grid of sediment sites, for several sinking speeds. We use the results that are obtained in the eddying OFES model (Masumoto et al., 2004; Sasaki et al., 2008) with a sinking speed of 6 m day$^{-1}$. Results with a sinking speed of 25m day$^{-1}$ can be found in the Appendix.

The sinking speeds and backtracking analysis from chapter 2 are specifically designed to be compatible with the life cycle of dinocysts: particles are released at the bottom of the ocean every 5 days, and tracked back in time until they reach 10 m depth, providing a particle distribution at the ocean surface (Fig. 2.1a). Single foraminifera typically sink at higher velocities than dinocysts ($\gtrsim 100$ m day$^{-1}$), and most of their lateral transport occurs during their life span, when they are passively advected while they control their buoyancy and remain at their preferential depth (Sebille et al., 2015b). However, we assume in this chapter that the strength, direction and 'mixing' of planktic foraminifera by ocean currents has a similar spatially varying character compared to sinking dinocysts. We test whether the clustering results match both dinocyst and foraminifera sample datasets.

Our goal is to obtain provinces of sediment sites from the back-tracked surface origin locations which are oceanographically (i) *disconnected* (i.e. provinces between which particles are not likely to travel) and (ii) *isolated* (i.e provinces with sediment sites which share similar origin locations compared to the sediment sites outside of the province). We quantify these areas by disconnected and isolated clusters of sedimentary sites. Assuming that the flow from 2000 to 2005, as simulated by the OFES model, is representative of the real ocean flow in the past decades (during which the microplankton actually sedimented; Jonkers et al., 2019), we ideally find the disconnectedness and isolation of clusters in the surface sediment sample datasets.

We use two types of clustering techniques. First, hierarchical clustering provides boundaries where sinking particles are less likely to cross (hence it finds oceanographically disconnected areas). This technique starts with the full ocean as only cluster and splits a cluster into two clusters at every iteration (see Appendix A.1.1 for more details). The clusters from this technique can be compared to areas that are known to be oceanographically (dis)connected from each other, and these clusters can be used to test if more similar species are found within each connected area compared to between connected areas. Advantages of the hierarchical clustering method are that the cluster structure is preserved as more iterations are applied, and it does not require many parameters. The only parameter that the hierarchical clustering uses is the stop-criterium (i.e. the iteration number where the algorithm stops with creating new clusters).

Second, we use the *Ordering Points To Identify the Clustering Structure* (OPTICS) algorithm to find oceanographically isolated clusters. OPTICS provides a density based value (the reachability) of sedimentary sites which quantifies how strongly a

site is connected to other sites. Oceanographically isolated clusters can be obtained from the 'dense regions' (i.e. areas with low reachability values), by setting a threshold on the slope that surrounds the dense values in the reachability plot ($\xi$; see Fig. 4.1a for an example). The sediment sites outside of these clusters are less isolated, and refered to as 'noisy.' These clusters allow us to test if sedimentary species compositions are more homogeneous inside isolated areas compared to outside of these areas (see Fig.4.1b).

The advantage of OPTICS is that parameter values have a clear interpretation. First, the parameter $s_{min}$ is the minimum number of particle release locations in clusters, which represents a minimum spatial scale of clusters (in $m^2$). The second parameter $\xi$ determines the degree of isolation of the clustering: OPTICS generally finds less and smaller clusters if $\xi$ is larger. Another advantage of OPTICS is that not all areas are clustered, such that it allows to distinguish between 'noisy' (not clustered) and oceanographically isolated (clustered) areas (see Appendix A.1.2 for more details about OPTICS).

We also tested the seasonal dependence of hierarchical clusters (see Appendix Fig. A.3 and A.4), by only considering particles that started their sinking journey in a specific season. While some of the boundaries changed between summer and winter, the change in the overall clustering structure was limited if only a specific season of origin locations was considered (similar to Sebille et al., 2015a, who only found a small seasonal effect in temperature offsets due to lateral transport of foraminifera).

### 4.2.3 Statistical analyses

We apply several statistical tools to test hypotheses about the sediment sample sites and the clusters in which they are located. A partial Mantel test (Legendre & Legendre, 2012) is used to test whether the reachability from the OPTICS algorithm correlates with the sediment sample taxonomy, independent of the spatial distance between sediment sample site locations. A partial Mantel test requires at least three types of distance matrices, which contain distances between the sediment sample sites. We calculate the Mantel correlation between taxonomic distance and a distance which is determined from the reachability of the OPTICS clustering (see Appendix A.2), while we control for the spatial distance between sites.

We use Canonical Correspondence Analysis (CCA; Braak & Verdonkschot, 1995) to infer the relation between species in clustered sediment sites and environment parameters at the ocean surface. In this context, CCA ideally shows unique species responses to changes in environment input parameters. We use sea surface temperature (SST) and surface nitrate ($NO_3$) as environmental parameters, as prior literature reported them to explain a major part of the species variability in the Southern Ocean (Esper & Zonneveld, 2007; Prebble et al., 2013). This study infers SST and $NO_3$ for sediment sample locations from $1° \times 1°$ fields of the *World Ocean Atlas* (Garcia et al., 2013; Locarnini et al., 2013). Further parameters, such as phosphorus, silicate, salt concentration, were tested (as in Hohmann et al., 2019), though spurious CCA response led to their exclusion from further analysis in this chapter. We compare the CCA's explained variation of sedimentary samples only drawn from (i)

only isolated clusters and (ii) with samples drawn from all available locations. Comparing the explained species variation of both cases allows us to draw conclusions about the source of variation between both CCA results in order to quantify the significance of the clustering approach. We apply a one-sided randomization test to investigate whether the increase of explained variance is significant. This implies that we randomly take subsamples of the full dataset, which are equally sized to the amount of clustered sediment samples. The p-value of the permutation test is the fraction of random subsamples that resulted in a higher explained variance compared to the CCA analysis with the clustered samples.

The foraminifera dataset also contains deep dwelling species, which live near the thermocline (typically a few 100 meters depth). Although it is often assumed that these deep dwelling species relate to sea surface variables in statistical analyses, this assumption might not be valid (Telford & Kucera, 2013). We applied the CCA analysis while only using the species which are known to be near-surface dwelling in the subtropical Atlantic (the red group in figure 7 of Rebotim et al., 2017; Appendix Fig. A.8). This leads to similar conclusions, although less significant values are obtained because the dataset size is lower.

The clusters that are obtained from the OPTICS algorithm represent areas of relative oceanographic isolation. We test whether the species distributions in sediments outside clusters are more mixed compared than samples inside clusters during their sinking journey. We use Shannon entropy (Shannon, 1948) to quantify taxonomic mixing, which is defined at site $j$ as $N_s^j = -\sum_i p_{ij} \ln(p_{ij})$. Here $p_{ij}$ denotes the relative abundance of a species $i$ at site $j$. Shannon entropy is often used as a biodiversity index (Morris et al., 2014), being a combined signal of species richness (amount of species in the sediment sample) and evenness (how evenly these species are distributed). We choose the Shannon entropy here as biodiversity index, because it can be compared to the mixing of sinking particles, and Shannon entropy is often used to quantify the loss of information by mixing (e.g. in thermodynamics). We compare the average Shannon entropy of sediment sample sites within ($\overline{N}_s^c$) and outside ($\overline{N}_s^{nc}$) clusters.

## 4.3 Results

The particle tracking results from chapter 3 provide us with distributions of surface origin locations for a global $1° \times 1°$ grid of sediment sites. We obtain provinces of sediment sites from these surface origin locations which are oceanographically (i) disconnected (i.e. provinces between which particles are not likely to travel) and (ii) isolated (i.e provinces with sediment sites which share similar origin locations compared to the sediment sites outside of the province). We quantify these areas by disconnected and isolated clusters of sedimentary sites, and also find this disconnection and isolation of clusters in the surface sediment sample datasets. We use two types of clustering techniques. First, the hierarchical clustering technique (see the method section) finds oceanographically disconnected areas. Since, these clusters are disconnected, sediment samples from the same cluster contain more similar

4
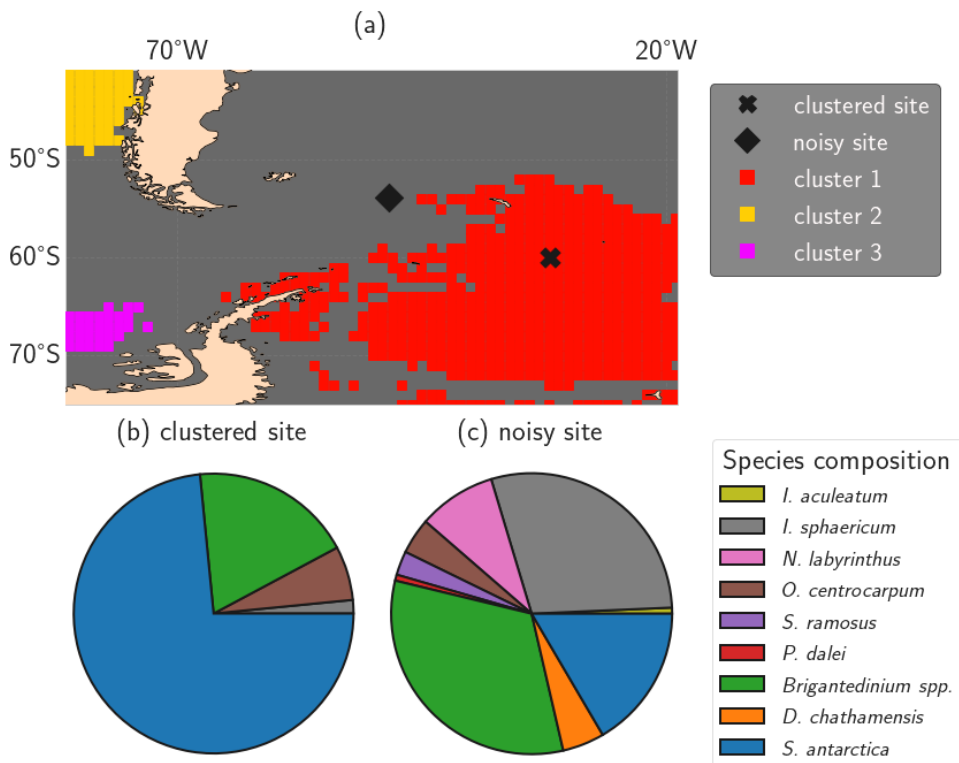


**Figure 4.1:** Illustration of the impact of isolated clusters on sedimentary microplankton composition. (a) A (noisy) sediment sample site outside of the isolated clusters (station J299) and a site within oceanographically isolated OPTICS cluster 1 (station J285) in the South Atlantic. (b), (c) Pie charts of the dinocyst species composition in the sites from (c). The clustered site contains a species composition which is less biodiverse compared to the noisy site. The Shannon biodiversity indices of respectively the clustered and noisy site are 0.7788 and 1.6842. This illustration uses the same OPTICS clusters as are shown later in figure 4.4.
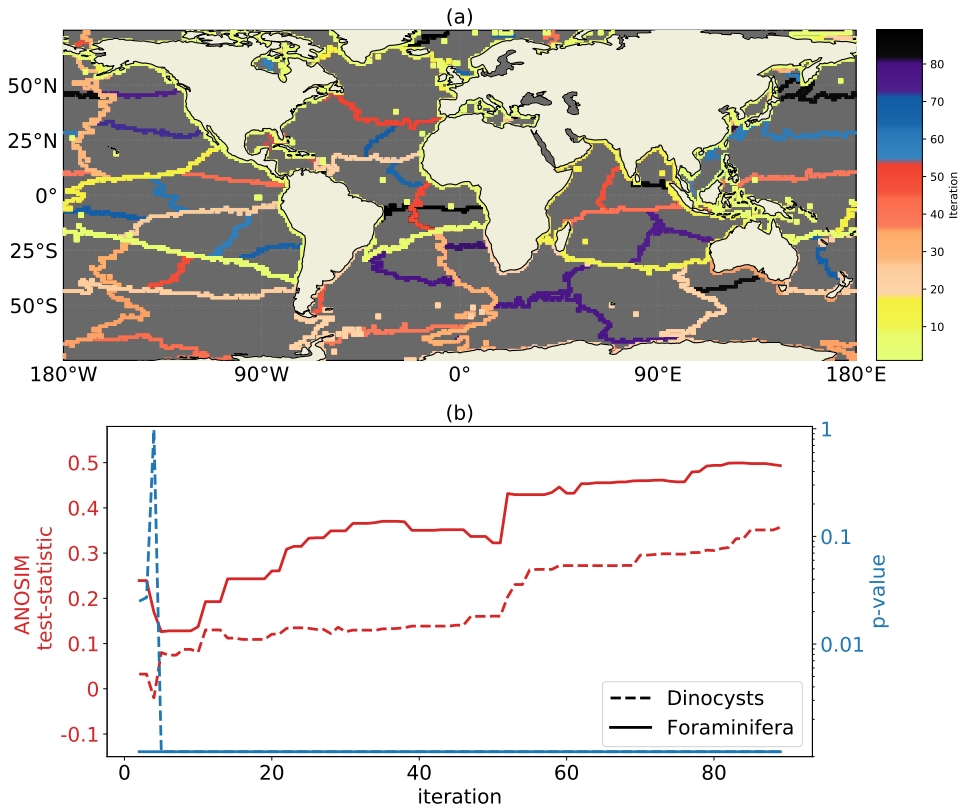
**Figure 4.2:** Oceanographically disconnected clusters of sedimentary particle release locations from the hierarchical clustering method. (a) The clusters edges after 90 iterations, where the color indicates at which iteration number a cluster edge is created. (b) The ANOSIM test-statistic (red) and p-values (blue; 999 permutations; logarithmic scale) for the clusters at every iteration number, which tests whether the sedimentary microplankton composition (both dinocysts and foraminifera; sites below 65°N) is more similar within than between clusters.

species compared to samples from different clusters. Second, the *Ordering Points To Identify the Clustering Structure* (OPTICS; see the method section) algorithm finds oceanographically isolated clusters. Sinking particles that end up in an isolated cluster do not mix with sinking particles that end up in bottom sediments outside of this cluster. Hence, the oceanographic isolation of sediment sample sites decreases the biodiversity of their microplankton composition (see Fig. 4.1) and they have a clearer relationship with environmental variables at the surface.

### 4.3.1 Oceanographically disconnected clusters

We interpret splits of oceanographically disconnected clusters from the hierarchical clustering method as boundaries with a low connectivity across them (Fig. 6.3). The probability that particles cross these boundaries is larger if the iteration number

is higher. We observe that these cluster edges compare well to large-scale ocean connectivity. The first iteration splits the Mediteranean Sea from the global ocean, because no sinking particles travel through the Gibraltrar strait in the simulation. Next, the Pacific is separated from the Arctic, since few particles are transported through Bering strait (Coachman & Aagaard, 1988). At the subsequent iterations, the large-scale ocean basins disconnect: The Pacific, Atlantic and Indian ocean are split from the Southern ocean at approximately 25°S. We find that areas near Western boundary currents may only split into clusters at relatively high iterations, because the sediments in these areas have a relatively large connectivity, with particles originating from a large area (see also chapter 3).

In the North-Atlantic region, we find that Hudsons Bay becomes a cluster and the subtropical Atlantic is split from the Nordic seas at the Greenland-Scotland ridge (Bower et al., 2019; Fratantoni, 2001; McClean et al., 2002). The Irminger Basin is still connected with the Labrador Sea, where sinking of water occurs (Katsman et al., 2018; Pickart et al., 2003), which makes transport of sinking particles outside of this area less likely. Only a few particles cross the connection between the Labrador Sea and Baffin Bay (Fischer et al., 2018; McClean et al., 2002).

We do not find a cluster at high (subpolar) latitudes which isolates Antarctica along latitudinal bands (only the Weddell and the Ross Sea are a cluster). One might expect such a cluster, because near-surface currents are known to isolate Antarctica (Döös et al., 2008; Dufour et al., 2015; Fraser et al., 2018). However, deep passive particles advected by three-dimensional flow are shown to move upwards along isopycnals towards Antarctica (Drake et al., 2018; Tamsitt et al., 2018). As a result, the sinking particles can be transported towards Antarctica at depth. The location of southward particle transport is mainly determined by topographic steering of the flow, resulting in five hotspots of southward particle transport (Tamsitt et al., 2017) which roughly coincide with the Southern Ocean clusters in Fig. 4.2.

Some of the clusters in Fig. 4.2 are similar to connected regions based on the surface flow (see figure 8 from Froyland et al., 2014). The North and South Atlantic are split similarly from West-Africa to Venezuela. The North Pacific and South Pacific are split in a similar way from Australia to the south of Chile. A cluster around the Pacific cold tongue (East Tropical Pacific) develops (Froyland et al., 2014; Moum et al., 2013). Moreover, the Benguela upwelling area (Nelson & Hutchings, 1983) near South West Africa is more connected with the Southern Ocean than with the Atlantic. Near-surface currents have an important influence on the total lateral transport of sinking particles in these areas, since they are similar to the surface connectivity areas from Froyland et al., 2014.

We test whether sites within hierarchical clusters have a lower (Euclidean) taxonomic distance compared to sites of different clusters with *Analysis of similarities* (ANOSIM; Clarke, 1993). The ANOSIM tests-statistics (Fig. 4.2c) is positive for statisically significant results (p-value<0.001) for all iterations. Hence, sediment samples within clusters are more similar than those between clusters. The

test-statistic increases at higher iteration numbers, for both the dinoflagellate cyst (dinocyst) and foraminifera dataset. Although these ANOSIM results look promising, it is important to note that the ANOSIM test-statistics are partly positive because the sediment sites within clusters are closer to each other (i.e. there is a distance effect independent of the clustering).

The hierarchical clustering is overall insensitive to the used sinking speed of particles (see the Appendix Fig. A.2 with sinking speed 25 m day$^{-1}$). Only some minor differences occur in the North Pacific, and some cluster separations occur at slightly different iteration numbers. The fact that similar boundaries of little cross-transport emerge at a different sinking speed proves that the clustering does not greatly depend on the sinking speed of particles.

### 4.3.2 Oceanographically isolated clusters

The OPTICS clustering algorithm provides a density based value (the reachability) of sedimentary sites, which quantifies how strongly a site is connected to other sites. Oceanographically isolated clusters can be obtained from the 'dense regions' (i.e. areas with low reachability values), by setting a threshold on the slope that surrounds the dense values in the reachability plot ($\xi$). The sediment sites outside of these clusters are less isolated, and refered to as 'noisy.'

According to the OPTICS algorithm, the Western boundary currents are unlikely to be part of any isolated cluster, since the points near the Western boundary currents have a relatively high reachability (Fig. 4.3b). This is expected, because the origin locations of sediment samples near Western boundary currents comprise a large area. Dense areas are those at higher latitudes, close to Antarctica and in the Nordic Seas, and the midlatitude gyres. Sediment sample sites within these areas have more similar surface origin locations compared to sediment sites outside of dense areas. The high reachability values in the Mediterranean Sea and Red Sea are rather artificial. OPTICS searches for dense regions (low reachability) by searching for sedimentary sites with relatively many other sites having similar surface origin locations. Since the Mediterranean Sea and Red Sea are enclosed by land, these sedimentary sites have only few neighbouring sites, resulting in a relatively high reachability.

The reachability distance ($D^r$; see Appendix A.2) between sediment sample sites correlates positively with sediment sample taxonomy. Furthermore, this correlation is independent of the spatial distance between sites, according to the partial Mantel tests (Fig.4.3c; see the method section). This means that oceanographically connected sites have a similar taxonomy, independent of their spatial distance. Large values of $s_{min}$ (>600; i.e. the OPTICS parameter which determines the minimum surface area in m$^2$ of OPTICS clusters) tend to have the largest correlation (also at other sinking speeds; see the Supporting Information). This is probably because the reachability is smoother at higher $s_{min}$, which makes the reachability distance less

4
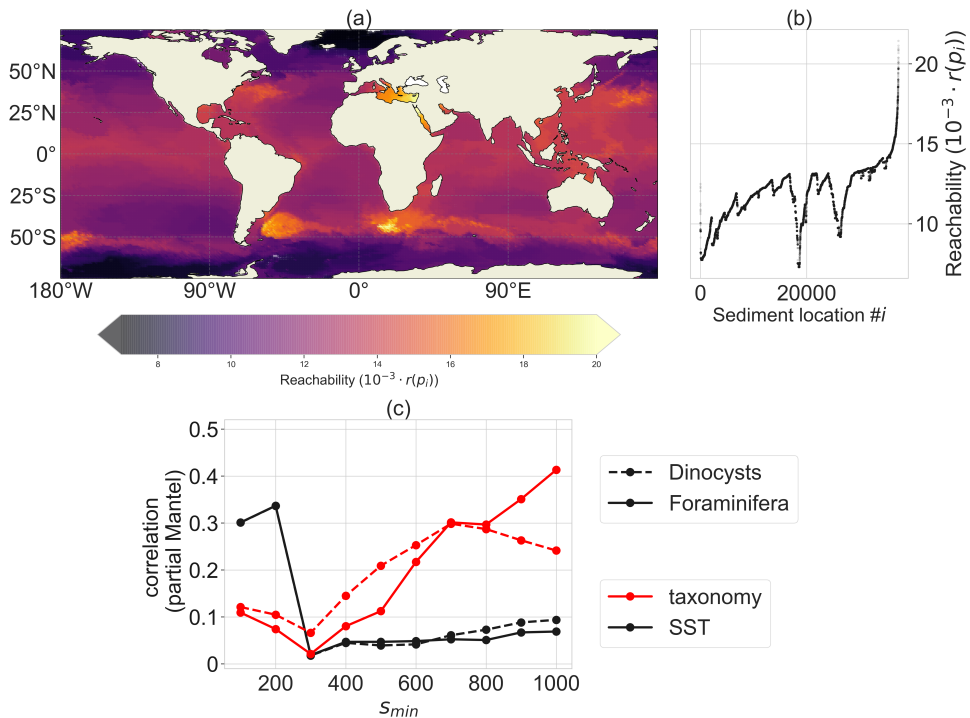
**Figure 4.3:** Reachability plot of the sedimentary particle release locations from the OPTICS algorithm. Sediment locations in dense areas (i.e. with low reachability values) share a similar surface origin particle distribution. A sinking speed of 6 m day$^{-1}$ is used and parameter $s_{min} = 300$ (i.e. OPTICS clusters will consist of a minimum of 300 sediment sites). (a) Site reachability in space: sites in dense areas with a low reachability are oceanographically isolated. (b) A scatter plot of the ordering of the sediment locations $i$ against their reachability $r(p_i)$. (c) Partial Mantel correlation of the reachability distance $D^r$ (a lower value of $D^r$ between two sites indicates a stronger oceanographic connection between these sites) with the taxonomy (red) and SST (black), both with spatial distance held constant, for different $s_{min}$ values. A total of 999 permutations were used for every partial Mantel test; every test with respect to the taxonomy (red) is significant with p-value$< 0.003$.
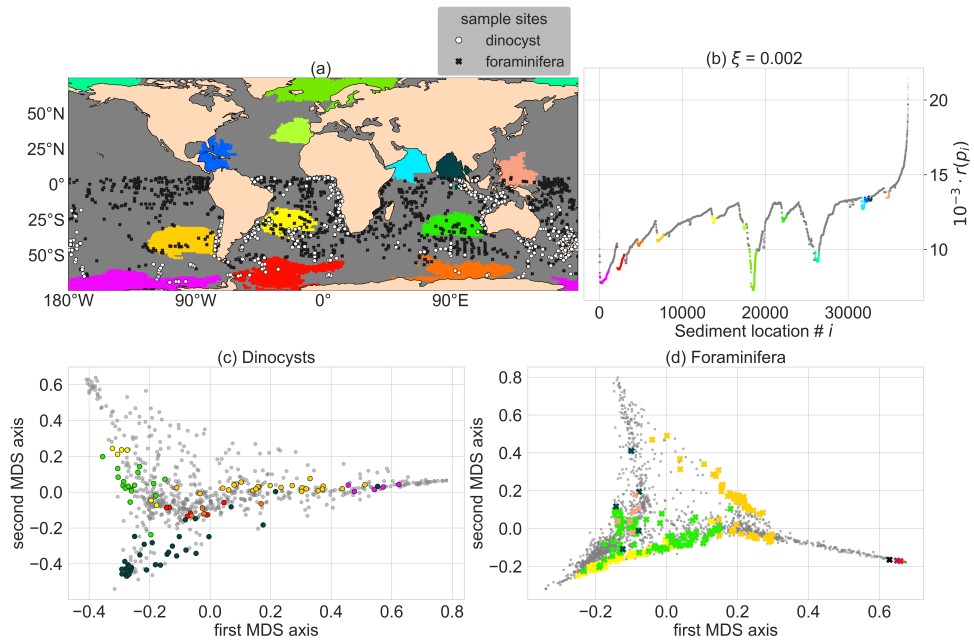
**Figure 4.4:** Oceanographically isolated OPTICS clusters of sedimentary particle release locations with clustering parameters $s_{min} = 300$ (i.e. the minimum size of clusters) and $\xi = 0.002$ (i.e. the level of isolation). The clustering is applied globally and the clusters are compared to Southern Hemisphere sediment sample sites. The colored regions are clusters, the gray regions are "noisy", and therefore not part of a cluster. These colors were used for all subpanels. (a) Global map of the position of the clusters (colored regions), and dinocyst- (white) and foraminifera (black) sample locations. (b) Ordering of sedimentary locations $i$ against their reachability $r(p_i)$. To visualize the sediment sample site taxonomy for (c) the dinocysts and (d) the planktic foraminifera in two dimensions, we use *classical multidimensional scaling* (MDS; Fouss et al., 2016). MDS creates a two-dimensional approximation of the species composition in the sediment samples in this figure (instead of 91 and 50 dimensions/species for the dinocysts and foraminifera respectively).

noisy. At small spatial scales ($s_{min} \leq 200$), the correlation between dinocyst taxonomy and $D^r$ could be indirect, because then $D^r$ correlates more strongly with the environment (in terms of sea surface temperature) compared to taxonomy.

We compute clusters by setting a threshold on the slope ($\xi$) that surrounds the valleys/dense reachability regions in Fig. 4.3a. For $\xi = 0.002$ and $s_{min} = 300$ (Fig. 4.4), we obtain 13 clusters, of which three regions are isolated by the Antarctic Circumpolar Current (ACC), three in the Indian ocean, one in the Pacific warm pool, the South Atlantic gyre, near the Humboldt upwelling zone, near the Caribean Sea, the Eastern North Atlantic and two clusters near the Arctic. The clusters represent locations that are oceanographically isolated, with sediment sample sites that have backtracked origin locations which are similar to the other sites in the cluster. The environmental variability witin these clusters can be reasonably large (e.g. the sea

surface temperatures at backtracked origin locations in the cluster West of Australia range between 10-25°C; see planktondrift.science.uu.nl).

The comparison between the clusters and taxonomic distance of Southern Hemisphere sample sites in these clusters (Fig. 4.4c and 4.4d) becomes interesting for clusters which are spatially close (Fig. 4.4b). For instance, the red and yellow cluster in the South-Atlantic Ocean are spatially close, but sediment samples in those clusters are separated by their observed dinocysts taxonomy (Fig. 4.4c). This implies that we find a signal of the oceanographic separation of these areas in the sedimentary data. If noisy sites (such as the noisy site in Fig. 4.1) would be part of clusters, sites in different clusters are likely to contain a similar microplankton composition and the taxonomic separation of clusters is unclear.

To test if sedimentary sites within clusters are better correlated with environmental conditions at the surface, we applied Canonical Correspondence Analysis (CCA; see the method section) either including or excluding the sedimentary sites outside the isolated clusters (Fig.4.5). We find that the amount of explained variance by the canonical axes increases significantly if noisy sediment samples are excluded for the foraminifera ($\sim$0.92 to $\sim$0.95) and especially for the dinocysts ($\sim$0.82 to $\sim$0.98), for the same OPTICS clusters as in Fig.4.4. Hence, we find that the linear relationship between environmental variables and microplankton composition of the CCA explains a larger part of the sedimentary species compisition if noisy sites are excluded. In that sense, the signal is 'cleaner' for sediment sample sites within compared to outside clusters.

The robustness of the relationship between sedimentary sites and environmental variables is investigated by testing the sensitivity of the CCA results to these parameters $\xi$ and $s_{min}$ (Fig. 4.6). For the dinocyst dataset we find an increase of explained variance by the canonical axes for most tested values of $s_{min}$ and $\xi$. By increasing the reachability slope that surrounds the oceanographically isolated clusters ($\xi$), a higher constraint is put on the isolation of these clusters and less sediment sample sites are part of a cluster. If this slope $\xi$ is chosen too high, no clusters exist or they are too small to contain any sediment sample sites at all. Moreover, a higher value of $\xi$ means that less sedimentary sites are used in the CCA (i.e. the dataset size is reduced), which may lead to an insignificant result according to the randomnization test. A relatively low value of $\xi$ on the other hand, may lead to insignificant results due to the inclusion of noisy sites in clusters. Hence, there seems to be an optimal value $\xi$, for which this increase of variance is maximized. These results are more often insignificant for the dinocysts compared to the foraminifera, because the dinocyst dataset is smaller. If $s_{min}$ is higher (i.e. the OPTICS algorithm finds larger clusters; in $km^2$), the negative and insignificant values in Fig. 4.6 are partly caused by including noisy sites in clusters. These results highlight the importance of choosing an appropriate combination of $\xi$ and $s_{min}$ for the CCA to show a significant increased explained species variability if only clustered sites are used.

The clustered samples are less taxonomically mixed (i.e. are less biodiverse) for

4
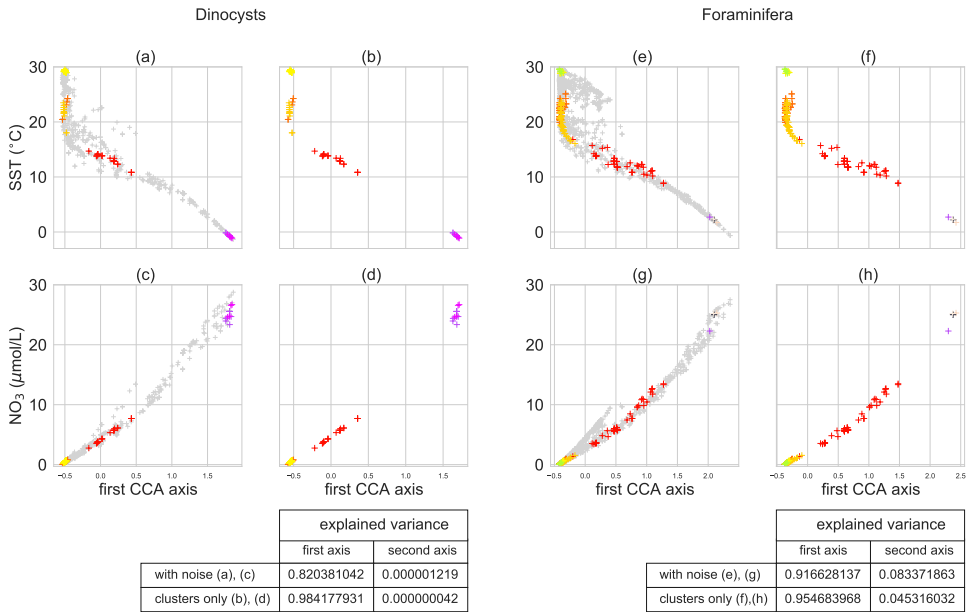


**Figure 4.5:** The relation between microplankton species variability and environmental variables according to a CCA analysis, while including and excluding unclustered sediment samples (using the isolated clusters from Fig.6.4). Sea surface temperature (top) and nitrate concentration (bottom) at sediment sample sites with dinocysts (left; (a), (b), (c), (d)) and foraminifera (right; (e), (f), (g), (h)) against the first canonical axis from the CCA analysis, including ((a),(c),(e),(g)) and excluding ((b),(d),(f),(h)) sediment sample sites outside of the oceanographically isolated clusters. The sediment sample sites that belong to a cluster are colored, 'noisy' samples (i.e. not part of any cluster) are gray. The tables at the bottom show the proportion of total variance that is explained by the canonical axes if the noisy samples are included or excluded. 13.5% (for dinocysts) and 10.8% (for foraminifera) of the sediment sample sites is in clusters, the remainder is in 'noisy' regions. The increase of explained variance is supported by a permutation test with 999 permutations (p-values are <0.0001 and 0.024 for dinocysts and foraminifera respectively).
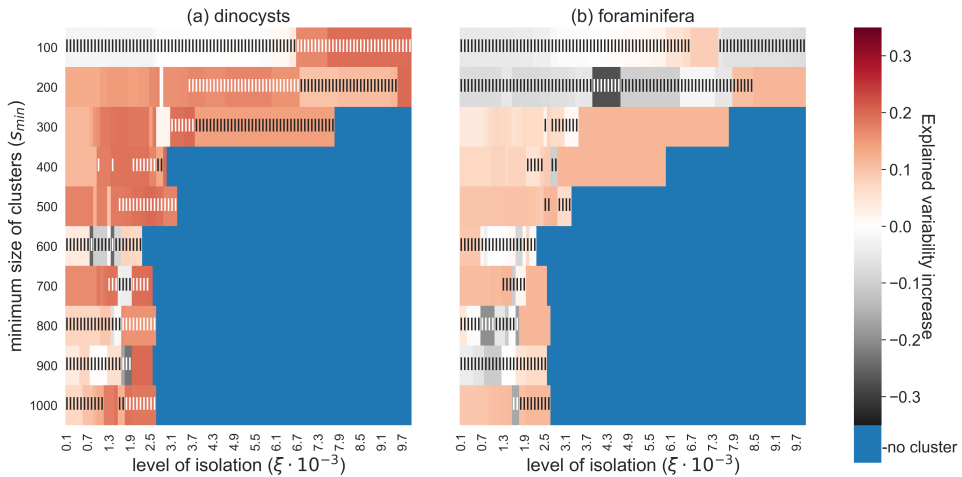
**Figure 4.6:** Increase of explained environmental variability by microplankton sediment sample sites in the CCA analyses if sediment samples outside of the oceanographically isolated OPTICS clusters are excluded, for different parameter values $s_{min}$ (i.e. the minimum size of clusters) and $\xi$ (i.e. the level of isolation). (a) the dinocyst and (b) the foraminifera dataset. High and significant values indicate that sediment samples within clusters have a clearer relationship with the surface environment. Blue are configurations of $s_{min}$ and $\xi$ for which no sediment sample sites are part of a cluster. Only Southern Hemisphere sedimentary microplankton data were used here. Vertical stripes indicate an insignificant randomization test with 999 permutations at a 5% significance level.

most values of $\xi$ and $s_{min}$, as we can see from the comparsion between the Shannon entropy ($N_s$; see method section) within and outside of clusters (Fig. 4.7). For the high values of $s_{min}$, we find that the clusters are less taxonomically mixed if $\xi$ is increased. This result supports that measured microplankton biodiversity in sediments is relatively large in areas with strong mixing of sinking particles by ocean currents. However, this is also influenced by the species distribution at the ocean surface. At smaller values of $s_{min}$ ($s_{min} < 200$ and $s_{min} < 300$ for the dinocysts and foraminifera respectively; Fig. 4.7), also high (surface) productivity areas are clustered (e.g. the South-West Atlantic or the Humboldt area; see Fig. 4.4). Hence, a relatively high sedimentary biodiversity in these clusters can be explained by the high biodiversity at the ocean surface, before these particles start sinking.

We also tested the OPTICS results for sinking velocities higher than 6 m day$^{-1}$ (25m day$^{-1}$; see Appendix Figs. A.5-A.7 in the Appendix). Similar clusters can be found with the other sinking velocities. A higher sinking speed decreases the particle travel time, hence the lateral transport and the mixing of sinking particles is overall lower (chapter 3). However, the spatial dependence of the lateral transport is similar: both at low and high sinking velocities, the lateral particle transport is relatively large near Western boundary currents, and low in the middle of midlatitude gyres (see chapter 5). As a result, the clusters are located in similar areas for different sinking speeds. It is only the spatial scale of these clusters that might be different.
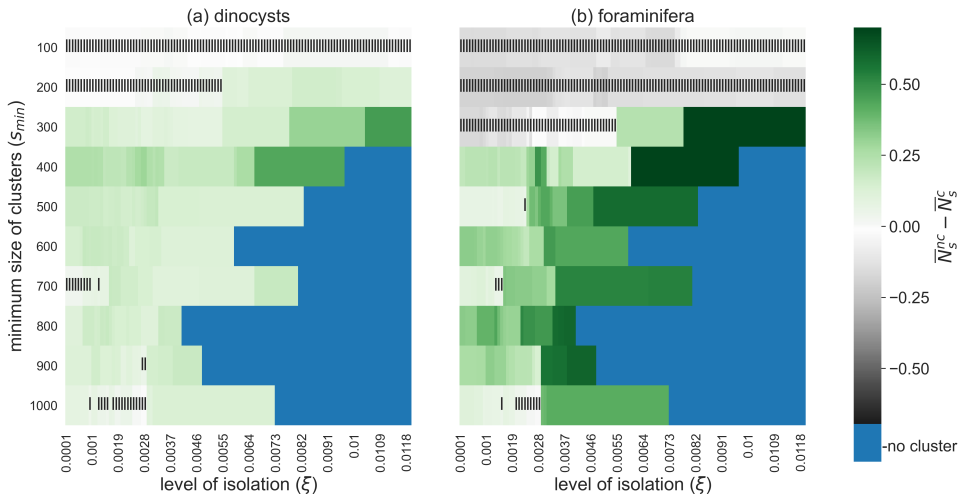
**Figure 4.7:** Sedimentary microplankton biodiversity outside minus inside oceanographically isolated provinces. The average Shannon entropy of (a) dinocysts and (b) foraminifera sediment samples inside OPTICS clusters $\overline{N}_s^c$ compared to outside clusters $\overline{N}_s^{nc}$ for different values of $s_{min}$ (i.e. the minimum size of clusters) and $\xi$ (i.e. the level of isolation). High values indicate that the number of species in samples within clusters are lower and species are distributed less evenly in samples compared to samples outside clusters. Blue are configurations of $s_{min}$ and $\xi$ for which no sediment sample sites are part of a cluster. Vertical stripes indicate an insignificant permutation test with 999 permutations at a 5% significance level.

The spatial scale (i.e. the size) of the clusters can again be controlled by the parameters $s_{min}$ and $\xi$. Note that high productivity areas are less likely clustered at higher sinking speeds, which has implications for the Shannon entropy within and outside clusters (Fig. 4.7): Higher biodiversity is measured outside compared to within clusters for a larger area of $s_{min}$ and $\xi$ values as the sinking speed increases.

## 4.4 Discussion

We clustered sediment sites based on the ocean surface origin locations of sinking particles that end up at these sites in an ocean model. These clusters reveal which sedimentary areas are oceanographically (i) (dis)connected or (ii) isolated. The connectivity which is given by the clusters is an aggregate of the ocean connectivity at all depths that the sinking particles traverse before ending up in the sediments. This type of connectivity, and the way it shapes the sedimentary microplankton composition, is additive to the environment and surface ocean connectivity which influences the plankton community structure at the ocean surface (Jonnson & Watson, 2016; Wilkins et al., 2013). Nevertheless, the near-surface flow likely has a large imprint on the clusters since these contain the strongest ocean currents.

It was shown before, that the ocean surface ecological affinity of certain sedimentary microplankton species can improve if the lateral advection of sinking particles

is taken into account (chapter 3). Here we explore why sedimentary plankton assemblages include species that occur outside their surface water habitat range. Microplankton species mix by turbulent ocean currents during their sinking journey, which can result in a relevant lateral displacement along transport. The extent by which this occurs differs strongly in the world oceans, and is larger in areas that are referred to as noisy in this chapter.

We conclude that ocean sediments are to a spatially varying degree provincial, and province boundaries are governed by near-surface and deep currents in the ocean. These provinces have implications for sedimentary microplankton assemblages. Their quantification helps to determine ocean sediment regions that are oceanographically (a) (dis)connected and (b) isolated from the area outside of these regions. Quantification of connected and isolated provinces have at least 4 implications for future studies.

First, the clustering methods that are presented in this chapter can help to improve the application of transfer functions on microplankton assemblages. Transfer functions train a model on surface sediment samples and ocean surface environmental variables (in the present-day), in order to make quantitative climate reconstructions of past climates from microplankton in deeper sediments. Hence, these transfer function models use spatial variability of an environmental variable to predict its temporal variability in a single location. One challenge of transfer functions is to choose a proper spatial extent to train the prediction model (Hohmann et al., 2019; often in the present-day situation). A small spatial extent does not capture enough of species and environment variability. If the spatial extent is too large, different processes determine the sedimentary species distribution which reduces the transfer function skill.

The hierarchical clustering method (which finds oceanographically disconnected clusters) can help to determine bounds on the spatial extent that is used for the training of transfer functions (e.g. a transfer function can be trained on sites within a single cluster), since it shows areas which are oceanographically separated from each other. These clusters are created in a present-day configuration in this study, and may change in past climates (see Appendix D). The OPTICS clustering can be used to find oceanographically isolated clusters to determine the spatial extent of a regional transfer function model. In this case, it is advisable to check if the OPTICS cluster is large enough (i.e. the deep sediments do not contain species outside of the cluster).

Second, the connectivity between provinces could have an effect on biogeochemical properties of microplankton species that are applied as a proxy of the ocean surface environment. These provinces can be used to correct for ocean connectivity by providing a different reference frame (Weyl, 1978) if the proxies are used to assimilate e.g. global sea surface temperature fields (as in Tierney et al., 2020a). This may require the computation of these clusters using palaeoceanographic models. Moreover, spatially varying Bayesian regression is used to some of these biogeochemical

proxies, because the proxy response differs across oceanic basins (Tierney & Tingley, 2015, 2018). Since proxy calibration residuals are often high in specific areas and related to lateral advection (Tierney & Tingley, 2018), the (dis)connected provinces from this chapter could provide a spatial structure that such a regression model uses for core-top calibration.

Third, the results in this chapter have implications for other types of sinking particles in the ocean. For instance, a large fraction of marine plastic sinks to the ocean floor (Canals et al., 2020; Kooi et al., 2017). Sedimentary plastic distributions might be subject to similar mechanisms of mixing during their sinking journey. Clustering of sedimentary sites might indicate where the largest inhomogenities of sedimentary plastics appear (Fuente et al., 2021), or boundaries where sinking plastic is less likely to cross.

Fourth, our study provides micropalaeontologists with a tool to qualitatively assess the importance of lateral transport to sedimentary particle assemblages, which can be used in studies that compare measured biological diversity and environmental conditions in surface waters with their sedimentary remains (e.g. Jonkers et al., 2019; Meilland et al., 2020), particularly in those regions for which we here demonstrate 'noisy' behaviour. Within oceanographically isolated clusters, sedimentary microplankton biodiversity is only weakly determined by lateral particle transport compared to the microplankton biodiversity near the ocean surface and species-specific dissolution (Frenger et al., 2018; Taylor et al., 2018).

Drivers of biodiversity at the ocean surface, such as species interactions (Lima-Mendez et al., 2015), ecological limits and evolutionary dynamics (Fenton et al., 2016), are complex. It is possible that oceanographically isolated provinces do not directly drive a low biodiversity, but indirectly cause a low biodiversity through a lower variation of abiotic factors. Moreover, these provinces are likely located in areas with relatively little eddy activity, while mesoscale eddies can explain relatively high biodiversity values (Frenger et al., 2018).

The backtracking analysis on which we applied the clustering was designed for dinocysts, and not for foraminifera. In particular, near-surface advection during the foraminifera life span may have a larger impact on its sedimentary distribution compared to the lateral transport during sinking (Ottens & Nederbragt, 1992). Clustering results from this paper compared well with the foraminifera dataset in most cases, because the areas with strong particle mixing and lateral transport (i.e. their spatial dependence) are likely similar for foraminifera (and likely similar at the near-surface compared to other depth levels). Nevertheless, future work could apply these clustering methods on a backtracking analysis which is designed for foraminifera (similar to Lange & Sebille, 2017b; Sebille et al., 2015b). This means that particles are released at the ocean bottom, tracked back in time until they reach the foraminifera dwelling depth, and finally tracked back during their life span at this dwelling depth.

## 4.5 Code availability

The code used for this chapter is distributed under the MIT license and can be found at the website `https://github.com/pdnooteboom/ClusterSinkingParticles`.

4
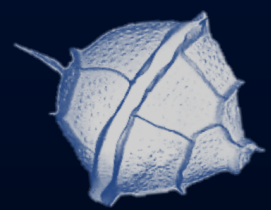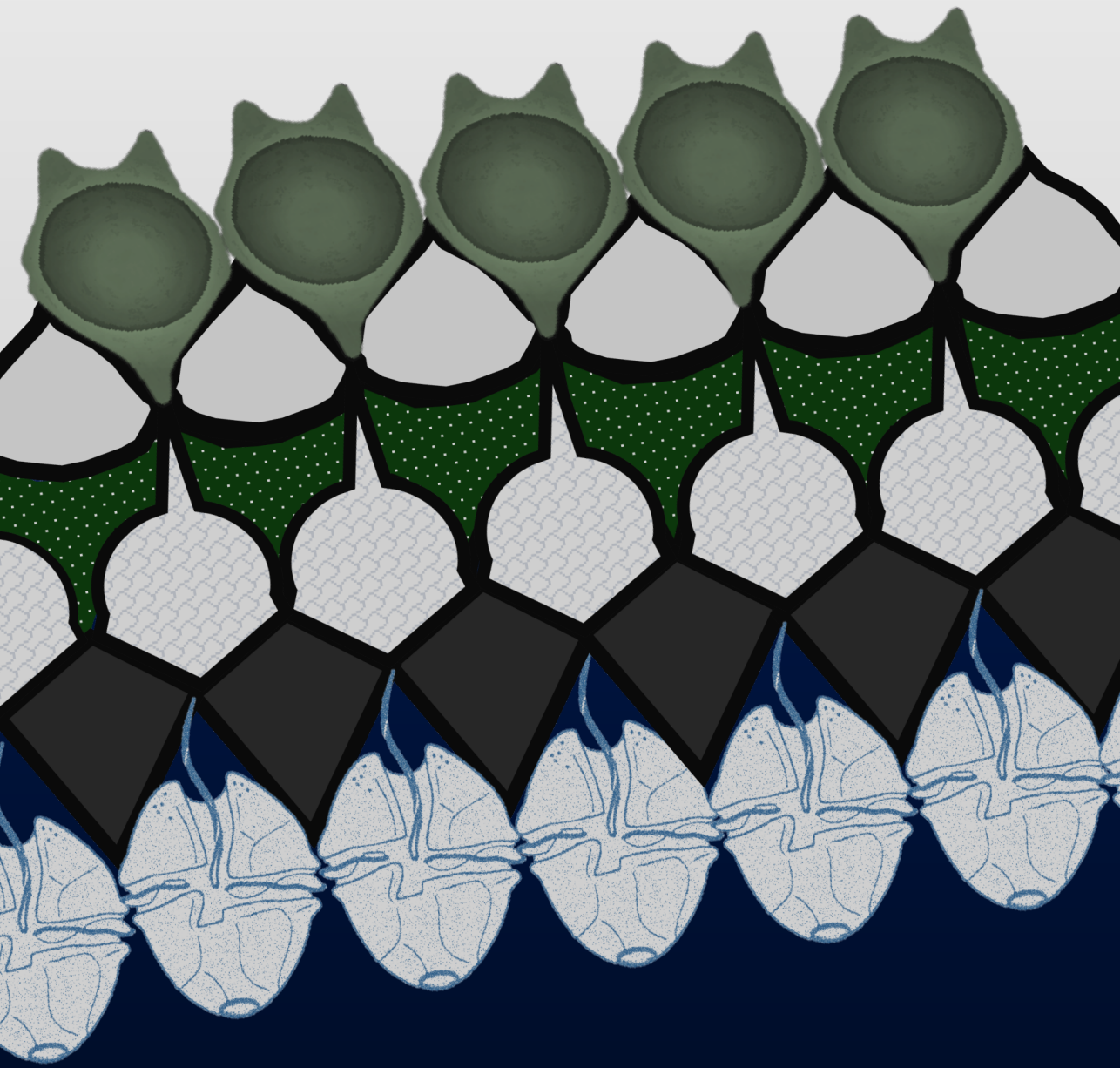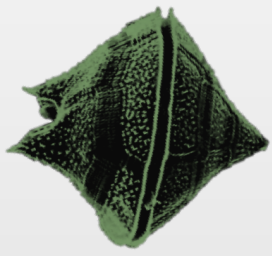
# CHAPTER 5

Resolution dependency of sinking Lagrangian particles in ocean general circulation models

Nooteboom, P. D., P Delandmeter, E. V. Sebille, P. K. Bijl, H. A. Dijkstra & A. S. von der Heydt (2020), "Resolution dependency of sinking Lagrangian particles in ocean general circulation models", *PLoS One*, vol. 15, no. 9, pp. 1–16

**Any type of non-buoyant material in the ocean is transported horizontally by currents during its sinking journey. This lateral transport can be far from negligible for small sinking velocities. To estimate its magnitude and direction, the material is often modelled as a set of Lagrangian particles advected by current velocities that are obtained from Ocean General Circulation Models (OGCMs). State-of-the-art OGCMs are strongly eddying, similar to the real ocean, providing results with a spatial resolution on the order of 10 km on a daily frequency. While the importance of eddies in OGCMs is well-appreciated in the physical oceanographic community, other marine research communities may not. Further, many long term climate modelling simulations (e.g. in palaeoclimate) rely on lower spatial resolution models that do not capture mesoscale features. To demonstrate how much the absence of mesoscale features in low-resolution models influences the Lagrangian particle transport, we simulate the transport of sinking Lagrangian particles using low- and high-resolution global OGCMs, and assess the lateral transport differences resulting from the difference in spatial and temporal model resolution. We find major differences between the transport in the non-eddying OGCM and in the eddying OGCM. Addition of stochastic noise to the particle trajectories in the non-eddying OGCM parameterises the effect of eddies well in some cases (e.g. in the North Pacific gyre). The effect of a coarser temporal resolution (once every 5 days versus monthly) is smaller compared to a coarser spatial resolution ($0.1°$ versus $1°$ horizontally). We recommend to use sinking Lagrangian particles, representing e.g. marine snow, microplankton or sinking plastic, only with velocity fields from eddying Eulerian OGCMs, requiring high-resolution models in e.g. paleoceanographic studies. To increase the accessibility of our particle trace simulations, we launch planktondrift.science.uu.nl, an online tool to reconstruct the surface origin of sedimentary particles in a specific location.**

## 5.1 Introduction

Sinking particles are involved in fundamental processes in the ocean. They serve as a primary mode of carbon export out of the exogenic carbon pool and deliver sediment to the world ocean floor: An important archive for understanding the climate system. The lateral advection of the sinking particles by ocean currents complicates the estimation of downward particle fluxes captured by sediment traps (Buesseler et al., 2007; Ma et al., 2021), the paleoceanographic reconstructions based on sedimentary microplankton distributions (Dale, 1996; Fahl & Nöthing, 2007; Honjo et al., 1982; Weyl, 1978), and the estimation of micro-plastic distributions in the ocean (Jalón-Rojas et al., 2019). Initially buoyant micro-plastic in the ocean sinks when it gets biofouled and its density increases (Kooi et al., 2017), meaning that a large fraction of the plastic in the ocean has already sunk to the ocean floor (Koelmans et al., 2017). The lateral transport of sinking particles can be estimated using Ocean General Circulation Models (OGCMs) and Lagrangian tracking techniques (Sebille et al., 2018). The Lagrangian techniques are used to model the sinking particle trajectories in the modern ocean (Monroy et al., 2019; Siegel & Deuser, 1997; Siegel et al., 2008; Waniek et al., 2000; Wekerle et al., 2018; Zhongfeng et al., 2014), specif-

ically for sinking microplankton (Nooteboom et al., 2019; Sebille et al., 2015b) and microplastic (Hardesty et al., 2017).

Where possible, these Lagrangian techniques make use of an eddying flow field. However, eddying simulations are not available for all applications to provide such a flow field. For example, model simulations of the geological past use OGCMs with at most $1°$ horizontal (non-eddying) resolution (Baatsen et al., 2018a,b; Haywood et al., 2013; Hutchinson et al., 2018; Lunt et al., 2012). The latter is due to the fact that palaeoclimate model simulations require coupled climate model simulations (because the atmospheric forcing is not known from observations) and long spin-up times (typically a few 1000 model years) in order to reach a reasonable climate equilibrium.

The spatial and temporal resolution of the underlying flow field generated by OGCMs will affect the spreading of particles in the Lagrangian tracking. It has already been shown that Lagrangian trajectories of neutrally buoyant particles are sensitive to the temporal resolution in an OGCM with $\sim 2°$ horizontal resolution (Valdivieso Da Costa & Blanke, 2003), and the temporal resolution influences the divergence timescale of trajectories in an OGCM of $0.1°$ horizontal resolution (Qin et al., 2014).

The spatial resolution of the OGCM determines if the flow is eddying, which played an important role in simulations of sinking particles near the northern Gulf of Mexico (Liu et al., 2018) and in the Benguela region (Monroy et al., 2019), and for passive tracers near Sellafield (Simonsen et al., 2017) and globally (Döös et al., 2011) ($0.25°$ versus $1°$ resolution). Eddying OGCMs generate a different time-mean flow compared to non-eddying OGCMs which parameterise the eddy effects (Berloff et al., 2007; Holland, 1978). The interplay between eddies and the mean flow is found to be important for the representation of internal variability of the flow (i.e. the variability of the system under constant atmospheric forcing; Penduff et al., 2011). This results in a better representation of interannual or multidecadal variability (Le Bars et al., 2016) and the separation location of western boundary currents such as the Gulf Stream (Hecht & Smith, 2013). Additionally, eddies cause mixing of tracers (e.g. heat and salinity). The non-eddying OGCMs rely on parameterisations of this tracer mixing such as the Gent-McWilliams (GM) parameterisation (Gent, 2011; Gent & McWilliams, 1990), which shows difficulties to represent this effect locally (Viebahn et al., 2016; Volkov et al., 2008).

In this chapter, we will assess how the sinking Lagrangian particle trajectories vary for different temporal or spatial resolutions of an Eulerian OGCM. We investigate the effect of eddies on the particle trajectories. Moreover, we study whether a stochastic lateral diffusion of Smagorinsky (Smagorinsky, 1963) type could parameterise the effects of the eddies in the non-eddying OGCM. The results concern any type of application with sinking Lagrangian particles, such as the comparison of sediment trap data with OGCMs (Liu et al., 2018; Wekerle et al., 2018) or the representation of sinking microplankton (Nooteboom et al., 2019; Sebille et al., 2015b) and sinking

5

plastic (Kooi et al., 2017).

## 5.2 Method

We make use of present-day global ocean model simulations of the Parallel Ocean Program (POP) with $0.1°$ ($R_{0.1}$; eddying) and $1°$ ($R_{1m}$; non-eddying) horizontal resolution to advect virtual particles (also used in (Toom et al., 2014; Viebahn et al., 2016; Weijer et al., 2012)). The eddying POP version has a reasonably good representation of the modern circulation compared to other models at the same resolution (McClean et al., 2008). Both versions of POP are configured to be as consistent as possible with each other, but there are some differences (see the supplementary material of Weijer et al., 2012).

We release particles at the bottom of the ocean every three days for more than a year, and compute their trajectories in the changing flow field back in time (similar to Liu et al., 2018; Nooteboom et al., 2019; Sebille et al., 2015b; Wekerle et al., 2018) until the particles reached the surface. We stop a particle if it reaches 10m depth. The particles are released on a $1° \times 1°$ global grid. While the particles are advected back in time, a constant sinking velocity $w_f$ is added to the particle trajectories. The addition of a constant sinking velocity to an advected particle has been shown to be a proper way to incorporate the effect of gravity on a sinking particle (Monroy et al., 2017). Here, we focus on two sinking speeds: $w_f = 6$ and $25$ m day$^{-1}$, to study the dependence of the results on the sinking speed, i.e. we represent the sinking of individual dinoflagellate cysts and small aggregates, respectively. More scenarios of sinking speed $w_f$ were investigated in chapter 3. We used Parcels version 2.0.0 (Delandmeter & Sebille, 2019b) to calculate the particle trajectories in this chapter, which is compatible with the Arakawa B-grid that POP uses.

The particle trajectory is integrated using the velocity field of POP and a stochastic term parameterising the effect of unresolved processes on the velocity. This last term is equivalent to diffusion in Eulerian models (Sebille et al., 2018) and is a function of the diffusivity $\nu$. Here we define $\nu$ as a function of the mesh size (i.e. the size of the grid cell) and the flow shear, following the Smagorinsky (Smagorinsky, 1963) parameterisation, which is commonly used in OGCMs and Large Eddy Simulations (LES). This implies that the particle trajectories are computed by (repetition of equation 2.1):

$$\vec{x}(t - \Delta t) = \vec{x}(t) + \int_{t}^{t-\Delta t} \vec{v}(\vec{x}, \tau)d\tau + \vec{c}\Delta t + \vec{q}\sqrt{2\nu(\vec{x})\Delta t}, \qquad (5.1)$$

with $\vec{x}(t)$ the three-dimensional position of the particle at time $t$, $\vec{v}(\vec{x}, t)$ the flow velocity at location $\vec{x}$ and time $t$ (linearly interpolated in space and time from the flow field), and $\vec{c} = \begin{pmatrix} 0 & 0 & -w_f \end{pmatrix}^T$ the sinking velocity. The vertical part of the flow $\vec{v}$ can be relevant compared to the particle sinking velocity $w_f$ (see Fig 7 in Nooteboom et al., 2019). The flow consists of two components in the non-eddying POP model: $\vec{v} = \vec{v}_a + \vec{v}_b$, where $\vec{v}_a$ is the Eulerian flow field that is solved by POP. $\vec{v}_b$ is the bolus

velocity from the GM parameterisation, which represents the flow that is responsible for the mixing of tracers along isopycnals (Gent, 2011; Gent & McWilliams, 1990). $\vec{v}_b = \vec{0}$ in the eddying POP model.

The last term of Eq. 5.1 is the horizontal diffusivity term (only used in the non-eddying model), where $\vec{q} = \begin{pmatrix} R_1 & R_2 & 0 \end{pmatrix}^T$ represents (independent) white noise in the zonal and meridional direction, with mean $\mu_{R_1} = \mu_{R_2} = 0$ and variance $\sigma_{R_1}^2 = \sigma_{R_2}^2 = 1$, and

$$\nu(\vec{x}) = c_s A \sqrt{\left(\frac{\partial u}{\partial x}\right)^2 + \frac{1}{2}\left(\frac{\partial u}{\partial y} + \frac{\partial v}{\partial x}\right)^2 + \left(\frac{\partial v}{\partial y}\right)^2}, \tag{5.2}$$

where $A$ is the horizontal surface area of the grid cell where the particle is located, $u = u(\vec{x})$ and $v = v(\vec{x})$ are respectively the (depth dependent) zonal and meridional velocity components. As such, the magnitude of the stochastic noise depends on the local velocity field, and its variance increases linearly over the time that a particle is advected. The Smagorinsky viscosity depends strongly on the flow shear compared to other parameterisations (Jochum et al., 2008). Apart from the diffusion that is added in this chapter, the backtracking method is the same as in chapter 3.

The strength of the noise can be determined with the parameter $c_s \geq 0$. Multiple methods exist in LES to determine the value of $c_s$ in each application (Ma et al., 2009). The velocity gradients $\left(\frac{\nu}{c_s A}\right)$ in the non-eddying version of POP typically range from $10^{-9}$s$^{-1}$ to $10^{-7}$s$^{-1}$ and $A \approx 10^4$ km$^2$, so the estimated standard deviation of the zonal and meridional stochastic noise ($\hat{\sigma}_x(t)$, $\hat{\sigma}_y(t)$) after 20 days ($\Delta t \approx 1.6 \cdot 10^6$s) range from $6\sqrt{c_s}$ km to $60\sqrt{c_s}$ km. These scales are similar to the mesoscale: 10-30 days and 10-100km for mesoscale eddies (Gill, 1983).

Altogether, we apply the particle tracking analysis in four different model configurations (see Table 5.1), and compare the distributions of particles at the ocean surface after the back-tracking from a single release location; 130 particles are used at every release location to determine the particle distributions. These configurations represent the differences between state-of-the-art, global OGCM resolutions of the past (1° horizontally and monthly model output) and the present-day (0.1° horizontally and model output on a daily scale). The single effect of model output with lower temporal resolution compared to the state-of-the-art present-day OGCMs is investigated in a separate configuration $R_{0.1m}$.

We use three measures to compare the particle distributions between the configurations (see Fig 5.1b-d): (i) the average lateral distance (km) travelled from the release location (along the red lines in Fig 5.1b), (ii) the surface area spanned by the particles approximated by the summed surface area of the 1° × 1° grid boxes (blue boxes in Fig 5.1c), and (iii) the Wasserstein distance $W_d$ as a measure of difference between two distributions resulting from two simulations. The Wasserstein distance is the minimum distance that one has to displace the particles resulting from one

**Table 5.1:** **The configurations with simulations in varying OGCM resolutions**

| Configuration | resolution | output | diffusion | remark |
|---|---|---|---|---|
| $R_{0.1}$ | 0.1° | once every 5 days | $c_s = 0$ | $\vec{v}_b = 0$, eddying |
| $R_{0.1m}$ | 0.1° | monthly | $c_s = 0$ | $\vec{v}_b = \vec{0}$, eddying |
| $R_{1m}$ | 1° | monthly | $c_s = 0$ | non-eddying |
| $R_{1md}$ | 1° | monthly | $c_s \in [0.25, 0.5, 1.0, 1.5, 2.0, 5.0]$ | non-eddying |

simulation (along the dashed lines in Fig 5.1d) to transform it into another particle distribution (and is calculated with Flamary & Courty, 2017).
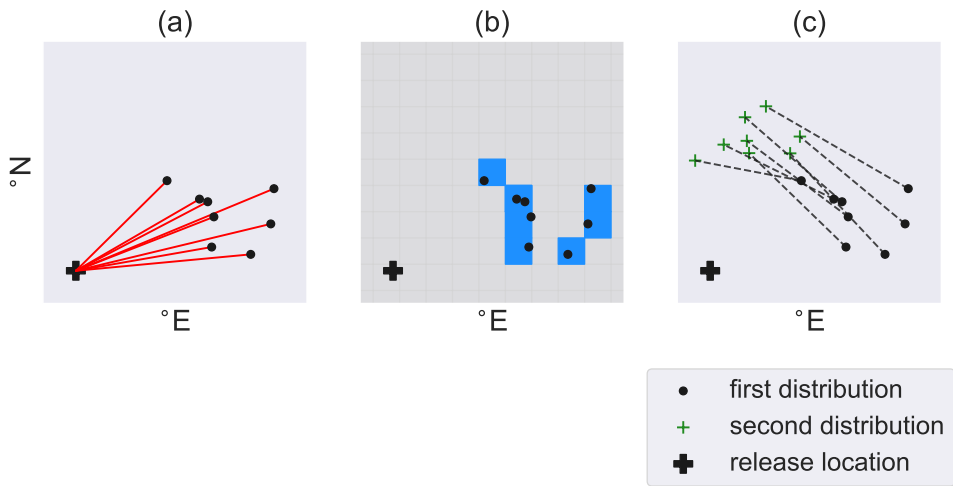


**Figure 5.1:** Schematic illustration of (a) the back-tracking analysis and (b)-(d) the three measures which are used to compare the particle distributions at the ocean surface. (a) Three-dimensional illustration: Particles are released at the bottom every three days for a period of around six years, back-tracked until they get close to the surface (10m depth), which results in a particle distribution at the surface. A map of (b) the average lateral distance (km) traveled from the release location (along the red lines), (c) the surface area (blue; km$^2$) spanned by the particle distribution (approximated by the summed surface area of the $1° \times 1°$ blue boxes), (d) the Wasserstein distance ($W_d$; km), which is the minimum distance that one has to displace the particles (along the dashed lines) to transform one distribution into another distribution.

## 5.3 Results

We first analyse the overall differences between the configurations $R_{0.1m}$, $R_{1m}$, $R_{1md}$ and the reference configuration $R_{0.1}$ in terms of the three measures described above (see Fig 5.1). Thereafter, we show specific release locations to explain why the configurations with lower spatial resolution do or do not provide similar solutions to the reference configuration $R_{0.1}$.

### 5.3.1 Global analysis

The average lateral travel distances of the particles are globally different between the four configurations (Fig 5.2). In the configuration with lower spatial resolution $R_{1m}$, the average lateral displacement is more extreme compared to the reference configuration (i.e. it is larger in regions with relatively large displacement and lower in regions with low displacement; Fig 5.2c). The average travel distance in $R_{0.1m}$ is similar to the reference case $R_{0.1}$ (see Fig 5.2d for the global averages).

The average lateral displacement becomes globally less 'extreme' (especially the
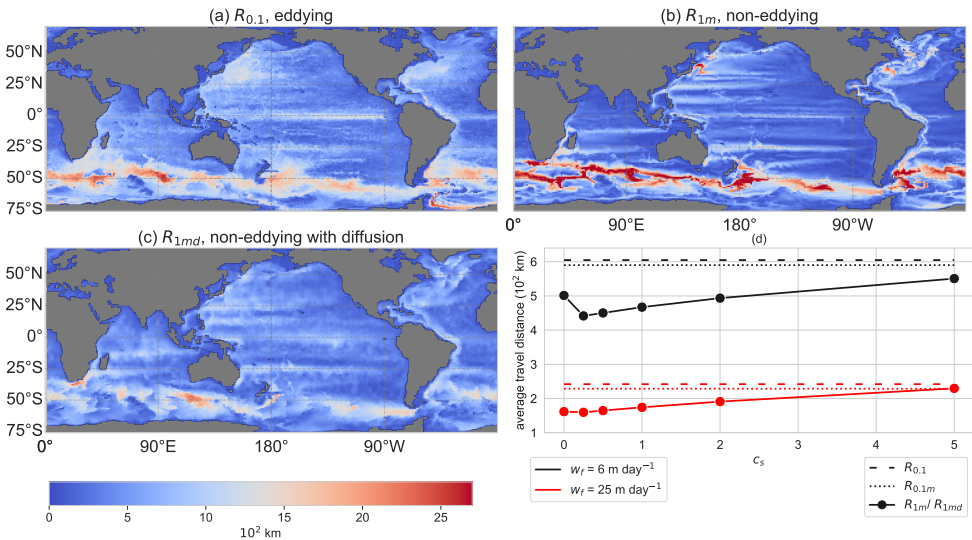


**Figure 5.2:** (a), (b), (c) The average horizontal distance between the release location and the final back-tracked location at the ocean surface with $w_f = 6$ m day$^{-1}$ respectively in configuration $R_{0.1}$, $R_1$, $R_{1md}$ with diffusion strength $c_s = 2.0$ (see Fig 5.4 for $R_{0.1m}$). (d) Global averaged lateral travel distance in all configurations (for several values of $c_s$ in $R_{1md}$). $w_f = 6$ m day$^{-1}$ in black and $w_f = 25$ m day$^{-1}$ in red.

Southern Ocean peaks are lower) if the Smagorinsky diffusion is added to the flow dynamics in $R_{1md}$ compared to $R_{1m}$ (Fig 5.2c). The less extreme pattern of the travel distances explains why the globally averaged lateral travel distance is minimal at $c_s = 0.25$ (for $w_f = 6$ m day$^{-1}$ in Fig 5.2d), and not at $c_s = 0$. The coefficient $c_s$ influences the lateral displacement in two ways. First, more displacement is added per time step if the noise is stronger (for larger $c_s$), and the lateral displacement will on average be larger for larger $c_s$. Second, the noise will be larger in areas with strong flow ($u$ and $v$ in Eq. 1 and 2). Hence, for small $c_s$ the noise is large enough for the particles to travel outside of the areas with a relatively strong flow and large displacement (such as in the Southern Ocean), such that the globally averaged lateral displacement is lower than for $c_s = 0$.

The surface area spanned by the particle distributions (5.1b) is often smaller in $R_{0.1m}$ compared to $R_{0.1}$, as can be seen from the global average of this measure

(Fig 5.3d). The lower surface area could be explained by the tendency of nearby particles to follow more similar pathways in $R_{0.1m}$ than in $R_{0.1}$ (see the animation in the supporting material; Qin et al., 2014). As a result, the particles will end up in clusters closer to each other at the surface. Hence, the surface area of the particle distributions is on average smaller in $R_{0.1m}$ compared to $R_{0.1}$.

Mesoscale eddies are abundant in the reference configuration $R_{0.1}$, while they are
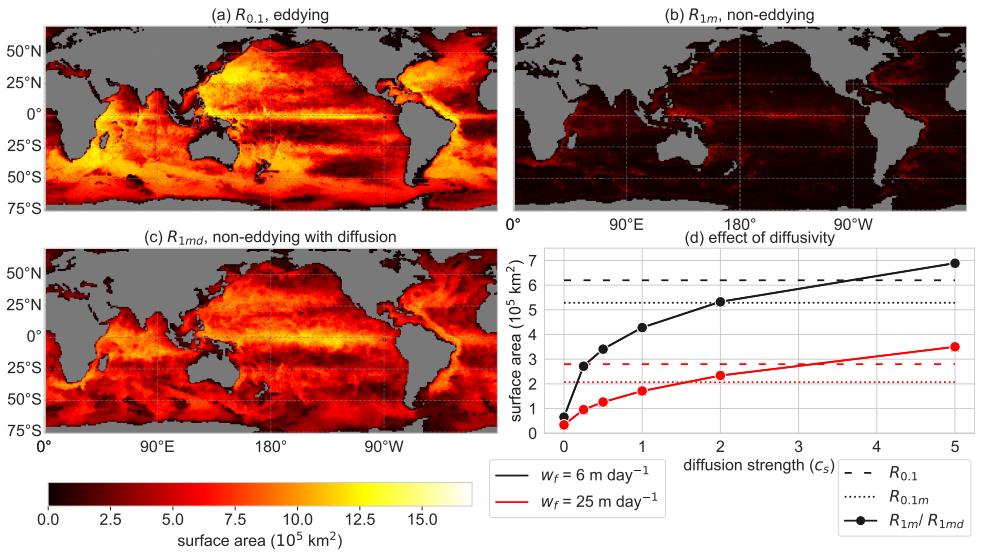


**Figure 5.3:** (a), (b), (c) The surface area of the back-tracked particle distributions with $w_f = 6$ m day$^{-1}$ respectively in configuration $R_{0.1}$, $R_1$, $R_{1md}$ with diffusion strength $c_s = 2.0$ (see Fig 5 for $R_{0.1m}$). (d) Globally averaged surface area of the particle distributions in all configurations (for several values of $c_s$ in $R_{1md}$). $w_f = 6$ m day$^{-1}$ in black and $w_f = 25$ m day$^{-1}$ in red.

absent in the low spatial resolution configuration $R_{1m}$. Therefore, tracked particles tend to end up in a much more confined area at the surface in the lower resolution configuration $R_{1m}$ than in the reference configuration (Fig 5.3d). The stochastic noise in $R_{1md}$ induces fluctuations in the particle trajectories, leading to a larger surface area of the particle distributions. In $R_{1md}$, the global average surface area of the particle distributions increases monotonically with increasing magnitude of the noise ($c_s$).

Interestingly, the value of $c_s$ that approximates configuration $R_{0.1}$ ($c_s \approx 3.5$) and $R_{0.1m}$ ($c_s \approx 2$) best, is the same for both sinking velocities 6, 25 m day$^{-1}$. These values of $c_s$ must result in a similar scale of the flow fluctuations ($\sigma_x$, $\sigma_y$) in configurations $R_{0.1}$ and $R_{0.1m}$. It also indicates that, given $c_s$, the subgrid-scale parameterisation performance is similar for both sinking velocities. Nevertheless, the particle distributions match better with the reference configuration if the sinking velocity is higher (according to the $W_d$ in Fig 2), because a lower particle travel time leads to less spread of the particle trajectories and a lower lateral displacement.

Locally, the surface area of the particle distributions shows a different pattern in $R_{1md}$ compared to the reference $R_{0.1}$ (Fig 5.3a vs c). In contrast to the magnitude of the noise, the direction of the noise vector does not depend on the flow field (it is horizontally isotropic). Therefore, the surface area of the particle distributions in configuration $R_{1md}$ is overestimated in the tropics compared to the reference configuration $R_{0.1}$, where the flow is mostly zonal. Interestingly, this measure remains low in areas with sinking waters for both configurations $R_{0.1}$ and $R_{0.1md}$, such as the Ross sea and the Weddell sea (see Fig 2 in Gebbie & Huybers, 2011).

The loss of information in $R_{0.1m}$ due to the monthly averaging of the flow fields in $R_{0.1}$ is clearer in the difference plots of the surface area and travel distance of the particle distributions (Fig 5.4). The surface area of the particle distributions is mostly lower in $R_{0.1m}$ compared to $R_{0.1}$ (Fig 5.4a). The particles tend to be advected by a similar flow field in $R_{0.1m}$ if they are located close to each other. Hence, groups of particles are trapped in the same eddies, and travel from origin locations at the ocean surface which are closer to each other. This could result in notably different back-tracked particle distributions, especially if the shear of the flow field is high (see for instance the location $45.5°S$, $39.5°E$ on planktondrift.science.uu.nl or Fig Comparison between the reference configuration $R_{0.1}$ (red) and the temporally averaged configuration $R_{0.1m}$ (blue) at two release locations ($w_f = 6$ m day$^1$). (a) $45.5°S$, $39.5°E$ at 2068m depth (red on top of blue) (b) $46.5°S$, $42.5°E$ at 2238m depth (blue on top of red). for two similar locations with opposite behaviour).

In general, we find that a reduction of the temporal resolution ($R_{0.1m}$ vs. the ref-
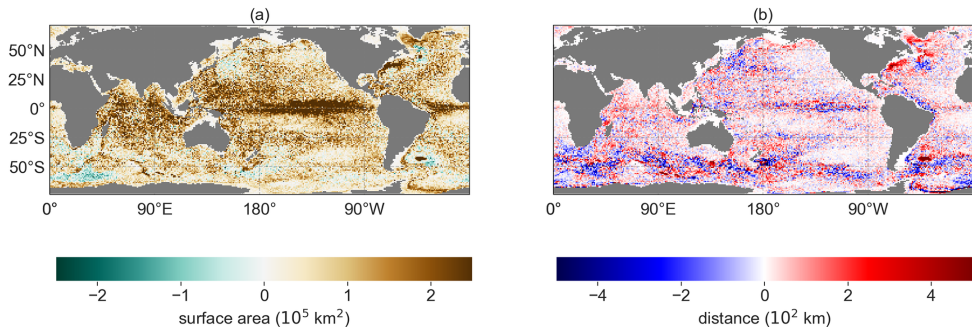


**Figure 5.4:** The differences between $R_{0.1m}$ and $R_{0.1}$ ($R_{0.1m}$ subtracted from $R_{0.1}$) in terms of (a) the surface area of the particle distributions (Fig 5.1c) and (b) the average travel distances of the particle distributions (Fig 5.1b).

erence case $R_{0.1}$) does not have a major effect on the Wasserstein distance $W_d$ (Fig 5.5). The travel time of the particles is perhaps too short (at most a few years) for the errors in $R_{0.1m}$ to grow substantially, and remains smaller compared to $R_{1m}$. The global average $W_d$ between $R_{0.1m}$ and the reference case ($W_d(R_{0.1}, R_{0.1m})$) is slightly larger compared to the check of $R_{0.1}$ with itself (the global average $W_d(R_{0.1}, R_{0.1})$; dashed versus dotted in Fig 5.5d). In this 'check', we did the same analysis as in $R_{0.1}$, but with a 1.5 day shift of the particle release times. As a result,

the particle distributions will be different in the check, but as similar as one could get to the particle distributions of $R_{0.1}$ in the other configurations.

On the other hand, altering the spatial resolution in $R_{1m}$ and $R_{1md}$ does lead to



**Figure 5.5:** The global Wasserstein distance ($W_d$) as a distance measure between the back-tracked particle distributions of the configurations from table 5.1. $W_d$ for sinking speed $w_f = 6$ m day$^{-1}$ between the eddying reference configuration $R_{0.1}$ and (a) the eddying $R_{0.1m}$ wi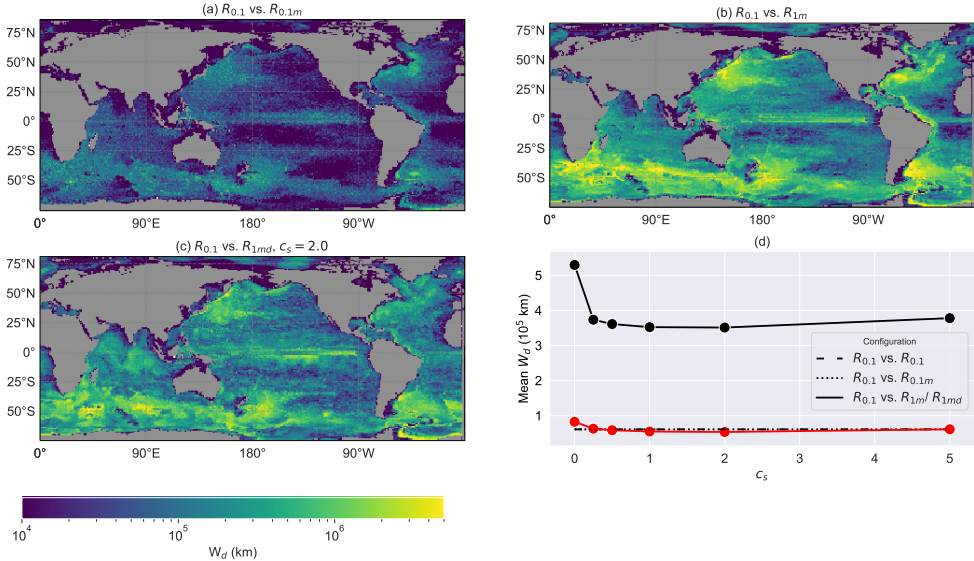th monthly model output, (b) the non-eddying $R_{1m}$, (c) the non-eddying $R_{1md}$ with diffusion strength $c_s = 2$. (d) Global average $W_d$ in all configurations (for several diffusion strengths $c_s$ in $R_{1md}$). $w_f = 6$ m day$^{-1}$ in black and $w_f = 25$ m day$^{-1}$ in red. The globally averaged $W_d$ of configuration $R_{0.1}$ with itself is a check ($W_d(R_{0.1}, R_{0.1})$; only for $w_f = 6$ m day$^{-1}$), as the globally averaged $W_d$ is shown between the particle distribution of the same configuration, but with a 1.5-day shift of the particle release times.

different values of the $W_d$. We find that any value of $c_s > 0$ reduces the $W_d$ by a similar amount, but the $W_d$ is the smallest for $c_s = 2$ with both sinking speeds $w_f = 6, 25$ m day$^{-1}$ (Fig 5.5d). For $c_s = 2$, the approximated zonal and meridional standard deviation of the diffusion ($\hat{\sigma}_x(t)$, $\hat{\sigma}_y(t)$) ranges between 8km and 80km in 20 days (depending on the strength of the local velocity gradients in the model). At this value of $c_s$, the magnitude of the fluctuations from the eddies lead to the optimal parameterisation, such that the particle distributions spread enough to better match with the particle distributions in the reference case. However, we find that the global averaged $W_d$ for $c_s = 2$ is approximately eight times larger compared to the check ($W_d(R_{0.1}, R_{0.1})$) for $w_f = 6$ m day$^{-1}$, which implies that the particle distributions differ substantially from the reference case. In all configurations $R$, $W_d(R_{0.1}, R)$ is lower in areas where the divergence of particle trajectories is relatively small, such as areas of relatively low eddy kinetic energy (e.g. in the gyres; see Appendix B.2), and in areas where the travel time of the particles is relatively short because of the shallow bathymetry (or the particles sink faster).

### 5.3.2 Regional analysis

In general, the particle trajectories in the lower spatial resolution configuration $R_{1m}$ without diffusion are different compared to the trajectories in the reference configuration $R_{0.1}$, because these trajectories lack the fluctuations provided by eddies and hence they spread less. The only trajectory spread in the non-eddying $R_{1m}$ is caused by flow variability on a larger timescale, such as seasonality. We focus here on some specific locations to see how this can lead to different particle distributions.

If Smagorinsky diffusion is added to the dynamics of the flow ($R_{1md}$), the fluctuations from the eddies are parameterised and the trajectories spread more. The North Pacific gyre is a location where this parameterisation works well (Fig 5.6a). Within the gyre, the diffusion is relatively low in the reference configuration and the eddies spread the particle trajectories uniformly in all directions. Adding fluctuations to the flow field in $R_{1md}$ using stochastic noise captures the spread of these eddies in $R_{0.1}$ well. Occasionally the parameterisation also works well in locations with larger shear and eddy activity compared to the North Pacific gyre. For example, for a location in the Antarctic Circumpolar Current (ACC, Fig 5.6b), the mean flow field (averaged over 6 years) in $R_{1m}$ is similar to the mean flow field in $R_{0.1}$. The stochastic noise can again adequately capture the effect of fluctuations provided by the eddies on the particle distributions.

However, it is well known that non-eddying OGCMs do not get the mean flow field right in all of the locations, because the eddies influence the mean flow field through rectification (Mana & Zanna, 2014). The Agulhas region is such an example where the mean flow field is different in $R_{1m}$ compared to the reference case $R_{0.1}$ (Fig 5.6c). The analysis in $R_{1md}$ provides a particle distribution which only comprises a subset of the particle distribution from the analysis in $R_{0.1}$. If the strength of the noise ($c_s$) is increased here, at most the spread of the particle distribution increases, but one will not find that any particle originates from the area around Madagascar.

Finally, the addition of spatially dependent noise has one more unrealistic property: The particles tend to artificially accumulate in areas with relatively low horizontal gradients, and hence weak stochastic noise (Hunter et al., 1993; Ross & Sharples, 2004; Visser, 1997). A result of this effect can be found in another location near the ACC, South of Australia (Fig 5.6d). At this location, configuration $R_{1md}$ results in two clusters of particles, which are separated by an area with high shear, and where the noise is large, while the particles in the reference configuration $R_{0.1}$ clearly form one (more connected) distribution.

## 5.4 Discussion

We assessed the variations of Lagrangian trajectories of sinking particles in flow fields which were generated by OGCMs of different resolutions. We released sinking particles at the bottom of the ocean, tracked them backwards in time until they reached the surface, and investigated how the particle distributions at the ocean
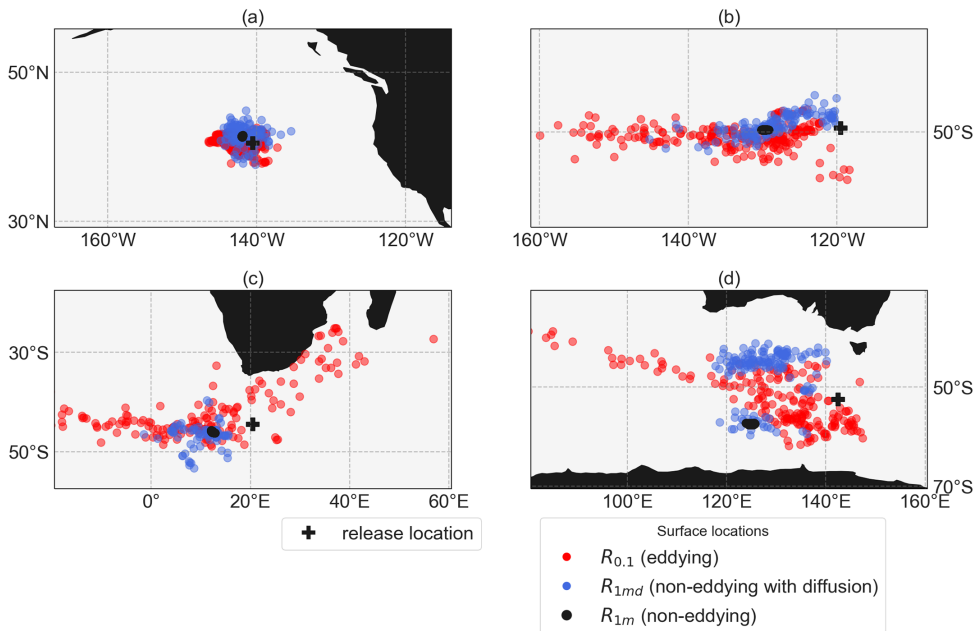
**Figure 5.6:** Comparison between reference configuration $R_{0.1}$ (red), configurations $R_{1m}$ (yellow) and $R_{1md}$ with $c_s = 2$ (blue) at four different locations (yellow on top of blue, blue on top of red; $w_f = 6$ m day$^{-1}$). Each distribution consists of $\sim 160$ particles. The release locations at (a) 40.5°N, 140.5°W and respectively 4601 and 4542 m depth in $R_{0.1}$ and $R_{1m}$, (b) 49.5°S, 119.5°W and respectively 3122 and 3249 m depth in $R_{0.1}$ and $R_{1m}$, (c) 44.5°S, 20.5°E and respectively 4249 and 4249 m depth in $R_{0.1}$ and $R_{1m}$, (d) 52.5°S, 142.5°E and respectively 3070 and 2916 m depth in $R_{0.1}$ and $R_{1m}$.

surface depend on the OGCM resolution.

If the model output of the high-resolution OGCM is averaged from 5-daily to monthly data, the particle tracking analysis provides similar results in most cases. However, in some specific regions with large shear, we find notable differences of the back-tracked particle distributions at the ocean surface.

Overall, the sinking Lagrangian particles give unrealistic results in the non-eddying models, because (1) the back-tracked distributions show too little spread due to the absence of ocean eddies and (2) these models often do not capture the mean flow fields correctly (as shown in e.g. Berloff et al., 2007; Hecht & Smith, 2013; Holland, 1978). Lateral stochastic diffusion in the low-resolution configuration (re-)introduced part of the eddy fluctuations and hence increased the relative dispersion of particle trajectories, and increased the lateral travel distance (Fig 5.2) and the spread (Fig 5.3) of the back-tracked particle distributions. Hence this method is promising for locations where the low resolution OGCMs capture the mean flow field well. However, the particle distributions are often distant from the distributions of the reference configuration, as is shown from the Wasserstein distance in Fig 5.5, which implies that the surface origin location is different between the coarse and

high resolution models. Therefore, overall the Smagorinsky diffusion is insufficient to parameterise the eddies in most areas.

Altogether, we recommend to compute the sinking Lagrangian particle trajectories only in eddying OGCMs. We used the Smagorinsky parameterisation in this chapter as a first attempt to represent the subgrid-scale processes if the eddies are absent in the flow. Other types of parameterisations could be applied. Several other parameterisations for eddy-induced mixing of tracers are available in POP (Smith et al., 2010). However, the improvement of either the Eulerian or Lagrangian parameterisation of the subgrid scale variability in the flow remains a challenge in ocean modelling (Fox-Kemper et al., 2019; Hewitt et al., 2020; Le Sommer et al., 2018).

These conclusions have implications for Lagrangian particles in paleoceanographic models. OGCMs used in most paleo studies lack the eddying flow characteristics and do not generate a locally representative time mean flow for the time period of interest. Since Lagrangian particles use the local flow field, they require eddying paleoceanographic models that better represent the time mean flow for the considered time period. For the application of Lagrangian particle tracking techniques in paleoceanographic models, which are usually not eddying, we recommend to test model results first against independent information of ocean flow, such as biogeographic patterns of microplankton (Bijl et al., 2011; Huber et al., 2004). In turn, it should be appreciated that a regional paleoceanographic signal could be influenced by flow characteristics which are not represented by the non-eddying models. This represents a cautionary tale in putting too much confidence in flow fields from low-resolution fully coupled GCM simulations.

Future work could investigate the sinking Lagrangian particles in other configurations with different OGCM resolutions. The model output of configuration $R_{0.1}$ could be coarsened to a $1°$ grid before the back-tracking analysis, to separate out the effects on the Lagrangian analysis of (a) a coarsened grid (see also Huntley et al., 2011; Putman & He, 2013) and (b) a lower resolution of the underlying Eulerian model. Moreover, particle trajectories could be sensitive to the vertical resolution of the OGCM (e.g. Bracco et al., 2018; Stewart et al., 2017).

Future studies could apply different types of schemes that allow for spatially and temporally varying diffusion and result in more accurate representation of turbulent flow compared to the approach that is used in this chapter (Gräwe, 2011). Moreover, the addition of stochastic noise during the tracking of sinking particles in the flow could be extended. For instance, the stochastic noise could be made horizontally anisotropic instead of isotropic (Sebille et al., 2018), or vertical diffusion could be added to the dynamics (Danilov, 2012).
A challenge in these approaches remains that only the effect of the large-scale flow on the particle diffusion is parameterised, while the effect of small scales on the large scale flow is neglected.

When models do not resolve the so-called internal Rossby deformation radius (about

50 km at midlatitudes), no eddies can be represented. When the model grid scale is only slightly smaller than the deformation radius, say 25 km at midlatitudes, eddies form but their interaction is not fully captured; such a model is called 'eddy permitting.' Only for models at about 1 km horizontal midlatitude resolution (so-called eddy-resolving models), eddy interactions are fully resolved. The 10 km resolution POP model, as is used here ($R_{0.1}$), is therefore often called 'strongly eddying.' An OGCM of ~1km resolution also has a better representation of the spatial/temporal submesoscale that can be important for sinking Lagrangian particles which represent the carbon flux to the ocean bottom (Boyd et al., 2019). Although the mesoscale flow contains most of the energy that is responsible for the tracer dispersion (Uchida et al., 2019), submesoscale (1-20km) dynamics have proven to be of importance for the vertical advection of iron in specific regions with strong flow-bathymetric interactions (Rosso et al., 2016). Future work could analyse the transport of sinking particles in models with higher resolutions, and with models which better represent internal tides (Vic et al., 2019) or improved interaction of the bottom-flow with topography (Miramontes et al., 2019).

The effect of eddies on the flow should be appreciated outside the physical oceanography community. In order to facilitate increased understanding on this matter, interactively disseminate our results, and allow users to self-explore and verify the surface-ocean location of origin for sedimentary particles, we developed the website planktondrift.science.uu.nl containing our results.

We also tested an additional configuration without the bolus velocity in the non-eddying POP model (i.e. the same as $R_{1md}$ and $R_{1m}$, but where $v_b = \vec{0}$). The results for this configuration are very similar to the results that are obtained in configuration $R_{1md}$ and $R_{1m}$ in this chapter. The bolus velocity is weaker compared to the Eulerian flow velocity (typically $v_b$ is approximately 5% of $v_a$ at the surface layer). Parameterisations like GM improve the temperature and salinity distribution in Eulerian models. GM is a type of 'extra advection' which assumes that dynamic tracers such as temperature and salinity mix along surfaces of contstant potential density (Gent, 2011). However, GM does not make a relevant difference if Lagrangian particles are applied offline to represent other tracers. The results for this additional configuration can be found and downloaded from the planktondrift.science.uu.nl website.

## 5.5 Code and data availability

The code that is used to obtain the results in this chapter is distributed under the MIT license and can be found here: `https://github.com/pdnooteboom/PO_res_error`. The planktondrift.science.uu.nl website contains the results which are presented in this chapter, for every release location in every configuration.
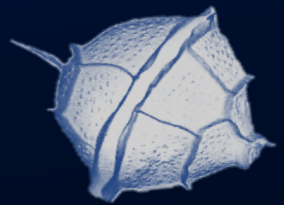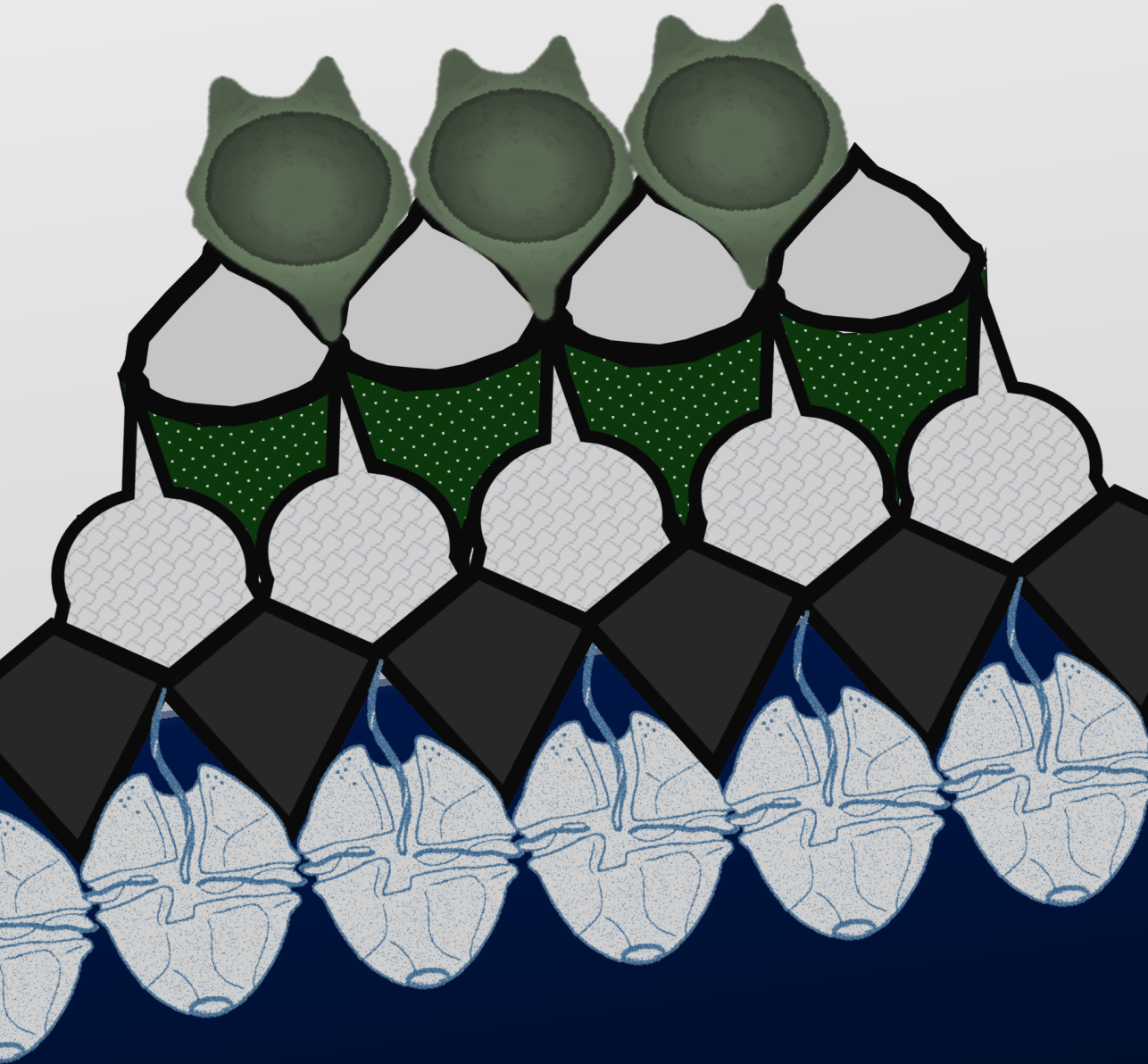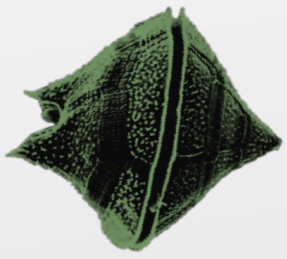
# CHAPTER 6

Model-data comparison in a strongly eddying Eocene ocean

**Model simulations of past climates are increasingly found to compare well with proxy data at a global scale, but regional discrepancies remain. A persistent issue in modelling past greenhouse climates has been the temperature difference between equatorial and (sub-)polar regions, which is typically much larger in simulations than proxy data suggest. Particularly in the Eocene, multiple temperature proxies suggest extreme warmth in the southwest Pacific Ocean, where model simulations consistently suggest cool conditions. Here we present new global ocean model simulations at 0.1° horizontal resolution for the middle-late Eocene. The eddies in the high-resolution model affect poleward heat transport and time-mean flow in critical regions compared to the non-eddying flow in the low-resolution simulations. As a result, the high-resolution simulations produce higher surface temperatures near Antarctica and lower surface temperatures near the equator compared to the low-resolution simulations, leading to better correspondence with proxy reconstructions. Crucially, the high resolution simulations are also much more consistent with biogeographic patterns in endemic-Antarctic and low-latitude-derived plankton micro-fossils, and thus resolves the long-standing discrepancy of warm subpolar ocean temperatures and isolating polar gyre circulation. The results imply that strongly eddying model simulations are required to reconcile discrepancies between regional proxy data and models, and demonstrate the importance of accurate regional palaeobathymetry for proxy-model comparisons.**

## 6.1 Introduction

Model-data comparisons for warm periods in the geologic past are used to understand climates considerably different from today (Braconnot et al., 2012; Cramwinckel et al., 2018; Dowsett et al., 2013; Hutchinson et al., 2021; Kennedy-Asser et al., 2020; Liu et al., 2009; Lunt et al., 2021; Schmidt et al., 2014a; Tabor et al., 2016; Tierney et al., 2020b; Zhu et al., 2020). Using state-of-the-art geographic boundary conditions (Baatsen et al., 2016), and estimated atmospheric $CO_2$ levels, model results of the Eocene are consistent with deep-sea temperatures (Cramwinckel et al., 2018) and are broadly found to match well with reconstructions of Sea Surface Temperatures (SST) from proxy data, but large regional discrepancies remain (Baatsen et al., 2020; Huber & Caballero, 2011; Hutchinson et al., 2021; Kennedy-Asser et al., 2020; Lunt et al., 2012; Lunt et al., 2021). Critically, most models are not able to obtain the low meridional SST gradient as suggested by proxies, independently of the boundary conditions of radiative forcing used (Lunt et al., 2021). Equatorial SSTs are generally warmer or high latitude SSTs colder in the models compared to the proxy data (which depends on these model boundary conditions). Regional SST mismatches remain, in particular near the equator and in the southwest Pacific (Lunt et al., 2021).

One challenge in palaeoclimate model-data comparisons is the scale difference between proxies and models. The proxies capture a regional environment and effects

of small-scale regional setting (e.g. geography, bathymetry, and oceanography), while general circulation models have difficulties capturing regional climate correctly due to the coarse resolution that is typically used (1° horizontally or coarser for the ocean) (Dowsett et al., 2013; Eyring et al., 2019; Harrison et al., 2016; Kennedy-Asser et al., 2020; Nooteboom et al., 2020; Tabor et al., 2016). It is well-known that the quality of ocean models improves considerably at a higher horizontal resolution (0.1°) (Dong et al., 2014; Griffies et al., 2015; Hewitt et al., 2016; McClean et al., 2006; McWilliams et al., 2014; Müller et al., 2019; Sun et al., 2019; Viebahn et al., 2016), especially their regional flow (Delworth et al., 2012; Marzocchi et al., 2015; Nooteboom et al., 2020). The improvement is not only due to higher level of detail, but also because of the smaller scale interactions resolved (including mesoscale eddies of 10-30km size) that influence the large-scale flow properties (Porta Mana & Zanna, 2014) and increase the importance of the local setting (i.e. the palaeogeography and bathymetry) in the resulting regional ocean flow.

Biogeographic patterns of microplankton (e.g. dinoflagellate cysts; dinocysts) in Southern Ocean marine sediments have been used as tracer of past surface oceanography. For instance, Eocene sediments deposited near Antarctica contain dinocyst species that are endemic to circum-Antarctic locations (Bijl et al., 2011). Hence, Southern Ocean regions with many of these endemic species, as opposed to those with abundant cosmopolitan species, must be oceanographically connected. This implies that these biogeographic patterns of dinocysts provide a direct proxy of the flow direction itself (Bijl et al., 2011). So far, climate models were broadly able to match the circulation patterns deduced from microplankton endemism in the Southern Ocean, sometimes after adaptations of the model palaeobathymetry (Bijl et al., 2013; Houben et al., 2019; Huber et al., 2004) or details of the configuration of critical Southern Ocean gateways (Sijp et al., 2016). However, these model simulations cannot explain the occurrence or absence of endemic dinocysts at some sites.

Moreover, regional discrepancies with low-resolution ocean flow simulations remain in these biogeographic patterns. Matching geographic boundary conditions so that simulated ocean flow is consistent with those from plankton records led to profoundly cooler simulated southwest Pacific SSTs than the proxy records suggest. State-of-the-art fully coupled climate model simlations did come close to the proxy-based warmth in the southwest Pacific Ocean, but this required a throughflow through the Tasmanian Gateway which was incompatible with microplankton-based evidence of surface ocean flow (Cramwinckel et al., 2020; Stickley et al., 2004). As a result, no model simulation exists that can reconcile southwest Pacific Ocean warmth with ocean flow that is compatible with the plankton records. We here assess whether a high resolution ocean model is able to improve this mismatch. Recently, it was shown that these biogeographic patterns of microplankton can be represented in models using sinking Lagrangian particles (Huber et al., 2004; Nooteboom et al., 2019), which requires time-evolving flow patterns from eddying ocean models (Nooteboom et al., 2020).

6

Here we present the first simulations of a global eddying Eocene ocean model with a $0.1°$ horizontal resolution (HR2 and HR4; Table 5.1). These simulations are initialized and forced with atmospheric fields from an equilibrium state of a coarser ($1°$) resolution model having a fully coupled ocean and atmosphere (LR2 and LR4; see Table 5.1) (Baatsen et al., 2020). Hence, the high- and low-resolution simulations have a similar atmospheric forcing and bathymetry. These high-resolution simulations are run for a few decades (42 and 27 years for HR2 and HR4 respectively), sufficient for upper-ocean circulation to equilibrate.

**Table 6.1:** The ocean model simulations of the middle-late Eocene (38Ma) in this chapter, for different atmospheric Pre-Industrial (PI) $CO_2$ levels (Baatsen et al., 2020).

| Simulation | resolution | layers | type | forcing | years run |
|---|---|---|---|---|---|
| LR2 (Baatsen et al., 2020) | $1°$ | 60 | fully coupled | $2\times$PI $CO_2$ | 3000 |
| LR4 (Baatsen et al., 2020) | $1°$ | 60 | fully coupled | $4\times$PI $CO_2$ | 4000 |
| HR2 | $0.1°$ | 42 | ocean-only, LR2 atmosphere | $2\times$ PI $CO_2$ | 42 |
| HR4 | $0.1°$ | 42 | ocean-only, LR4 atmosphere | $4\times$PI $CO_2$ | 27 |

## 6.2 Methods

### 6.2.1 Data

We used two datasets in this chapter. The first includes the SST proxies from $U^K_{37}$, $TEX^H_{86}$, Mg/Ca, $\Delta_{47}$ and $\delta^{18}O$, which are described in detail in (Baatsen et al., 2020). Proxy-based SST reconstructions come with uncertainties, limitations and biases (Hollis et al., 2019), related to the depth, or season they represent.

The second dataset are sediment samples with dinocysts from (Bijl et al., 2011), combined with the samples described in (Bijl et al., 2021; Cramwinckel et al., 2020; Houben et al., 2019). We averaged dinocyst abundance of Antarctic-Endemic, cosmopolitan and low-latitude-derived for the respective time slices.

### 6.2.2 Model set-up

We used the Parallel Ocean Program (POP) (Smith et al., 2010; Toom et al., 2014; Viebahn et al., 2016) to perform eddying ocean model simulations for the middle-late Eocene (38Ma). To derive the forcing of this model, we made use of the fully-coupled (ocean and atmosphere) simulations with Community Earth System Model v1.0.5 (CESM) from (Baatsen et al., 2020), with a non-eddying ocean. We used both the CESM simulations with $2\times$ pre-industrial atmospheric $CO_2$ (LR2) and $4\times$ pre-industrial $CO_2$ (LR4) configuration.

The high-resolution POP is forced at the surface by a fixed atmosphere of the CESM simulation. To construct the surface forcing, we interpolated the average (over the last 50 model years of LR2 and LR4) Sea Surface Temperature (SST),
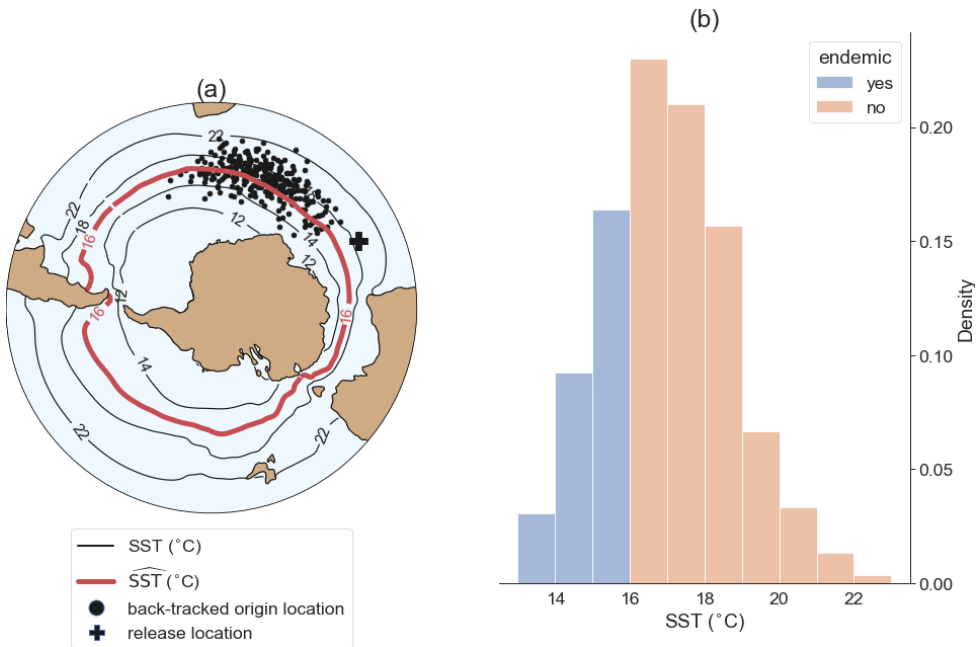
**Figure 6.1:** Illustration of the modelled dinocyst endemism near Antarctica. (a) Virtual particles are released at the bottom release location and tracked back in time with some sinking speed to determine their surface origin location. If the SST at the back-tracked origin location is lower than the threshold SST ($\widehat{SST} = 16°\text{C}$ in this illustration), it is assumed to originate close to Antarctica, hence it is flagged as endemic. (b) A histogram of SSTs at the surface origin locations.

Sea Surface Salinity (SSS) and wind stress (zonal and meridional) of the CESM simulation for every month of the year (such that a seasonal cycle is included in the surface forcing). These SST and SSS fields were used as restoring boundary conditions at the surface. The restoring boundary conditions imply that POP is 'pushed' towards the SST and SSS output of the CESM at the surface with a specific timescale (30 and $10^{20}$ days respectively). This means that differences between the SST and SSS at different model resolutions arise due to the internal transport (vertical and horizontal) of heat and salt in the ocean, not due the surface forcing. The bathymetry that CESM uses was interpolated linearly on the high-resolution grid that POP uses, making both bathymetries similar (see the code at https://github.com/pdnooteboom/MCEocene).

For initialisation of the eddying model, the three-dimensional ocean output at the end of the CESM simulations (LR2 and LR4) is interpolated on the higher resolution grid that the POP (HR2 and HR4) uses. We simulated 42 and 27 years in total for HR2 and HR4, respectively. Since we investigate the response of the simulations to an increase in horizontal resolution, the same 5 model years of both HR2 and HR4 are used in most analyses in this chapter: year 23 to 27. For the same analyses of the low-resolution simulations (LR2 and LR4), we used the last 5 years of these simulations.

Using this setup of POP, we can investigate the sensitivity of simulations to the studied resolution difference only, because the model is forced by the same atmosphere and their geographic boundary conditions are based on the same reconstruction of (Baatsen et al., 2016), and the three-dimensional eddying ocean is initialized by the equilibrated output of the CESM. As a result, the atmosphere is representative of the middle-late Eocene climate, but does not respond to changes in the ocean. We hence cannot investigate the effect of atmospheric feedbacks on the results (Arzel et al., 2011; Rahmstorf & Willebrand, 1995; Toom et al., 2012; Zhang et al., 2015).

The model set-up is suited to study the effects of model resolution on Eocene ocean flows, but it is not suitable to study dynamics which involve atmospheric coupling, such as the El Niño Southern Oscillation. The model set-up can best be used to investigate the upper ocean circulation, as the deep ocean is not in equilibrium yet. Therefore, we can only use this setup to obtain a transient response of the deep meridional overturning, not its equilibrium.

### 6.2.3 Sinking Lagrangian particles

We released particles on a $2° \times 1°$ grid of locations between 32-80°S every day for a year and waited until all of the particles reached the near-surface (i.e. 17,520 particles in total). This analysis requires a higher than monthly temporal resolution of model output (chapter 5). Therefore we used daily fields for the years 35-42 (HR2) and years 20-27 (HR4) to perform this backtracking analysis.

The used particle sinking speed of the Lagrangian particles in this chapter is 6 m day$^{-1}$. This represents a low sinking speed for single dinocysts (Anderson et al.,

1985). We choose this low sinking speed, because it is considered as a lower bound of the realistic sinking speeds where most lateral transport occurs, which makes it easier to explain low abundances of dinocyst species. However, this sinking speed could in reality be different due to e.g. aggregation with other particles. We also applied a sinking speed of 25 m day$^{-1}$ (see Fig. C.8), which represent small aggregates (chapter 2). The main conclusions on the model-data comparison do not change if 25 m day$^{-1}$ instead of 6 m day$^{-1}$ sinking speed is used.

The percentage of dinocyst endemism in the model is determined by the percentage of particles that originated from an environment with a temperature below $\widehat{SST}$ (which must be close to Antarctica; see Fig.6.1; similar approach as in Huber et al., 2004; see Appendix D). The percentage of modeled dinocyst endemism is not expected to compare well with the percentage of measured endemic dinocyst, because this match is also sensitive to the species-specific susceptibility of dissolution during the sinking journey and their productivity at the ocean surface (chapter 3 and 4). Therefore, we compare whether any endemic species occur in sites (0 or >0%) between model and data instead of the exact percentage.

We assume that the sinking Lagrangian particles are not greatly influenced by the fact that the deep circulation is not in full equilibrium yet in the eddying simulations. Most of the lateral particle displacement occurs near the surface which is in equilibrium and where the currents are the strongest. Moreover, the eddying simulations are initialised with output from the non-eddying simulations, which are in reasonable equilibrium. The mechanistic development of the flow, given the heat and salt distribution from the initialisation, occurs in a few years (see also Fig. 6.4c-h). Hereafter, the flow changes slowly and may equilibrate after ~1000 years due to the flow response to changing density distributions. The assumption that sinking Lagrangian particles are not greatly affected by the deep ocean equilibration, is supported by the results that use sinking Lagrangian particles in HR2 and HR4: These results are similar, even though the deep ocean circulation is different in HR2 and HR4.

### 6.2.4 Decomposition of meridional heat transport

The Meridional Heat Transport ($MHT$) is computed as:

$$MHT = c_p \rho_0 \int \int vT dx dz, \qquad (6.1)$$

with $c_p$ the ocean heat capacity and $\rho_0 = 1\text{gr cm}^{-3}$ the reference density, $v$ the meridional flow velocity and $T$ the ocean temperature. We use two decompositions of the MHT (Viebahn et al., 2016). The first is to distinguish the time-mean from the transient eddy component:

$$MHT = \overline{MHT} + MHT', \qquad (6.2)$$

with

$$\overline{MHT} = c_p \rho_0 \int \int \bar{v} \bar{T} dx dz$$

$$MHT' = c_p \rho_0 \int \int \overline{vT} - \bar{v} \bar{T} dx dz$$

Here a bar denotes a time mean.
Second, the $\overline{MHT}$ is decomposed in an overturning part ($MHT_O$) and a part which represents the heat transport due the horizontal flow ($MHT_H$; such as gyres):

$$\overline{MHT} = MHT_O + MHT_H, \tag{6.3}$$

with

$$MHT_O = c_p \rho_0 \int \int \bar{\bar{v}}^x \bar{T} dx dz,$$

$$MHT_H = c_p \rho_0 \int \int \left( \bar{v} - \bar{\bar{v}}^x \right) \bar{T} dx dz,$$

where $\cdot^x$ denotes a zonal mean.

## 6.3 Results

### 6.3.1 Effect of model resolution on Eocene flow

The ocean circulation is different between the eddying and non-eddying configurations (Fig. 6.2). In the eddying model, the time-mean flow strength has a higher spatial variability, the bathymetry has a larger influence on the flow strength and direction (especially in the Southern Ocean; see Fig. C.2 for the bathymetry), and local scale features are much more pronounced, compared to the low-resolution model. All western boundary and equatorial currents increase in strength, except in the North Atlantic. The spatial structure and separation locations of the western boundary currents are also shifted. For instance, the eastward Agulhas separation (near South-Africa) is only present in the eddying simulations (it retroflects more eastward compared to the present day). Moreover, east of Australia, the East Australia Current (EAC) extends further southeastwards in the eddying compared to the non-eddying simulation, while there is a narrow but strong northward current east of Tasmania that is not present in the low-resolution simulations.

The EAC flow provides an example of the stronger influence of the palaeobathymetry on the flow in HR4 compared to LR4, even though the bathymetry is the same in both configurations. Eddies are responsible for the downward transfer of momentum input at the ocean surface by winds that is eventually balanced by bottom form stresses (Munday et al., 2015). As a consequence, the flow is strongly determined by isobaths (i.e. lines of constant bathymetry) (Marshall, 1994; Rintoul, 2018). Hence, the bathymetry has a much larger influence on the flow if the ocean is eddying (in

## (a) 1° resolution



## (b) 0.1° resolution



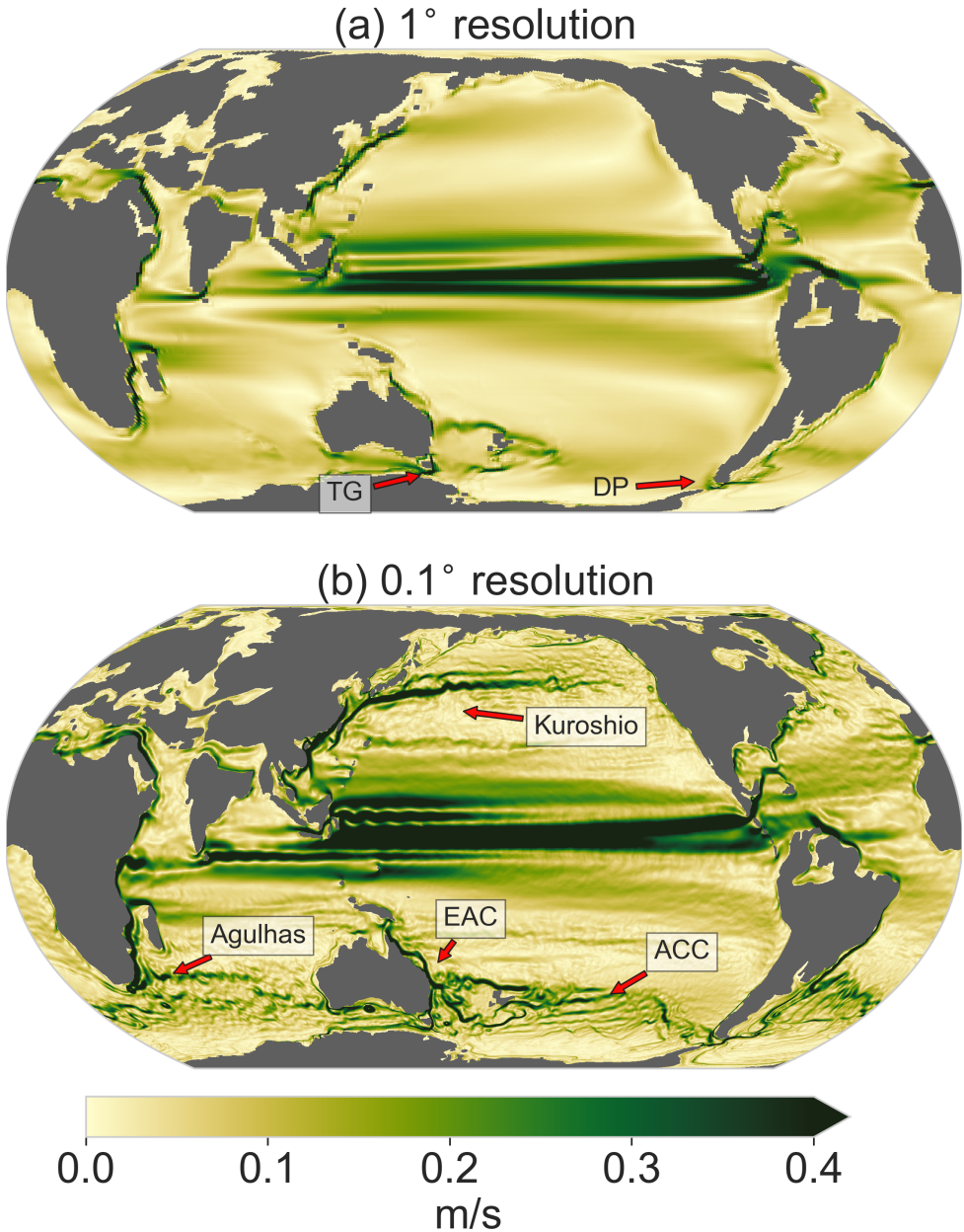**Figure 6.2:** Magnitude of the time-mean surface horizontal flow velocity in the model of (a) 1° (mean over years 3995-4000) and (b) 0.1° horizontal resolution (mean over years 23-27). Both with $4\times$pre-industrial atmospheric carbon (LR4 and HR4). The Drake Passage (DP), Tasman Gateway (TG), East Australian Current (EAC), Kuroshio current and proto-Antarctic Circumpolar Current (ACC) are labeled.

HR4 and HR2) than if it is not (LR4). In HR4, the EAC is steered further southeast-ward than in LR4 along the submerged continental block of Lord Howe Rise (see Fig. C.2 for the bathymetry). Moreover, jets like the EAC have a narrower structure in the eddying flow, due to interactions between eddies and the time-mean flow (Waterman et al., 2011), which has profound impacts on the regional oceanography.

### 6.3.2 Model-data comparison: plankton biogeography

The new Eocene ocean model velocity fields enable us to use sinking Lagrangian particles (Nooteboom et al., 2020) to reveal biogeographic provinces of microplank-ton in the Eocene Southern Ocean. In this way, we can test how representative the modeled flow is compared to the reconstructed ocean flow from sediment records. In this approach, it is determined where sedimentary particles originated from at the ocean surface, while taking into account how the particles were advected by ocean currents during their sinking journey. If these virtual particles originate from an environment with a temperature below a threshold value indicated by $\widehat{SST}$, the particle is assumed to originate close to Antarctica, and flagged as representing Antarctic-endemic dinocyst species (see Materials and Methods section and Fig. 6.1 for an illustration).

Due to the circulation differences between eddying and non-eddying simulations, the model-derived occurrence of Antarctic-endemic sedimentary dinocysts is clearly different between both configurations (Fig. 6.3). While the endemism is more strongly dependent on latitude and a sharper boundary exists between low-endemism and high-endemism in LR4, sinking particles are transported further away from Antarctica in specific areas (especially near western boundary currents) in HR4. As a consequence, the occurrence of several recorded endemic species can be explained in HR4, while it cannot in LR4 (see e.g. site SanB). Moreover, the modeled endemism in the non-eddying LR4 cannot match with both DSDP277 and MH at the same time, because these sites contain an opposite signal (i.e. MH contains endemic species and DSDP277 does not) while being located closely to each other. In HR4 on the other hand, the sedimentary particles in site DSDP277 (Fig. 6.3) originate only from the warm waters of the southeastward flowing EAC, while the closely located site MH also contains particles originating from cold waters in the east, in agreement with the occurrence of endemic species at MH.

Overall we find that only the eddying simulations produce circulation patterns consistent with plankton biogeographic patterns. As a result, the model-data comparison has a better overall fit in HR4 compared to LR4 (Fig. 6.3a,c). The model-data fit improvement in HR4 compared to LR4 highlights the need for accurate reconstructions of the geographic boundary conditions (Baatsen et al., 2016) to optimize model-data matches as in Fig. 6.3a,b: It are the details in the ocean flow that induce a better model-data fit in HR4 compared to LR4.

The modeled dinocyst endemisms in the $2\times$ and $4\times$ pre-industrial atmospheric $CO_2$ configurations are similar (see Fig. C.7), even though HR2 and HR4 are forced by
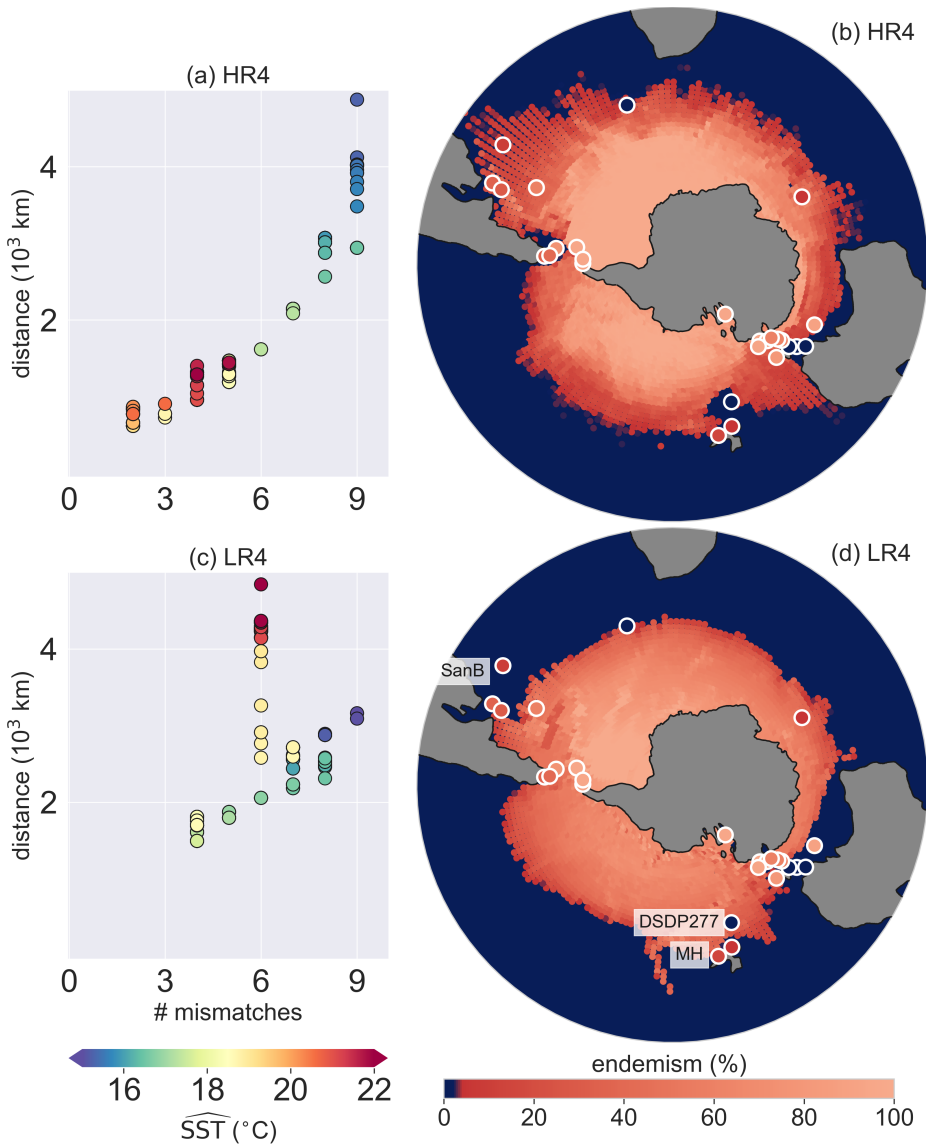
**Figure 6.3:** Model-data comparison: Antarctic endemism of sedimentary dinocysts in configurations HR4 and LR4. The model dinocyst endemism at the ocean bottom is determined by the percentage of virtual particles that started sinking (with 6 m day$^{-1}$ sinking speed) in a surface environment with temperature below $\widehat{SST}$ (see Supporting Information Fig. S4 for an illustration). (a), (c) Model-data fit for HR4 and LR4 respectively, for different values of $\widehat{SST}$ (given by the dot colors). Model and data compare better if the following two measures of fit are lower: 1) the number of sites with a point-to-point model-data mismatch in terms of endemic dinocyst species occurrence and 2) shortest cumulative distance of these sites to a location in the model that does match in terms of endemic dinocyst occurrence (i.e. $\sum_i D_i$, where $D_i$ is the distance between a site $i$ and a location in the model that does match with site $i$ in terms of the endemic dinocyst occurrence). (b), (d) Model-data comparison of dinocyst endemism at the $\widehat{SST}$ value that minimizes the measures of fit in (a), (c). The sedimentary endemism of the data is the percentage of measured endemic species at the site (Bijl et al., 2011), representative of 41-39 Ma. Labeled sites are named in the main text.

a different atmosphere and respond differently after initialisation (Fig. 6.4). However, the transient response of the upper ocean equilibrates similarly in the 2× and 4×pre-industrial $CO_2$ cases in a few decades, which also results in a similar time-mean surface flow (Fig. C.1).This implies that plankton biogeographic patterns and surface ocean circulation are to a large extent affected by bathymetry, rather than the climate boundary conditions of the model.

At the beginning of the HR2 and HR4 simulations, much of the energy input at the surface is used to set up the circulation and the development of eddies, as can be seen from a reduction of Southern Ocean gateway transports in the first 5 years (similar in both HR2 and HR4), after which they recover (Fig. 6.4c-f). After 9 years, the Drake Passage transport (through the gateway between South America and Antarctica) exceeds the transport in the low-resolution simulations and equilibrates at a higher level. The increased Drake Passage transport is mainly caused by the lower (more realistic) viscosity that the high-resolution models allows compared to the low-resolution model (which becomes numerically unstable at this low viscosity value). Interestingly, the volume transport through the Tasman Gateway in HR2 and HR4 does not exceed the volume transport in LR2 and LR4. Instead, a larger fraction of the water is transported north of Australia, resulting in the stronger southeastward East Australian Current (EAC; Fig. 6.2).

### 6.3.3 Model-data comparison: sea surface temperatures

Now that we have established that the high-resolution POP model simulates an Eocene ocean flow, which is consistent with proxy data for ocean circulation, we compare the results of these simulations to proxy data for SST. SST distributions however, are also influenced by the model background state and sensitive to their global-scale equilibration. Moreover, the background flow affects the distribution of heat differently in the eddying versus non-eddying simulations. Meso-scale eddies are important for the distribution of heat, and eddying ocean models do a better job in representing heat transport compared to non-eddying models that use parameterizations for eddy-induced heat transport (Griffies et al., 2015; McWilliams et al., 2014; Viebahn et al., 2016).

Indeed, heat is distributed differently in the top km of the eddying compared to the non-eddying simulations (Fig. 6.4a and 6.4b). Eddies efficiently transport heat to the subsurface (Delworth et al., 2012), which leads to subsurface warming in both eddying simulations (HR2 and HR4) and a lower vertical temperature gradient compared to LR2 and LR4. However, in HR2 the surface cools more, while the subsurface warms less compared to HR4.

Much of the heat transport change from LR to HR is related to the Southern and Northern Meridional Overturning Circulation (SMOC and NMOC respectively). In both HR2 and HR4, North Pacific sinking develops (in a few decades) next to existing South Pacific sinking, while in the low-resolution simulations there is only Southern Hemisphere sinking (Fig. C.3). Overall, the North Pacific sinking leads to an increase in the NMOC and a decrease in the SMOC. These changes in the MOC
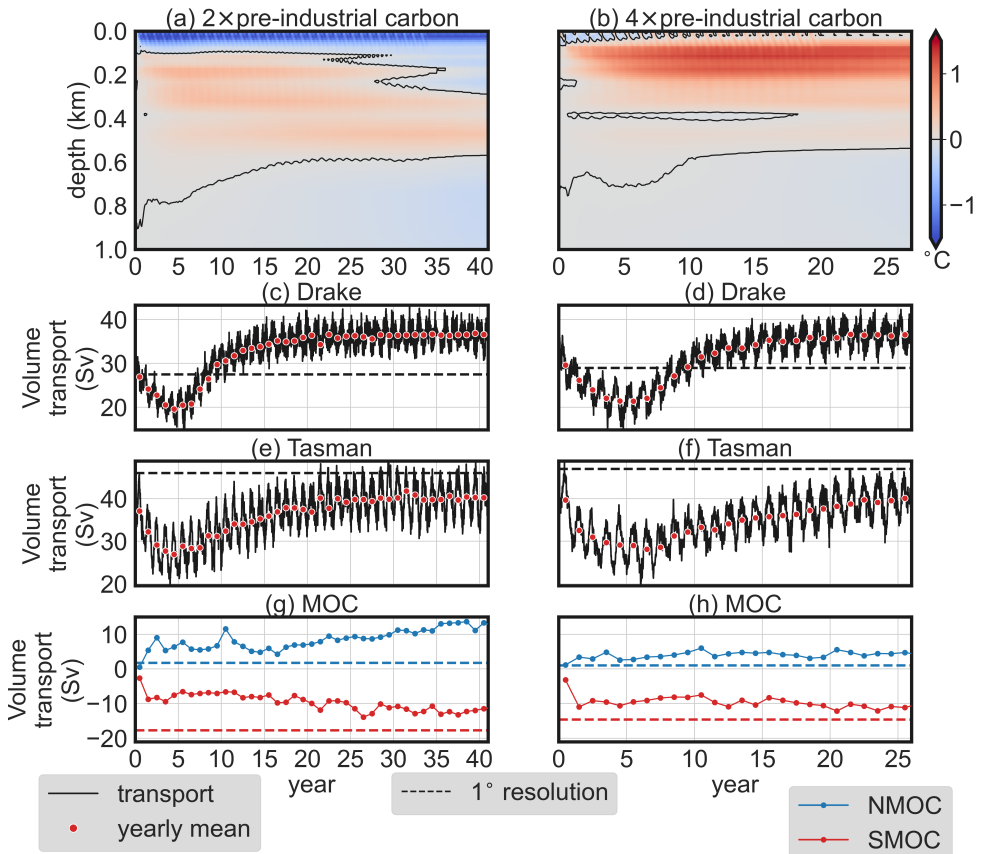
**Figure 6.4:** Response of the ocean model after initialisation, HR2 (left) and HR4 (right). Note that the initial state of HR2 (HR4) corresponds to LR2 (LR4). (a), (b) Depth-dependent evolution of the horizontal mean temperature increase compared to the initialisation state (upper 1km only). Water volume transport through the (c), (d) Drake Passage ($65°$W) and (e),(f) Tasman Gateway ($150°$E). (g), (h) Northern and southern maximum meridional overturning. MOC=Meridional Overturning Circulation, NMOC=Northern MOC, SMOC=Southern MOC, Sv=Sverdrup.

are stronger in HR2 compared to HR4, and both the NMOC and SMOC are still increasing in magnitude at the end of the HR2 simulation.

The SMOC also differs in structure between the high- and low-resolution simulations (see the mixed layer depth in Fig. C.3). In HR2 and HR4, more volume transport through the Drake Passage increases the surface salinity in the South Atlantic resulting in denser surface water in the Weddell Sea (Tumoulin et al., 2020). Therefore, the main deepwater formation location is the South Atlantic in HR2 and HR4, while it is the South Pacific in LR2 and LR4.

These results imply that HR2 and HR4 are run long enough for the upper-ocean circulation to equilibrate, while the deep ocean is not in equilibrium yet, as can be seen from the MOC in HR2 (Fig. 6.4g). Although the transient evolution of the deep ocean circulation differs between HR2 and HR4, we can nevertheless investigate their impact on SST distributions and compare those to proxy-data.

Both the tropical and Arctic Ocean cool significantly in HR2 compared to LR2, while in HR4 the equatorial regions cool less and high-latitude (north and south) regions warm more as compared to LR4 (see Fig.6.5). For both atmospheric $CO_2$ levels, local SST differences between the high- and low-resolution simulations mostly occur near western boundary currents of which the location shifts in the eddying simulation (Fig 6.5a and d). These shifts have an effect on the model-data comparison at sites near western boundary currents. In fact, the EAC transports warm waters southeastwards in the southwest Pacific, which (partly) explains why sites in the southwest Pacific are found to be warmer compared to model simulations with a coarse resolution. Notably, similar SST changes occur near the Kuroshio and Agulhas currents. The Weddell Sea warms up in HR2 and HR4 compared to LR2 and LR4 respectively, which is related to the South Atlantic sinking that occurs in HR2 and HR4.

Climate models generally do not produce the low meridional temperature gradients of warm climates as inferred from proxy data (Huber & Caballero, 2011; Sijp et al., 2014). While the simulations LR2 and LR4 were found to generate a lower meridional SST gradient compared to other models of 1° horizontal resolution or coarser (Baatsen et al., 2020), this gradient reduces further in HR2 and HR4. The tropics are cooler in HR2 and HR4 compared to LR2 and LR4, while in the zonal-mean the southern high-latitudes are only slightly warmer in HR4 (Fig.6.5d-f). Regionally, there is, however, significant warming of Southern Ocean SSTs in HR4. Overall, this improves comparison of the high-resolution model results with SST proxies in the tropics, while the modeled high-latitude SST values are often still lower than the proxy-derived SST values. The eddying simulations show stronger horizontal gradients in the time-mean SST field compared to the non-eddying simulations, which results in a higher time-mean SST variation in the model around the sediment sample sites. The model-data fit greatly improves in the eddying compared to non-eddying simulations (figs 6.5 g-j), although a mismatch with some sites remains (especially for the 2×pre-industrial $CO_2$ case) and the high-latitude temperatures are overall lower compared to the proxy data.
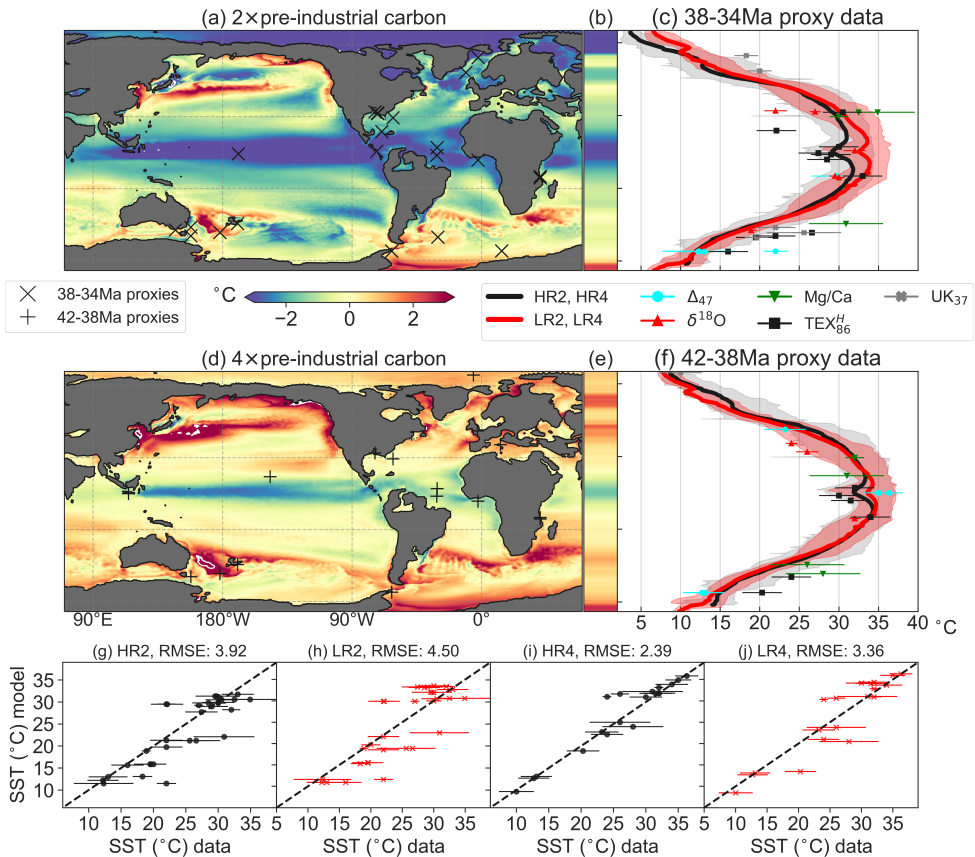
**Figure 6.5:** Model-proxy data comparison: sea surface temperature (SST). The 2× and 4×pre-industrial case are compared to SST proxy data of 38-34Ma and 42-38Ma respectively. (a), (d) SST difference of the high- compared to the low-resolution model with the site locations of the SST proxies for 2× and 4×pre-industrial carbon configuration, respectively and (b), (e) their zonal mean. Solid white lines indicate ±5°C contours. (c), (f) the zonally averaged annual mean SST in the high resolution (black) and the low resolution (red) model for 2× and 4×pre-industrial carbon configuration respectively. The shaded areas show zonal spread (i.e. minimum and maximum) of the annual mean SST. Markers indicate SST proxy estimates with their uncertainty. (g-j) Scatter plots between proxy-derived and model-derived SST for all four configurations, with Root Mean Squared Errors (RMSE). Error bars represent proxy calibration errors. To consider the palaeolocation uncertainty of sites (Hinsbergen et al., 2015), each site is compared to the model SST value from up to 3° distance of the site that minimizes the RMSE of the scatter plot (similar to (Baatsen et al., 2020); see Fig. **C.10** for a point-to-point comparison). The dashed black line is the one-to-one line representing the perfect match between model and proxy data.

Overall, the eddying ocean model reduces the SST model-data mismatch from the non-eddying model, because it alters the local transport of heat. However, the SST model-data comparison is also sensitive to the model background state (i.e. the state of the ocean at a global scale), which depends on the used atmospheric forcing and long time scales phenomena, such as the deep meridional overturning circulation. Hence, the SST model-data mismatch could be reduced even further if better model boundary conditions are used which lead to a more realistic background state of the late Eocene. To distinguish between the mechanisms which are reponsible for
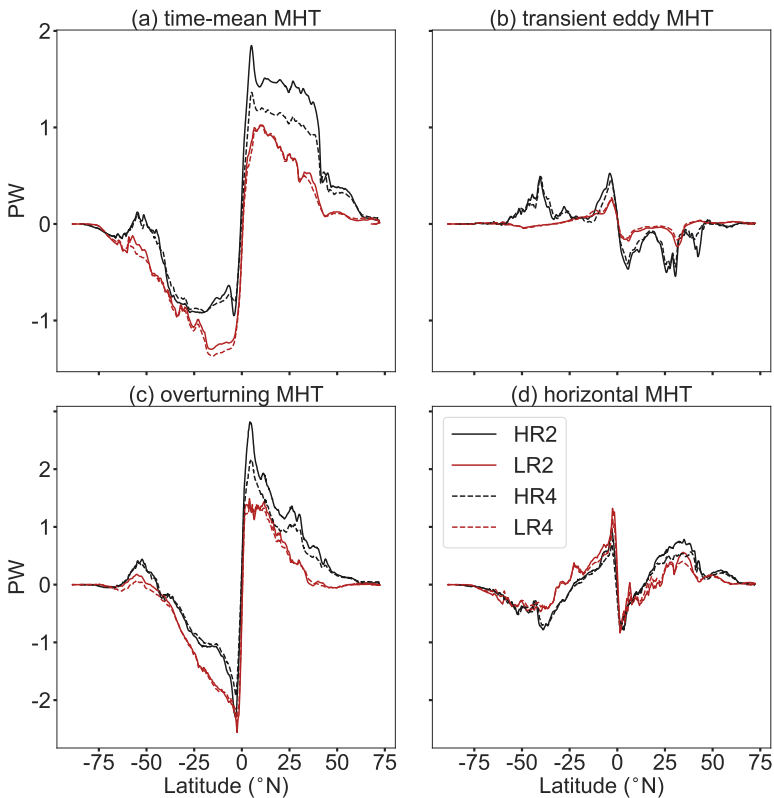


**Figure 6.6:** Decompositions of the ocean advective meridional heat transport (MHT; zonally and vertically integrated; see Viebahn et al., 2016). The (a) time-mean versus the (b) transient eddy component of MHT. The (c) overturning versus (d) horizontal MHT.

any changes in meridional heat transport (MHT), we use two types of decompositions (fig. 6.6). The first distinguishes between the time-mean and transient eddy component (Fig. 6.6a and 6.6b respectively). We find from the time-mean MHT that more heat is transported towards the North Pole in the high- compared to the low-resolution simulations. The additional heat that is transported from the equator towards the North Pole and hence there is less southward MHT at the Southern Hemisphere (the so-called 'heat piracy' effect; (Sijp et al., 2014)).

The transient eddy component typically compensates the dominant time-mean heat transport towards the poles and hence it is pointed equatorward. The transient eddy MHT is typically stronger in the high- compared to the low-resolution simulations, where the eddy-driven heat transport is parameterized with the Gent-McWilliams parameterization. Since both the time-mean and transient eddy component of the MHT are higher at southern midlatitudes in HR2 and HR4 compared to LR2 and LR4, the three-dimensional Southern Ocean is more isolated in the high- compared to the low-resolution.

The second decomposition is spatial, and distinguishes between the MHT that is caused by the horizontal (gyre) circulation and the MHT part that is caused by both deep and shallow overturning. Both high-resolution simulations have a stronger horizontal gyre circulation in both hemispheres and stronger western boundary currents compared to LR2 and LR4, resulting in more poleward horizontal heat transport in HR2 and HR4 (Fig 6.6d). At the same time, the North Pacific sinking in HR2 and HR4 induces a stronger heat transport towards the North Pole (Fig 6.6c) compared to LR2 and LR4. This increase in northward heat transport also leads to a lower southward heat transport in the Southern Hemisphere.

The different background states responses of HR2 and HR4 are also visible in the MHT decompositions (Fig. 6.6). Although the MHT in LR2 and LR4 are similar, the northward heat transport in HR2 is much larger than HR4, which is caused by the stronger North Pacific sinking in HR2. The MHT difference between HR2 and HR4 is unrelated to a heat piracy effect, since the MHT transport in the Southern Hemisphere is similar in both simulations. In contrast, the equator cools more strongly in HR2 compared to HR4.

## 6.4 Conclusion and outlook

We have shown that an eddying Eocene ocean model provides a more detailed ocean flow compared to a non-eddying version of the same model. As a result, model-data mismatches in the geologic past (Baatsen et al., 2020; Bijl et al., 2011; Houben et al., 2019; Huber et al., 2004; Hutchinson et al., 2021; Lunt et al., 2021) can at least partly be explained by the lack of eddies in the ocean models used. Our eddying simulations of the late Eocene are better able to explain the occurrence or absence of endemic dinocyst species near Antarctica compared to non-eddying simulations. The SST model-data comparison also improved in the eddying compared to non-eddying simulations.

The explicit representation of eddies in ocean models may have implications for comparison of models with other proxy types than considered here. For instance, pollen-based temperature reconstructions imply that it did not freeze at the Antarctic coast during winter in the early Eocene (globally $\sim 6°C$ warmer than the late Eocene), despite polar darkness (Pross et al., 2012). Eddy-induced flow, and its impact on ocean heat transport, could in part explain such conditions.

The simulations in this chapter are computationally expensive. However, other types of model set-ups may be interesting if not limited by computational capabilities. First, the strong influence of bathymetry on the eddying flow implies that the uncertainty of palaeogeography reconstructions has a major impact on model-data comparisons. Future studies could make adaptations on the bathymetry within uncertainty of palaeogeograhic reconstructions, to find its impact on the modeled ocean circulation and model-data comparison. Moreover, since the eddying flow has a direct response to bottom topography, it seems suitable for a downscaling, or eddy parameterization type of approach to obtain this influence of bathymetry on the flow with reduced computational costs. However, these type of approaches are found to be challenging in present-day configurations (Fox-Kemper et al., 2019; Lanzante et al., 2018; Nooteboom et al., 2020).

Second, we used the model equilibrium of the non-eddying climate model simulations (which are in radiative equilibrium (Baatsen et al., 2020)) to start and force the eddying model. However, this switch induces a drift of the deep ocean circulation, which is not equilibrated yet in the high-resolution simulations of this chapter. Hence, the background state of the model will change further if the model is run for longer time periods (a few millennia). Future simulations may have the capabilities to perform longer simulations. These changes of the model background state on long time scales might have implications for the regional flow and the quality of the model-data comparisons.

Finally, atmospheric feedbacks greatly influence the ocean model background state on long time scales, such as the meridional overturning circulation (Arzel et al., 2011; Rahmstorf & Willebrand, 1995; Toom et al., 2012; Zhang et al., 2015). Hence, the high-resolution ocean should be coupled to a high-resolution atmosphere, which could further enhance the meridional transport of heat and lead to an improved model-data comparison.

## 6.5 Code and data availability

The code that is used for this work is distributed under MIT license and can be found here: `https://github.com/pdnooteboom/MCEocene`, and for the MHT decompositions: `https://github.com/pdnooteboom/MHeatTransport`. The model data used to generate the main figures in this chapter are publicly available on the Utrecht University Yoda platform: `https://doi.org/10.24416/UU01-AYNLZP`.
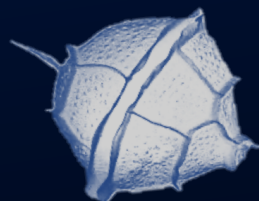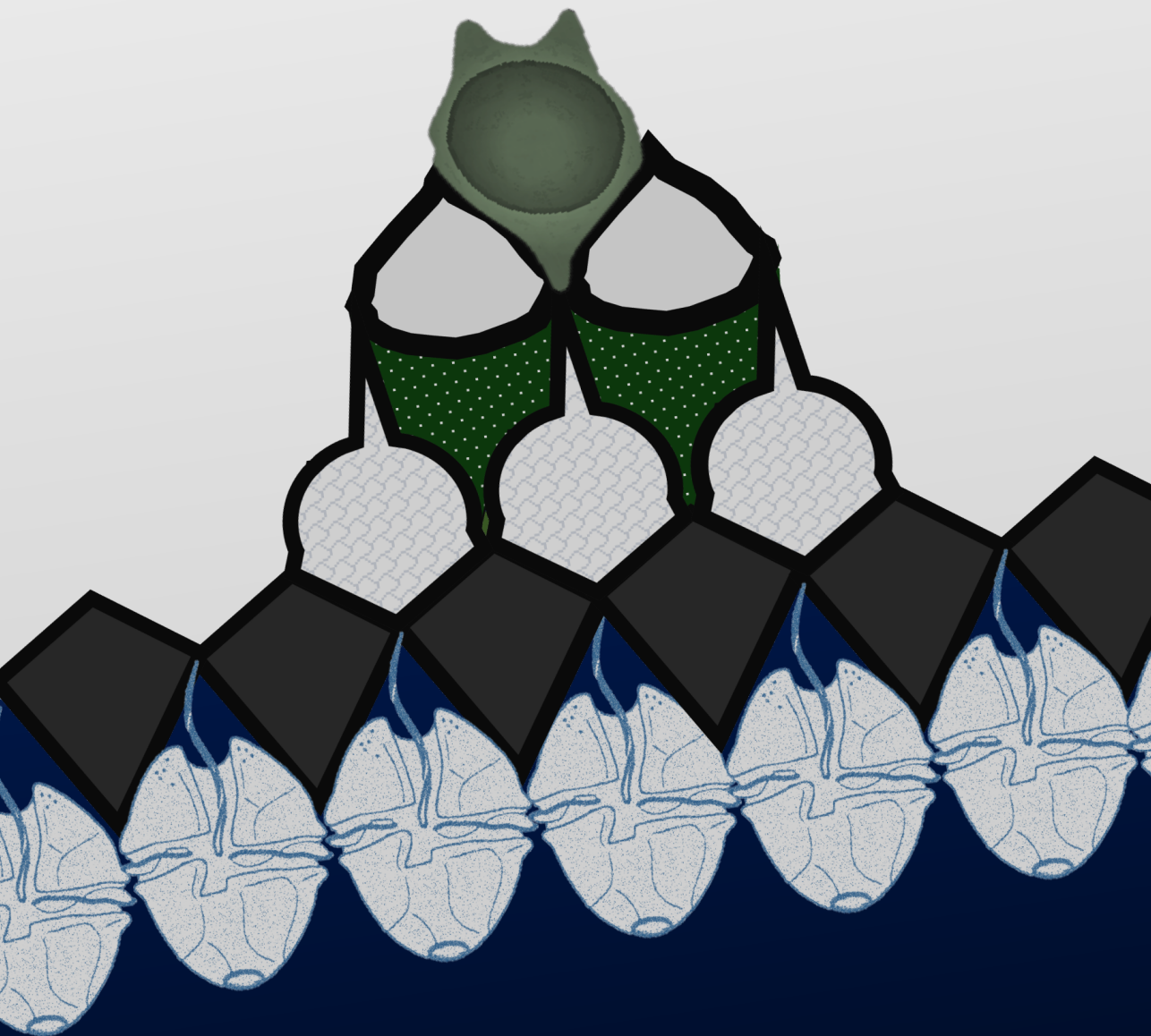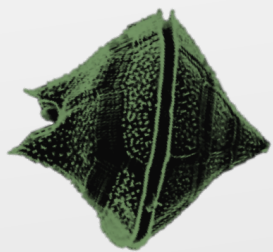
# CHAPTER 7

## Summary and outlook

In this chapter we summarize the main conclusions of the thesis by answering the research questions as formulated in chapter 1. We also provide an outlook of future research, dealing with outstanding questions that arise from the conclusions of this thesis.

# 7.1 Summary

**How much can the lateral transport of microplankton influence their sedimentary species composition, and does this impact their relation with environmental variables at the ocean surface?**

Using sinking speeds of single dinocysts, chapter 3 shows that sinking microplankton can transport up to 1500km in extreme cases. This could lead to differences between the environment at overlying and at back-tracked surface origin locations of up to ±16°C and ±4PSU. Sedimentary microplankton could hence represent a very different climate compared to the environment at the overlying surface. This environmental difference depends on 1) the water depth, 2) the particle sinking speed, 3) the strength of local ocean currents, 4) the orientation of those ocean currents and 5) the gradients of environmental variables in the directions of these currents.

As a consequence of the lateral displacement of microplankton species by ocean currents, some of these species may occur in marine sediments which are located outside of their typical habitat region at the ocean surface, as was shown for the dinocyst species *S. antarctica* and *S. delicatus* (chapter 3). Hence, this lateral displacement does influence the sedimentary species composition.

The influence of ocean transport on sedimentary microplankton composition is further generalised in chapter 4: this influence is provincial, due to the spatial varying character that these backtracking analyses have. This implies that sinking particles become relatively more mixed in specific areas (e.g. near Western boundary currents). It was shown that the measured sedimentary biodiversity is often higher in these areas with strong mixing, partly because of the species occurrence in sediments that are located outside of their habitat area at the surface. Moreover, a clearer relationship between the sedimentary microplankton composition and environmental variables at the surface could be obtained if the sediment samples in those areas of 'strong mixing' were excluded. An interesting observation in this chapter is that the provinces of strong mixing do not change much if different particle sinking speeds are used.

**What is the impact of resolving eddies in an ocean model on sinking Lagrangian particles, and hence the modelled transport of sinking microplankton?**

Spatial resolution is a relevant property of an ocean model to determine the trajectories of sinking Lagrangian particles in chapter 5, where back-tracked particle distributions are compared in different OGCM configurations (with different spatial and temporal resolutions of the OGCM and its output respectively). Lagrangian

particles are transported differently in a strongly eddying OGCM, with $0.1°$ horizontal resolution, compared to a non-eddying OGCM of $1°$ horizontal resolution. Differences between the back-tracked particle distributions in both model types arise because 1) eddies provide mesoscale (10-30km) fluctuations in the flow field that cause a stronger divergence of particle trajectories and 2) the time-mean flow field is different in the eddying compared to the non-eddying OGCM, because the smaller scales that are resolved in the eddying OGCM have an influence on the large scale flow.

Fluctuations can be added to the non-eddying flow field, to mimic the transport of sinking particles by eddies. In chapter 5, these fluctuations are added with the addition of stochastic noise while particles were tracked in the flow field. Using this approach, similar back-tracked particle distributions are obtained between the eddying and non-eddying configurations in locations where the local time-mean flow was similar in both eddying and non-eddying OGCM. Such locations exist, but there are very few, and it is not possible to foresee where these are located from the non-eddying flow field alone. Moreover, the effect of eddies on the time-mean flow is not captured if stochastic noise is added to the particle trajectories after the flow field has already been created. Hence, this approach is insufficient to mimic the transport of sinking Lagrangian particles in eddying OGCMs in most locations.

Not only the spatial resolution of the OGCM, but also the temporal resolution of its model output influences the results of the back-tracking analysis. Performing the back-track analysis with both monthly and 5-daily model output, it was found that the particle distributions of surface origin locations can greatly differ in some cases. Overall, it is recommended to only apply sinking Lagrangian particles using an eddying OGCM with model output which has a temporal resolution in the order of days.

**Do model-data comparisons of past climates improve if an eddying ocean model is used instead of a non-eddying model?**

Chapter 6 shows the potential of eddying model simulations to explain model-data mismatches in past climates. Except for their spatial detail, the eddying ocean simulations in this chapter are similar to the non-eddying simulations in their set-up: they use the same atmospheric forcing and geographic boundary condition representative of the middle-late Eocene. Nevertheless, the meso-scale eddies induce a different time-mean flow in the eddying configuration. As a result of the adapted time-mean flow, the eddying simulations improve the model-data fit with two types of proxy-derived quantities.

First, eddying models are better able to explain the occurrence and absence of Antarctic-endemic dinocysts in the middle-late Eocene compared to non-eddying models. Sinking Lagrangian particles are used to determine the model-derived Antarctic endemism of species, which is why this quantitiy is expected to be different in eddying and non-eddying models (chapter 5). The eddying horizontal flow

is more strongly determined by the bathymetry compared to the non-eddying flow, which implies that this type of model-data fit strongly depends on the geographic boundary condition that the model uses. Moreover, since eddying simulations better represent surface flow compared to non-eddying simulations, eddying ocean models should be used to study ocean connectivity (Appendix D and chapter 4).

Second, the eddying model simulations compare better than non-eddying simulations with proxy-derived sea surface temperatures. This type of model-data fit is different in the eddying and non-eddying simulation due to differences in the time-mean flow and caused by the eddy-induced ocean heat transport that is more realistic in the eddying models and parameterized in the non-eddying models. However, a discrepancy of sea surface temperatures remains, because this type of model-data comparison is sensitive to the background ocean state of the model. Hence, this model-data fit could be further improved by choosing a different atmosperic forcing or by coupling the ocean to an atmospheric model.

## 7.2 Outlook

In this thesis, we find a great potential for the application of sinking Lagrangian particles in eddying Ocean Genereal Circulation Models (OGCMs) to represent sinking microplankton and to explain discrepancies between palaeoclimate model results and proxy data. This indicates that the usage of high-resolution, eddying palaeo-models has the potential to bridge model-data gaps in other time periods than the late Eocene. Interesting topics for future research are already discussed in the chapters of this thesis. Here we identify two fundamental challenges.

### Microplankton-environment relationship

First, it is important to understand how the relationship between sedimentary microplankton species and overlying environmental variables can be described, in order to make accurate palaeoceanographic reconstructions of these variables using microplankton. Hence, the first challenge is to explain how sedimentary microplankton distributions are shaped, in both the present-day and in the past, to obtain a better understanding of the relationship between sedimentary microplankton and the ocean surface environment.

More realistic simulations of sinking Lagrangian particles could explain microplankton biogegraphic patterns in more detail. In this thesis, we often applied sensitivity studies on the sinking speed, such as in chapter 3. However, one could incorporate the mechanisms that determine the sinking speed as discussed in chapter 2, possibly also including particle-particle interactions, integrating species-specific susceptibility for dissolution and designing these backtracking analyses for specific microplankton types (e.g. dinocysts, planktic foraminifera or coccoliths). Measured sedimentary microplankton distributions could be compared with similar measurements near the ocean surface. Then ideally, one could quantify a downward species flux, making the Lagrangian analysis better comparable with relative abundances of sedimentary

microplankton species, instead of comparing only the occurrence or absence of microplankton species in sediment sites as is done in chapters 6 and 3 of this thesis.

Apart from their sinking journey, sedimentary microplankton distributions are also determined by the plankton community structure near the ocean surface. It is unclear how surface plankton distributions are exactly shaped in the first place (Lima-Mendez et al., 2015), and the processes that shape plankton community structures may have changed through time. Especially for dinocysts, little is known about their near-surface distributions, which is partly due to the fact that specific biological producers (i.e. the dinoflagellate types) of dinocysts are unknown. Hence, a better understanding of the processes that determine surface plankton distributions may contribute to the reliability of palaeoceanographic reconstructions that use sedimentary microplankton.

Some proxies use the biogeochemical properties of specific microplankton species instead of the species composition that is considered in this thesis. These biogeochemical properties could be shaped in a different way by the advection of sinking microplankton compared to the species composition (Dämmer et al., 2020; Turney et al., 2020). Future research could investigate the effect of particle advection on all types of specific microplankton biogeochemical properties.

**Computational costs and opportunities of high-resolution simulations**

The second challenge concerns the computational cost (i.e. computing power and internal memory usage) of both the climate model simulations (i.e. the GCMs) and the application of Lagrangian particles. The usage of sinking Lagrangian particles in eddying ocean GCMs improves the comparison between modelled and measured bioprovencialism in the late Eocene (see chapter 6), which shows the potential of these high-resolution model simulations to resolve model-data mismatches in past climates. However, in chapter 6 we only used two model simulations (with different atmospheric forcing), because these simulations are computationally expensive. Two approaches can tackle this computational challenge: either by increasing the computional power or by reducing the computational costs of the simulations.

Computational costs could be reduced by improving the parameterisation of sub-grid scale effects in the non-eddying OGCMs. Sub-grid scale parameterisation is known as a great challenge in both the Eulerian and Lagrangian setting (Fox-Kemper et al., 2019; Le Sommer et al., 2018), due to the influence of sub-grid scales on the large-scale flow (as discussed in chapter 5). Nevertheless, attempts have been made while considering the effect of mesoscale eddies on the large-scale flow (Hewitt et al., 2020).

If this computational challenge can be overcome, high-resolution ocean model simulations provide several opportunities. First, we could apply more eddying simulations compared to the two simulations in chapter 6, under more boundary conditions such as atmospheric $CO_2$ and bathymetry configurations. Since boundary conditions are often uncertain in past climates, these type of sensitivity studies may result in

considerably different realisations of the model, which has a relevant impact on model-data comparisons such as those in chapter 6. The application of simulations under multiple boundary conditions could further improve model-data comparisons, and show which boundary conditions are most realistic for specific time periods.

Second, we could perform longer eddying simulations ($\sim 1000$ years), such that the ocean fully equilibrates. If the ocean is fully equilibrated, the simulations can be used to study large-scale features of the ocean, such as the deep meridional overturning circulation. The explicit representation of eddies in GCMs is known to have implications for the deep overturning circulation in the present-day (Hirschi et al., 2020; Jackson et al., 2020).

Third, atmospheric feedbacks influence the ocean flow, among which the deep overturning circulation, and the ocean background state on long time scales (Arzel et al., 2011; Rahmstorf & Willebrand, 1995). We could perform high-resolution palaeoclimate GCMs with a fully coupled ocean and atmosphere, which also allows us to study processes in past climates that are influenced by the atmosphere such as El Niño Southern Oscillation (Oldeman et al., 2021). Moreover, the atmosphere is responsible for a large part of the meridional heat transport (Fasullo & Trenberth, 2008; Trenberth & Caron, 2001; Yang et al., 2015). If the ocean is coupled to a high-resolution atmosphere, processes such as tropical cyclones (Roberts et al., 2020) and their effect on heat transport (Scoccimarro et al., 2011) are represented, which may result in a better match with the low equator-to-pole temperature difference in the Eocene that is inferred from proxy data compared to chapter 6.

It is in particular the ocean models with $0.1°$ horizontal resolution that greatly improve characteristics of the large-scale flow and the location of boundary current separations compared to non-eddying models with $\geq 1°$ horizontal resolution (Chassignet et al., 2020; Smith et al., 2000). However, $0.1°$ resolution models do not fully resolve the dynamics of mesoscale eddies everywhere (Fig. 7.1). If computational limits do not exist, at which model resolution should one stop? Recently, $0.02°$ horizontal resolution models have been shown to substantially improve ocean variability, western boundary currents (Ajayi et al., 2020; Chassignet & Xu, 2021) and the transport of heat (Su et al., 2018) compared to $0.1°$ resolution models in the present-day.

Since proxy data exhibit large uncertainty and are unlikely to include detailed ocean variability, a higher model resolution should substantially improve large-scale features in order to reduce model-data mismatches (e.g. the East Australia Current that substantially transports more heat southeastward in the eddying compared to the non-eddying simulation; chapter 6). Nevertheless, the variability that is contained in increasingly higher resolution palaeoclimate model simulations is interesting to investigate, since it may be different from the type of variability that we observe today and could be similar to the variability in a warm future climate.
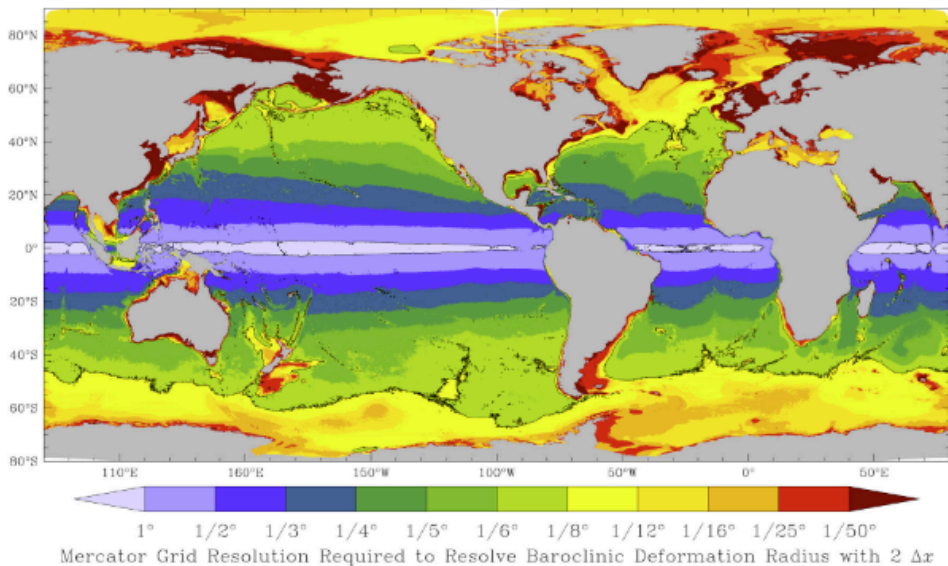
**Figure 7.1:** Figure from (Hallberg, 2013). Estimation (based on a 1/8° Mercator grid) of the horizontal resolution needed to resolve the first baroclinic deformation radius with two grid points. The solid line shows the contour where the deformation radius is resolved with two grid points at 1° and 1/8° resolutions.

7

# Appendices

# APPENDIX A

---

## Clustering methods (chapter 4) explained

### A.1 Additional information on oceanographically connected clusters in the present-day

#### A.1.1 Hierarchical clustering
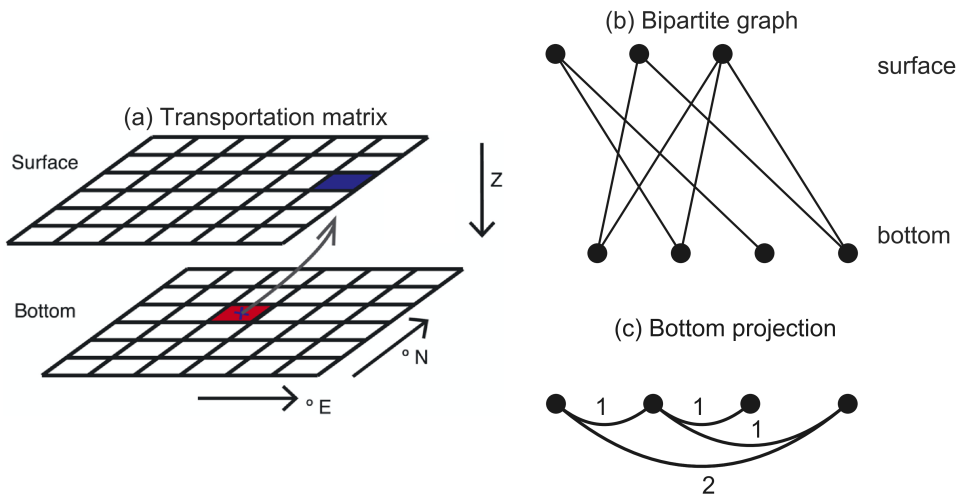


**Figure A.1:** Illustrations for the embedding types that the hierarchical clustering method uses. (a) Illustration of the surface-bottom transportation matrix (figure adapted from (Nooteboom et al., 2019)). The transportation matrix contains the probabilities that a particle that is found in a bottom box, originated from a surface box. The transportation matrix can also be interpreted as a bipartatite graph in (b), which has a bottom projection (c): the bottom nodes are linked with a weight that is determined by the amount of mutually linked surface vertices in the bipartite graph.

The particle tracking results from (Nooteboom et al., 2019) can be described by a bipartite graph (or transportation matrix; Fig A.1a). This bipatite graph consists of bottom and surface nodes (representative of surface and bottom boxes in the trans-

A

portation matrix; we use $1° \times 1°$ boxes in chapter 4). Bottom and surface nodes are linked if the probability that a particle which is found in a bottom box originates from the surface box is greater than zero. We will use the projection of this bipartite graph on the bottom nodes (Fig A.1c). This provides us with a graph of only bottom nodes, where the weight of a link between two nodes is determined by the amount of common surface nodes they are linked to in the bipartite graph.

Given the projection of the bipartite graph on the bottom nodes, we apply the hierarchical clustering method as described in (Wichmann et al., 2020). Starting with the largest connected component in the bottom projection as the only cluster (which represents the full global ocean), the clustering algorithm chooses one cluster at every iteration and splits it into two clusters, such that the Normalized Cut (NCut) is minimized (Shi & Jitendra, 2000). For $K$ clusters $S_1, \cdots, S_K$, the NCut is defined as:

$$\mathrm{NCut}(S_1, \cdots, S_K) := \sum_{i=1}^{K} \frac{Q\left(S_i, S_i^C\right)}{Q\left(S_i, S\right)},$$

where $Q\left(S_i, S_j\right)$ is the sum of all weigths connecting $S_i$ and $S_j$, $S_i^C$ is the complement of $S_i$. By definition, the NCut increases at every iteration (i.e. if the amount of clusters is higher).

### A.1.2 Ordering Points To Identify Clustering Structure

We use OPTICS to compare clusters with the sediment sample sites, which is density based and distinguishes different clusters from 'noise' (Wichmann et al., 2020). We apply OPTICS to the 'direct embedding' of surface origin distributions (Fig. 2.1a).

The main result from OPTICS is the reachability plot (see (Wichmann et al., 2021) for more details). The reachability plot is a representation of the global and local distribution of points (which represent sedimentary sites in chapter 4) at once. The valleys correspond to dense regions with similar surface origin location, while the hills correspond to the 'noisy' locations. The reachability plot depends on a parameter $s_{min}$, for which we test multiple values ($s_{min} \in [100, 200, 300, 400, 500, 600, 700, 800, 900, 1000]$). $s_{min}$ sets the minimum amount of 'nearby' points in the reachability plot for every point in a cluster (MinPts in (Ester et al., 1996)). In general, a larger $s_{min}$ results in a smoother reachability plot and larger clusters. If we let every particle release location (released on a $1° \times 1°$ grid) represent an area of 1 square degree ($\sim 10^4$ km$^2$), the OPTICS algorithm searches for a cluster with a spatial scale $\sim s_{min} \cdot 10^4$ km$^2$.

In chapter 4, we use $\xi$-clustering to obtain clusters from the reachability plot (Ankerst et al., 1999). This implies that we set a threshold on the steepness of the density ($\xi$), and cluster the valley of points that is surrounded by this steepness $\xi$. In general, a larger $\xi$ will reduce both the size and the amount of clusters.

## A.2 The distance matrices defined

We use (symmetric) distance matrices based on four different metrics. First, we use a matrix that contains Euclidean taxonomic distances, calculated from the relative abundances (fractions) of species. Second, we use the absolute SST differences between the sites. Third, we use a distance which is based on the reachability from the OPTICS algorithm. Specifically, if $r(p_k)$ is the reachability of point $p_k$ and the $n$ points are ordered from $p_0 \cdots p_n$, the reachability distance between two sediment sample sites (located near $p_i$ and $p_j$ respectively with $i \leq j$) is $D_{ji}^r = D_{ij}^r = \max_{i \leq k \leq j} r(p_k) - \min_{i \leq k \leq j} r(p_k)$. Intuitively, $D_{ij}^r$ represents how much one has to climb or descent in the reachability 'landscape,' if one likes to move from point $i$ to $j$. Fourth, we use a distance matrix which contains the spatial distance (in meters) between sediment sample sites. The partial Mantel test determines the correlation between the reachability distance and either SST or taxonomy distance matrices, keeping the spatial distance matrix constant.

## A.3 Supporting figures chapter 4

A
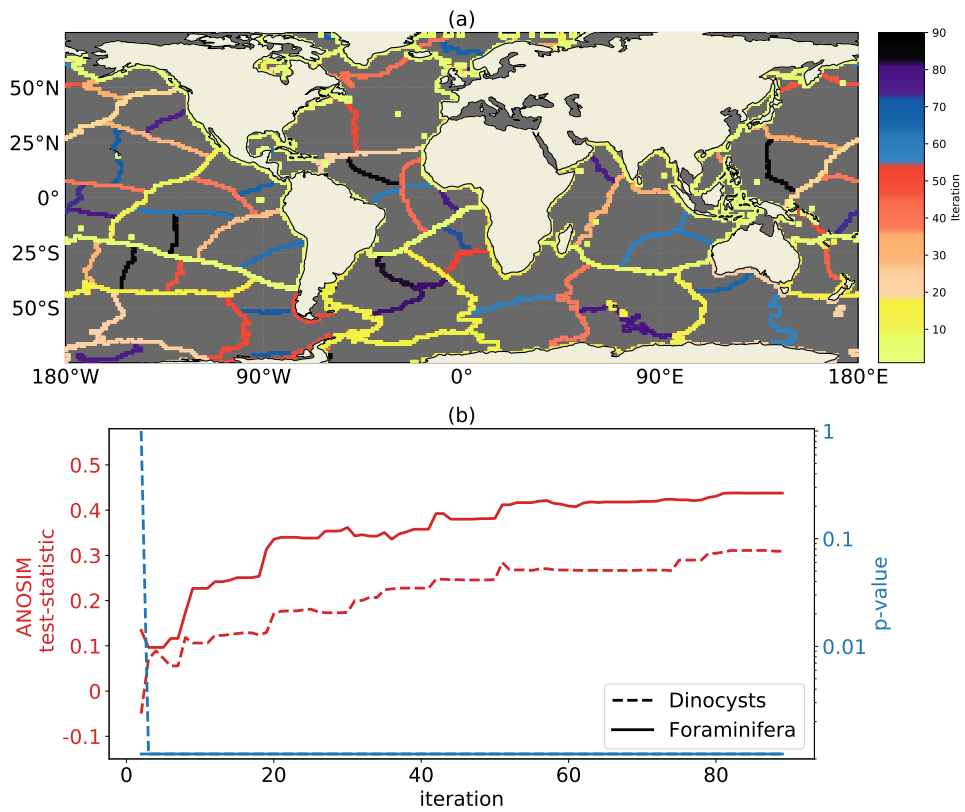


**Figure A.2:** Same as figure 4.2, but with 25 m day$^{-1}$ sinking speed.

A
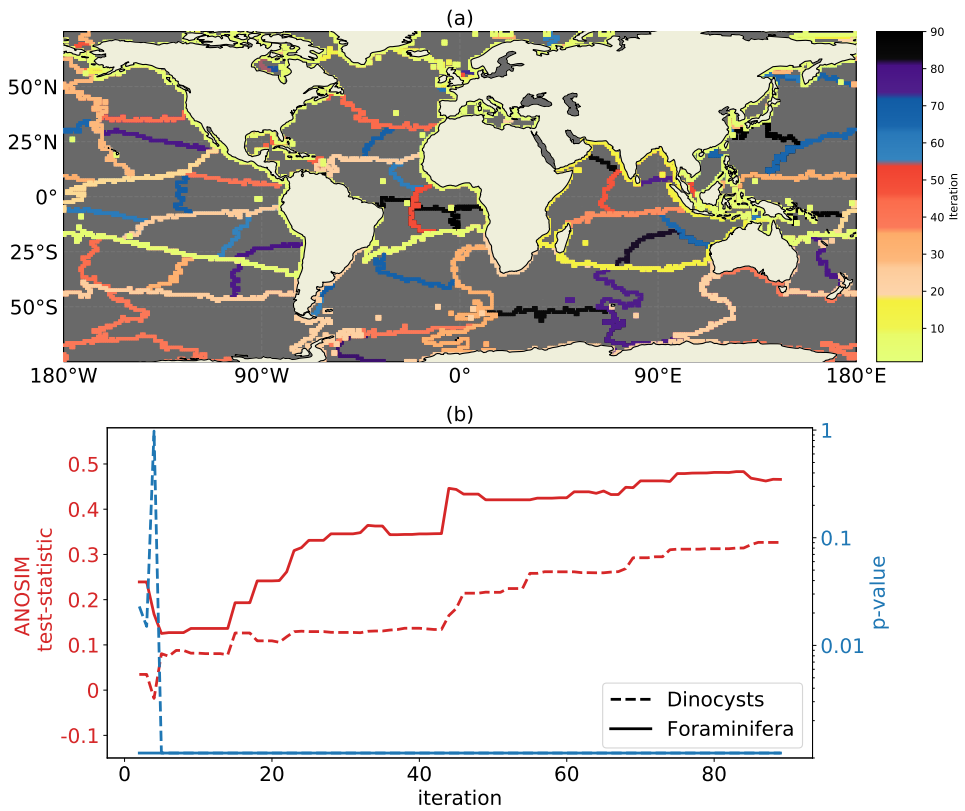


**Figure A.3:** Same as figure 4.2, but if only particles are used that started sinking in summer.

A
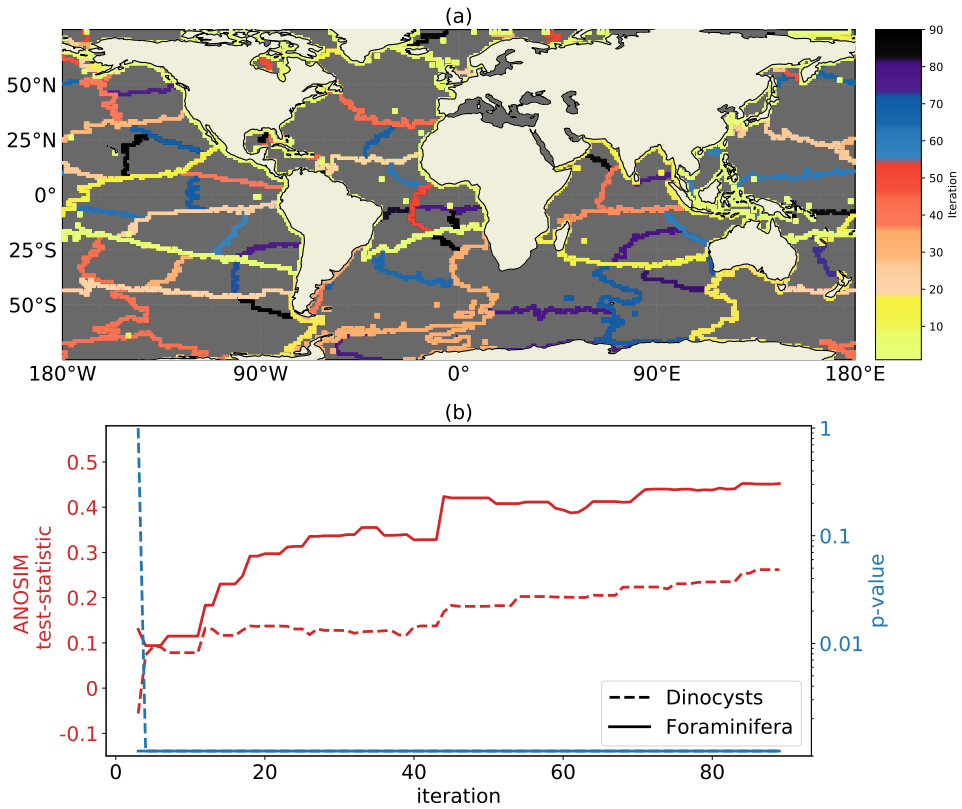


**Figure A.4:** Same as figure 4.2, but if only particles are used that started sinking in winter.
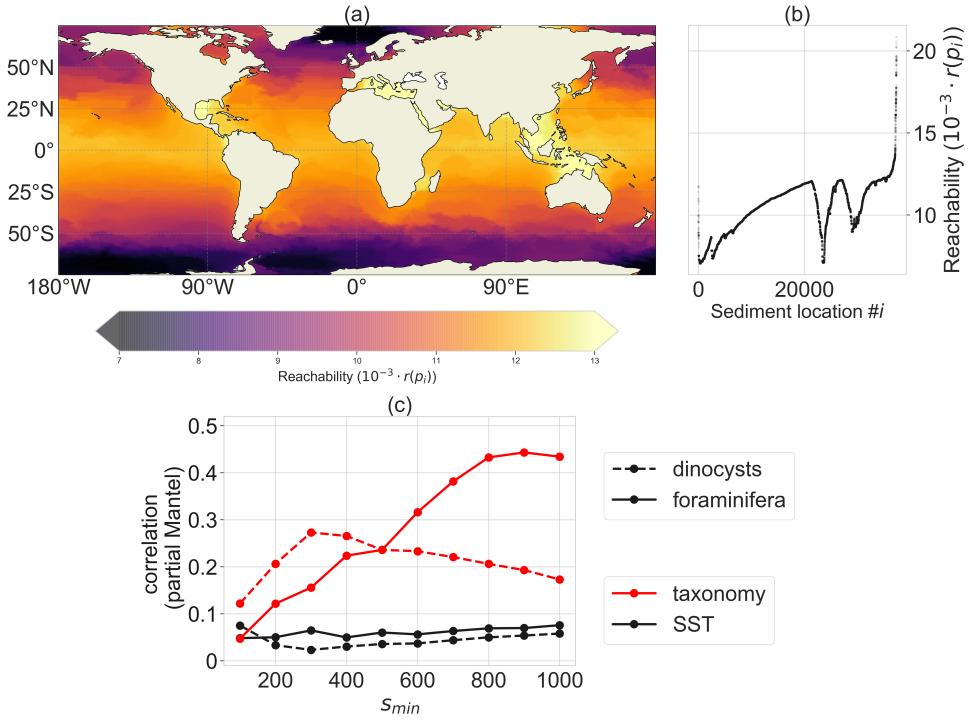
**Figure A.5:** Same as figure 4.3, but with 25 m day$^{-1}$ sinking speed.
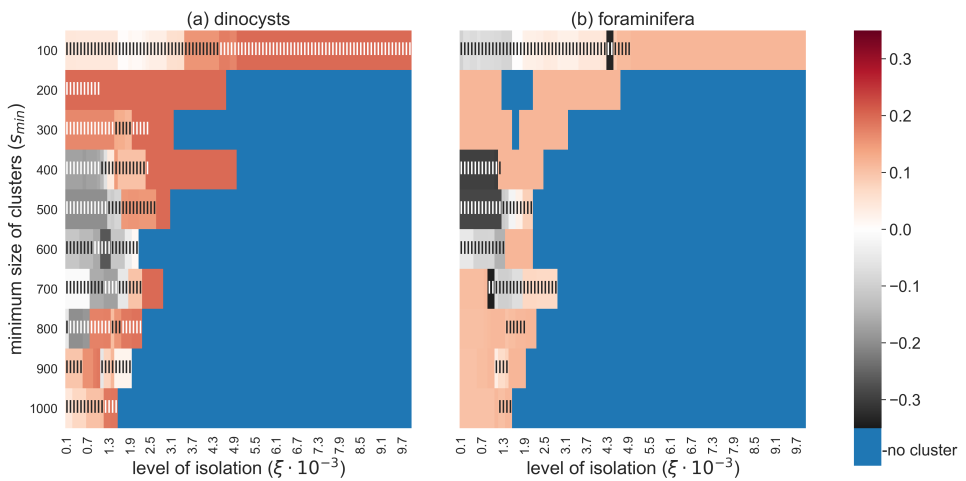


**Figure A.6:** Same as figure 4.6, but with 25 m day$^{-1}$ sinking speed.

A
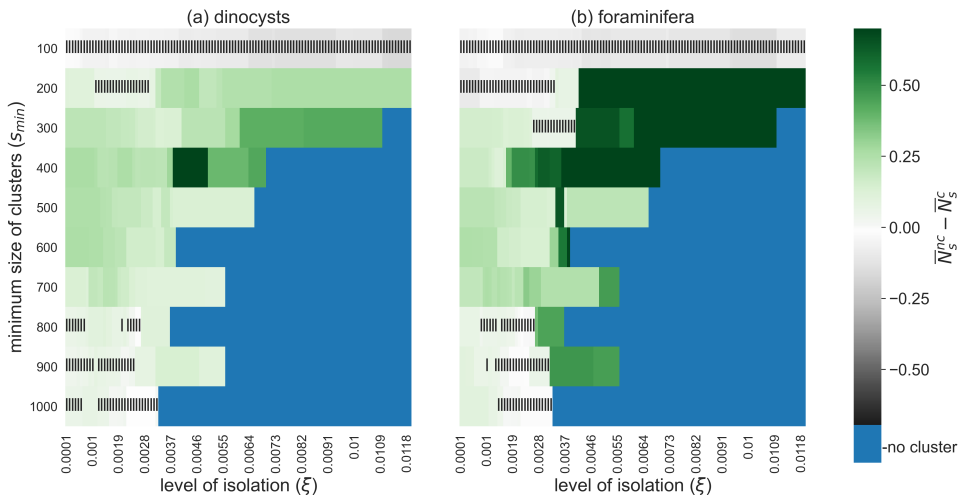


**Figure A.7:** Same as figure 4.7, but with 25 m day$^{-1}$ sinking speed.
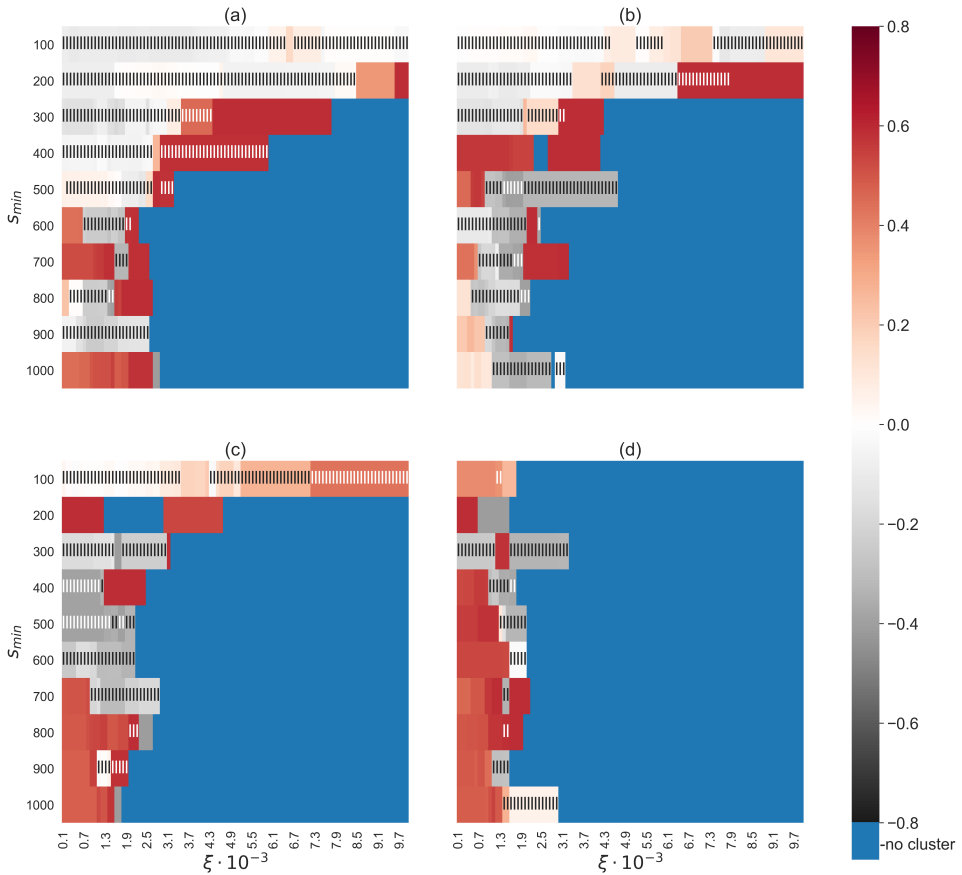
**Figure A.8:** Same as figure 4.6b, but if only the near-surface dwelling foraminifera species are used, and for (a) 6 m day$^{-1}$ (b) 11 m day$^{-1}$ (c) 25 m day$^{-1}$ (d) 250 m day$^{-1}$ sinking speed. The CCA analyses lead to significant results for fewer combinations of $\xi$ and $s_{min}$, but the increase of CCA variance is higher if it is significant, compared to the case where the full ForCens dataset is used.

A

# APPENDIX B

## Supporting figures with chapter 5
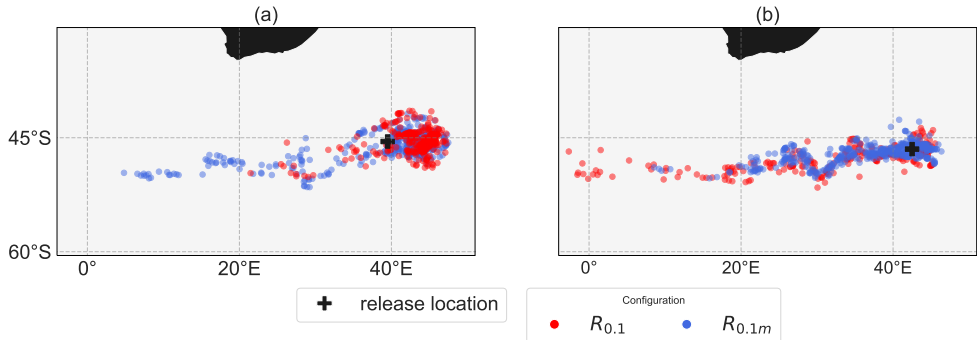


**Figure B.1:** Comparison between the reference configuration $R_{0.1}$ (red) and the temporally averaged configuration $R_{0.1m}$ (blue) at two release locations ($w_f = 6$ m day$^1$). (a) 45.5°S, 39.5°E at 2068m depth (red on top of blue) (b) 46.5°S, 42.5°E at 2238m depth (blue on top of red).
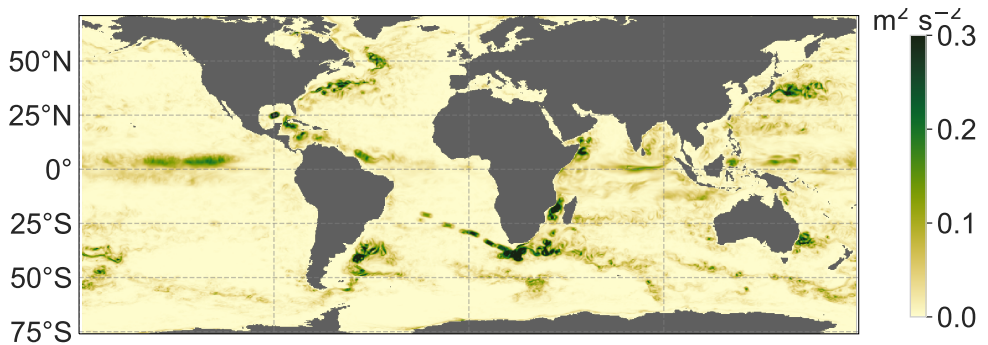


**Figure B.2:** Geographic plot of the time mean eddy kinetic energy at the surface. The eddy kinetic energy is defined as $\frac{1}{2}\overline{u'u'}$, where the bar denotes the time mean and $u'$ the deviation from the time mean velocity vector $u$ (so $u(\vec{x}, t) = \overline{u}(\vec{x}) + u'(\vec{x}, t)$).

B

**Figure B.3:** Animation (back in time) of particle back-tracking analysis ($w_f$ = 6 m day$^1$) with particle release at the Uruguayan margin (47.9°E and 37.15°S, $\sim$4800m depth). (a) the configuration $R_{0.1}$ with 5-daily model ouput and (b) the configuration $R_{0.1m}$ with monthly model output.

# APPENDIX C

Description of the eddying Eocene model simulations

**C.1 Supporting figures chapter 6**

C

## (a) 1° resolution

## (b) 0.1° resolution

0.0     0.1     0.2     0.3     0.4
m/s
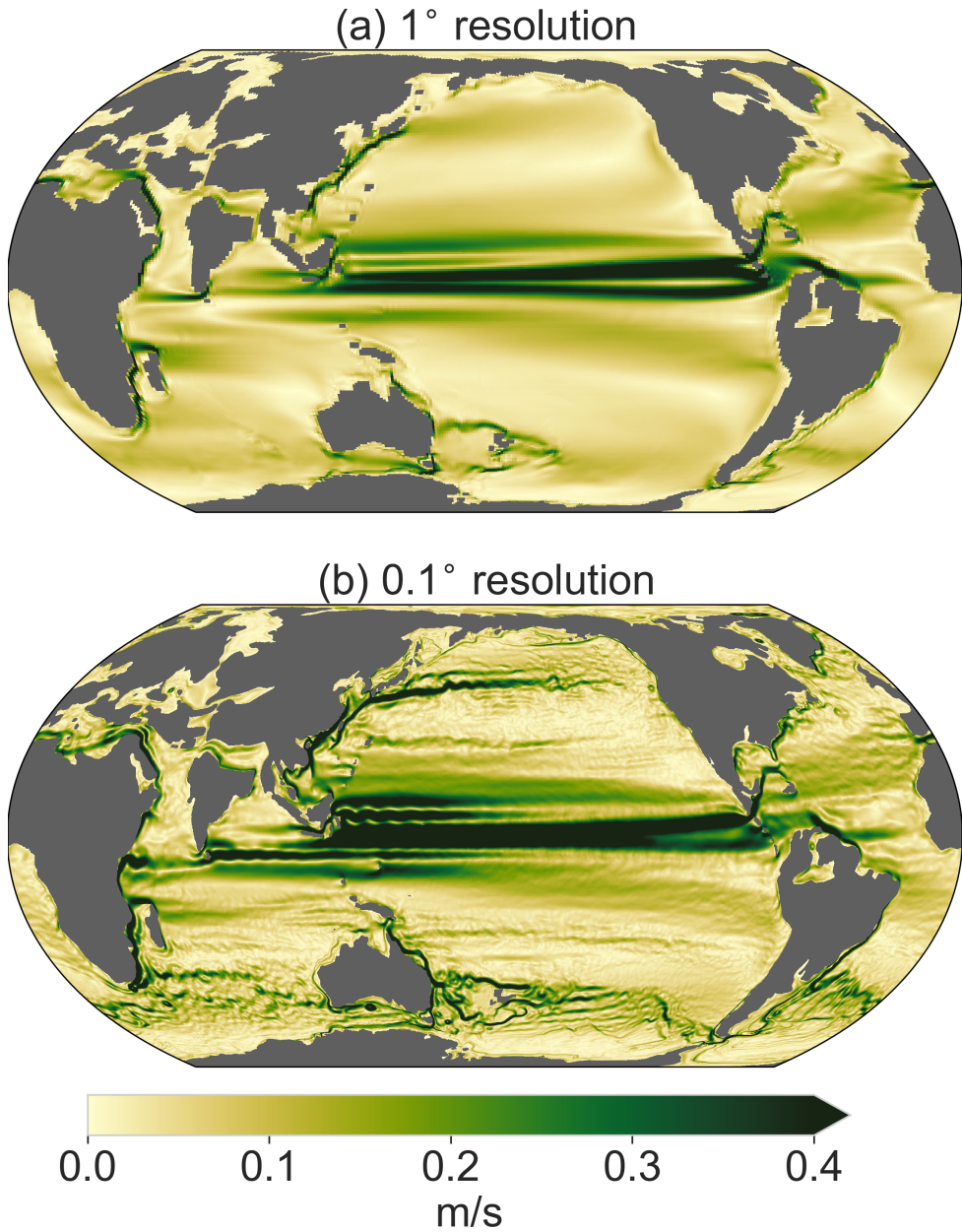
**Figure C.1:** Same as figure 6.2, but for the $2\times$pre-industrial $CO_2$ case (LR2 and HR2).

C
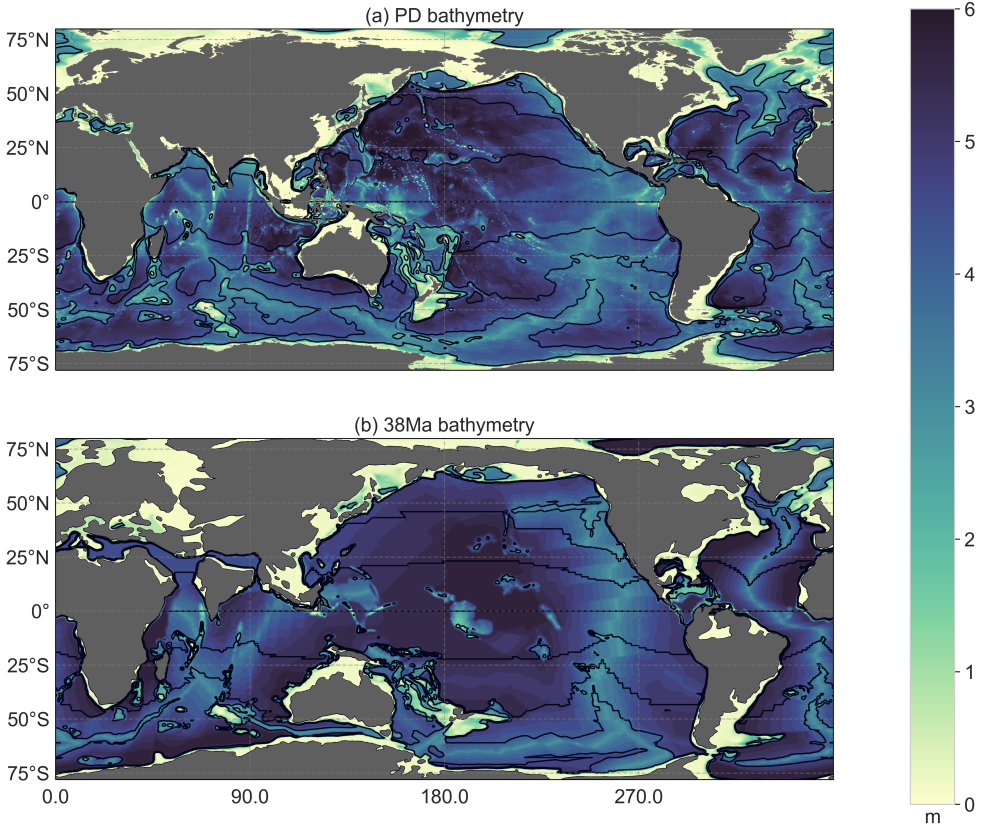


**Figure C.2:** Global bathymetry in (a) the present-day (PD) and (b) the middle-late Eocene (38Ma). Black contours are lines of constant $\frac{f}{H}$ that the flow tends to follow in eddying simulations to conserve potential vorticity, with $f = 2\Omega \sin(\phi)$ the coriolis parameter ($\Omega$ is the rotation rate of the Earth and $\phi$ the latitude) and $H$ the bathymetry.
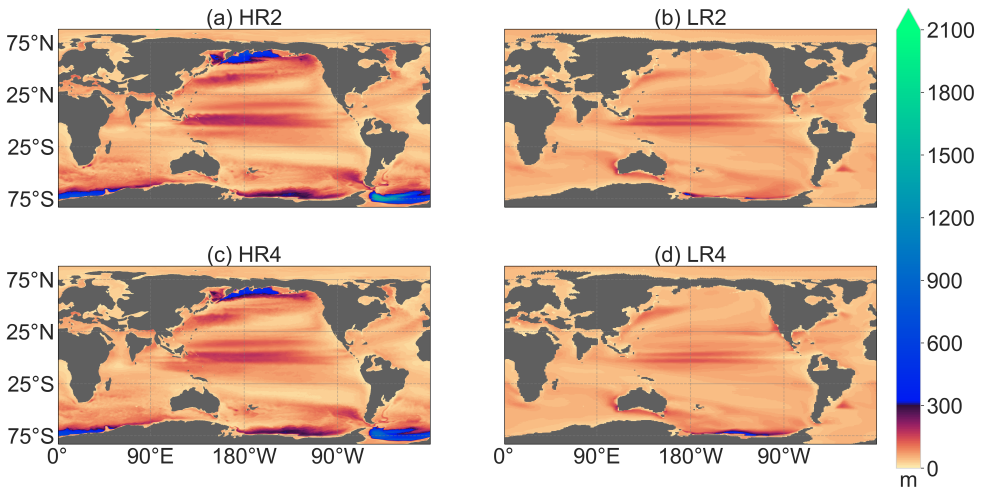


**Figure C.3:** Maximum monthly mean of the mixed layer depth.
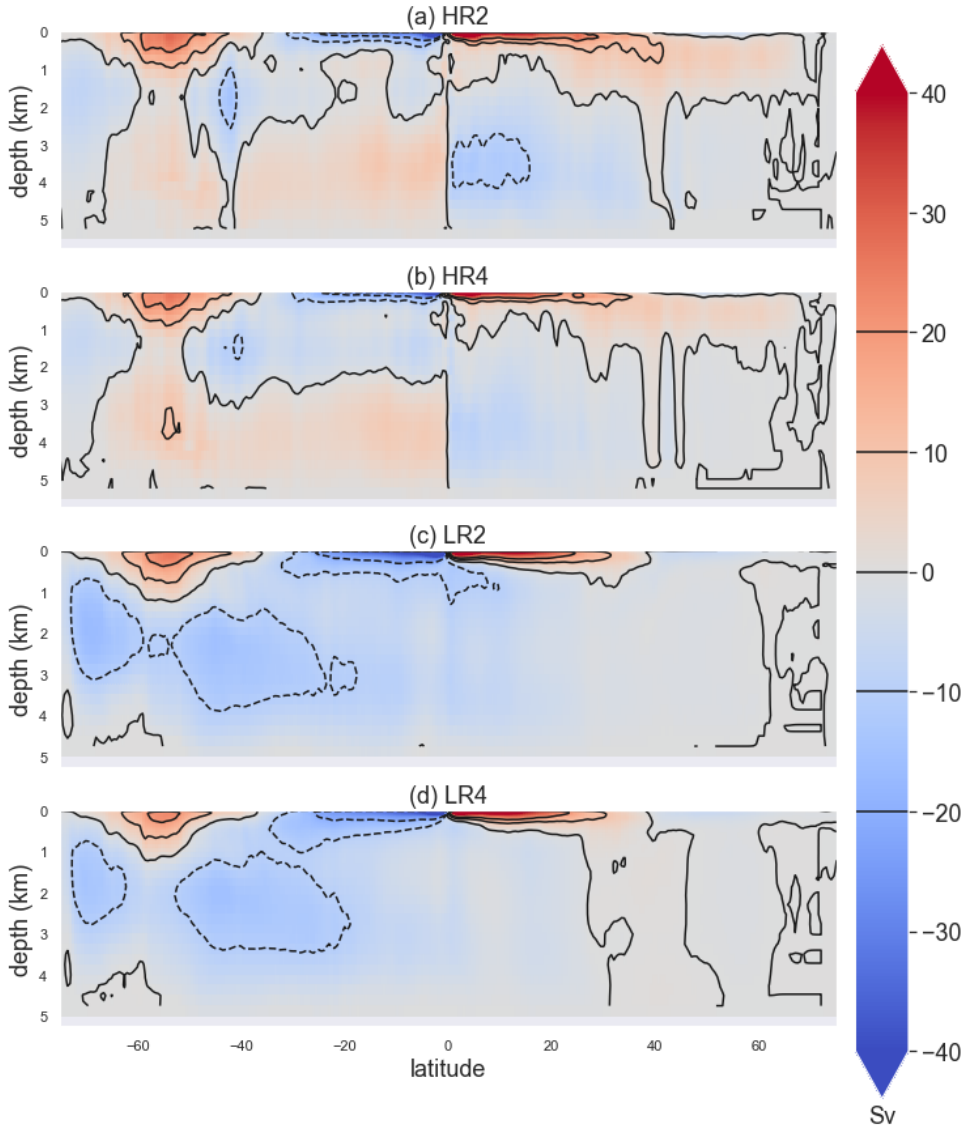
**Figure C.4:** Meridional overturning stream function of the time-mean flow (over the same years as figure 6.4) in configuration (a) HR2, (b) HR4, (c) LR2 and (d) LR4

C
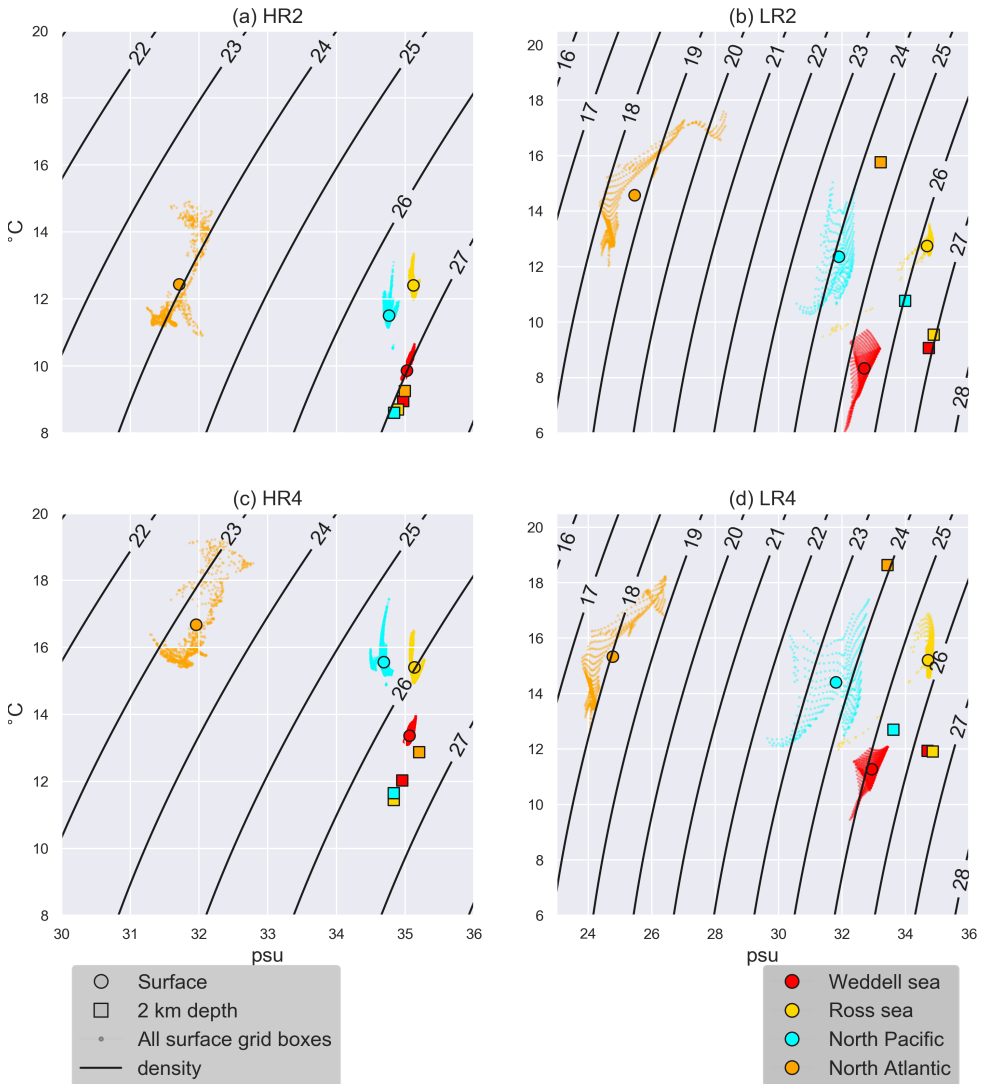


**Figure C.5:** Temperature versus salinity diagram. Contours indicate lines of constant density (in gram m$^{-3}$ anomaly from 1kg m$^{-3}$).
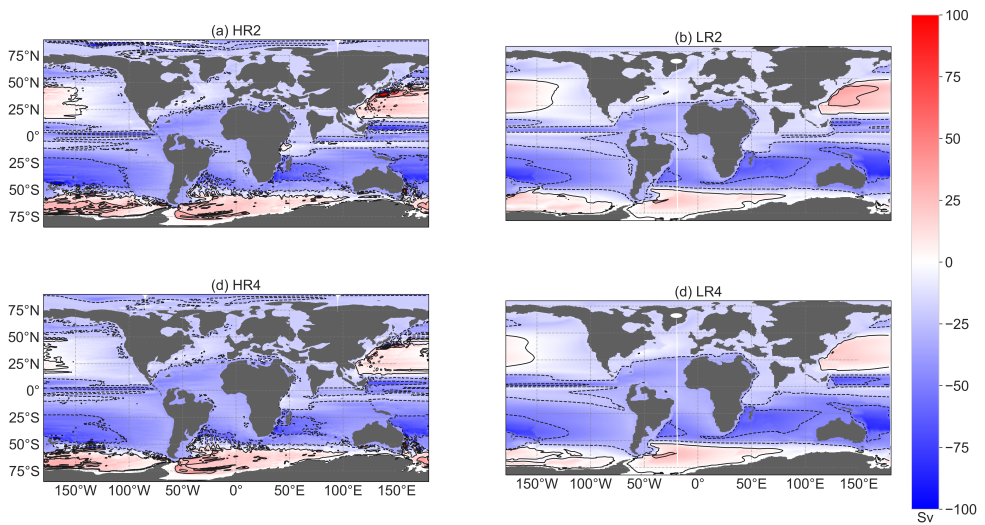
**Figure C.6:** Barotropic stream functions of the four configurations.
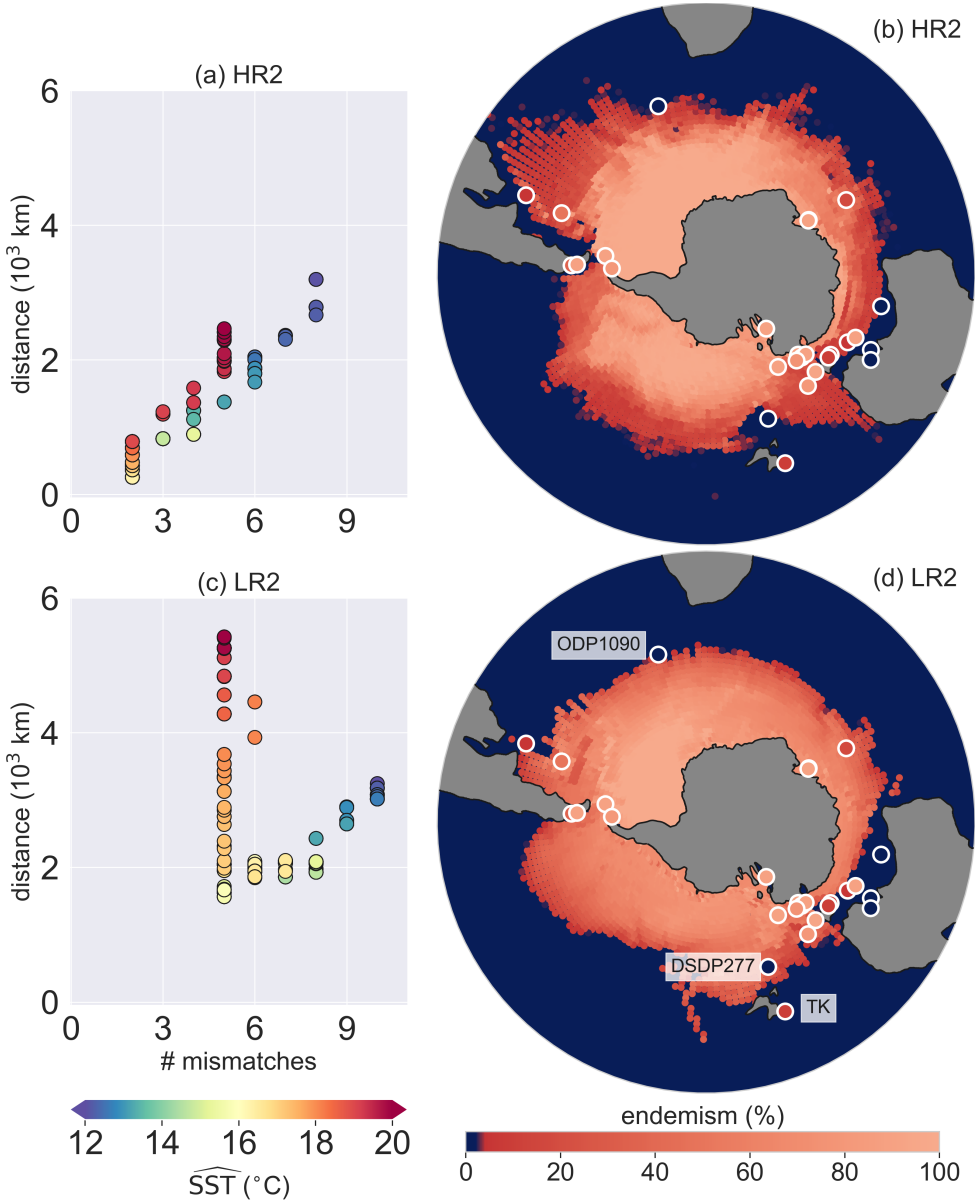
**Figure C.7:** Same as figure 6.3, but for the 2×pre-industrial case (LR2 and HR2).

**Figure C.8:** Same as figure 6.3, but with 25 m day$^{-1}$ sinking speed
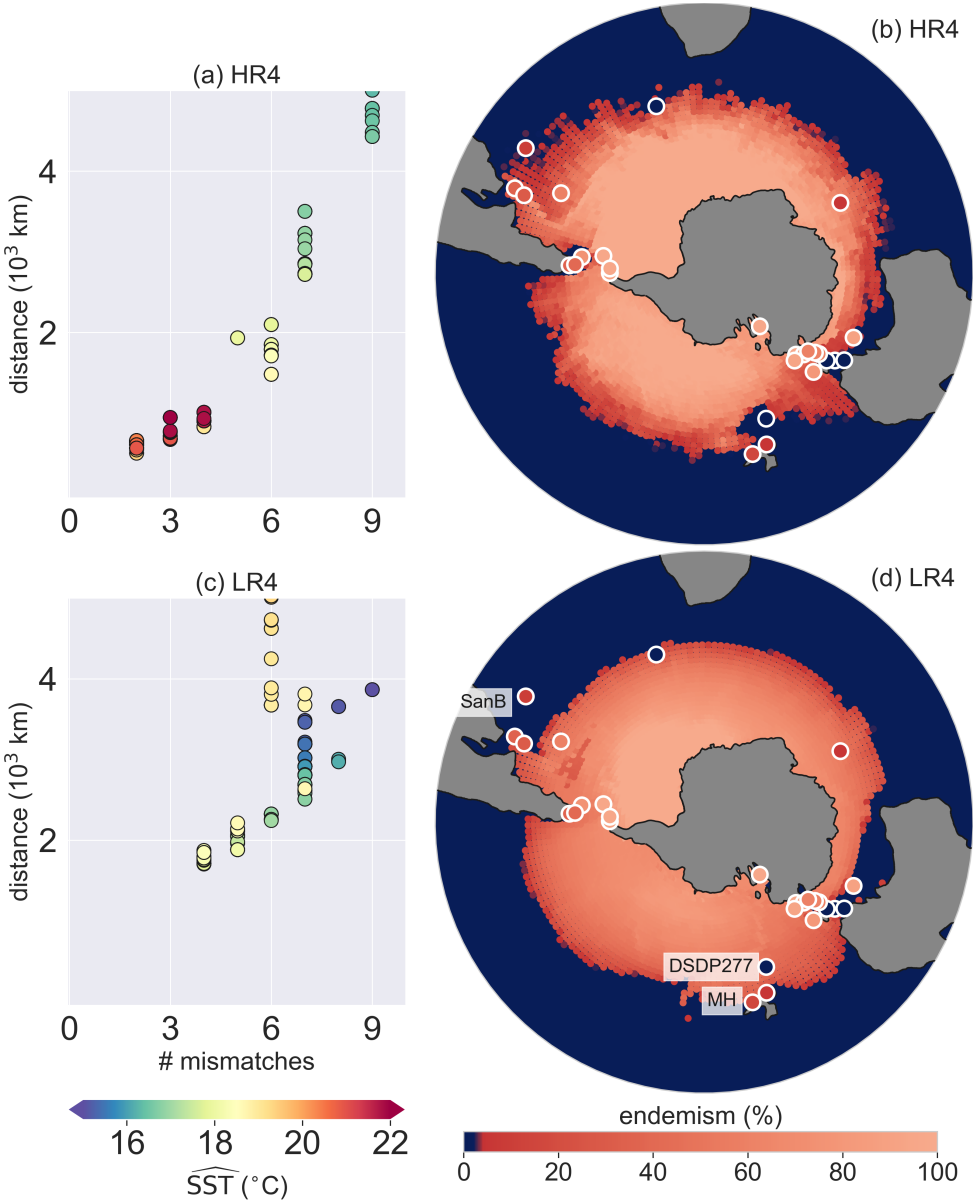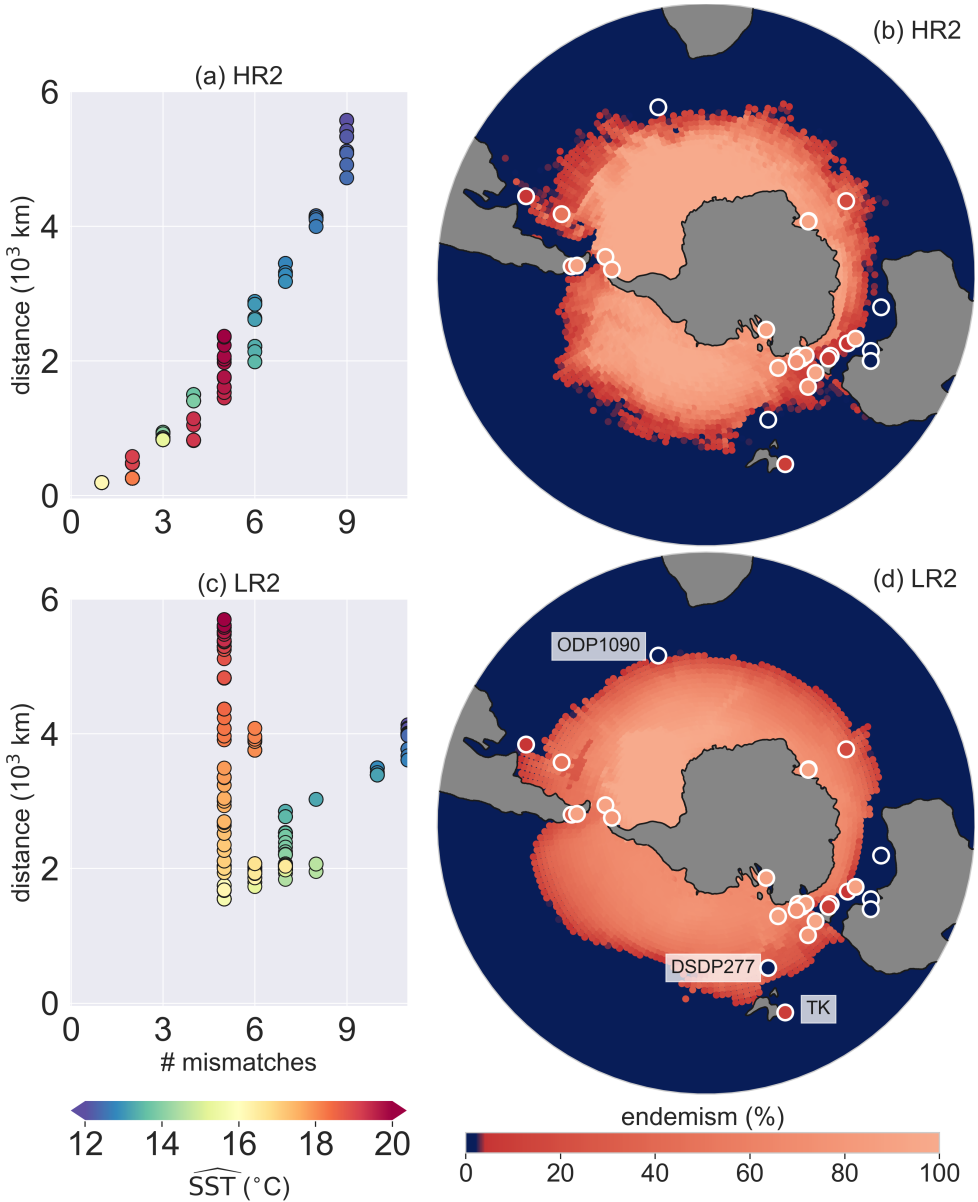
**Figure C.9:** Same as figure 6.3, but with 25 m day$^{-1}$ sinking speed and 2×pre-industrial case (LR2 and HR2)

C
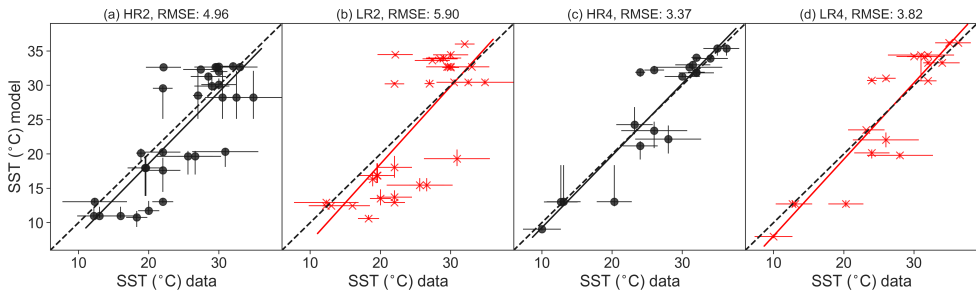


**Figure C.10:** Same as figure 6.5, but with a point-to-point comparison of model and data. The vertical uncertainty bars show the SST spread (minima and maxima) within a $4\times4°$ box around the sites.

# APPENDIX D

---

## Surface ocean connectivity in the Eocene compared to the present-day

In chapter 6, we assume that Antarctic-endemic dinocyst species are always represented by sinking Lagrangian particles that originate from cold surface waters (Fig. 6.3). In reality however, it may be that cold surface waters exist where the Antarctic-endemic biological producers of the dinocysts do not occur, because Antarctic-endemic plankton species are isolated from these cold waters. In this Appendix section, we quantify on which timescales different areas in the ocean are connected by surface currents in both the Eocene and the present-day. We find that the Eocene surface ocean is in general connected on shorter timescales compared to the present-day, which implies that dinoflagellate species spread more easily towards areas in which they can survive. Hence, sedimentary microplankton distributions are more strongly determined by the environment in the Eocene, instead of oceanographic isolation by surface currents.

## D.1 Method

### D.1.1 Ocean model simulations

We used the surface currents from five years of Parallel Ocean Program (POP) model output (ocean-only) in all three configurations (Table D.1). The horizontal resolution of these model simulations is $0.1°$ ($\sim 10$km). The temporal resolution of the output is daily, which is enough to capture realistic divergence timescales of La-

**Table D.1:** Ocean model simulations used in this Appendix section

| Simulation | Time period | Atmospheric forcing |
|---|---|---|
| $P_c$ (Weijer et al., 2012) | Present-day | Atmosphere of the present-day |
| HR2 (chapter 6) | Eocene (38Ma) | $2\times$pre-industrial $CO_2$ case from (Baatsen et al., 2020) |
| HR4 (chapter 6) | Eocene (38Ma) | $4\times$pre-industrial $CO_2$ case from (Baatsen et al., 2020) |
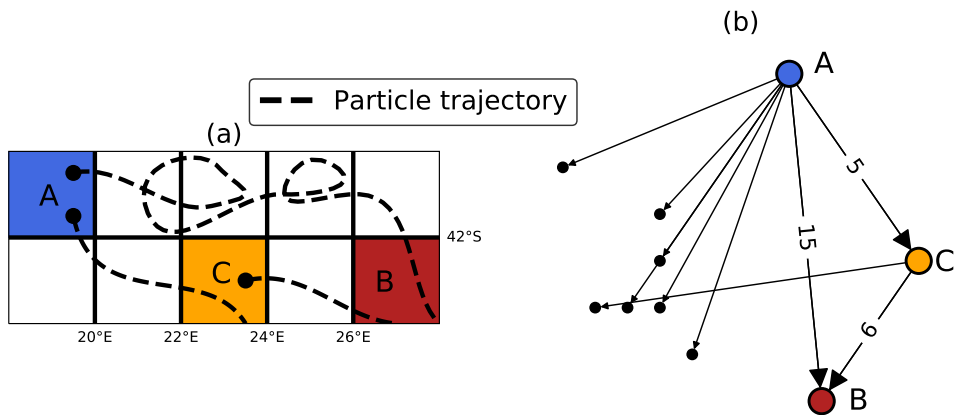
**Figure D.1:** Illustration of the connectivity timescales between patches. (a) Three particle trajectories that connect patches A, B and C. (b) The same patches as nodes in a directed network, where the edge weight is the minimum time (days) that particles took to travel between patches (i.e. the raw connectivity time). The Dijkstra connectivity time between two patches is the shortest path in the network (the Dijkstra connectivity time from A to B is 11 days).

grangian particles (Qin et al., 2014). The Eocene configurations (HR2 and HR4) are repetitively forced by the 50-year climatological mean atmospheres from the equilibrated model simulations with a fully coupled ocean-atmosphere of (Baatsen et al., 2020). This implies that the seasonal cycle is present in the atmospheric forcing of every configuration.

The Eocene simulations (HR2 and HR4) use the same geographic boundary conditions, based on the reconstruction from (Baatsen et al., 2016). Their surface forcing is different, using the different configurations of atmospheric greenhouse gas concentrations in (Baatsen et al., 2020). Their surface flow is similar, but diverges most in the North Pacific, since the Kuroshio current is stronger in HR2 compared to HR4.

### D.1.2 Lagrangian experiments

We released particles at a uniform global $0.5 \times 0.5°$ grid in the surface layer (0-10m depth) at the first day of every month during the first year of the simulation (>4 million particles in total) and saved their locations every 2 days. These particles are passively advected by two-dimensional surface currents with the Parcels framework (Delandmeter & Sebille, 2019b). We advected the particles for 40 years in total, by looping the 5 years of available velocity fields. We performed the same analysis with Lagrangian particles in every configuration of Table D.1. We also performed these Lagrangian experiments by releasing particles in the fourth depth layer (30-41m depth) instead of the surface layer (see Appendix C).

### D.1.3 Connectivity timescales

To determine timescales of surface ocean connectivity, we applied an analysis similar to (Jonnson & Watson, 2016). The ocean surface is divided in $2 \times 2°$ patches. Our goal is to find the minimum times that particles can travel between these patches,

because only a very low connection probability is required for plankton to spread from a patch A to another patch B (Hedgecock et al., 2007) . Two types of connection times are considered in this Appendix section (see Fig. D.1).

First, the 'raw' connection time from patch A to B is determined by the shortest time period that a particle released (i.e. created) in A takes to end up in B (i.e. the minimum time over all particles released in A). A lot of particles are required if raw connectivity times are used to determine the shortest possible connection time between all patches in the ocean model simulations, which makes it computationally infeasible to find all shortest possible paths between the patches. However, we can use the raw connectivity times that are computed with the Lagrangian experiment of this Appendix section (and the number of particles that these experiments use), to determine a shorter pathway between patch A and B.

Second, the 'Dijkstra' connection time better represents the shortest possible connectivity between patches (Jonnson & Watson, 2016). Raw connectivity times between patches can be interpreted as a directed network, where nodes represent patches and edges repesent their raw connectivity times (Fig. D.1b). The Dijkstra connectivities between patches are the shortest paths (in time) between nodes in this network, as determined with Dijkstra's shortest path algorithm.

If the Dijkstra algorithm is applied, artificially short connectivity times may emerge over long distances, because a patch may have an artificially short raw connectivity time with its neighbouring patch if a particle is released near the boundary of a patch. Hence, we removed all raw connectivity times below 1 year before applying the Dijkstra algortithm, to limit the effect of including these within-patch crossing times (Jonnson & Watson, 2016). As a result, Dijkstra connectivity times below 1 year are identical to raw connectivity times in this Appendix section.

All model simulations in this Appendix section are similar: POP ocean-only with the same resolution and repetitively forced by the same atmosphere every year. Because the Lagrangian experiment is also the same in every configuration, the applied set-up is ideal to study connectivity differences between these configurations (Table D.1). However, it is possible that additional variability in the atmosphere, which is not present in these simulations (e.g. El Niño Southern Oscillation), changes the absolute connectivity timescales by increasing the number of pathways between patches. Moreover, even with the large number of particles ($>$4 million) used in every experiment, it is possible that shorter connectivity times exist between patches if more particles are used. Therefore, it may be that shorter absolute connectivity times are possible than found in this Appendix section.

## D.2 Timescales of connectivity

The Eocene surface ocean was much better connected compared to the present-day (Fig. D.2). We find a large imprint from upwelling and downwelling areas on the connectivity timescales. In general, the connectivity timescales are short towards and long from downwelling areas where particles accumulate.

D
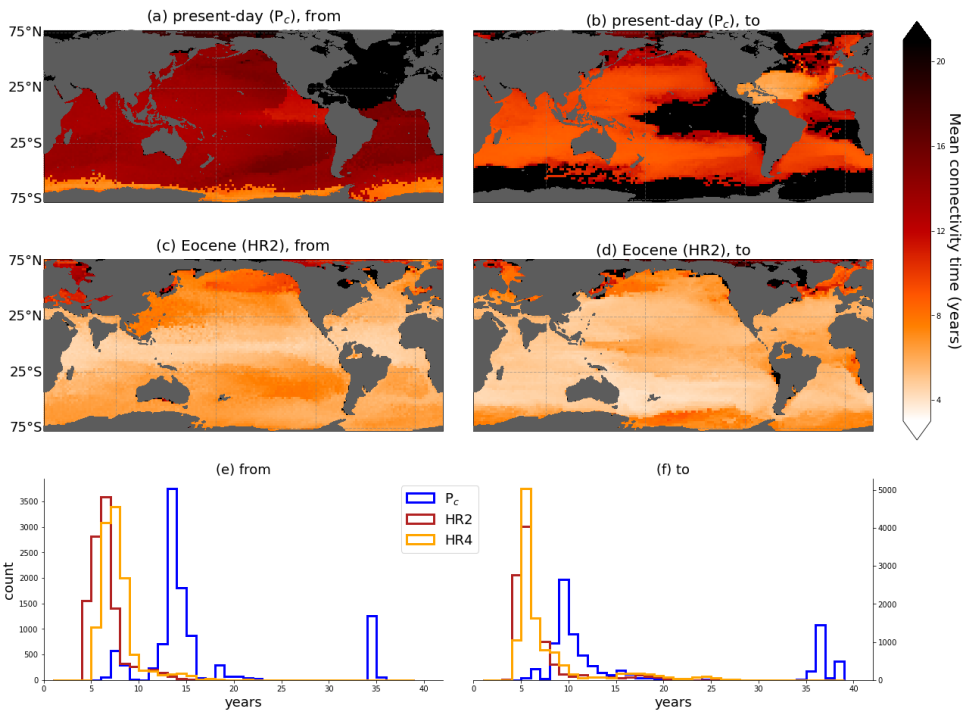


**Figure D.2:** Mean of Dijkstra connectivity times from (left) and towards (right) the $2\times2°$ patches with other patches for (a), (b) the present-day and (c), (d) the Eocene. (e), (f) Histograms of these mean connectivity times from and towards the patches, respectively. If a patch is not reached from another patch, the connectivity time between these patches is set to 40 years (i.e. the total time that particles are advected in this Appendix section).

In the present-day, all particles near Antarctica are transported northward and none towards Antarctica (Fraser et al., 2018). As a consequence, the connectivity time towards the Southern Ocean and Benguala and Peruvian upwelling systems is long (more than 20 years in Fig. D.2). Since the Southern Ocean strongly repells particles, and also because patches within the Southern Ocean are strongly connected due to the eastward circumpolar flow, connectivity times from the Southern Ocean to other parts of the ocean are short. In the Eocene on the other hand, connections towards Antarctica exists, because the ACC is weaker and Antarctica is less isolated compared to the present-day.

The mean connectivity times between the configurations are best summarized in histograms (Fig. D.2e, f). Overall, these histograms clearly show that the surface Eocene ocean is better connected (i.e. on shorter time-scales) compared to the present-day. Particle attracting and repelling areas do not attract or repel particles as strongly in the Eocene as in the present-day, which results in a unimodal distribution of Eocene connectivity times and typically shorter timescales. In the histograms of the present-day configuration however, a peak with relatively short (from) connection times exist (but still longer than in the Eocene) that represents the Southern Ocean and a peak with long connection times exists that represents the North Atlantic. Patches that are located in particle-repelling areas contain on average long connection times (see Fig. D.4d, f; particle distributions are low in particle-repelling areas).

Although the ocean surface is better connected in both configurations of the Eocene (HR2 and HR4; see Table D.1) compared to the present-day ($P_c$), some differences between HR2 and HR4 exist. The HR2 ocean is globally connected on shorter timescales compared to HR4 (Fig. D.2e). This difference cannot be caused by different geographic boundary conditions, as those are identical in the HR2 and HR4 simulations. Hence, the difference must be attributed to properties of the flow, which is dependent on (i) the atmospheric forcing and (ii) the initialisation of the simulation. The surface flow is similar in HR2 and HR4, except for the Kuroshio current in the North Pacific, which is stronger in HR2 than HR4, which is likely due to a different temperature distribution in this area (see chapter 6). As a result, the North Pacific particle accumulation area is stronger in HR4 compared to HR2 (see Fig. D.5), and the HR2 connectivity times are overall shorter from patches in the North Pacific compared to HR4.

The horizontal flow divergence weakens at the near-surface compared to the surface layer (Wichmann et al., 2019). As a consequence, particle-accumulation areas are weaker attractors of particles at deeper layers compared to the surface, and basins become better connected with each other. Hence, we find that connectivity times are generally shorter if particles in the Lagrangian set-up are released in the fourth depth layer (30-41m depth; see Appendix Figs. D.6 and D.7) instead of the surface layer. Connectivity times remain shorter in the Eocene compared to the present-day configurations if particles are released in the fourth depth layer.

## D.3 Supporting figures
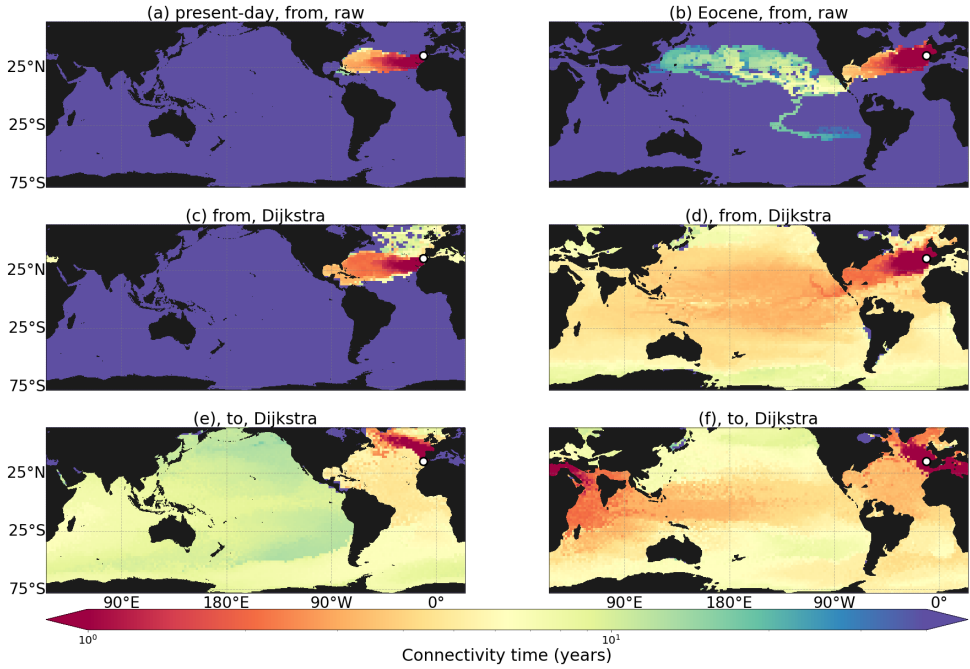


**Figure D.3:** Connectivity from and towards a $2 \times 2°$ patch near the Straigt of Gibraltar (the white dot; 35°N and 6°W) in the present-day (left; $P_c$) and the Eocene (right; HR2). (a), (b) The raw connectivity time from the patch. (c), (d) The Dijkstra connectivity time from the patch. (e), (f) The Dijkstra connectivity time towards the patch. Note that the colormap is logarithmic from 1 to 40 years.

D
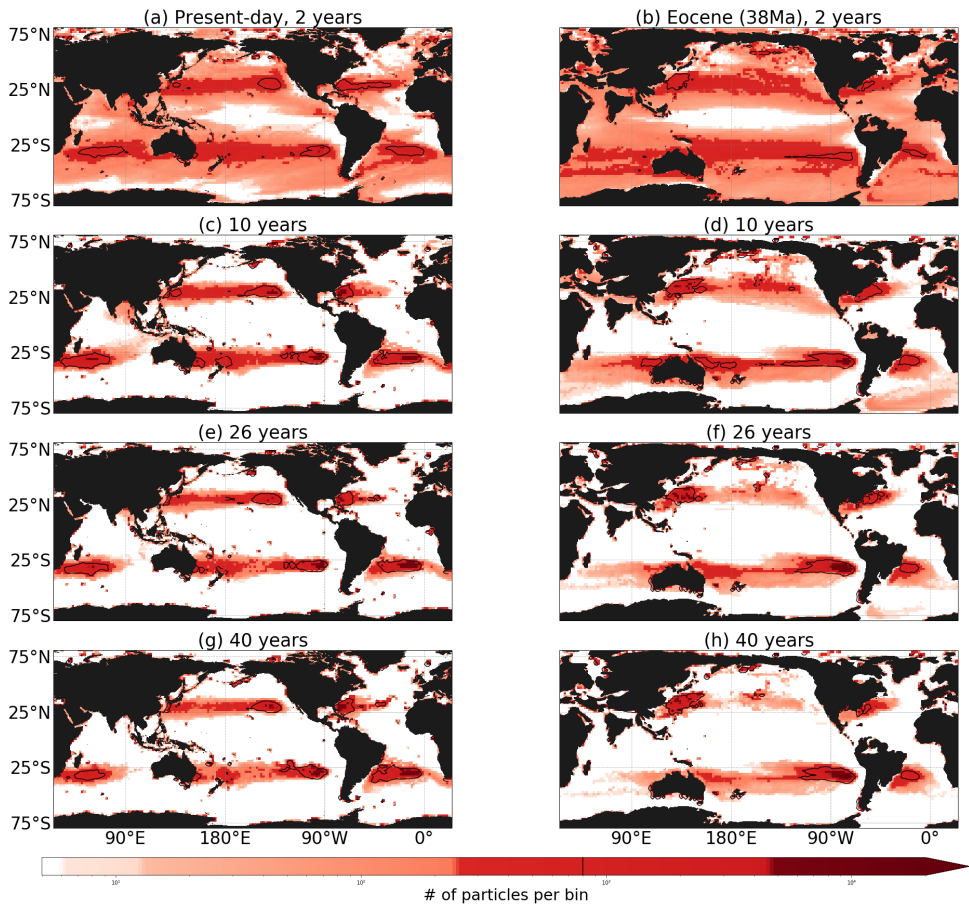


**Figure D.4:** Particle distributions in the present-day ($P_c$; left) and the Eocene (HR2; right) after (a), (b) 2 years, (c), (d) 10 years, (e), (f) 26 years and (g), (h) 40 years of simulation.

D
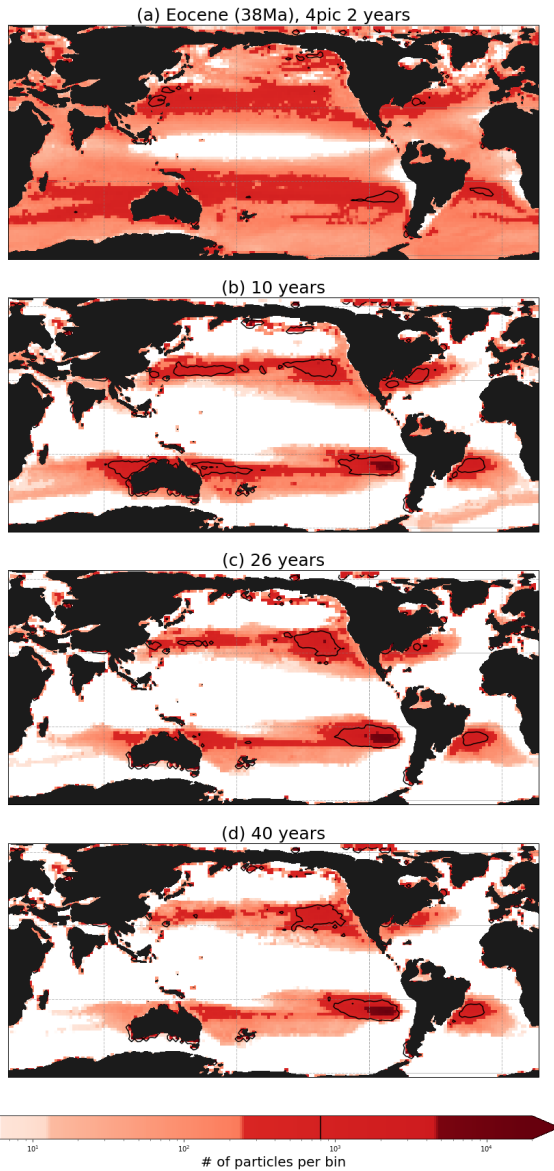


**Figure D.5:** (a)-(d) Same as Figure D.4b, d, f, h respectively, but for the 4× instead of 2×pre-industrial atmospheric $CO_2$ case (i.e. HR4 instead of HR2).

D
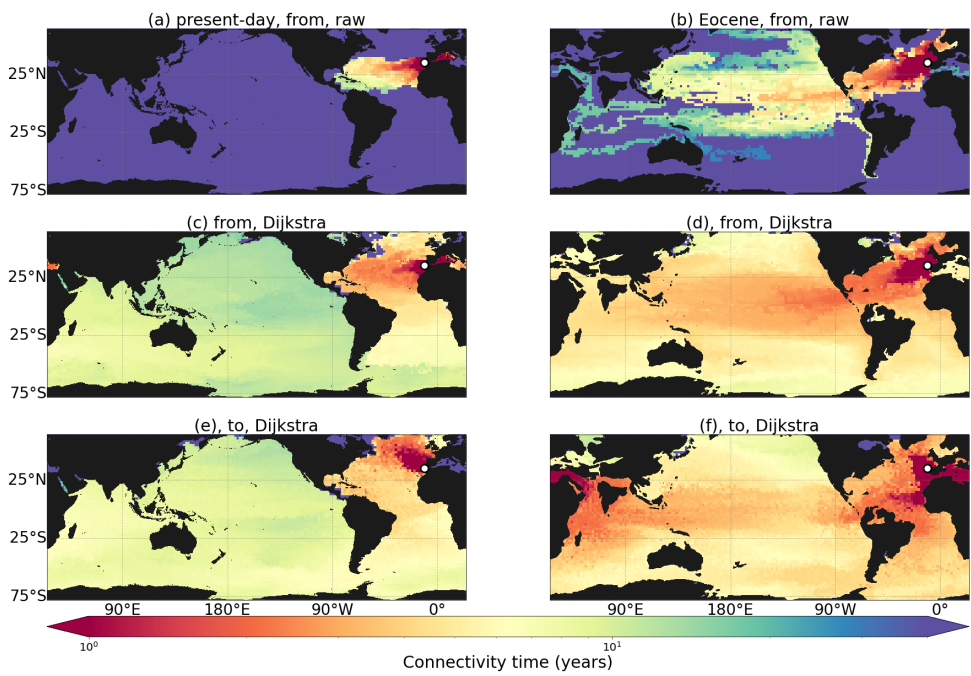


**Figure D.6:** (a)-(d) Same as Figure D.3, but if particles are released in the fourth depth layer (~35m depth) instead of the surface layer.

D
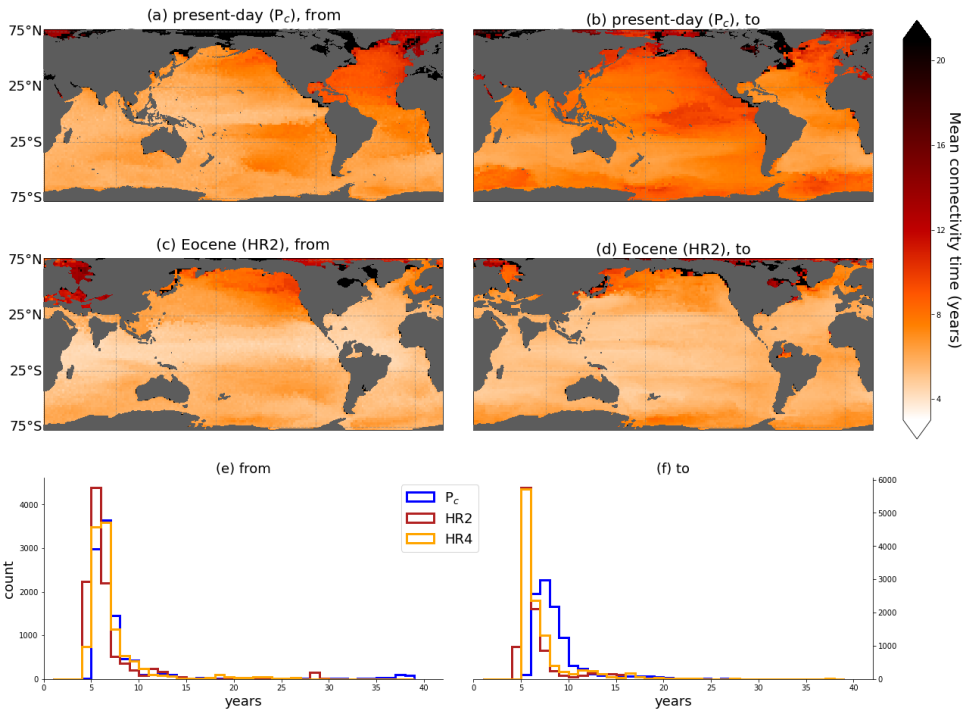


**Figure D.7:** (a)-(d) Same as Figure D.2, but if particles are released in the fourth depth layer (∼35m depth) instead of the surface layer.

# Bibliography

Ajayi, A. et al. **(2020)**, "Spatial and Temporal Variability of the North Atlantic Eddy Field From Two Kilometric-Resolution Ocean Models", *J. Geophys. Res. Ocean.* Vol. 125, no. 5.

Alldredge, A. L., U Passow & S. H. D. Haddock **(1998)**, "The characteristics and transparent exopolymer particle (TEP) content of marine snow formed from the-cate dinoflagellates", *J. Plankt. Res.* Vol. 20, no. 3, pp. 393–406.

Alldredge, A. L. & K. M. Crocker **(1995)**, "Why do sinking mucilage aggregates accumulate in the water column?", *Sci. Total Environ.* Vol. 165, pp. 15–22.

Alldredge, A. L. & C. Gotschalk **(1988)**, "In situ settling behavior of marine snow", *Limnol. Ocean.* Vol. 33, no. 3.

Alldredge, A. L. & M. W. Silver **(1988)**, "Characteristics , Dynamics and Significance of Marine Snow", *Prog. Ocean.* Vol. 20, pp. 41–82.

Alonso-González, I. J. et al. **(2010)**, "Role of slowly settling particles in the ocean carbon cycle", *Geophys. Res. Lett.* Vol. 37, pp. 1–5.

Anagnostou, E. et al. **(2016)**, "Changing atmospheric CO2 concentration was the primary driver of early Cenozoic climate", *Nature*, vol. 533, no. 7603, pp. 380–384.

Anderson, D. M., J. J. Lively, E. M. Reardon & C. A. Price **(1985)**, "Sinking characteristics of dinoflagellate cysts", *Limnol. Ocean.* Vol. 30, no. 5, pp. 1000–1009.

Ankerst, M., M. M. Breunig, H.-p. Kriegel & J. Sander **(1999)**, "OPTICS: Ordering Points to Identify the Clustering Structure OPTICS", *SCM Sigmod Rec.*

Armstrong, R. A., M. L. Peterson, C. Lee & S. G. Wakeham **(2009)**, "Settling velocity spectra and the ballast ratio hypothesis", *Deep. Res. II*, vol. 56, pp. 1470–1478.

Arzel, O., M. H. England & O. A. Saenko **(2011)**, "The Impact of Wind Stress Feedback on the Stability of the Atlantic Meridional Overturning Circulation", *J. Clim.* Vol. 24, pp. 1965–1984.

Asper, V. **(1987)**, "Measuring the flux and sinking speed of marine snow aggregates", *Deep. Res.* Vol. 34, no. 1, pp. 1–17.

Aumont, O & L Bopp **(2006)**, "Globalizing results from ocean in situ iron fertilization studies", *Glob. Biogeochem. Cycles*, vol. 20, no. January, pp. 1–15.

Aumont, O, C Ethé, A Tagliabue, L Bopp & M Gehlen **(2015)**, "PISCES-v2: An ocean biogeochemical model for carbon and ecosystem studies", *Geosci. Model Dev.* Vol. 8, no. 8, pp. 2465–2513.

Azetsu-Scott, K. & B. D. Johnson **(1991)**, "Measuring physical characteristics of particles: a new method of simultaneous measurement for size, settling velocity and density of constituent matter", *Deep. Res.* Vol. 39, no. 6, pp. 1057–1066.

Azetsu-Scott, K. & U. Passow **(2004)**, "Ascending marine particles: Significance of transparent exopolymer particles (TEP) in the upper ocean", *Limnol. Ocean.* Vol. 49, no. 3, pp. 741–748.

Baatsen, M. L. J., A. S.V. D. Heydt, M Kliphuis, J Viebahn & H. A. Dijkstra **(2018a)**, "Multiple states in the late Eocene ocean circulation", *Glob. Planet. Chang.* Vol. 163, no. June 2017, pp. 18–28.

Baatsen, M. L. J., A. S. **von der** Heydt, M Kliphuis, J Viebahn & H. A. Dijkstra **(2018b)**, "Multiple states in the late Eocene ocean circulation", *Glob. Planet. Chang.* Vol. 163, no. February, pp. 18–28.

Baatsen, M. **(2018)**, "The Middle-to-late Eocene Greenhouse Climate", PhD thesis, Utrecht University, p. 223, ISBN: 9789039370872.

Baatsen, M. et al. **(2016)**, "Reconstructing geographical boundary conditions for palaeoclimate modelling during the Cenozoic", *Clim. Past*, vol. 12, no. 8, pp. 1635–1644.

Baatsen, M. et al. **(2020)**, "The middle to late Eocene greenhouse climate modelled using the CESM 1.0.5", *Clim. Paste*, vol. 16, pp. 2573–2597.

Bach, L. T., T Boxhammer, A Larsen, N Hildebrandt, K. G. Schulz & U Riebesell **(2016)**, "Influence of plankton community structure on the sinking velocity of marine aggregates", *Glob. Biogeochem. Cycles*, vol. 30, no. 8, pp. 1145–1165.

Bach, L. T., U. Riebesell, S. Sett, S. Febiri, P. Rzepka & K. G. Schulz **(2012)**, "An approach for particle sinking velocity measurements in the 3-400 micrometer size range and considerations on the effect of temperature on sinking rates", *Mar. Biol.* Vol. 159, pp. 1853–1864.

Beerling, D. J. & D. L. Royer **(2011)**, "Convergent Cenozoic CO2 history", *Nat. Geosci.* Vol. 4, no. 7, pp. 418–420.

Berelson, W. M. **(2002)**, "Particle settling rates increase with depth in the ocean", *Deep. Res. II*, vol. 49, pp. 237–251.

Berloff, P, A. Hogg & W Dewar **(2007)**, "The Turbulent Oscillator: A Mechanism of Low-Frequency Variability of the Wind-Driven Ocean Gyres", *Am. Meteorol. Soc.* Vol. 37, pp. 2363–2386.

Bettencourt, J. H., C. López & E. Hernández-garcía **(2012)**, "Oceanic three-dimensional Lagrangian coherent structures: A study of a mesoscale eddy in the Benguela upwelling region", *Ocean Model.* Vol. 51, pp. 73–83.

Bettencourt, J. H. et al. **(2015)**, "Boundaries of the Peruvian oxygen minimum zone shaped by coherent mesoscale dynamics", *Nat. Geosci.* Vol. 8, no. November.

Bijl, P. K. et al. **(2013)**, "Eocene cooling linked to early flow across the Tasmanian Gateway", *Proc. Natl. Acad. Sci.* Vol. 110, no. 24, pp. 9645–9650.

Bijl, P. K. et al. **(2011)**, "Environmental forcings of Paleogene Southern Ocean dinoflagellate biogeography", *Paleoceanography*, vol. 26, pp. 1–12.

Bijl, P. K. et al. **(2018)**, "Paleoceanography and ice sheet variability offshore Wilkes Land, Antarctica - Part 2: Insights from Oligocene-Miocene dinoflagellate cyst assemblages", *Clim. Past*, vol. 14, no. 7, pp. 1015–1033.

Bijl, P., J. Frieling, M. Cramwinckel, C. Boschman, A. Sluijs & F. Peterse **(2021)**, "Maastrichtian-Rupelian paleoclimates in the southwest Pacific a critical eval-

uation of biomarker paleothermometry and dinoflagellate cyst paleoecology at Ocean Drilling Program Site 1172", *Clim. Past Discuss.* No. March, p. 6.

Boltovskoy, E., D. B. Op & F. Brandini **(2000)**, "Planktonic Foraminifera from south-western Atlantic epipelagic waters: abundance , distribution and year-to-year variations", *J. Mar. Biol. Assoc. United Kingdom79*, vol. 79, pp. 203–213.

Bower, A. et al. **(2019)**, "Lagrangian Views of the Pathways of the Atlantic Meridional Overturning Circulation", *J. Geophys. Res. Ocean.* Pp. 5313–5335.

Box, G. E. **(1976)**, "Science and statistics", *J. Am. Stat. Assoc.* Vol. 71, no. 356, pp. 791–799.

Boyd, P. W., C. Herve, M. Levy, D. A. Siegel & T. Weber **(2019)**, "Multi-faceted particle pumps drive carbon sequestration in the ocean", *Nature*, vol. 568, pp. 327–335.

Braak, C. J.F. F. & P. F.M. M. Verdonkschot **(1995)**, "Canonical correspondence analysis and related multivariate methods in aquatic ecology", *Aquat. Sci.* Vol. 57, no. 3, pp. 255–289.

Bracco, A., J. Choi, J. Kurian & P. Chang **(2018)**, "Vertical and horizontal resolution dependency in the model representation of tracer dispersion along the continental slope in the northern Gulf of Mexico", *Ocean Model.* Vol. 122, no. December 2017, pp. 13–25.

Braconnot, P. et al. **(2012)**, "Evaluation of climate models using palaeoclimatic data", *Nat. Clim. Chang.*

Brassell, S. C., G Eglinton, I. T. Marlowe, U Pflaumannt & M Sarntheint **(1986)**, "Molecular stratigraphy: a new tool for climatic assessment", *Nature*, vol. 320, pp. 129–133.

Bravo, I. & R. Figueroa **(2014)**, "Towards an Ecological Understanding of Dinoflagellate Cyst Functions", *Microorganisms*, vol. 2, no. 1, pp. 11–32.

Briggs, N. et al. **(2011)**, "High-resolution observations of aggregate flux during a sub-polar North Atlantic spring bloom", *Deep. Res. 1*, vol. 58, pp. 1031–1039.

Bringué, M., R. C. Thunell, V. Pospelova, J. L. Pinckney, O. E. Romero & E. J. Tappa **(2018)**, "Physico-chemical and biological factors influencing dinoflagellate cyst production in the Cariaco Basin", *Biogeosciences*, vol. 15, pp. 2325–2348.

Bringué, M., V. Pospelova, E. J. Tappa & R. C. Thunell **(2019)**, "Progress in Oceanography Dinoflagellate cyst production in the Cariaco Basin: A 12.5 year-long sediment trap study", *Prog. Ocean.* Vol. 171, no. July 2018, pp. 175–211.

Buesseler, K. O. et al. **(2007)**, "An assessment of the use of sediment traps for estimating upper ocean particle fluxes", pp. 345–416.

Burd, A. B. & G. A. Jackson **(2009)**, "Particle Aggregation", *Ann. Rev. Mar. Sci.* Vol. 1, no. 1, pp. 65–90.

Burke, K. D., J. W. Williams, M. A. Chandler, A. M. Haywood, D. J. Lunt & B. L. Otto-bliesner **(2018)**, "Pliocene and Eocene provide best analogs for near- future climates", *Proc. Natl. Acad. Sci.* Vol. 115, no. 52.

Canals, M. et al. **(2020)**, "The quest for seafloor macrolitter: A critical review of background knowledge, current methods and future prospects", *Environ. Res. Lett.*

Carpaij, O. A. **(2020)**, "Novel views on endotyping asthma, its remission, and COPD its remission, and COPD", PhD thesis, Rijksuniversiteit Groningen, ISBN: 9789463755863.

Chang, H., H. S. Huntley, A. D. K. Jr, B. L. L. Jr & M. H. M. Sulman **(2018)**, "Transport structures in a 3D periodic flow", *Commun. Nonlinear Sci. Numer. Simul.* Vol. 61, pp. 84–103.

Chassignet, E. P. & X. Xu **(2021)**, "On the Importance of High-Resolution in Large-Scale Ocean Models", vol. 38, no. October, pp. 1621–1634.

Chassignet, E. P. et al. **(2020)**, "Impact of horizontal resolution on global ocean-sea ice model simulations based on the experimental protocols of the Ocean Model Intercomparison Project phase 2 (OMIP-2)", *Geosci. Model Dev.* Vol. 13, no. 9, pp. 4595–4637.

Chen, M., Q. Ma, L. Guo, Y. Qiu, Y. Li & W. Yang **(2012)**, "Importance of lateral transport processes to Chukchi Sea during summer 2003", *Deep. Res. Part II*, vol. 81-84, pp. 53–62.

Chi, L., C. L. P. Wolfe & S. Hameed **(2018)**, "Intercomparison of the Gulf Stream in ocean reanalyses: 1993-2010", vol. 125, no. January, pp. 1–21.

Church, J. A. et al. **(2013)**, "Sea level change", in: *Clim. Chang. 2013 Phys. Sci. Basis Work. Gr. I Contrib. to Fifth Assess. Rep. Intergov. Panel Clim. Chang.* Cambridge University Press, Cambridge, United Kingdom and New York, NY, USA, pp. 1137–1216, ISBN: 9780128130810.

Clarke, K. R. **(1993)**, "Non-parametric multivariate analyses of changes in community structure", *Aust. J. Ecol.* Vol. 18, no. 1988, pp. 117–143.

Coachman, L. K. & K Aagaard **(1988)**, "Transports Through Bering Strait' Annual and Interannual Variability", *J. Geophys. Res.* Vol. 93, no. 3, pp. 535–539.

Collins, M. et al. **(2013)**, "Long-term climate change: Projections, commitments and irreversibility", in: *Clim. Chang. 2013 Phys. Sci. Basis Work. Gr. I Contrib. to Fifth Assess. Rep. Intergov. Panel Clim. Chang.* Cambridge University Press, Cambridge, United Kingdom and New York, NY, USA, chap. 12, pp. 1029–1136, ISBN: 9781107415324.

Commission, I. O. **(2010)**, *The international thermodynamic equation of seawater - 2010: Calculation and use of thermodynamic properties*, Manuals an, UNESCO (English).

Cook, T. M. **(2010)**, *Paleoclimate: Understanding Climate Change Past and Present*, New York Chichester: Columbia University Press, p. 1920.

Cram, J. A., T. Weber, S. W. Leung, J.-h. Liang & C. Deutsch **(2018)**, "Global Biogeochemical Cycles The Role of Particle Size , Ballast , Temperature , and Oxygen in the Sinking Flux to the Deep Sea", *Glob. Biogeochem. Cycles*, vol. 32, pp. 858–876.

Cramwinckel, M. J. et al. **(2018)**, "Synchronous tropical and polar temperature evolution in the Eocene", *Nature*, vol. 559, pp. 382–386.

Cramwinckel, M. J. et al. **(2019)**, "Harmful algae and export production collapse in the equatorial Atlantic during the zenith of Middle Eocene Climatic Optimum warmth.", *Geology*, vol. 47, no. 3.

Cramwinckel, M. J. et al. **(2020)**, "Surface-circulation change in the southwest Pacific Ocean across the Middle Eocene Climatic Optimum: inferences from dinoflagellate cysts and biomarker paleothermometry", *Clim. Past*, vol. 16, pp. 1667–1689.

Crouch, E. M., D. C. Mildenhall & H. L. Neil **(2010)**, "Distribution of organic-walled marine and terrestrial palynomorphs in surface sediments, offshore eastern New Zealand", *Mar. Geol.* Vol. 270, no. 1-4, pp. 235–256.

Crouch, E. M., P. S. Willumsen, D. K. Kulhanek & S. J. Gibbs **(2014)**, "A revised Paleocene (Teurian) dinoflagellate cyst zonation from eastern New Zealand", *Rev. Palaeobot. Palynol.* Vol. 202, pp. 47–79.

Dale **(1996)**, "Palynology principles and applications", in: *Palynol. Princ. Appl.* Chap. 31, pp. 1249–1275, ISBN: 0931871034.

Dale, B. **(1976)**, "Cyst formation, sedimentation, and preservation: Factors affecting dinoflagellate assemblages in recent sediments from trondheimsfjord, Norway", *Rev. Palaeobot. Palynol.* Vol. 22, no. 1, pp. 39–60.

Dale, B., A. L. Dale & J. H. F. Jansen **(2002)**, "Dinoflagellate cysts as environmental indicators in surface sediments from the Congo deep-sea fan and adjacent regions", *Palaeoecology*, vol. 0182, no. June 2018, pp. 309–338.

Dämmer, L. K., L. **de** Nooijer, E. **van** Sebille, J. G. Haak & G. J. Reichart **(2020)**, "Evaluation of oxygen isotopes and trace elements in planktonic foraminifera from the Mediterranean Sea as recorders of seawater oxygen isotopes and salinity", *Clim. Past*, vol. 16, no. 6, pp. 2401–2414.

Danilov, S **(2012)**, "Two finite-volume unstructured mesh models for large-scale ocean modeling", *Ocean Model.* Vol. 47, pp. 14–25.

Datema, M., F. Sangiorgi, A. **de** Vernal, G. J. Reichart, L. J. Lourens & A. Sluijs **(2017)**, "Comparison of qualitative and quantitative dinoflagellate cyst approaches in reconstructing glacial-interglacial climate variability at West Iberian Margin IODP 'shackleton' Site U1385", *Mar. Micropaleontol.* Vol. 136, no. May 2016, pp. 14–29.

De Schepper, S., E. I. Fischer, J. Groeneveld, M. J. Head & J. Matthiessen **(2011)**, "Deciphering the palaeoecology of Late Pliocene and Early Pleistocene dinoflagellate cysts", *Palaeogeogr. Palaeoclim. Palaeoecol.* Vol. 309, no. 1-2, pp. 17–32.

DeConto, R. M. & D. Pollard **(2003)**, "Rapid Cenozoic glaciation of Antarctica induced by declining atmospheric CO2", *Nature*, vol. 421, no. 6920, pp. 245–249.

Delandmeter, P. & E. **van** Sebille **(2019a)**, "The Parcels v2.0 Lagrangian framework: new field interpolation schemes", *Geosci. Model Dev. Discuss.* No. January, pp. 1–24.

Delandmeter, P. & E. **van** Sebille **(2019b)**, "The Parcels v2.0 Lagrangian framework: new field interpolation schemes", *Geosci. Model Dev.* Vol. 12, pp. 3571–3584.

Delworth, T. L. et al. **(2012)**, "Simulated Climate and Climate Change in the GFDL CM2.5 High-Resolution Coupled Climate Model", *J. Clim.* Pp. 2755–2781.

Devries, T. & T. Weber **(2017)**, "The export and fate of organic matter in the ocean : New constraints from combining satellite and oceanographic tracer observations", *Glob. Biogeochem. Cycles*, vol. 31, pp. 535–555.

Diercks, A. R. & V. L. Asper **(1997)**, "In situ settling speeds of marine snow aggregates below the mixed layer: Black Sea and Gulf of Mexico", *Deep. Res. 1*, vol. 44, no. 3.

Dong, C., J. C. McWilliams, Y. Liu & D. Chen **(2014)**, "Global heat and salt transports by eddy movement", *Nat. Commun.* Vol. 5, p. 3294.

Döös, K, J Nycander & A. C. Coward **(2008)**, "Lagrangian decomposition of the Deacon Cell", *J. Geophys. Res.* Vol. 113, pp. 1–13.

Döös, K., V. Rupolo & L. Brodeau **(2011)**, "Dispersion of surface drifters and model-simulated trajectories", *Ocean Model.* Vol. 39, pp. 301–310.

Dowsett, H. J. et al. **(2012)**, "Assessing confidence in Pliocene sea surface temperatures to evaluate predictive models", *Nat. Clim. Chang.* Vol. 2, no. May, pp. 365–371.

Dowsett, H. J. et al. **(2013)**, "Sea Surface Temperature of the mid-Piacenzian Ocean: A data-model comparison", *Sci. Rep.* Vol. 3, pp. 1–8.

Drake, H. F., A. K. Morrison, S. M. Griffies, J. L. Sarmiento, W. Weijer & A. R. Gray **(2018)**, "Lagrangian Timescales of Southern Ocean Upwelling in a Hierarchy of Model Resolutions", *Geophys. Res. Lett.* Vol. 45, pp. 891–898.

Drótos, G., P. Monroy, E. Hernández-garcía & C. López **(2019)**, "Inhomogeneities and caustics in the sedimentation of noninertial particles in incompressible flows", *Chaos*, vol. 013115, no. January.

Dufour, C. O. et al. **(2015)**, "Role of Mesoscale Eddies in Cross-Frontal Transport of Heat and Biogeochemical Tracers in the Southern Ocean", *J. Phys. Ocean.* Vol. 45, pp. 3057–3081.

Durkin, C. A., M. L. Estapa & K. O. Buesseler **(2015)**, "Observations of carbon export by small sinking particles in the upper mesopelagic", *Mar. Chem.* Vol. 175, pp. 72–81.

Eaton, J. K. & J. R. Fessler **(1994)**, "Preferential concentration of particles by turbulence", *Int. J. Multiph. Flow*, vol. 20, no. 94, pp. 169–209.

Elfasakhany, A & X. S. Bai **(2019)**, "Numerical and experimental studies of irregular-shape biomass particle motions in turbulent flows", *Eng. Sci. Technol. an Int. J.* Vol. 22, no. 1, pp. 249–265.

Elsworth, G., E. Galbraith, G. Halverson & S. Yang **(2017)**, "Enhanced weathering and CO2 drawdown caused by latest Eocene strengthening of the Atlantic meridional overturning circulation", *Nat. Geosci.* Vol. 10, no. January, pp. 213–216.

Epstein, S, R Buchsbaum, H. A. Lowenstam & H. C. Urey **(1953)**, "Revised carbonate-water isotopic temperature scale", *Geol. Soc. Am. Bull.* Vol. 11, pp. 1315–1326.

Esper, O. & K. A. F. Zonneveld **(2007)**, "The potential of organic-walled dinoflagellate cysts for the reconstruction of past sea-surface conditions in the Southern Ocean", *Mar. Micropaleontol.* Vol. 65, no. 3-4, pp. 185–212.

Ester, M., H.-P. Kriegel, J. Sander & X. Xu **(1996)**, "A Density-Based Algorithm for Discovering Clusters in Large Spatial Databases with Noise", *KDD*, vol. 96.

Evitt, W. R. **(1985)**, *Sporopollenin Dinoflagellate Cysts. Their Morphology and Interpretation*, Dallas: American Association of Stratigrafic Palynologists Foundation, p. 333.

Eynaud, F, J Giraudeau, J. J. Pichon & C. J. Pudsey **(1999)**, "Sea-surface distribution of coccolithophores, diatoms, silicoflagellates and dinoflagellates in the South Atlantic Ocean during the late austral summer 1995", *Deep. Res.* Vol. 46, pp. 451–482.

Eyring, V. et al. **(2019)**, "Taking climate model evaluation to the next level", *Nat. Clim. Chang.* Vol. 9, no. February.

Fahl, K. & E.-m. Nöthing **(2007)**, "Lithogenic and biogenic particle fluxes on the Lomonosov Ridge (central Arctic Ocean) and their relevance for sediment accumulation: Vertical vs . lateral transport", *Deep. Res. Part 1*, vol. 54, pp. 1256–1272.

Fasullo, J. T. & K. E. Trenberth **(2008)**, "The annual cycle of the energy budget. Part II: Meridional structures and poleward transports", *J. Clim.* Vol. 21, no. 10, pp. 2313–2325.

Fenchel, T. **(2001)**, "How Dinoflagellates Swim", *Protist*, vol. 152, no. December, pp. 329–338.

Fenton, I. S., P. N. Pearson, T. D. Jones & A. Purvis **(2016)**, "Environmental Predictors of Diversity in Recent Planktonic Foraminifera as Recorded in Marine Sediments", *PLoS One*, vol. 11, no. 11, pp. 1–22.

Fischer, G & G Karakas **(2009)**, "Sinking rates and ballast composition of particles in the Atlantic Ocean: implications for the organic carbon fluxes to the deep ocean", *Biogeosciences*, vol. 6, pp. 85–102.

Fischer, J., J. Karstensen, M. Oltmanns & S. Schmidtko **(2018)**, "Mean circulation and EKE distribution in the Labrador Sea Water level of the subpolar North Atlantic", *Ocean Sci.* Vol. 14, pp. 1167–1183.

Flamary, R. & N. Courty **(2017)**, *POT Python Optimal Transport library*.

Fouss, F., M. Saerens & M. Shimbo **(2016)**, "Classical Multidimensional Scaling: Basic Notions", in: *Algorithms Model. Netw. Data Link Anal.* Cambridge University Press, chap. 10.3.

Fowler, S. W. & L. F. Small **(1971)**, "Sinking rates of Euphausiid fecal pellets", *Limnol. Ocean.* Vol. 17, pp. 293–296.

Fox-Kemper, B. et al. **(2019)**, "Challenges and Prospects in Ocean Circulation Models", *Front. Mar. Sci.* Vol. 6, no. February, pp. 1–29.

Fraser, C. I. et al. **(2018)**, "Antarctica's ecological isolation will be broken by storm-driven dispersal and warming", *Nat. Clim. Chang.* Vol. 8, no. August.

Fratantoni, D. M. **(2001)**, "North Atlantic surface circulation during the 1990's observed with satellite-tracked drifters", *J. Geophys.* Vol. 106.

Frenger, I., M. Münnich & N. Gruber **(2018)**, "Imprint of Southern Ocean mesoscale eddies on chlorophyll", pp. 4781–4798.

Frieling, J. & A. Sluijs **(2018)**, "Towards quantitative environmental reconstructions from ancient non-analogue microfossil assemblages: Ecological preferences of Paleocene-Eocene dinoflagellates", *Earth-Science Rev.* Vol. 185, no. May, pp. 956–973.

Froyland, G., K. Padberg, M. H. England & A. M. Treguier **(2007)**, "Detection of Coherent Oceanic Structures via Transfer Operators", *Phys. Rev. Lett.* Vol. 224503, no. June, pp. 1–4.

Froyland, G., R. M. Stuart & E. **van** Sebille **(2014)**, "How well-connected is the surface of the global ocean?", *Chaos*, vol. 24, pp. 0–10.

Fuente, R. **de la**, G. Drótos, E. Hernández-García, C. López & E. **van** Sebille **(2021)**, "Sinking microplastics in the water column: simulations in the Mediterranean Sea", *Ocean Sci.* Vol. 17, pp. 431–453.

Furbish, D. J. & A. J. Arnold **(1997)**, "Hydrodynamic strategies in the morphological evolution of spinose planktonic foraminifera", *GSA Bull.* Vol. 109, no. 8, pp. 1055–1072.

Garcia, H. E. et al. **(2013)**, "NOAA Atlas NESDIS 76", *WORLD Ocean ATLAS 2013*, vol. 4, no. September.

Gasson, E et al. **(2014)**, "Uncertainties in the modelled CO2 threshold for Antarctic glaciation", *Clim. Past*, vol. 10, pp. 451–466.

Gebbie, G. & P. Huybers **(2011)**, "How is the ocean filled?", *Geophys. Res. Lett.* Vol. 38, no. February, pp. 1–5.

Gent, P. R. **(2011)**, "The Gent-McWilliams parameterization: 20/20 hindsight", *Ocean Model.* Vol. 39, pp. 2–9.

Gent, P. R. **(2018)**, "A commentary on the Atlantic meridional overturning circulation stability in climate models", *Ocean Model.* Vol. 122, no. June 2017, pp. 57–66.

Gent, P. R. & J. C. McWilliams **(1990)**, "Isopycnal mixing in ocean circulation models", *J. Phys. Ocean.* Vol. 20, pp. 150–155.

Gill, A. E. **(1983)**, "Instabilities, fronts and the general circulation", in: *Atmos. Dyn.* Ed. by Donn, W. L., San Diego: Acadamic press, chap. 13.

Goldner, A, N Herold & M Huber **(2014)**, "Antarctic glaciation caused ocean circulation changes at the Eocene-Oligocene transition", *Nature*, vol. 511, no. 7511, pp. 574–577.

Gräwe, U. **(2011)**, "Implementation of high-order particle-tracking schemes in a water column model", *Ocean Model.* Vol. 36, no. 1-2, pp. 80–89.

Griffies, S. R. et al. **(2015)**, "Impacts on Ocean Heat from Transient Mesoscale Eddies in a Hierarchy of Climate Models", *J. Clim.* Vol. 28, pp. 952–977.

Hallberg, R. **(2013)**, "Using a resolution function to regulate parameterizations of oceanic mesoscale eddy effects", *Ocean Model.* Vol. 72, pp. 92–103.

Hardesty, B. D. et al. **(2017)**, "Using Numerical Model Simulations to Improve the Understanding of Micro-plastic Distribution and Pathways in the Marine Environment", *Front. Mar. Sci.* Vol. 4, no. March, pp. 1–9.

Harland, R. & C. J. Pudsey **(1999)**, "Dinoflagellate cysts from sediment traps deployed in the Bellingshausen, Weddell and Scotia seas , Antarctica", *Mar. Micropaleontol.* Vol. 37, pp. 77–99.

Harrison, S. P., P. J. Bartlein & I. C. Prentice **(2016)**, "What have we learnt from palaeoclimate simulations?", *J. Quat. Sci.* Vol. 31, pp. 363–385.

Hartman, J. D., P. K. Bijl & F. Sangiorgi **(2018)**, "A review of the ecological affinities of marine organic microfossils from a Holocene record offshore of Adélie Land (East Antarctica)", *J. Micropalaeontology*, vol. 37, no. 2, pp. 445–497.

Hawkins, E et al. **(2011)**, "Bistability of the Atlantic overturning circulation in a global climate model and links to ocean freshwater transport", *Geophys. Res. Lett.* Vol. 38, pp. 1–6.

Haywood, A. M. et al. **(2013)**, "Large-scale features of Pliocene climate: results from the Pliocene Model Intercomparison Project", *Clim. Past*, vol. 9, pp. 191–209.

Haywood, A. M. et al. **(2019)**, "What can Palaeoclimate Modelling do for you?", *Earth Syst. Environ.* Vol. 3, no. 1, pp. 1–18.

Hecht, M. W. & R. D. Smith **(2013)**, "A Review of North Atlantic Ocean Modeling in an Eddying Regime", *Geophys. Monogr. Ser.* Vol. 177, pp. 108–109.

Hedgecock, D., P. H. Barber & S. Edmands **(2007)**, "Genetic approaches to measuring connectivity", *Oceanography*, vol. 20, pp. 70–79.

Heiskanen, A. S. **(1993)**, "Mass encystment and sinking of dinoflagellates during a spring bloom", *Mar. Biol.* Vol. 116, pp. 161–167.

Hellweger, F. L. **(2014)**, "Biogeographic patterns in ocean microbes emerge in a natural agent-based model", *Science*, vol. 345, no. 1346.

Henson, S. **(2019)**, "Drivers of Carbon Export Efficiency in the Global Ocean", *Glob. Biogeochem. Cycles*, vol. 33, pp. 891–903.

Hewitt, H. T. et al. **(2016)**, "The impact of resolving the Rossby radius at mid-latitudes in the ocean: results from a high-resolution version of the Met Office GC2 coupled model", *Geosci. Model Dev.* Pp. 3655–3670.

Hewitt, H. T. et al. **(2020)**, "Resolving and Parameterising the Ocean Mesoscale in Earth System Models", *Curr. Clim. Chang. Reports*, vol. 6, no. 4, pp. 137–152.

Hill, D. J. et al. **(2013)**, "Paleogeographic controls on the onset of the Antarctic circumpolar current", *Geophys. Res. Lett.* Vol. 40, no. 19, pp. 5199–5204.

Hinsbergen, D. J. J. **van** et al. **(2015)**, "A Paleolatitude Calculator for Paleoclimate Studies", *PLoS One*, vol. 10, no. 6, pp. 1–21.

Hirschi, J. J. M. et al. **(2020)**, "The Atlantic Meridional Overturning Circulation in High-Resolution Models", *J. Geophys. Res. Ocean.* Pp. 1–35.

Hohmann, S., M. Kucera & A. D. Vernal **(2019)**, "Identifying the signature of sea-surface properties in dinocyst assemblages: Implications for quantitative palaeoceanographical reconstructions by transfer functions and analogue techniques", *Mar. Micropaleontol.* No. December.

Holland, D. M. **(2001)**, "Explaining the Weddell Polynya - a Large Ocean Eddy Shed at Maud Rise", *Science*, vol. 292, no. June, pp. 1697–1701.

Holland, W. R. **(1978)**, "The role of mesoscale eddies in the general circulation of the ocean - Numerical experiments using a wind-driven quasi-geostrophic model", *Am. Meteorol. Soc.* Vol. 8, pp. 363–392.

Hollis, C. J. et al. **(2019)**, "The DeepMIP contribution to PMIP4: Methodologies for selection, compilation and analysis of latest Paleocene and early Eocene climate proxy data, incorporating version 0.1 of the DeepMIP database", *Geosci. Model Dev.* Vol. 12, no. 7, pp. 3149–3206.

Honjo, S. **(1996)**, "Fluxes of particles to the interior of the open oceans", in: *Part. flux Ocean*, ed. by Ittekot, V, Schafer, P, Honjo, S & Depetris, P, New York: John Wiley and Sons, pp. 91–154.

Honjo, S., D. W. Spencer & J. W. Farrington **(1982)**, "Deep Advective Transport of Lithogenic Particles in Panama Basin", *Science*, vol. 216, pp. 516–518.

Houben, A. J. P., C. A. V. Mourik, A. Montanari, R. Coccioni & H. Brinkhuis **(2012)**, "The Eocene-Oligocene transition: Changes in sea level, temperature or both?", *Palaeogeogr. Palaeoclim. Palaeoecol.* Vol. 335-336, pp. 75–83.

Houben, A. J. P. et al. **(2013)**, "Reorganization of Southern Ocean Plankton Ecosystem at the Onset of Antarctic Glaciation", *Science*, vol. 340, no. April, pp. 341–344.

Houben, A. J. P., P. K. Bijl, A. Sluijs & S. Schouten **(2019)**, "Late Eocene Southern Ocean cooling and invigoration of circulation preconditioned Antarctica for full-scale glaciation", *Geochemistry, Geophys. Geosystems*, vol. 20, pp. 2214–2234.

Huber, M. & R Caballero **(2011)**, "The Early Eocene Equable Climate Problem Revisited", *Clim. past*, vol. 7, pp. 603–633.

Huber, M. & D. Nof **(2006)**, "The ocean circulation in the southern hemisphere and its climatic impacts in the Eocene", *Palaeogeogr. Palaeoclim. Palaeoecol.* Vol. 231, pp. 9–28.

Huber, M. et al. **(2004)**, "Eocene circulation of the Southern Ocean: Was Antarctica kept warm by subtropical waters?", *Paleoceanography*, vol. 19.

Hunter, J. R., P. D. Craig & H. E. Phillips **(1993)**, "On the Use of Random Walk Models with Spatially Variable Diffusivity", *J. Comput. Phys.* Vol. 106, pp. 366–376.

Huntley, H. S., B. L. Lipphardt Jr. & A. D. Kirwan jr. **(2011)**, "Lagrangian predictability assessed in the East China Sea", *Ocean Model.* Vol. 36, no. 1-2, pp. 163–178.

Hutchinson, D. K., A. M. D. Boer, H. K. Coxall, R. Caballero, J. Nilsson & M. Baatsen **(2018)**, "Climate sensitivity and meridional overturning circulation in the late Eocene using GFDL CM2.1", *Clim. Past*, vol. 14, no. 2016, pp. 789–810.

Hutchinson, D. K. et al. **(2021)**, "The Eocene-Oligocene transition: A review of marine and terrestrial proxy data, models and model-data comparisons", *Clim. Past*, vol. 17, no. 1, pp. 269–315.

Hwan, M., S. Kyung & W. Seo **(2011)**, "Determination of the swimming trajectory and speed of chain- forming dinoflagellate Cochlodinium polykrikoides with digital holographic particle tracking velocimetry", *Mar. Biol.* Vol. 158, pp. 561–570.

Iversen, M. H., N. Nowald, H. Ploug, G. A. Jackson & G. Fischer **(2010)**, "High resolution profiles of vertical particulate organic matter export off Cape Blanc , Mauritania: Degradation processes and ballasting effects", *Deep. Res. Part I*, vol. 57, no. 6, pp. 771–784.

Jackson, L. C. et al. **(2020)**, "Impact of ocean resolution and mean state on the rate of AMOC weakening", *Clim. Dyn.*

Jalón-Rojas, I., X. Wang & E. Fredj **(2019)**, "Technical note: On the importance of a three-dimensional approach for modelling the transport of neustic microplastics", *Ocean Sci.* Vol. 15, pp. 717–724.

Jochum, M, G Danabasoglu, M Holland, Y. O. Kwon & W. G. Large **(2008)**, "Ocean viscosity and climate", *J. Geophys. Res.* Vol. 113, pp. 1–24.

Johnson, C. P., X. Li & B. E. Logan **(1996)**, "Settling Velocities of Fractal Aggregates", *Environ. Sci. Technol.* Vol. 30, no. 6, pp. 1911–1918.

Jokulsdottir, T. & D. Archer **(2016)**, "A stochastic, Lagrangian model of sinking biogenic aggregates in the ocean (SLAMS 1.0): Model formulation, validation and sensitivity", *Geosci. Model Dev.* Vol. 9, no. 4, pp. 1455–1476.

Jonkers, L., H. Hillebrand & M. Kucera **(2019)**, "Global change drives modern plankton communities away from the pre-industrial state", *Nature*, vol. 372.

Jonnson, B. F. & J. R. Watson **(2016)**, "The timescales of global surface-ocean connectivity", *Nat. Commun.* Vol. 7, pp. 1–6.

Kajihara, M. **(1971)**, "Settling Velocity and Porosity of Large Suspended Particle*", *J. Ocean. Soc. Japan*, vol. 27, no. 4, pp. 158–162.

Katsman, C. A., S. S. Dijfhout, H. A. Dijkstra & M. A. Spall **(2018)**, "Sinking of Dense North Atlantic Waters in a Global Ocean Model: Location and Controls", *J. Geophys. Res. Ocean.* Pp. 3563–3576.

Katz, M. E. et al. **(2010)**, "Traditional and Emerging Geochemical Proxies in Foraminifera", *J. Foraminifer. Res.* Vol. 40, no. 2, pp. 165–192.

Kennedy, A. T., A Farnsworth, D. J. Lunt, C. H. Lear & P. J. Markwick **(2015)**, "Atmospheric and oceanic impacts of Antarctic glaciation across the Eocene-Oligocene transition", *Philos*, vol. 373.

Kennedy-Asser, A. T., D. J. Lunt, A Farnsworth & P. J. Valdes **(2019)**, "Assessing Mechanisms and Uncertainty in Modeled Climatic Change at the Eocene-Oligocene Transition", *Paleoceanogr. Paleoclimatology*, vol. 34, pp. 16–34.

Kennedy-Asser, A. T., D. J. Lunt, P. J. Valdes, J.-b. Ladant, J. Frieling & V. Lauretano **(2020)**, "Changes in the high-latitude Southern Hemisphere through the Eocene-Oligocene transition: a model-data comparison", *Clim. Past*, vol. 16, pp. 555–573.

Kennett, J. P. **(1977)**, "Cenozoic evolution of Antarctic glaciation, the Circum-Antarctic Ocean, and their impact on global paleoceanography", *J. Geophys. Res.* Vol. 82, no. 27.

Kiko, R et al. **(2017)**, "Snowfall at the equator", *Nat. Geosci.* Vol. 10, no. November.

Kirtman, B. et al. **(2013)**, "Near-term climate change: Projections and predictability", in: *Clim. Chang. 2013 Phys. Sci. Basis Work. Gr. I Contrib. to Fifth Assess. Rep. Intergov. Panel Clim. Chang.* Cambridge University Press, Cambridge, United Kingdom and New York, NY, USA, pp. 953–1028, ISBN: 9781107415324.

Kluijfhout, W. **(2017)**, "Parathyroid imaging", PhD thesis, Utrecht University, ISBN: 9789462335370.

Koelmans, A. A., M. Kooi, K. L. Law & E. V. Sebille **(2017)**, "All is not lost: deriving a top-down mass budget of plastic at sea", *Environ. Res. Lett.* Vol. 12.

Komar, P. D., A. P. Morse, L. F. Small & S. W. Fowler **(1981)**, "Euphausiid fecal pellets '", *Limnol. Ocean.* Vol. 26, no. l, pp. 172–180.

Kooi, M., E. H. V. Nes, M. Scheffer & A. A. Koelmans **(2017)**, "Ups and Downs in the Ocean: Effects of Biofouling on Vertical Transport of Microplastics", *Environ. Sci. Technol.* Vol. 51, pp. 7963–7971.

Kriest, I & A Oschlies **(2008)**, "On the treatment of particulate organic matter sinking in large-scale models of marine biogeochemical cycles", *Biogeosciences*, vol. 5, pp. 55–72.

Kucera, M. et al. **(2005)**, "Reconstruction of sea-surface temperatures from assemblages of planktonic foraminifera: multi-technique approach based on geographically constrained calibration data sets and its application to glacial Atlantic and Pacific Oceans", *Quat. Sci. Rev.* Vol. 24, pp. 951–998.

Kutzbach, J. E. **(1985)**, "Modeling of paleoclimates", *Adv. Geophys.* Vol. 28A, pp. 159–196.

Ladant, J, Y Donnadieu, L Bopp, C. H. Lear & P. A. Wilson **(2018)**, "Meridional Contrasts in Productivity Changes Driven by the Opening of Drake Passage", *Paleoceanogr. Paleoclimatology*, vol. 33, pp. 302–317.

Lampitt, R. S.I. F. **(1985)**, "Evidence for the seasonal deposition of detritus to the deep-sea floor and its subsequent resuspension", *Deep. Res.* Vol. 32, pp. 885–897.

Lange, M. & E. **van** Sebille **(2017a)**, "Parcels v0.9: prototyping a Lagrangian Ocean Analysis framework for the petascale age", *Geosci. Model Dev. Discuss.* No. July, pp. 1–20.

Lange, M. & E. V. Sebille **(2017b)**, "Parcels v0.9: Prototyping a Lagrangian ocean analysis framework for the petascale age", *Geosci. Model Dev.* Vol. 10, no. 11, pp. 4175–4186, arXiv: 1707.05163.

Lanzante, J. R., K. W. Dixon, M. J. Nath, C. E. Whitlock & D. Adams-Smith **(2018)**, "Some pitfalls in statistical downscaling of future climate", *Am. Meteorol. Soc.* Vol. 99, no. 4, pp. 791–804.

Lau, R., H. Kai & L. Chuah **(2013)**, "Dynamic shape factor for particles of various shapes in the intermediate settling regime", *Adv. Powder Technol.* Vol. 24, no. 1, pp. 306–310.

Laurenceau-cornec, E. C., T. W. Trull, D. M. Davies, C. L.D. L. Rocha & S. Blain **(2015)**, "Phytoplankton morphology controls on marine snow sinking velocity", *Mar. Ecol. Prog. Ser.* Vol. 520, no. Buesseler 1998, pp. 35–56.

Laurenceau-cornec, E. C. et al. **(2019)**, "New guidelines for the application of Stokes' models to the sinking velocity of marine aggregates", *Limnol. Ocean.* Pp. 1–22.

Le Bars, D, J. P. Viebahn & H. A. Dijkstra **(2016)**, "A Southern Ocean mode of multidecadal variability", *Geophys. Res. Lett.* Vol. 43, pp. 2102–2110.

Le Sommer, J., E. P. Chassignet & A. J. Wallcraft **(2018)**, "Ocean Circulation Modeling for Operational Oceanography: Current Status and Future Challenges", in: *New Front. Oper. Oceanogr.* August 2018, chap. 12.

Lear, C. H. et al. **(2020)**, "Geological Society of London Scientific Statement: what the geological record tells us about our present and future climate", *J. Geol. Soc. London.* Vol. 178.

Lebreton, L. C., S. D. Greer & J. C. Borrero **(2012)**, "Numerical modelling of floating debris in the world's oceans", *Mar. Pollut. Bull.* Vol. 64, no. 3, pp. 653–661.

Legendre, P. & L. Legendre **(2012)**, *Numerical Ecology*, 3rd, Amsterdam: Elsevier, p. 990, ISBN: 9780444538680.

Li, X.-y. & Y. Yuan **(2002)**, "Settling velocities and permeabilities of microbial aggregates", *Water Res.* Vol. 36, no. December 2001, pp. 3110–3120.

Lima-Mendez, G. et al. **(2015)**, "Determinants of community structure in the global plankton interactome", *Science*, vol. 348, no. 6237, pp. 1–10.

Liu, G., A. Bracco & U. Passow **(2018)**, "The influence of mesoscale and submesoscale circulation on sinking particles in the northern Gulf of Mexico", *Elem. Sci. Athropocene*, vol. 6, no. 36.

Liu, Z et al. **(2009)**, "Transient Simulation of Last Deglaciation with a New Mechanism for Bølling-Allerød Warming", *Science*, vol. 325, pp. 310–315.

Locarnini, R. A. et al. **(2013)**, "NOAA Atlas NESDIS 73", *WORLD Ocean ATLAS 2013*, vol. 1, p. 40.

Logan, B. E. & D. B. Wilkinson **(1990)**, "Fractal geometry of marine snow and other biological aggregates", *Limnol. Ocean.* Vol. 35, no. 1, pp. 130–136.

Lunt, D. J. et al. **(2012)**, "A model-data comparison for a multi-model ensemble of early Eocene atmosphere-ocean simulations: EoMIP", *Clim. Paste*, vol. 8, pp. 1717–1736.

Lunt, D. J. et al. **(2013)**, "Warm climates of the past - a lesson for the future?", *Philosofical Trans. R. Soc. A*, vol. 371.

Lunt, D. et al. **(2017)**, "The DeepMIP contribution to PMIP4: experimental design for model simulations of the EECO , PETM , and pre-PETM (version 1.0 )", *Geosci. Model Dev.* Vol. 10, pp. 889–901.

Lunt, D. J. et al. **(2016)**, "Palaeogeographic controls on climate and proxy interpretation", *Clim. past*, vol. 12, pp. 1181–1198.

Lunt, D. J. et al. **(2021)**, "DeepMIP: Model intercomparison of early Eocene climatic optimum (EECO) large-scale climate features and comparison with proxy data", *Clim. Past*, vol. 17, no. 1, pp. 203–227.

Ma, J., F. Wang & X. Tang **(2009)**, "Comparison of Several Subgrid-Scale Models for Large-Eddy Simulation of Turbulent Flows in Water Turbine", in: *Fluid Mach. Fluid Mech.* Pp. 328–334.

Ma, W. et al. **(2021)**, "The impact of mesoscale eddies on the source funnel of trap measurements in the South China Sea.", *Prog. Oceanogr.* Vol. 194, p. 102566.

Macintyre, S., A. L. Alldredge & C. C. Gotschalk **(1995)**, "Accumulation of marine snow at density discontinuities in the water column", *Limnol. Ocean.* Vol. 40, no. May, pp. 449–468.

Madec, G. **(2016)**, *NEMO ocean engine*, 27.

Madin, L. P., W. Hole & W. Hole **(1982)**, "Production , Composition and Sedimentation of Salp Fecal Pellets in Oceanic Waters", *Mar. Biol.* Vol. 67, pp. 39–45.

Mana, P. P. & L. Zanna **(2014)**, "Toward a stochastic parameterization of ocean mesoscale eddies", *Ocean Model.* Vol. 79, pp. 1–20.

Mari, X., U. Passow, C. Migon, A. B. Burd & L. Legendre **(2017)**, "Progress in Oceanography Transparent exopolymer particles: Effects on carbon cycling in the ocean", *Prog. Ocean.* Vol. 151, pp. 13–37.

Marret, F., A. De Vernal, F. Benderra & R. Harland **(2001)**, "Late quaternary sea-surface conditions at DSDP Hole 594 in the Southwest Pacific Ocean based on dinoflagellate cyst assemblages", *J. Quat. Sci.* Vol. 16, no. 7, pp. 739–751.

Marret, F. et al. **(2019)**, "From bi-polar to regional distribution of modern dinoflagellate cysts, an overview of their biogeography", *Mar. Micropaleontol.* No. July, p. 101753.

Marshall, D. **(1994)**, "Topographic steering of the Antarctic circumpolar current", *J. Phys. Ocean.* Vol. 25, pp. 1636–1650.

Marshall, J. & T. Radko **(2003)**, "Residual-Mean Solutions for the Antarctic Circumpolar Current and Its Associated Overturning Circulation", *J. Phys. Ocean.* Vol. 33, no. 11, pp. 2341–2354.

Marzocchi, A., J. J. M. Hirschi, N. P. Holliday, S. A. Cunningham, A. T. Blaker & A. C. Coward **(2015)**, "The North Atlantic subpolar circulation in an eddy-resolving global ocean model", *J. Mar. Syst.* Vol. 142, pp. 126–143.

Masson-Delmote, V et al. **(2013)**, "Information from Paleoclimate Archives", in: *Clim. Chang. 2013 Phys. Sci. basis. Contrib. Work. Gr. 1 to Fifth Assess. Rep. Intergov. Panel Clim. Chang.* Cambridge: Cambridge University Press, chap. 5.

Masumoto, Y. **(2010)**, "Sharing the results of a high-resolution ocean general circulation model under a multi-discipline framework - a review of OFES activities", *Ocean Dyn.* Vol. 60, pp. 633–652.

Masumoto, Y. et al. **(2004)**, "A Fifty-Year Eddy-Resolving Simulation of the World Ocean - Preliminary Outcomes of OFES (OGCM for the Earth Simulator)", *J. Earth Simulator*, vol. 1, no. April 2014, pp. 35–56.

Matano, R. P., E. D. Palma & A. R. Piola **(2010)**, "The influence of the Brazil and Malvinas Currents on the Southwestern Atlantic Shelf circulation", *Ocean Sci.* Vol. 6, no. 4, pp. 983–995.

Matthiessen, J. **(1997)**, "Organic-walled dinoflagellate cysts: Palynologycal tracers of sea-surface conditions in middle to high latitude marine environments", *Geobios*, vol. 30, no. 7, pp. 905–920.

McAdam, R. & E. **van** Sebille **(2018)**, "Surface Connectivity and Interocean Exchanges From Drifter-Based Transition Matrices", *J. Geophys. Res. Ocean.* Vol. 123, pp. 514–532.

McClean, J, S Jayne, M Maltrud & D Ivanova **(2008)**, "The Fidelity of Ocean Models With Explicit Eddies", in: *Ocean Model. an Eddying regime*, ed. by Hecht, M. W. & Hasumi, H, Washington, DC: American Geophysical Union, chap. 2, pp. 149–164, ISBN: 978-0-87590-442-9.

McClean, J. L., P.-M. Poulain, J. W. Pelton & M. E. Maltrud **(2002)**, "Eulerian and Lagrangian Statistics from Surface Drifters and a High-Resolution POP Simulation in the North Atlantic", *J. Phys. Ocean.* Vol. 32, pp. 2472–2491.

McClean, J. L., M. E. Maltrud & F. O. Bryan **(2006)**, "Eddying Ocean Models", *Adv. Comput. Ocean.* Vol. 19, no. 1, pp. 104–117.

McDonnell, A. M. P. & K. O. Buesseler **(2010)**, "Variability in the average sinking velocity of marine particles", *Limnol. Ocean.* Vol. 55, no. 5, pp. 2085–2096.

McWilliams, J. C., Y. Liu, C. Dong & D. Chen **(2014)**, "Global heat and salt transports by eddy movement", *Nat. Commun.* Vol. 5, pp. 1–6.

Meilland, J., H. Howa, V. Hulot, I. Demangel, J. Salaün & T. Garlan **(2020)**, "Population dynamics of modern planktonic foraminifera in the western Barents Sea", *Biogeosciences*, vol. 17, pp. 1437–1450.

Middleton, G. V. **(2003)**, *Encyclopedia of sedimentary rocks*, ed. by Middleton, G. V., Church, M. J., Coniglio, M., Hardie, L. A. & Longstaffe, F. J., KlUWER ACADEMIC PUBLISHERS, ISBN: 1402008724.

Miramontes, E. et al. **(2019)**, "Contourite distribution and bottom currents in the NW Mediterranean Sea: Coupling seafloor geomorphology and hydrodynamic modelling", *Geomorphology*, vol. 333, pp. 43–60.

Mitchell, J. G., H. Yamazaki, L. Seuront, F. Wolk & H. Li **(2008)**, "Phytoplankton patch patterns: Seascape anatomy in a turbulent ocean", *J. Mar. Syst.* Vol. 69, pp. 247–253.

Monroy, P., E. Hernández-García, V. Rossi & C. López **(2017)**, "Modeling the dynamical sinking of biogenic particles in oceanic flow", *Nonlinear Process. Geophys.* Vol. 24, no. 2, pp. 293–305.

Monroy, P., G. Drótos, E. Hernández-garcía & C. López **(2019)**, "Spatial Inhomogeneities in the Sedimentation of Biogenic Particles in Ocean Flows: Analysis in the Benguela Region", *J. Geophys. Res. Ocean.* Vol. 124, no. May, pp. 1–19.

Montresor, M., L. Nuzzo & M. G. Mazzocchi **(2003)**, "Viability of dinoflagellate cysts after the passage through the copepod gut", *J. Exp. Mar. Bio. Ecol.* Vol. 287, no. 2, pp. 209–221.

Morey, A., A. C. Mix & N. G. Pisias **(2005)**, "Planktonic foraminiferal assemblages preserved in surface sediments correspond to multiple environment variables", *Quat. Sci. Rev.* Vol. 24, pp. 925–950.

Morris, E. K. et al. **(2014)**, "Choosing and using diversity indices: insights for ecological applications from the German Biodiversity Exploratories", *Ecol. Evol.* Vol. 4, pp. 3514–3524.

Moum, J. N., A. Perlin, J. D. Nash & M. J. Mcphaden **(2013)**, "Seasonal sea surface cooling in the equatorial Pacific cold tongue controlled by ocean mixing", *Nature*, vol. 500, pp. 1–4.

Mudie, P. **(1996)**, "Pellets of dinoflagellate-eating zooplankton", in: *Palynol. Princ. Appl.* Pp. 1087–1089.

Müller, V., D. Kieke, P. G. Myers, C. Pennely, R. Steinfeldt & I. Stendardo **(2019)**, "Heat and Freshwater Transport by Mesoscale Eddies in the Southern Subpolar North Atlantic", *J. Geophys. Res. Ocean.* Pp. 1–21.

Munday, D. R., H. L. Johnson & D. P. Marshall **(2015)**, "The role of ocean gateways in the dynamics and sensitivity to wind stress of the early Antarctic Circumpolar Current", *Paleoceanography*, vol. 30, no. 3, pp. 284–302.

Nelson, G & L Hutchings **(1983)**, "The Benguela Upwelling Area", *Prog. Ocean.* Vol. 12, pp. 333–356.

Nicoud, F & F Ducros **(1999)**, "Subgrid-Scale Stress Modelling Based on the Square of the Velocity Gradient Tensor", *Flow, Turbukence Combust.* Pp. 183–200.

Nicoud, F. et al. **(2011)**, "Using singular values to build a subgrid-scale model for large eddy simulations", *Phys. Fluids*, vol. 085106, no. May 2013.

Nooteboom, C. **(1932)**, *De boomstamkano in Indonesie*, Leiden, p. 240.

Nooteboom, H. P. **(1975)**, *Revision of the symplocaceae of the old world, New Caledonia excepted*, Leiden: Universitaire Pers Leiden, p. 336.

Nooteboom, H. P. **(2011)**, "How did Magnolias (Magnoliaceae: Magnolioideae) reach Tropical Asia?", *Gard. Bull.* Vol. 63, pp. 299–306.

Nooteboom, P. D., P Delandmeter, E. V. Sebille, P. K. Bijl, H. A. Dijkstra & A. S. **von der** Heydt **(2020)**, "Resolution dependency of sinking Lagrangian particles in ocean general circulation models", *PLoS One*, vol. 15, no. 9, pp. 1–16.

Nooteboom, P. D. et al. **("unpublished manuscript")**, "Strongly eddying ocean simulations required to resolve Eocene model-data mismatch".

Nooteboom, P. D., P. K. Bijl, E. **van** Sebille, A. S. **von der** Heydt & H. A. Dijkstra **(2019)**, "Transport Bias by Ocean Currents in Sedimentary Microplankton Assem-

blages: Implications for Paleoceanographic Reconstructions", *Paleoceanogr. Paleoclimatology*, vol. 34.

Nooteboom, P. D. et al. **(2021)**, "Sedimentary microplankton distributions are shaped by oceanographically connected areas", *Earth Syst. Dyn. Discuss.* No. August, pp. 1–23.

Nooteboom, S. G. **(2006)**, *Adaptive networks. The governance for sustainable development.* Delft: Eburon Academic Publisher, p. 231.

Nowald, N, G. Fischer, M. H. Iversen & G. Wefer **(2009)**, "In-situ sinking speed measurements of marine snow aggregates acquired with a settling chamber mounted to the Cherokee ROV", *IEEE Xplore*, no. June.

Ohlwein, C. & E. R. Wahl **(2012)**, "Review of probabilistic pollen-climate transfer methods", *Quat. Sci. Rev.* Vol. 31, pp. 17–29.

Oldeman, A. M. et al. **(2021)**, "Reduced El-Niño variability in the mid-Pliocene according to the PlioMIP2 ensemble", *Clim. Past Discuss.* No. June.

Omand, M. M., R Govindarajan, J He & A Mahadevan **(2020)**, "Sinking flux of particulate organic matter in the oceans: Sensitivity to particle characteristics", *Sci. Rep.* Pp. 1–16.

Onink, V., D. Wichmann, P. Delandmeter & E. **van** Sebille **(2019)**, "The Role of Ekman Currents , Geostrophy , and Stokes Drift in the Accumulation of Floating Microplastic", *J. Geophys. Res. Ocean.* Vol. 124, pp. 1474–1490.

Orsi, A. H., T. Whitworth & W. D. Nowlin Jr **(1995)**, "On the meridional extent and fronts of the Antarctic Circumpolar Current.", *Deep. Res.* Vol. 42, no. 5, pp. 641–673.

Ottens, J. J. & A. J. Nederbragt **(1992)**, "Planktic foraminiferal diversity as indicator of ocean environments", *Mar. Micropaleontol.* Vol. 19, pp. 13–28.

Palmer, M. D., G. R. Harris & J. M. Gregory **(2018)**, "Extending CMIP5 projections of global mean temperature change and sea level rise due to thermal expansion using a physically-based emulator", *Environ. Res. Lett.* Vol. 13.

Parrenin, F. et al. **(2017)**, "Is there 1.5-million-year-old ice near Dome C, Antarctica?", *Cryosph.* Pp. 2427–2437.

Pearson, P. N. et al. **(2001)**, "Warm tropical sea surface temperatures in the Late Cretaceous and Eocene epochs", *Nature*, vol. 413, no. October, pp. 481–488.

Pearson, P. N., G. L. Foster & B. S. Wade **(2009)**, "Atmospheric carbon dioxide through the Eocene-Oligocene climate transition", *Nature*, vol. 461, no. 7267, pp. 1110–1113.

Penduff, T. et al. **(2011)**, "Sea Level Expression of Intrinsic and Forced Ocean Variabilities at Interannual Time Scales", *J. Clim.* Vol. 24, pp. 5652–5670.

Phillips, N. A. **(1956)**, "The general circulation of the atmosphere: a numerical experiment", *Quaterly J. R. Meteorol. Soc.* Vol. 352, pp. 123–164.

Pickart, R. S., F. Straneo & G. W. K. Moore **(2003)**, "Is Labrador Sea Water formed in the Irminger basin?", *Deep. Res. 1*, vol. 50, pp. 23–52.

Pilskaln, C. H., C. Lehmann, J. B. Paduan & M. W. Silver **(1998)**, "Spatial and temporal dynamics in marine aggregate abundance, sinking rate and flux: Monterey Bay, central California", *Deep. Res. Part II*, vol. 45, pp. 1803–1837.

Ploug, H. & H.-P. Grossart **(2000)**, "Bacterial growth and grazing on diatom aggregates: Respiratory carbon turnover as a function of aggregate size and sinking velocity", *Limnol. Ocean.* Vol. 45, no. 7, pp. 1467–1475.

Porta Mana, P. G. L. & L. Zanna **(2014)**, "Toward a stochastic parameterization of ocean mesoscale eddies", *Ocean Model.* Vol. 79, pp. 1–20.

Prebble, J. G., E. M. Crouch, L Carter, G Cortese, H Bostock & H Neil **(2013)**, "An expanded modern dinoflagellate cyst dataset for the Southwest Pacific and Southern Hemisphere with environmental associations", *Mar. Micropaleontol.* Vol. 101, pp. 33–48.

Pross, J. et al. **(2012)**, "Persistent neartropical warmth on the antarctic continent during the early eocene epoch", *Nature*, vol. 488, no. 7409, pp. 73–77.

Putman, N. & R. He **(2013)**, "Tracking the long-distance dispersal of marine organisms: Sensitivity to ocean model resolution", *J. R. Soc. Interface*, vol. 10, no. February 2016.

Qin, X., E. **van** Sebille & A. Sen Gupta **(2014)**, "Quantification of errors induced by temporal resolution on Lagrangian particles in an eddy-resolving model", *Ocean Model.* Vol. 76, pp. 20–30.

Rahmstorf, S. & J. Willebrand **(1995)**, "The role of temperature feedback in stabilizing the thermohaline circulation", *J. Phys. Ocean.* Vol. 25.

Ramdas, A., N. G. Trillos & M. Cuturi **(2017)**, "On Wasserstein Two-Sample Testing and Related Families of Nonparametric Tests", *Entropy*, vol. 19, no. 47, pp. 1–15.

Raymo, M. E. & W. F. Ruddiman **(1992)**, "Tectonic forcing of late Cenozoic climate", *Nature*, vol. 359, pp. 117–122.

Rebotim, A. et al. **(2017)**, "Factors controlling the depth habitat of planktonic foraminifera in the subtropical eastern North Atlantic", *Biogeosciences*, vol. 14, pp. 827–859.

Regier, L. & H. Stommel **(1979)**, "Float trajectories in simple kinematic flows", *Proc. Natl. Acad. Sci.* Vol. 76, no. 10, pp. 4760–4764.

Ribeiro, S., T. Berge, N. Lundholm & M. Ellegaard **(2011)**, "Phytoplankton growth after a century of ormancy illuminates past resilience to catastrophic darkness", *Nat. Commun.* No. May, pp. 1–7.

Riley, J. S., R Sanders, C Marsay, F. A.C. L. Moigne, E. P. Achterberg & A. J. Poulton **(2012)**, "The relative contribution of fast and slow sinking particles to ocean carbon export", *Glob. Biogeochem. Cycles*, vol. 26, pp. 1–10.

Rintoul, S. R. **(2018)**, "The global influence of localized dynamics in the Southern Ocean", *Nature*, vol. 558, pp. 209–218.

Rixen, T., B. Gaye, K.-c. Emeis & V. Ramaswamy **(2019)**, "The ballast effect of lithogenic matter and its influences on the carbon fluxes in the Indian Ocean", *Biogeosciences*, vol. 16, pp. 485–503.

Roberts, M. J. et al. **(2020)**, "Impact of model resolution on tropical cyclone simulation using the HighResMIP-PRIMAVERA multimodel ensemble", *J. Clim.* Vol. 33, no. 7, pp. 2557–2583.

Ross, O. N. & J. Sharples **(2004)**, "Recipe for 1-D Lagrangian particle tracking models in space-varying diffusivity", *Limnol. Ocean. Methods*, pp. 289–302.

Rosso, I., A. Mcc, R. Matear & P. G. Strutton **(2016)**, "Quantifying the influence of sub-mesoscale dynamics on the supply of iron to Southern Ocean phytoplankton blooms", *Deep. Res. Part I*, vol. 115, pp. 199–209.

Sarjeant, W. A. S., T. Lacalli & G. Gaines **(1987)**, "The cysts and skeletal elements of dinoflagellates: speculations on the ecological causes for their morphology and development", *micropaleontology*, vol. 33, no. 1, pp. 1–36.

Sasaki, H., M. Nonaka, Y. Masumoto, Y. Sasai, H. Uehara & H. Sakuma **(2008)**, "An Eddy-Resolving Hindcast Simulation of the Quasiglobal Ocean from 1950 to 2003 on the Earth Simulator", in: *High Resolut. Numer. Model. Atmos. Ocean*, ed. by Hamilton, K. & Ohfuchi, W., New York: Springer, chap. 10, pp. 157–185, ISBN: 9780387366715.

Schmeits, M. J. & H. A. Dijkstra **(2001)**, "Bimodal Behavior of the Kuroshio and the Gulf Stream", *J. Phys. Ocean.* Vol. 31, no. 12, pp. 3435–3456.

Schmidt, G. A. et al. **(2014a)**, "Using palaeo-climate comparisons to constrain future projections in CMIP5", *Clim. Past*, vol. 10, pp. 221–250.

Schmidt, K, C. L.D. L. Rocha, M Gallinari & G Cortese **(2014b)**, "Not all calcite ballast is created equal: differing effects of foraminiferan and coccolith calcite on the formation and sinking of aggregates", *Biogeosciences*, vol. 11, pp. 135–145.

Schouten, S., E. C. Hopmans, E. S. M & J. S. Sinninghe Damsté **(2002)**, "Distributional variations in marine crenarchaeotal membrane lipids: a new tool for reconstructing ancient sea water temperatures?", *Earth Planet. Sci. Lett.* Vol. 204, pp. 265–274.

Scoccimarro, E. et al. **(2011)**, "Effects of tropical cyclones on ocean heat transport in a high-resolution coupled general circulation model", *J. Clim.* Vol. 24, no. 16, pp. 4368–4384.

Sebille, E. **van**, M. H. England & G. Froyland **(2012)**, "Origin , dynamics and evolution of ocean garbage patches from observed surface drifters", *Environ. Res. Lett.* Vol. 7.

Sebille, E. **van** et al. **(2015a)**, "A global inventory of small floating plastic debris", *Environ. Res. Lett.* Vol. 10.

Sebille, E. **van** et al. **(2015b)**, "Ocean currents generate large footprints in marine palaeoclimate proxies", *Nat. Commun.* Vol. 6, p. 6521.

Sebille, E. **van** et al. **(2018)**, "Lagrangian ocean analysis: Fundamentals and practices", *Ocean Model.* Vol. 121, no. July 2016, pp. 49–75.

Shanks, A. L. **(2002)**, "The abundance , vertical flux , and still-water and apparent sinking rates of marine snow in a shallow coastal water column", *Cont. Shelf Res.* Vol. 22, pp. 2045–2064.

Shanks, A. L. & J. D. Trent **(1980)**, "Marine snow: sinking rates and potential role in vertical flux", *Deep. Res.* Vol. 27, pp. 137–143.

Shannon, C. E. **(1948)**, "A mathematical theory of communication", *Bell Syst. Tech. J.* Vol. XXVII, no. 3.

Sharqawy, M. H., J. H. L. V & S. M. Zubair **(2010)**, "Thermophysical properties of seawater: a review of existing correlations and data", *Desalin. water Treat.* Vol. 16, no. 10, pp. 354–380.

Shi, J. & M. Jitendra **(2000)**, "Normalized Cuts and Image Segmentation", *IEEE Trans. Pattern Anal. Mach. Intell.* Vol. 22, no. 8, pp. 888–905.

Shulman, I. et al. **(2012)**, "Can vertical migrations of dinoflagellates explain observed bioluminescence patterns during an upwelling event in Monterey Bay, California ?", *J. Geophys. Res.* Vol. 117, pp. 1–10.

Siccha, M. & M. Kucera **(2017)**, "Data Descriptor: ForCenS, a curated database of planktonic foraminifera census counts in marine surface sediment samples", *Sci. Data*, pp. 1–12.

Siegel, D. A. & W. G. Deuser **(1997)**, "Trajectories of sinking particles in the Sargasso Sea: modeling of statistical funnels above deep-ocean sediment traps", *Deep. Res. 1*, vol. 44, no. 9, pp. 1519–1541.

Siegel, D. A., E Fields & K. O. Buesseler **(2008)**, "A bottom-up view of the biological pump: Modeling source funnels above ocean sediment traps", *Deep. Res. Part 1*, vol. 55, pp. 108–127.

Sijp, W. P., A. S. **von der** Heydt, H. A. Dijkstra, S. Flögel, P. M. J. Douglas & P. K. Bijl **(2014)**, "The role of ocean gateways on cooling climate on long time scales", *Glob. Planet. Chang.* Vol. 119, pp. 1–22.

Sijp, W. P., A. S. **von der** Heydt & P. K. Bijl **(2016)**, "Model simulations of early westward flow across the Tasman Gateway during the early Eocene", *Clim. Past*, vol. 12, pp. 807–817.

Simonsen, M. et al. **(2017)**, "The impact of tidal and mesoscale eddy advection on the long term dispersion of 99Tc from Sellafield", *J. Environ. Radioact.* Vol. 177, pp. 100–112.

Sluijs, A., J. Pross & H. Brinkhuis **(2005)**, "From greenhouse to icehouse; organic-walled dinoflagellate cysts as paleoenvironmental indicators in the Paleogene", *Earth-Science Rev.* Vol. 68, no. 3-4, pp. 281–315.

Sluijs, A. et al. **(2006)**, "Subtropical Arctic Ocean temperatures during the Palaeocene/Eocene thermal maximum", *Nature*, vol. 441, no. 7093, pp. 610–613.

Sluijs, A., L. V. Roij, J. Frieling, J. Laks & G.-j. Reichart **(2018)**, "Single-species dinoflagellate cyst carbon isotope ecology across the Paleocene-Eocene Thermal Maximum", *Geology*, vol. 46, no. 1, pp. 79–82.

Smagorinsky, J **(1963)**, "General circulation experiments with the primitive equations", *Mon. Weather Rev.* Vol. 91, no. 3, pp. 99–163.

Smayda, T. J. **(1969)**, "Some measurements of the sinking rate of fecal pellets", *Limnol. Ocean.* Vol. 14, pp. 621–625.

Smayda, T. J. **(2002)**, "Turbulence, watermass stratification and harmful algal blooms: an alternative view and frontal zones as 'pelagic seed banks'", *Harmful Algae*, vol. 1, pp. 95–112.

Smith, R et al. **(2010)**, "The Parallel Ocean Program (POP) Reference Manual Ocean Component of the Community Climate System Model (CCSM) and Community Earth System Model (CESM)", *LAUR-01853*, vol. 141.

Smith, R. D., M. E. Maltrud, F. O. Bryan & M. W. Hecht **(2000)**, "Numerical simulation of the North Atlantic Ocean at 1/10°", *J. Phys. Oceanogr.* Vol. 30, no. 7, pp. 1532–1561.

Starz, M., W. Jokat, G. Knorr & G. Lohmann **(2017)**, "Threshold in North Atlantic-Arctic Ocean of the Greenland-Scotland Ridge", *Nat. Commun.* Vol. 8, pp. 1–13.

Steffen, W., J. Rockström, K. Richardson, T. M. Lenton, C. Folke & D. Liverman **(2018)**, "Trajectories of the Earth System in the Anthropocene", *Proc. Natl. Acad. Sci.* Vol. 115, no. 33, pp. 8252–8259.

Steinthorsdottir, M. et al. **(2021)**, "The Miocene: The Future of the Past", *Paleoceanogr. Paleoclimatology*, vol. 36, no. 4.

Stemmann, L., G. A. Jackson & D. Ianson **(2004)**, "A vertical model of particle size distributions and fluxes in the midwater column that includes biological and physical processes- Part I: model formulation", *Deep. Res. 1*, vol. 51, pp. 865–884.

Stewart, K. D. et al. **(2017)**, "Vertical resolution of baroclinic modes in global ocean models", *Ocean Model.* Vol. 113, pp. 50–65.

Stickley, C. E. et al. **(2004)**, "Timing and nature of the deepening of the Tasmanian Gateway", *Paleoceanography*, vol. 19, pp. 1–18.

Storkey, D et al. **(2014)**, "Forecasting the ocean state using NEMO: The new FOAM system", *J. Oper. Ocean.* Vol. 3, no. 1, pp. 3–15.

Su, Z., J. Wang, P. Klein, A. F. Thompson & D. Menemenlis **(2018)**, "Ocean submesoscales as a key component of the global heat budget", *Nat. Commun.* Vol. 9, no. 775, pp. 1–8.

Sun, B., C. Liu & F. Wang **(2019)**, "Global meridional eddy heat transport inferred from Argo and altimetry observations", *Sci. Rep.* Vol. 9.

Syvitski, J. P. M., K. W. Asprey & K. W. G. Leblanc **(1995)**, "In-situ characteristics of particles settling within a deep-water estuary", *Deep. Res. II*, vol. 42, no. I.

Tabor, C. R. et al. **(2016)**, "The cause of Late Cretaceous cooling: A multimodel-proxy comparison", *Geology*, vol. 44, no. 11, pp. 963–966.

Tamsitt, V, R. P. Abernathey, M. R. Mazloff, J Wang & L. D. Talley **(2018)**, "Oceans Upwelling Pathways in the Southern Ocean", *J. Geophys. Res. Ocean.* Vol. 123, pp. 1994–2017.

Tamsitt, V. et al. **(2017)**, "Spiraling pathways of global deep waters to the surface of the Southern Ocean", *Nat. Commun.* Vol. 8.

Tang, Y., N. Lemaitre, M. Castrillejo, P. Masqué & G. Stewart **(2019)**, "The export flux of particulate organic carbon derived from $^{210}Po/^{210}Pb$ disequilibria along the North Atlantic GEOTRACES GA01 transect: GEOVIDE cruise", *Biogeosciences*, vol. 16, pp. 309–327.

Tardif, D. et al. **(2020)**, "The origin of Asian monsoons: a modelling perspective", *Clim. Past*, vol. 16, pp. 847–865.

Taylor, B. J. et al. **(2018)**, "Distribution and ecology of planktic foraminifera in the North Pacific: Implications for paleo-reconstructions", *Quat. Sci. Rev.* Vol. 191, pp. 256–274.

Telford, R. J. & H. J. B. Birks **(2009)**, "Evaluation of transfer functions in spatially structured environments", *Quat. Sci. Rev.* Vol. 28, no. 13-14, pp. 1309–1316.

Telford, R. J. & M Kucera **(2013)**, "Mismatch between the depth habitat of planktonic foraminifera and the calibration depth of SST transfer functions may bias reconstructions", *Clim. Past*, vol. 9, no. 2011, pp. 859–870.

Tierney, J. E. & M. P. Tingley **(2015)**, "A TEX86 surface sediment database and extended Bayesian calibration", *Sci. Data*, vol. 2, pp. 1–10.

Tierney, J. E. & M. P. Tingley **(2018)**, "BAYSPLINE: A New Calibration for the Alkenone Paleothermometer", *Paleoceanogr. Paleoclimatology*, vol. 33, pp. 281–301.

Tierney, J. E., J. Zhu, J. King, S. B. Malevich, G. J. Hakim & C. J. Poulsen **(2020a)**, "Glacial cooling and climate sensitivity revisited", *Nature*, vol. 584.

Tierney, J. E. et al. **(2020b)**, "Past climates inform our future", *Science*, vol. 370, no. 680.

Toom, M. **den**, H. A. Dijkstra, A. A. Cimatoribus & S. S. Drijfhout **(2012)**, "Effect of Atmospheric Feedbacks on the Stability of the Atlantic Meridional Overturning Circulation", *J. Clim.* Vol. 25, pp. 4081–4096.

Toom, M. **den**, H. A. Dijkstra, W. Weijer, M. W. Hecht, M. E. Maltrud & E. **van** Sebille **(2014)**, "Response of a Strongly Eddying Global Ocean to North Atlantic Freshwater Perturbations", *J. Phys. Ocean.* Vol. 44, no. 2, pp. 464–481.

Tournadre, J., F. Girard-ardhuin & B. Legrésy **(2012)**, "Antarctic icebergs distributions, 2002-2010", *J. Geophys. Res.* Vol. 117.

Trenberth, K. E. & J. M. Caron **(2001)**, "Estimates of Meridional Atmosphere and Ocean Heat Transports", *J. Clim.* Vol. 14, no. 16, pp. 3433–3443.

Tumoulin, A, Y Donnadieu, J. B. Ladant, S. J. Batenburg, F Poblete & G Dupont-Nivete **(2020)**, "Quantifying the effect of the Drake Passage opening on the Eocene ocean", *Paleoceanography*.

Turner, J. T. **(2002)**, "Zooplankton fecal pellets, marine snow and sinking phytoplankton blooms", *Aquat. Microb. Ecol.* Vol. 27, pp. 57–102.

Turner, J. T. **(2015)**, "Progress in Oceanography Zooplankton fecal pellets, marine snow, phytodetritus and the ocean's biological pump", *Prog. Ocean.* Vol. 130, pp. 205–248.

Turney, C. S. et al. **(2020)**, "A global mean sea surface temperature dataset for the Last Interglacial (129-116ka) and contribution of thermal expansion to sea level change", *Earth Syst. Sci. Data*, vol. 12, no. 4, pp. 3341–3356.

Uchida, T., D. Balwada, R. Abernathey, G. McKlinley, S. Smith & M. Levy **(2019)**, "The Contribution of Submesoscale over Mesoscale Eddy Iron Transport in the Open Southern Ocean", *J. Adv. Model. earth Syst.* Vol. 11, pp. 3934–3958.

Ummenhofer, C. C. & G. A. Meehl **(2017)**, "Extreme weather and climate events with ecological relevance: a review", *Philosofical Trans. R. Soc. B*, vol. 372.

Uotila, P. et al. **(2017)**, "Comparing sea ice , hydrography and circulation", *Geosci. Model Dev.* Vol. 10, pp. 1009–1031.

Valdivieso Da Costa, M. & B. Blanke **(2003)**, "Lagrangian methods for flow climatologies and trajectory error assessment", *Ocean Model.* Vol. 6, pp. 335–358.

Vega, E. **de la**, T. B. Chalk, P. A. Wilson, R. P. B. Priya & G. L. Foster **(2020)**, "Atmospheric CO2 during the Mid- Piacenzian Warm Period and the M2 glaciation", *Sci. Rep.* Pp. 14–21.

Vernal, A **de** et al. **(1992)**, "Quaternary organic-walled dinoflagellate cysts of the North Atlantic Ocean and adjacent seas: ecostratigraphy and biostratigraphy.", in: *Neogene Quat. Dinoflag. cysts acritarchs*, Dallas, U.S.A, pp. 289–328.

Vic, C. et al. **(2019)**, "Deep-ocean mixing driven by small-scale internal tides", *Nat. Commun.* Vol. 10, no. 2099.

Viebahn, J. P., A. S. **von der** Heydt, D. Le Bars & H. A. Dijkstra **(2016)**, "Effects of Drake Passage on a strongly eddying global ocean", *Paleoceanography*, vol. 31, no. 5, pp. 564–581.

Villa-Alfageme, M et al. **(2016)**, "Geographical, seasonal, and depth variation in sinking particle speeds in the North Atlantic", *Geophys. Res. Lett.* Vol. 43, pp. 8609–8616.

Visser, A. W. **(1997)**, "Using random walk models to simulate the vertical distribution of particles in a turbulent water column", *Mar. Ecol. Prog. Ser.* Vol. 158, pp. 275–281.

Volkov, D. L., T. Lee & L. L. Fu **(2008)**, "Eddy-induced meridional heat transport in the ocean", *Geophys. Res. Lett.* Vol. 35, no. 20, pp. 1–5.

Vreman, A. W. **(2004)**, "An eddy-viscosity subgrid-scale model for turbulent shear flow: Algebraic theory and applications", *Phys. Fluids*, vol. 3670, no. May 2013.

Waniek, J., W. Koeve & R. D. Prien **(2000)**, "Trajectories of sinking particles and the catchment areas above sediment traps in the northeast Atlantic Trajectories of sinking particles and the catchment areas", *J. Mar. Res.* Vol. 58, pp. 983–1006.

Waterman, S., N. G. Hogg & S. R. Jayne **(2011)**, "Eddy-mean flow interaction in the kuroshio extension region", *J. Phys. Oceanogr.* Vol. 41, no. 6, pp. 1182–1208.

Weijer, W, M. E. Maltrud, M. W. Hecht, H. A. Dijkstra & M. A. Kliphuis **(2012)**, "Response of the Atlantic Ocean circulation to Greenland Ice Sheet melting in a strongly-eddying ocean model", *Geophys. Res. Lett.* Vol. 39, no. 9, pp. 1–6.

Weijer, W et al. **(2019)**, "Stability of the Atlantic Meridional Overturning Circulation: A Review and Synthesis", *J. Geophys. Res. Ocean.* Vol. 1124.

Wekerle, C., T. Krumpen, T. Dinter, W.-j. **von** Appen, M. H. Iversen & I. Salter **(2018)**, "Properties of Sediment Trap Catchment Areas in Fram Strait: Results From Lagrangian Modeling and Remote Sensing", *Front. Mar. Sci.* Vol. 5, no. November.

Westerhold, T. et al. **(2020)**, "An astronomically dated record of Earth's climate and its predictability over the last 66 million years", *Science*, vol. 1387, no. September, pp. 1383–1387.

Weyl, P. K. **(1978)**, "Micropaleontology and ocean surface climate.", *Science*, vol. 202, pp. 475–481.

Wichmann, D., P. Delandmeter & E. **van** Sebille **(2019)**, "Influence of Near-Surface Currents on the Global Dispersal of Marine Microplastic", *J. Geophys. Res. Ocean.* Vol. 124, no. 8, pp. 6086–6096.

Wichmann, D., C. Kehl, H. A. Dijkstra & E. V. Sebille **(2020)**, "Detecting flow features in scarce trajectory data using networks derived from symbolic itineraries: an application to surface drifters in the North Atlantic", *Nonlinear Process. Geophys.* Vol. 27, pp. 501–518.

Wichmann, D., C. Kehl, H. A. Dijkstra & E. V. Sebille **(2021)**, "Ordering of trajectories reveals hierarchical finite-time coherent sets in Lagrangian particle data: detecting Agulhas rings in the South Atlantic Ocean", *Nonlinear Process. Geophys.* Vol. 28, pp. 43–59.

Wiebe, P. H., S. H. Boyd & C. Winget **(1976)**, "Particulate matter sinking to the deep-sea floor at 2000m in the tongue of the ocean, Bahamas, with a description of a new sedimentation trap", *J. Mar. Res.* No. 3, pp. 341–354.

Wilkins, D., E. V. Sebille, S. R. Rintoul, F. M. Lauro & R. Cavicchioli **(2013)**, "Advection shapes Southern Ocean microbial environment effects", *Nat. Commun.* Vol. 4, no. May.

Xue, J. & R. A. Armstrong **(2009)**, "An improved benchmark method for estimating particle settling velocities from time-series sediment trap fluxes", *Deep. Res. II*, vol. 56, pp. 1479–1486.

Yang, H., Q. Li, K. Wang, Y. Sun & D. Sun **(2015)**, "Decomposing the meridional heat transport in the climate system", *Clim. Dyn.* Vol. 44, no. 9-10, pp. 2751–2768.

Yool, A, E. E. Popova & T. R. Anderson **(2011)**, "Model Development MEDUSA -1.0: a new intermediate complexity plankton ecosystem model for the global domain", *Geosci. Model Dev.* Vol. 4, pp. 381–417.

Yool, A, E. E. Popova & T. R. Anderson **(2013)**, "MEDUSA-2.0: An intermediate complexity biogeochemical model of the marine carbon cycle for climate change and ocean acidification studies", *Geosci. Model Dev.* Vol. 6, no. 5, pp. 1767–1811.

Zhang, H., H. Stoll, C. Bolton, X. Jin & C. Liu **(2018)**, "Technical note: A refinement of coccolith separation methods: measuring the sinking characteristics of coccoliths", *Biogeosciences*, vol. 15, no. 15.

Zhang, Z.-s., Y. Qing & H.-j. Wang **(2015)**, "Has the Drake Passage Played an Essential Role in the Cenozoic Cooling?", *Atmos. Ocean. Sci. Lett.* Vol. 3, no. 5, pp. 288–292.

Zhongfeng, Q., A. M. Doglioli & F Carlotti **(2014)**, "Using a Lagrangian model to estimate source regions of particles in sediment traps", *Sci. China Earth Sci.* Vol. 57, no. 10, pp. 2447–2456.

Zhu, J., C. J. Poulsen & B. L. Otto-bliesner **(2020)**, "High climate sensitivity in CMIP6 model not supported by paleoclimate", *Nat. Clim. Chang.* Vol. 1, pp. 1–2.

Zonneveld, K. et al. **(2013a)**, "Geographic distribution of dinoflagellate cysts in surface sediments", *PANGAEA*.

Zonneveld, K. A. F., E. Susek & G. Fischer **(2010)**, "Seasonal variability of the organic-walled dinoflagellate cyst production in the coastal upwelling region off cape blanc (mauritania): A five-year survey", *J. Phycol.* Vol. 46, no. 1, pp. 202–215.

Zonneveld, K. A. F. et al. **(2013b)**, "Atlas of modern dinoflagellate cyst distribution based on 2405 data points", *Rev. Palaeobot. Palynol.* Vol. 191, pp. 1–197.

# Acknowledgments

The PhD journey ends here, similar to some of the microplankton that started sinking 4 years ago and just reached the ocean bottom. In contrast to the microplankton, my journey has not been passive thanks to a lot of people.

First I would like to thank you, the reader. It is a difficult task to name all of you in likely the most read section of a PhD thesis (Carpaij, 2020; Kluijfhout, 2017), but realize that your effort is valued greatly. Nevertheless, there are some without whom this thesis would simply not have succeeded:

I would like to thank all colleagues and collaborators for making the PhD so unpassive, and in particular 'the team' that has been there from the start, to support me during the PhD 'trajectory.'

**Anna**, thank your for being my main supervisor of the past four years. You have been a great listener and always gave me the opportunity to develop myself. I will definitely recommend you as supervisor to any other PhD or postdoc.

**Peter**, as the only Earth scientist, you have been an invaluable member of this team. A supervisor with whom I can have meetings (and chats about other stuff) on a bicycle is more than I could have ever whished for.

**Erik**, thank you for welcoming me in the Parcels group, which started off with only four of us and grew so rapidly the past years. While studying microplankton, it has always been interesting to keep up-to-date about the latest microplastic facts. I am looking forward to start a completely new project with you about tuna in september!

**Henk**, you first allowed me to 'work' in Mallorca for 7 months during my master thesis. Afterwards you pointed me to this epic PhD position. Thank you for giving me these opportunities and it has always been great to work together.

**Michael**, you have not been my supervisor, but your technical support has definitely been an important component of my PhD (and the whole physcial oceanography group in general). It took quite some bench presses to get the Eocene model simulations working, and it was all worth it. Thanks for the effort.

There have been many inspriring people during the PhD journey, but three who really helped me out with some chapters. **Appy**, thanks for your contributions to the amazing Urbino 2018 summer school, and also for your great feedback on the project about model-data comparison in the Eocene. **Martin**, thank you for our collaboration, you kept me sharp on topics related to foraminifera and biodiversity. **Michiel**, thank you for making me enthousiastic about the palaeoclimate topic in the first place, and for your help with chapter 6.

Then I would like to thank my office mates. **David**, thank you for the great cof-

fee breaks and the inspiring talks about science and politics. **Philippe**, first I would like to thank you for the important stuff (the beers and runs), second I would like to thank you for all the other, unimportant stuff. **Christian**, thank you for the nice (sometimes virtual) coffee breaks, your great colormap-related feedback and your contributions to chapter 4.

Thanks to the **IMAU Palaeogroup** and the **OceaNice** group for the chats about past climates.

Special thanks to **the Parcel people** (also known as 'the Erik van Sebille soundsystem'). **Mikael**, in particular the final physical EGU version and the wave surfing after the NIOZ symposium have been great fun together, I forgive you for stealing my cruise ;). **Delphine**, you still owe me a salsa lesson, I will never forget.

I would like to thank the complexity centre (CCSS) for the best free coffee of the science park, and **Mark, Sem** and **Qingyi** for drinking it with me.

Ice ages, climate transitions, mass extinctions and pandemics come and go, but I am pretty sure that the cosy IMAU living room will always be where it is now: at the 6th floor of the Buys Ballot Building. I would like to thank all colleagues that shared time with me in this living room, and made the last years very enjoyable during the afternoon beers, lunch runs, ice skating and mountain biking. In particular **Dre**, **Tjebbe**, **Getachew**, **Anne**, **Abdel**, **Rene**, **Daniele**, **Matthias**, **Maurice**, **Claudia**, **Arthur**, **Erwin**, **Janneke**, **Ilja**. Thanks to the secretariat **Floor, Sandra** and **Clara**, it has been fun to organise a game now and then (BBOS games and IMAU christmas quiz).

Thanks to the people that were there for me to balance the time that I was working on my PhD, which is an important skill in 'the COVID era.' Het vinden van de juiste balans tussen werk en ontspanning leerde ik door te roeien, koffie te drinken en mergpijpen te eten met de medebewoners van **Roeierspaleis de Houtman**, vooral met **Jack** en **Hids** waarmee ik ook drie jaar lang in de roeiploeg zat.

**Thomas**, dankzij jou ben ik na het roeien fanatiek begonnen met hardlopen, dank voor het bitse schema dat we 3 jaar geleden hebben gevolgd, waarna jij wel dat begeerde doel hebt gehaald.

De meest epische en extreme hardloop, mountainbike sessies en bootcamps vonden toch plaats met **Piet** en **Wout**, in combinatie met de borrels (liefst bij een brandend vuur) en de koers die we na deze sportdagen voldaan vanaf de bank konden aanschouwen. Dank ook voor jullie fysiologische adviezen.

**Lucas**, dank dat je mij altijd scherp hield in de discussies over duurzaamheid en politiek, maar ook een reality check was als het op sporten aan komt: 60km op de racefiets is meer dan genoeg om te ontspannen.

**Mirte**, dank voor je gezelligheid op de Kemper en de huisloopjes.

**Oscar**, dank dat ik minstens twee dingen van je heb kunnen leren: 1) Tegenwind is een emotie die je kan uitschakelen, 2) het leven is te kort om slechte wijn te drinken.

**Daan**, dank voor de mooie fietsritten die we tot nu toe hebben gedaan. Het wordt tijd dat we weer eens een LBL klassieker doen.

**Olivier**, wat fijn dat je na een lange tijd weer in de buurt bent komen wonen, daar

ergens achter Woerden. Het heeft mij geholpen om ook de laatste anderhalf jaar van mijn promotie op een gezellige manier door te komen.

**Piet** en **Jap**, 'mad ontspannen' klinkt uit jullie mond vaak als een stopwoord, maar het heeft mijn leven veranderd. Deze term reserveer ik voor de zeldzame momenten waarop het lukt om ultieme ontspanning te vinden. Als het dan toch gebeurt, is dat verdacht vaak met jullie, samen met alle andere **huispapa's** natuurlijk.

**Loek**, jij toept over het thema 'ontspanning' heen, kan ik je bedanken voor je stressloze instelling en uitstraling?

**Bas** en **Sander**, dat jullie mij destijds op zijn komen zoeken in Mallorca heeft onze bloedband alleen maar meer versterkt: We zijn toen wel vergeten om het prachtige Magaluf te bezoeken, en als ik die verdediging haal hebben we toch een goede reden voor een examenreisje..

Dank **Sieb**, **Nel** en **Li**, jullie zijn er altijd voor mij geweest en zonder jullie was ik nooit in staat geweest om aan dit promotietraject te beginnen.

**Hans**, wat hoop ik dat je mijn verdediging kan meemaken. Het is in ieder geval heerlijk om dit boekje over plankton toe te voegen aan het lijstje 'De boomstamkano in Indonesië' (Nooteboom, 1932), 'Revision of the symplocaceae of the old world New Caledonia excepted' (Nooteboom, 1975) en 'Adaptieve netwerken' (Nooteboom, 2006).

Dank aan de familie **van der Graaf** en **van Harteveld**, jullie stonden altijd met open armen klaar en zo sociaal als jullie zijn, daar kan ik nog altijd van leren.

**Eef**, wat is het geweldig dat ik jou in mijn leven heb en heb gehad, de afgelopen vier jaar en ook daarvoor. Jij was de 'Vlaai' die af en toe kon zeggen dat het genoeg was met werk en sport, de huispsychologoog die de juiste mentale ondersteuning kon geven, en afgelopen jaar de collega waarmee ik al mijn echte (niet virtuele) koffie en lunch kon eten en drinken.

# About the Author

Peter Nooteboom was born on the 29th of July 1993 in Amersfoort, the Netherlands. After obtaining his high-school diploma in 2011, he enrolled in an undergaduate study about applied mathematics at Utrecht University. After finishing this bachelor program and a few months of back-packing in Southeast Asia, he started the master 'climate physics' in 2015, which was named 'Meteorology, physical oceanography and climate' at the time. He wrote his master thesis about El Niño prediction with machine learning techniques and network theory, under supervision of Prof. dr. ir. Henk Dijkstra at the physical oceanography group of the Institute for Marine and Atmospheric Research Utrecht (IMAU). During the master thesis project, he also worked in Mallorca and collaborated with Prof. Emilio Hernandez-Garcia and Prof. Cristobal Lopez.

After finishing the master program in 2017, Peter continued working at the physcial oceanography group and started the PhD project which lead to this thesis, initially titled 'the emergence of the Antarctic Circumpolar Current.' The PhD has been a collaboration between the Physics and Earth Science departments of Utrecht University, being supervised by Dr. Anna von der Heydt, Prof. dr. ir. Henk Dijkstra, Dr. Erik van Sebille and Dr. Peter Bijl. The PhD allowed Peter to meet scientists all over the world and present his work at international conferences such as EGU (Vienna), the International Conference on Paleoceanography (ICP; Sydney), the Past Earth Network (PEN) Conference (Leeds), the Urbino Summer School in Paleoclimatology (USSP) and the Summer School Mathematics of Planet Earth (Reading).



Sailing at the Jade (near Mellum, Germany)